Star formation : Dynamical study of interstellar dust

Ugo Lebreuilly

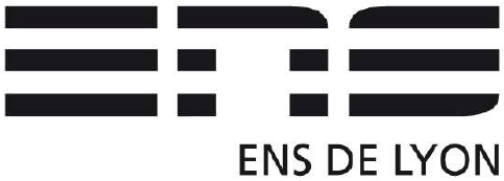

Numéro national de thèse: 2020LYSEN045

THÈSE de DOCTORAT DE L'UNIVERSITÉ DE LYON
Opérée au sein de :
l'École Normale Supérieure de Lyon

Ecole Doctorale No 52
École doctorale de Physique et Astrophysique de Lyon

Spécialité de doctorat : Physique - Astrophysique

Soutenue publiquements le 24/09/2020, par :
Ugo Lebreuilly

Formation d'étoiles:
Étude dynamique de la poussière interstellaire

Devant le jury composé de :

Pr. Romain Teyssier Professeur, CTAC, Université de Zurich	**Rapporteur**
Dr. Geoffroy Lesur Chargé de recherche, IPAG, Université Grenoble Alpes	**Rapporteur**
Dr. Anaëlle Maury Ingénieure de recherche, IRFU, CEA Saclay	**Examinatrice**
Dr. Sylvie Cabrit Astronome 1ère classe, LERMA, Observatoire de Paris	**Examinatrice**
Pr. Rolf Walder Professeur, CRAL, ENS de Lyon	**Examinateur**
Dr. Benoît Commerçon Chargé de recherche, CRAL, ENS de Lyon	**Directeur de thèse**

Remerciements/Acknowledgments

Il est bien évident qu'une thèse ne se fait pas tout seul.

Je tiens donc à remercier en premier lieu Benoît, tout d'abord pour son encadrement sans faille. Que ce soit du point de vue de la physique, du numérique, de l'écriture ou tout simplement de l'humain, il ne m'a jamais fait défaut ! Je le remercie également pour m'avoir fourni tant d'opportunité de voyages et de découvertes durant cette thèse, ces expériences m'ont forgé. En parlant de voyage, il va sans dire que je le remercie d'avoir conduit un pauvre sans-permis lors de nos road-trips en Australie et de ne pas avoir réussi à prendre une photo pendant que je galérais à faire mon lit ! Je le remercie également pour m'avoir supporté et tiré vers le haut pendant nos footings (qui furent parfois pluri-hebdomadaires!) de préparation au Run in Lyon.

Je remercie également Guillaume, qui est un peu mon "oncle de thèse", avec qui la collaboration est extrêmement enrichissante à tous points de vue. Ensuite, je remercie bien entendu Gilles pour son accueil très chaleureux dans l'équipe, pour sa sagesse et pour ses belles histoires. Un grand merci à Stéphanie pour sa gestion incroyable du labo, sans laquelle nous ne serions vraiment pas grand chose (Et aussi pour nous avoir loué son appart au ski ... Mais pas que hein ! ... c.f. la thèse de Florian). Ensuite je remercie tous mes compagnons de thèse en commençant par Maxime. Par où commencer ? Déjà un grand merci pour ton amitié inestimable au cours de ces années de thèse et de master, merci d'être un super colloc' et un musicien d'enfer avec qui j'ai adoré faire de la musique au cours des 4 dernières années ! Merci d'ailleurs de m'avoir supporté en tant que colloc', ce n'est pas chose facile, je sais! Ensuite, je te souhaite un bon courage pour ton intégration de l'équation de smaul..schauml..mochlu, enfin tu as compris ! Tu seras le bienvenu à Paris ! Merci aussi à Etienne et Florian d'avoir supporté mes chansons et autres onomatopées lors de ma thèse ! Merci à Quentin d'avoir géré la consommation de café du labo qui est composée à 80% de la mienne (le reste étant Guillaume et Stéphanie au passage). Arthur, merci de nous avoir rendu l'appareil à raclette, tu sais qu'il est si cher à mon coeur ! Merci également aux deux "Pierres" auxquels je souhaite un bel avenir ! Enfin je remercie tous les autres membres du labo, Christophe, Jérémy, Jenny, Jean-François, Thomas, Rolf etc..., ce remerciement s'étend à tous les physiciens qui s'aventurent dans notre salle de pause, e.g. Barbara (je n'oublie pas de te remercier en plus pour les madeleines !), Benjamin (un des rares à boire plus de café que moi !). Je remercie également Vincent Guillet pour ce début de collaboration prometteuse !

Il est maintenant temps de remercier ma famille. Je pourrais, je pense, écrire une thèse pour remplacer ce paragraphe, mais je vais devoir faire au plus simple. Merci à toi Papa de m'avoir toujours encouragé et d'avoir su partager mes passions pour la science et la musique, pour avoir eu cette patience de corriger mes lettres de motivation d'année en années. Merci pour ces voyages aux quatre coins du monde ces dernières années et merci enfin pour m'avoir donné le virus de la pêche et plus globalement l'amour de la nature. Merci à Maman de faire preuve d'une patience et d'un support sans faille ! Tu m'as bien entendu aussi toujours soutenu dans mes passions, tu as essayé (et c'est bien difficile avec moi) de m'apprendre l'application tout au long de ma vie et j'essaie toujours de m'en montrer digne ! Je pense qui c'est toi qui m'a

donné le virus de la science et une âme d'artiste ! Merci à vous deux de m'avoir fait grandir (pas assez du point de vue de la hauteur à mon goût, mais bon) tout au long de ces 28 années (et m'avoir forcé à faire mes devoirs) ! Merci à mes deux frères, José et Marin, même si on est taquins je dois vous le dire que j'aime énormément vous retrouver pendant les vacances, c'est un bol d'air frais pour moi. Cela va sans dire, je remercie ma famille dans son intégralité, Mamie Solange et Grand-mère, je n'oublie pas Coco qui me manque énormément, toutes mes tantes et mes oncles, les cousins et les cousines ! Et à ma famille, je tiens sincèrement à inclure tous les copains de Normandie (par ordre alphabétique, car je vous aime tous autant),Alex', Antoine, Antonin, Arthur, Baptiste, Edgar, Gweltaz, J-F, Jonathan, Timon etc... Je remercie tous mes autres amis !

Enfin, je veux absolument remercier ma petite Kaplan, seni seviyorum. Si ces trois dernières années ont été si bonnes (les meilleures !) c'est surtout grâce à toi. Il est, bien entendu, impossible de quantifier par les mots (ou par les nombres!) le bonheur et la joie que tu m'apportes au quotidien depuis que tu es entrée dans ma vie (best Halloween ever) ! Un grand merci à toi Nihan, pour ton soutien, ton amour, ton amitié ainsi que ta salakitude (private joke que personne ne va comprendre, mais c'est pas grave!). Cette thèse est dédiée à la vie que l'on construit ensemble chaque jour et aux nombreux bonheurs qu'elle va nous réserver.

I would like to thank two English speakers now. First, I deeply thank Mordecai, from whom I have learned so much and for giving me this amazing opportunity to collaborate with him for three months at the American Museum of Natural History in New York. It was a life changing opportunity for me and I hope that we will keep collaborating in the future. I also deeply thank Daniel for welcoming me for two amazing months at the Monash University, for the great chats during coffee breaks and his guidance on understanding dust dynamics ! I consider myself very lucky to collaborate with these two amazing people !

Résumé

Le milieu interstellaire se compose, en masse, d'environ 1% de poussière. Paradoxalement, malgré sa faible concentration, celle-ci un rôle très important dans la formation stellaire. La dynamique des grains de poussière peut différer de celle du gaz, entrainant des variations locales de concentration. Peu de travaux ont pourtant été consacrés à l'étude de cette dynamique différentielle lors de la formation stellaire. Ma thèse s'inscrit dans l'objectif de pallier ce manque et se décompose en quatre parties.

Dans la première partie, je développe un module traitant efficacement la dynamique des poussières et pouvant simultanément inclure plusieurs espèces de grains pour le code multi-dimensionnel sur grille adaptative `RAMSES` (Teyssier, 2002). Je teste ensuite mon module avec soin en comparant mes résultats à des solutions analytiques. Je montre par ailleurs que mon implémentation est robuste, précise et rapide.

Par la suite j'effectue des simulations de formation d'étoiles incluant plusieurs espèces de poussières. Grâce à cette étude, j'établis qu'un découplage entre les grains et le gaz apparaît pour les grains d'une taille supérieure ou équivalente à la centaine de micromètres. Je trouve également que ce découplage dépend fortement des propriétés initiales du coeur préstellaire.

Ensuite, je développe un formalisme analytique, similaire à la magnétohydrodynamique non idéale, mais incluant en plus la dynamique des grains chargés. Ce formalisme me permet de mettre en évidence différents régimes de couplage entre les grains, le champ magnétique et le gaz, selon la taille des grains, leur charge et leur environnement.

En parallèle, j'étudie la dynamique des poussières dans les zones faiblement ionisées des disques protoplanétaires afin d'étudier la formation des chondrules. Ce sont des grains de poussière retrouvés dans la majorité des météorites et qui sont des éléments clés pour la compréhension de la formation des disques et des planètes.

Abstract

The interstellar medium is composed by approximately 1% of dust in terms of mass. Surprisingly, this tiny amount of dust already plays a very important role in stellar formation. The dynamics of dust grains may differ from that of the gas particles, leading to local variations in concentration. However, very few studies have focused on the gas and dust differential dynamics during star formation. My thesis aims to fill this gap and is divided into four parts.

In the first part, I develop a module dealing efficiently with dust dynamics that can simultaneously include multiple grain species intended to the multidimensional adaptive grid code `RAMSES` (Teyssier, 2002). I then carefully test my module by comparing my results with known analytical solutions. I also show that my implementation is robust, fast and accurate.

Then I perform star formation simulations that consider multiple dust species. This study establishes that a decoupling between the dust and the gas appears for grains of sizes larger or equivalent to a hundred micrometers. I also find that this decoupling strongly depends on the initial properties of the prestellar core.

Then, I develop an analytical formalism, similar to the non-ideal magnetohydrodynamics but that includes the dynamics of charged grains. This formalism allows to highlight different coupling regimes between the grains, the magnetic field and the gas as a function of the grain size, its charge and its environment.

In parallel, I investigate the dynamics of dust in the weakly ionized zones of protoplanetary disks in order to study the formation of chondrules. Chondrules are dust grains found in most meteorites and are key to understand the formation of disks and planets.

Contents

Chapter 1

The life of gas and dust during star formation

Contents

"A long time ago in a galaxy far, far away ... "

- Star Wars

In this introductory chapter, I report our current understanding of stellar and disk formation as well as of the dust content of the interstellar medium (ISM). In that aim, I introduce star and disk formation from an observational point of view. Then, I shortly review the observational evidences of dust grains in the ISM. Finally, in the light of our current theoretical understanding of star formation, I explain why it is essential to understand the dynamics of dust grains in this context.

1.1 Introduction

Astronomy is at least as old as civilization. Historically, the stars and the celestial objects of the solar system such as the moon, the planets inside Saturn's orbit and of course, the sun, were the first source of wonder of astronomers. Archaeologists have found evidences that they were thoroughly studied in the Babylonian and Egyptian empires but also in the early Chinese, Indian and Mesoamerican societies. Yet, the general structure, composition and formation of stars were not understood until the XXth century.

In 1919, Jean Baptiste Perrin and Arthur Eddington proposed first that the sun was fueled by nuclear reactions within its core. A few years after, in 1925, Cecilia Payne-Gaposchkin discovered that the sun, a fairly typical star, was primarily made of Hydrogen and Helium. James Jeans understood in 1902 how stars were formed during the gravitational collapse of unstable giant nebula, known today as molecular clouds. Later, in 1930, Robert Trumpler discovered that these clouds were not only composed of gas, but they also contained small interstellar dust grains, the seeds of planets. The global picture of star formation in these molecular clouds and its relation to planet formation started to become clear in the 1960s with the rise of computer simulations such as the ones of Richard Larson, Peter Bodenheimer, Werner Tscharnuter and Alan Boss. The increase in computational power since the 1960s allowed astronomers to elaborate more sophisticated models of astrophysical objects, including more relevant physical processes such as magnetic fields, radiation etc..

Meanwhile, the colossal progresses made in observational astrophysics during the last 40 years revealed that the star and planet forming interstellar medium was far from being understood in the details. Space telescopes, such as Spitzer or Hubble, have shown that molecular clouds were made of very complex filaments and were driven by the interaction between turbulence, gravitation and magnetic fields. In 1995, Michel Mayor and Didier Queloz discovered the first exoplanet around a solar type star, 51-Pegasi. Since then more than 4000 planetary systems of incredible diversity have been discovered around stars within the sun neighborhood. Within the last ten years, giant interferometers such as the *Atacama Large Millimeter/submillimeter Array* (ALMA) were able to probe young stars and their planet forming disks, also called protoplanetary disks, revealing once again a surprising diversity of morphology.

Modern astrophysicists now have the technical possibility to go much further into the details than their predecessors when describing astrophysical objects. In that vein, the goal of this thesis is to add a new ingredient, traditionally overlooked and yet recently suspected of impacting quantitatively star formation processes: the dust dynamics.

1.2 The young life of stars

1.2.1 An overview on low mass star formation

Low mass stars, with masses smaller than a few $M_\odot$ [1], are the most abundant stars in the *Universe*. It is widely accepted that their formation takes place during three main stages (Andre et al., 2000)

- The *prestellar phase*, during which the parent molecular cloud, mostly composed of molecular hydrogen with a temperature of $\sim$ 10 K, undergoes an isothermal collapse in the regions where the thermal support is insufficient to counteract the effects of gravity. During this phase, the temperature remains almost constant as the gravitational energy

[1] $M_\odot \approx 1.9 \times 10^{33}$g the mass of the sun

is radiated away by the thermal dust emission. The free-falling material tends to show a universal density profile of $\rho \propto r^{-2}$ (Foster & Chevalier, 1993). Eventually, the collapse is stopped where the density reaches the typical value $\rho_{\rm ad} \sim 10^{-13}$ g cm^{-3} (Larson, 1969). At such high densities, the radiation becomes trapped in the core, mostly because of the dust absorption. This region of the cloud is in quasi-static equilibrium and is called the *first Larson core* that has a typical density of $\rho \sim 10^{-11}$ g cm^{-3} . As the radiation is cannot escape the core, the latter is in adiabatic contraction which causes the temperature to increase. Once it reaches $\sim$ 2000 K, H_2 starts to dissociate and a *second collapse* is triggered as the former reaction is endothermic. Once H_2 has completely dissociated, the newly formed *second Larson core*, begins a slow adiabatic contraction with an effective polytropic index $\gamma_{\rm eff} \sim 1.1$ (Masunaga & Inutsuka, 2000). This object has a typical density of $\rho \sim 1$ g cm^{-3} and a radius of a few solar radii [2].

- After the *second Larson core* formation, the *protostellar phase* begins. During this phase, the protostar mass increases by the accretion of the free-falling envelope. Conservation of angular momentum during the collapse has led to the formation of an accretion disk, also called a *protoplanetary disk* and the most probable birthplace of planets. Simultaneously, a fraction of the mass is being ejected from the system by bipolar outflows (Bachiller, 1996) most probably driven by magnetic fields.

- When the star almost reaches its final mass and when its temperature has become high enough to burn the deuterium at $\sim 10^6$ K it enters the *pre-main sequence phase* (PMS). The pre-main sequence protostar, now optically visible, contracts until hydrogen fusion is triggered when the peak temperature reaches $\sim 10^7$ K. At this stage, a star is born. It is on the so-called *main sequence* where it awaits its final fate as a planetary nebula or a supernova if its massive enough.

1.2.2 Observational evolutionary sequence

Young stellar objects (YSOs) are classified by observers according to their *spectral energy distribution* (SED) in the near and mid-infrared. More precisely, they are classified according to the logarithmic slope $\alpha_{\rm IR} = \frac{{\rm d}\log(\lambda F_\lambda)}{{\rm d}\lambda}$, F_λ being the radiative flux at the wavelength λ. At first, three different classes of objects were distinguished, the classes I to III.They correspond to objects that are increasingly evolved in time. Class I ($\alpha_{\rm IR} > 0$) are very early YSOs, but they already are in the protostellar phase. They might be surrounded by an early protolanetary disk and still have a massive envelope. The two most evolved classes, Class II ($-1.5 < \alpha_{\rm IR} < 0$) and III ($\alpha_{\rm IR} < -1.5$) are PMS stars or, equivalently, *T Tauri stars*[3]. Class II are surrounded by a protoplanetary disk while Class III are surrounded by a *debris disk*. Debris disks are not old protoplanetary disks but rather the consequence of them. They are mostly composed of reprocessed dust grains (less than $\approx 1-100$ µm) resulting of collision between small protoplanetary bodies.

Another earlier stage, the Class 0, was discovered by Andre et al. (1993). At this stage, a deeply embedded protostar is already formed but it is still less massive than the envelope. The age of the Class 0 objects has been estimated to be about 10^4 years (Barsony, 1994).

The empirical evolutionary sequence is summarized in the cartoon illustration of figure 1.1. Since the initial classification of YSOs, impressive developments have been made to improve our observational capabilities. The SEDs that were the original probes of protostars are now

[2] the solar radius is $R_\odot \approx 6.96 \times 10^{10}$ cm

[3] T Tauri is a YSO located in the Taurus constellation

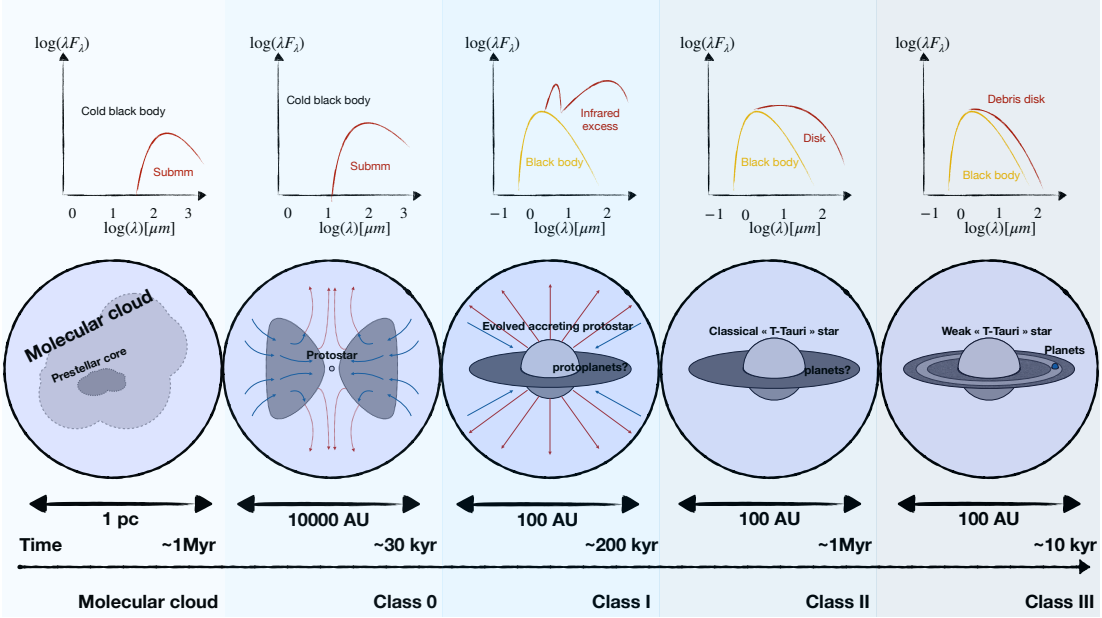

Figure 1.1: Observational evolution sequence of star formation. Cartoon illustration inspired from André (2002). Molecular clouds are cold clouds where star formation occurs, they live a few millions years. Once the protostellar collaspe starts in a molecular cloud, the prestellar core evolve through four classes. They are the observational evidence of the protostellar phase.

completed with resolved observations of molecular line emission (the most commonly observed molecule is CO), dust continuum or polarized emission.

1.3 Protoplanetary disks

1.3.1 Protoplanetary disks observations

During the protostellar collapse, a disk forms around the protostar because of angular momentum conservation. This so-called protoplanetary disk is most likely were planets are formed. If these disk where theorized (Von Weizsäcker, 1944; Gamow & Hynek, 1945; Hoyle, 1960; Terebey et al., 1984) and indirectly observed via SEDs (Mendoza V., 1968) quite early, the recent rise of highly sensitive and resolved ground based interferometers such as ALMA have completely changed our perspectives about them.

A large number of evolved protoplanetary disks[4] have been observed in recent campaigns such as the *Disk Substructures at High Angular Resolution Project* (DSHARP, Andrews et al., 2018; Huang et al., 2018a,b). The wide variety of structures of these disks is striking, indicating that their formation and evolution invoke complex physical processes. The most commonly observed structures of protoplanetary disks are

- *Cavities*. They are often observed in the inner regions of the disks and have typical sizes of $\sim$ 10 AU [5]. These cavities are most likely to be opened by MHD winds (Suzuki et al., 2016) or photoevaporation (Alexander et al., 2014).

- Annular *Gaps*. They are another commonly observed pattern. The most common explanation for their presence is embedded protoplanets (see Papaloizou & Lin (1984) for

[4] around T-Tauri like stars
[5] 1 AU = $1,496 \times 10^8$km

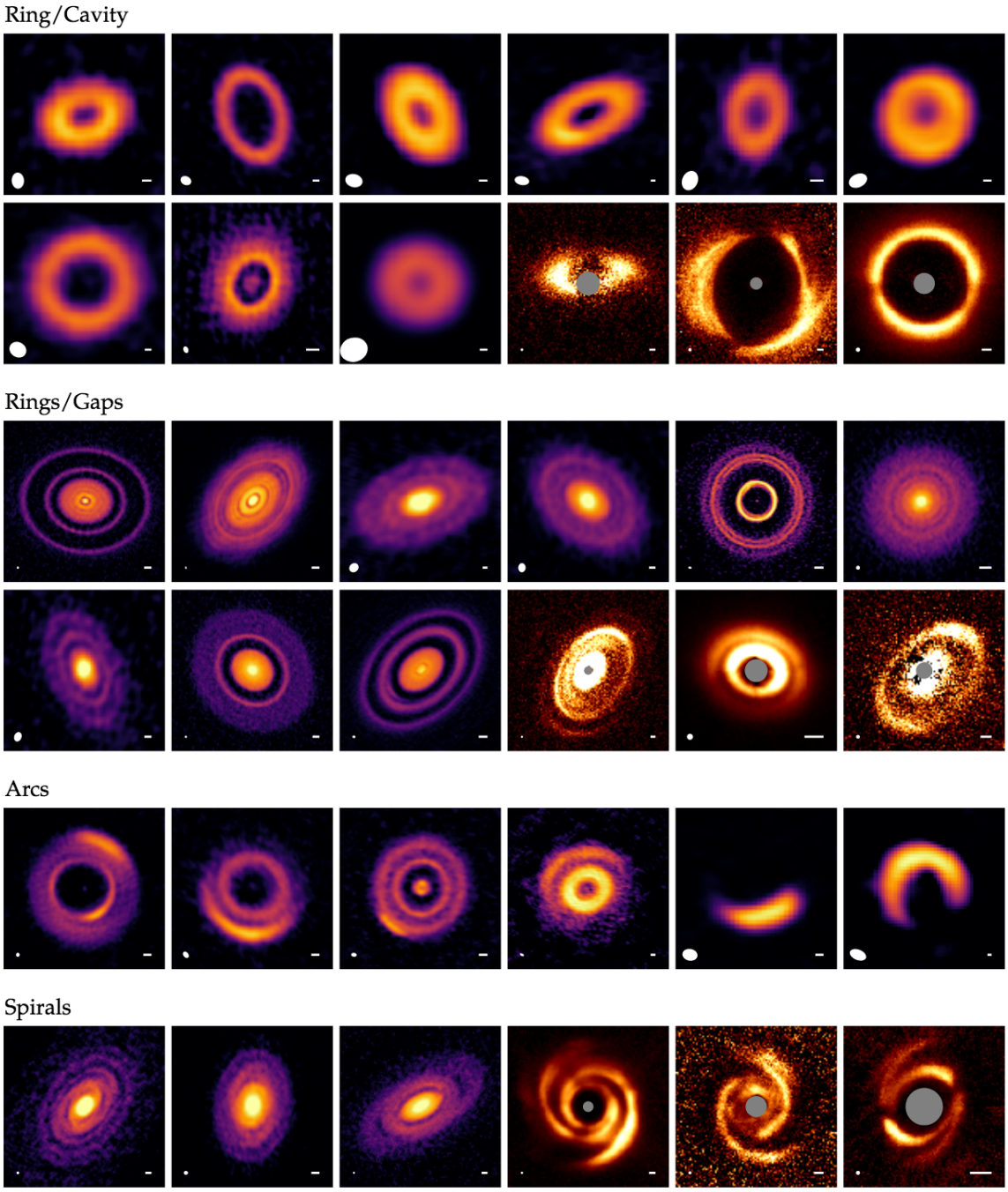

Figure 1.2: Gallery of observed evolved protoplanetary disks taken from the review Andrews (2020) showing the most commonly observed substructures of protoplanetary diks.

the theory and Pinte et al. (2019) for the recent observational evidence), non-ideal MHD effects (Ruge et al., 2016) or dust traps (Gonzalez et al., 2015).

- Non-axisymmetric *Arcs*. They are rarer structures that are most often observed around the inner cavities and eventually at the outer cavities or near a gap. Binary star interaction is the most frequently invoked mechanism for their formation (Ragusa et al., 2017; Price et al., 2018).

- *Spirals*. They are also often seen in protoplanetary disks. They usually show preferential $m = 2$ mode but can also exhibit some asymmetry. Their formation is usually explained by binary interaction (Price et al., 2018) or by rotating gas accretion (Hennebelle et al., 2017).

A gallery of protoplanetary disks exposing these most common structures can be seen in figure 1.2.

Recently, younger disk candidates have also been observed around Class 0 stars using the dust continuum emission and the molecular line emission (e.g. with the CO and SO molecule). It is a challenging task to get precise observations of them as they are still deeply embedded in a massive envelope. By observing the $C^{18}O$ ($J = 2 - 1$) and SO ($J = 6_5 - 6_4$) line emission of L1527 IRS, which is either a Class 0 or a Class I protostar, with ALMA, Ohashi et al. (2014) have found evidence of a keplerian disk. They claim to observe a disk with a radius of about $\sim$ 50 AU. This is significantly smaller than the size of the evolved disks around T-Tauri stars (in average $\sim$ 165 AU, Isella et al., 2009) and is an evidence that disks are formed quite small and increase in size during their evolution. Using the IRAM Plateau de Bure Interferometer for the CALYPSO (Continum And Lines in Young ProtoStellar Objects) survey, Maury et al. (2019) have observed 16 Class 0 and Class I objects where at least 11 are potentially surrounded by an early disk. Summarizing their results and those from other surveys they claim that disk around Class I protostar have median radii of $\sim$ 100 AU while this value is smaller that $\sim$ 50 AU for disk around Class 0 objects (see Tobin et al., 2020, for similar findings).

1.3.2 Exoplanets

Since the discovery of the first exoplanet *51 Peg b* around a solar type star by Mayor & Queloz (1995)[6], more than 4000 were either indirectly (with *Kepler*, *CoRot*, *HARPS* etc.) or directly observed (with *SPHERE*, *GPI* etc.). Figure 1.3 shows the mass as a function of the orbital period for a catalog of confirmed exoplanets generated using the website *exoplanet.eu*. The diversity of planets in terms of mass, radius, orbit, composition etc is already striking in the solar system where we observe 4 *telluric planets* (*Mercury*,*Venus*, the *Earth* and *Mars*), 2 *gas giants* (*Jupiter* and *Saturn*) and 2 *ice giants* (*Uranus* and *Neptune*). A wide diversity of exoplanets such as, *super-Earths* (Charbonneau et al., 2009; Borucki et al., 2011), *hot-Jupiter* (Mayor & Queloz, 1995), *ocean planets* (Charbonneau et al., 2009) etc., were recently discovered. This is unequivocally an evidence that their formation and evolution is complex and cannot only be explained by a model designed to understand the solar system solely. As explained in section 1.3.1, protoplanetary disks, that are the most probable locus of planet formation via dust *grain growth* (see the recent review by Birnstiel et al., 2016), are also very diverse in terms of shape and mass. Although it is difficult to correct bias in disks and exoplanets detection, it is natural to think that the diversity in protoplanetary disks and in exoplanets are connected. Therefore understanding star and disk formation is necessary to constrain planet formation which could, eventually, lead to an answer to the fundamental question: how do Earth-like planet form?

1.4 Dust in the interstellar medium

The *interstellar medium* (ISM), is defined as anything, matter or radiation, that lies between stellar system but is still in a galaxy. Although the dust grains represent a relatively small mass fraction of the ISM (about 1:100 Mathis et al., 1977; Weingartner & Draine, 2001), they are essential for its observation. In this section, I briefly review some of the major aspects of dust observations that are relevant in the star formation context.

[6]Nobel Prize in 2019

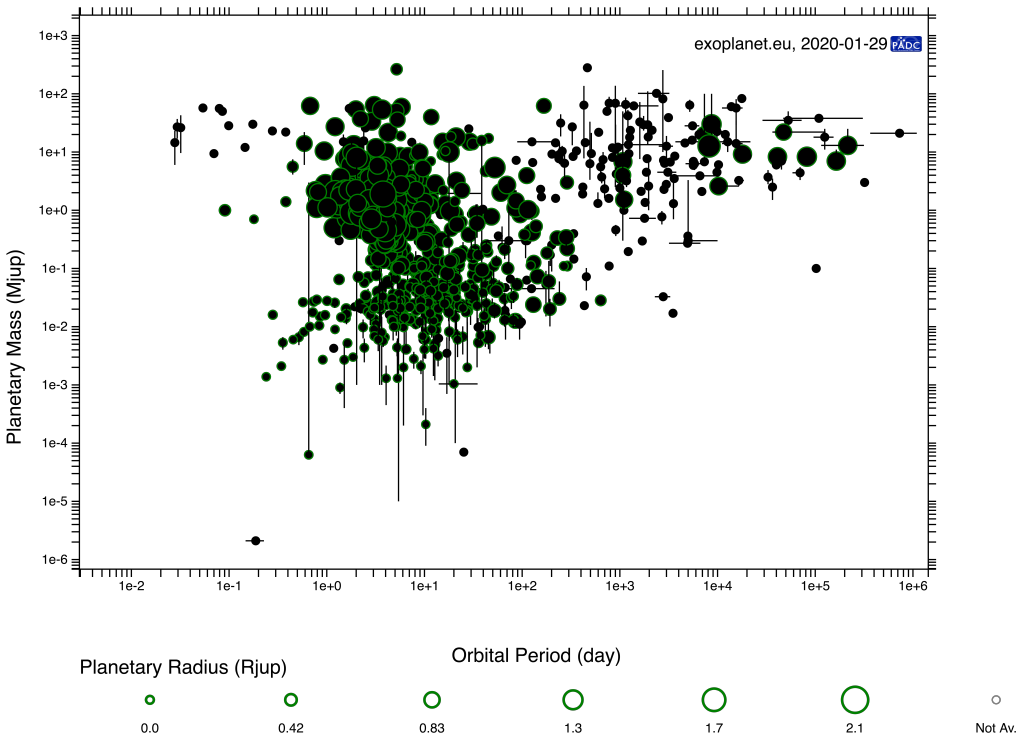

Figure 1.3: Catalog of the confirmed exoplanets generated using the website *exoplanet.eu* the 29th of January 2020. Planetary mass (in Jupiter mass) against the orbital period (in days). The radius of the planet is indicated by the size of the green circle when available.

1.4.1 Extinction

(a) Dust obscured cloud in NGC281 observed by the *Hubble* space telescope. Some of the regions of the cloud are reddened and some are so dense that even the red light does not penetrate (Credits: NASA/ESA).

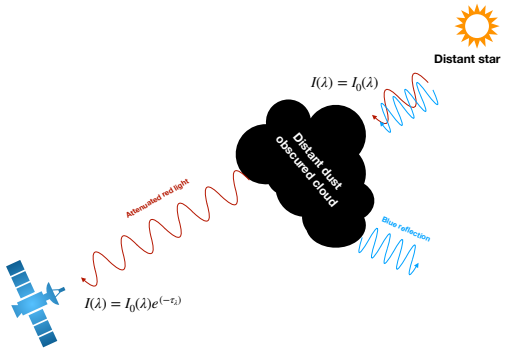

(b) Cartoon illustration explaining the dust extinction process. The blue light is almost completely absorbed by the dust while some of the red light can penetrate all the way through. A blue reflection, due to scattering by the dust grains, can be observed when the cloud is illuminated on the same side as the observer is.

Figure 1.4: Dust extinction process.

Extinction has been discovered in the early 20$^{\text{th}}$ century (Barnard, 1907, 1910). If in appearance it seemed like an *"absence of stars"*, Barnard understood that what he observed was a *"dark nebula"*. It was later established by Trumpler (1930) that this darkening of light was produced by fine interstellar dust particles.

Let us consider a star at a distance d, with an apparent magnitude $m_{\text{obs},\lambda}$ at a wavelength λ. The dust extinction A_λ is defined as

$$A_\lambda \equiv m_{\text{obs},\lambda} - m_\lambda, \tag{1.1}$$

m_λ being the apparent magnitude of the star if there was no extinction. It is related to the absolute magnitude of the star M_λ by the formula $m_\lambda \equiv M_\lambda + 5\log\left(\frac{d}{5\text{pc}}\right)$. If the star light, of specific intensity $I_0(\lambda)$, is absorbed by an uniform dust cloud of optical depth τ_λ, the intensity measured by the observer is $I_0(\lambda)e^{-\tau_\lambda}$. From the definition of the magnitude, we can show that in this case

$$A_\lambda \approx 1.086\tau_\lambda. \tag{1.2}$$

The extinction allows to estimate the optical depths of the cloud, which can be linked to the opacity and the grain properties.

Fitting the interstellar extinction at wavelengths ranging from infrared to ultraviolet and supposing that grains were composed of graphite and silicates, Mathis et al. (1977) were able to model the dust grain size distribution in the diffuse ISM. They have shown that this so-called *Mathis-Rumpl-Norsieck or MRN* size distribution was quite well approximated by a power-law. For a grain species of size $s_{\text{grain}} \in [\,5\text{nm}, 0.25\mu\text{m}\,]$, the number density $n\left(s_{\text{grain}}\right)$ scales as

$$n\left(s_{\text{grain}}\right) \propto s_{\text{grain}}^{-3.5}. \tag{1.3}$$

An interesting property of this size-distribution is that the number and surface is mostly in small grains while the mass that scales as $\propto s_{\text{grain}}^3$ is dominated by the larger grains. As we will see later the decoupling between the gas and the dust grains is mainly driven by the grain size so we can wonder : is the MRN distribution well preserved during star formation?

1.4.2 Continuum emission

Thermal emission of interstellar dust grains is a powerful observing tool. If we consider a grain of temperature T_{grain}, at the *local thermodynamic equilibrium* (*LTE*) and according to Kirchhoff's law (Kirchhoff, 1859), it behaves as a black body. The ratio between its emissivity ε_ν (expressed in erg s^{-1} Hz^{-1} ster^{-1}) and its absorption coefficient or opacity κ_ν^{abs} is thus equal to the Planck function at the temperature T_{grain}. In other words

$$\varepsilon_\nu = \kappa_\nu^{\text{abs}} B_\nu\left(T_{\text{grain}}\right). \tag{1.4}$$

This expression means that the light absorbed by the dust grains is re-emitted at a wavelength dependent efficiency. This so-called *thermal emission* or *dust continuum emission* is most efficient at wavelengths of the order of the grain size s_{grain} and thus provides an idea of its value. In the diffuse ISM and in molecular clouds, dust thermal emission is observed in the *infrared* (IR) and the *far infrared* (FIR), indicating dust sizes typically smaller than a micron. It is worth noting that in *L183*, a dense region of a molecular cloud, an unexpected peak of emission at 3.6 μm indicates the possible presence of micrometer (and even $\sim$ 10 μm) dust grains (coreshine, see Pagani et al., 2010). In protoplanetary disks, dust thermal emission can be observed at radio wavelengths indicating millimeter grains (see figure. 1.2). It appears that

the maximum dust grain size increases with density (see Section. 1.4.3 for intermediate densities between *L183* and protoplanetary disks). A multi-scale and extensive dust evolution study should thus be devoted to determine if this is due to dust growth, dynamical segregation of dust grains, both or a misinterpretation of the observations.

In addition, as the opacity typically traces the dust column density, the dust continuum is often used in observations as a proxy for the gas density, assuming a certain *dust-to-gas mass ratio* [7]. Typically the *dust-to-gas ratio* is assumed to be 1:100 (Mathis et al., 1977). Some notable object observed with the dust continuum emission are protoplanetary disks (see figure. 1.2), molecular clouds, galactic disks, supernovae remnants etc. A natural question can be asked : is the dust-to-gas ratio really uniform or constant in these objects and can we use dust to trace the gas? This question is addressed in the case of the protostellar collapse in Chapter 4.

1.4.3 Polarized emission

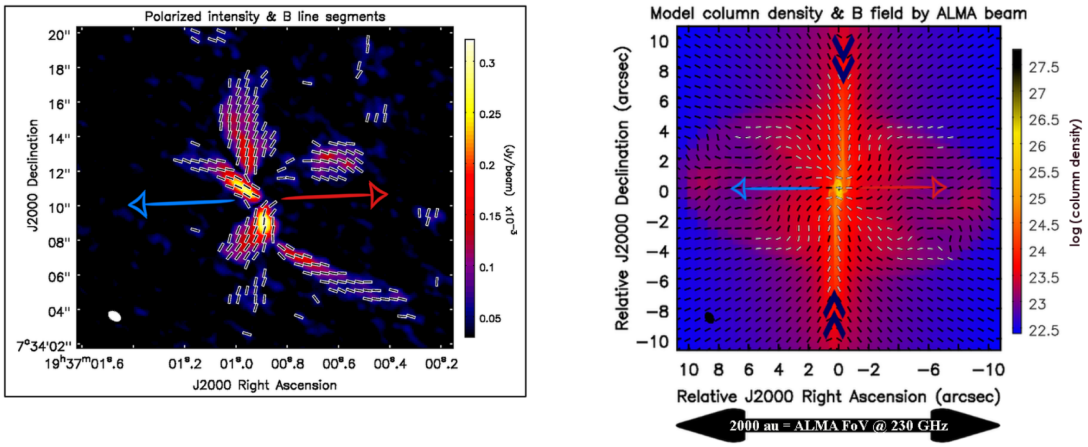

Figure 1.5: (Left) polarized dust continuum emission and magnetic field direction inferred from the dust polarization angle (black lines). (Right) column density corrected with the ALMA beam for a magnetically regulated collapse and magnetic field direction (grey and black lines). Only the grey magnetic fields can be detected with ALMA's sensitivity. The arrows at the two poles indicate the main direction of the inflow. In both figures, the red and blue arrow indicate the direction of the outflow. The horizontal black arrow shows the size of ALMA's field of view at 230GHz.

Interstellar dust grains are typically non-spherical, they are usually elongated in their semi-major axis. One of the consequences of their asymmetry is that dust emission observed from earth can be polarized if grains are in average aligned with a particular axis. The properties of the dust polarized emission can provide some information on the object of interest if the grain alignment mechanism is understood.

Two aspects of dust polarization are particularly interesting in the context of this thesis.

- In a magnetized environment, dust grains are believed to align perpendicularly to the magnetic fields (Lazarian & Hoang, 2007). The polarization angle can therefore be used to determine the direction of the magnetic field for various kind of sources. With the interferometer ALMA, Maury et al. (2018) claim to have measured the direction of the magnetic field in the Class 0 protostar B335. Their measurement seems in very good

[7] *dust-to-gas ratio* hereafter

agreement with a magnetic protostellar collapse simulation made with the RAMSES code (Teyssier, 2002, see Chapter 3 for details on the code and Chapter 4 for details on collapse calculations), which is a strong argument in favor of a magnetically dominated collapse. The left panel of figure 1.5 shows the polarized dust continuum emission of B335 and the direction of the magnetic field inferred from the dust polarization angle. The results of the collapse calculation are displayed in the right panel. It shows a column density estimate, taking into account the distance of the object, and the magnetic field direction.

- It was theorised by Kataoka et al. (2015) that large dust grains could scatter light with high polarization degrees. They demonstrated that this so-called *self-scattering* is efficient when the grain size is of the order of $\approx \frac{\lambda}{2\pi}$. Recent studies (Sadavoy et al., 2018a,b, 2019) later found evidences of self-scattering in millimeter observation of Class 0 protostars which might indicate the presence of 100 µm grains in these objects. This is particularly interesting because this size is intermediate between the potential 10 µm grains supposely at the origin of the coreshine of molecular clouds (Pagani et al., 2010) and the millimeter grains observed in evolved protoplanetary disks.

1.4.4 Interplanetary dust and chondrules

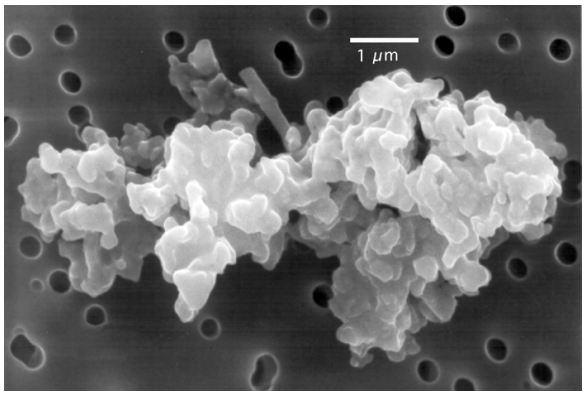

(a) Taken from (Jessberger et al., 2001). Interplanetary dust grain (*porous chondrule* collected in the stratosphere) taken with a scanning electron microscope. The aggregate is non-spherical and larger than 10 µm.

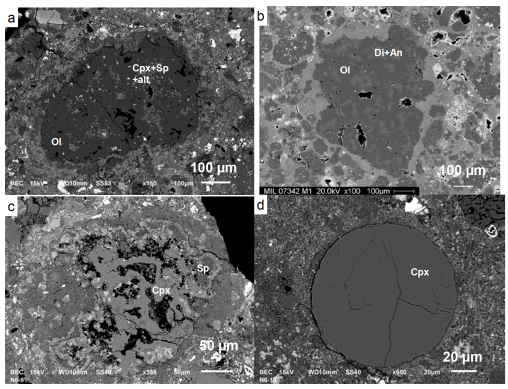

(b) Taken from Jacquet & Marrocchi (2017) (collection of the Muséum National d'Histoire Naturelle de Paris). Back-scattered electron images of various chondrules from the NWA 5958 meteorite (a,c and d) and AOA N1-14 meteorite (b). The diversity in shape, composition and size is striking.

Figure 1.6: Laboratory evidences of cosmic dust (left) and meteoric dust (right).

On Earth, we have no direct access to interstellar dust, however it is possible to collect grains from the solar system with balloons, U2 aircrafts or even spacecrafts (e.g. with *Pionner 10* and *11*, *Ulysse* and *Galileo* aroung Jupiter and *Cassini* around Saturn). This so-called *interplanetary dust*, better known as *cosmic dust*, although being reprocessed during the formation and evolution of the solar system, are essential to understand the more distant and unavailable interstellar dust grains. Figure 1.6a shows an example of interplanetary dust grain, collected in the stratosphere, taken with a scanning electron microscope and presented by Jessberger et al. (2001). Among other things, one can see that it is rather large (about 10 µm×20 µm) compared to the grains expected from the diffuse ISM, which indicates that it has undergone dust growth at some point of its evolution. It is an aggregate made of smaller dust grains and is clearly

non-spherical. Laboratory studies of such dust grains suggest that their intrinsic density are most of the time comprised between ~ 1 g cm^{-3} and ~ 3 g cm^{-3} (Love et al., 1994). According to the same study, the grain densities can, in rarer cases, reach values as low as 0.3 g cm^{-3} and as high as 6 g cm^{-3}.

Another way to indirectly probe the properties of interstellar dust is through meteorites. They have the advantage of being directly found on Earth but the disadvantage of being more strongly reprocessed than isolated dust grains. Found in most of the chondrites, that represent 80% of the meteorites, *chondrules* among the most abundant meteoritic material. They are almost spherical grains of sizes ranging from a few µm to ~ 1 cm. They are mainly composed of silicate minerals such as *olivine* or *pyroxene* but, in the details, they do present a wide diversity of composition (see figure 1.6b for some example of chondrules). Some evidences suggest that chondrules are formed by successive fast heating events[8] where they reach temperatures as high as a few 2000 K during a few minutes of even less followed by a slow cool down (Connolly et al., 1998). How these flashes occur and where chondrules are formed is still under debate. Joung et al. (2004) proposed that non-ideal magnetohydrodynamics (MHD) effects could generates strong and very localized current sheets where the flash and thus the chondrule formation could occur. I investigate this theory in Chapter 6.

1.5 Theory of star formation: essentials

In this section, I briefly review some of the fundamental theoretical knowledge of the protostellar collapse. Although simplified up to some extent, the theoretical concepts introduced below cover many key aspects of the dynamics of star formation and can be further refined when required. This kind of approach represents the backbone of an extensive number of studies in the field.

1.5.1 Virial equilibrium

The state of a self-gravitating cloud can be described by the *Virial theorem* (Clausius, 1870). If we consider a particle of mass m_p at a position $\mathbf{r}$ and subject to a force $\mathbf{F}$, according to Newton's second law

$$m_\mathrm{p} \frac{\mathrm{d}^2\mathbf{r}}{\mathrm{d}t^2} = \mathbf{F}, \tag{1.5}$$

by multiplying this equation by $\mathbf{r}$, one can show that

$$m_\mathrm{p} \frac{\mathrm{d}}{\mathrm{d}t}\left(\mathbf{r}\cdot\frac{\mathrm{d}\mathbf{r}}{\mathrm{d}t}\right) = m_\mathrm{p}\left(\frac{\mathrm{d}\mathbf{r}}{\mathrm{d}t}\right)^2 + \mathbf{F}\cdot\mathbf{r}. \tag{1.6}$$

We now consider $\mathcal{N}_\mathrm{p}$ particles j with masses $m_{\mathrm{p},j}$. From equation (1.6), we obtain

$$\frac{1}{2}\frac{\mathrm{d}^2\mathcal{I}}{\mathrm{d}t^2} = 2E_\mathrm{k} + \sum_j^{\mathcal{N}_\mathrm{p}} \mathbf{F}_j\cdot\mathbf{r}_j, \tag{1.7}$$

where $\mathcal{I} = \sum_j^{\mathcal{N}_\mathrm{p}} m_{\mathrm{p},j}\mathbf{r}_j^2$ is the inertial momentum of the system and $E_\mathrm{k} = \frac{1}{2}\sum_j^{\mathcal{N}_\mathrm{p}} m_{\mathrm{p},j}\left(\frac{\mathrm{d}\mathbf{r}}{\mathrm{d}t}\right)^2$ its kinetic energy.

[8] called *flashs* hereafter

Let us consider the simple case where the particles are only interacting via the gravitational force. Then $\sum_j^{\mathcal{N}_\mathrm{p}} \mathbf{F}_j \cdot \mathbf{r}_j$ is exactly the gravitational potential energy of the system $E_\mathrm{p} = -\sum_i^{\mathcal{N}_\mathrm{p}} \sum_{i\neq j}^{\mathcal{N}_\mathrm{p}} m_{\mathrm{p},j} \mathbf{r}_j \frac{\mathcal{G} m_{\mathrm{p},i}(\mathbf{r_j}-\mathbf{r}_i)}{|\mathbf{r}_j-\mathbf{r}_i|^3}$ where $\mathcal{G} \simeq 6.67 \times 10^{-8}$ cm^3 g^{-1} s^{-2} is the gravitational constant. If the system is in the so-called *Virial equilibrium* then necessarily $\frac{\mathrm{d}^2 \mathcal{I}}{\mathrm{d}t^2} = 0$ and

$$E_\mathrm{p} = -2E_\mathrm{k}. \tag{1.8}$$

If a cloud satisfies this condition, it means that its thermal support is perfectly balancing its self-gravity and the cloud is stable against the *gravitational collapse*. The stability of a cloud can thus be expressed in terms of a dimensionless parameter α, the *thermal-to-gravitational energy ratio*, that writes as

$$\alpha = \frac{E_\mathrm{k}}{|E_\mathrm{p}|}. \tag{1.9}$$

For the cloud to be stable against gravitational collapse one must have $\alpha > \frac{1}{2}$. In the simplified case of an isothermal and spherical cloud of mass M_0, radius R_0 at temperature T_g and mean molecular weight μ_g we obtain

$$\alpha = \frac{5}{2} \frac{R_0}{\mathcal{G} M_0} \frac{k_\mathrm{B} T_\mathrm{g}}{\mu_\mathrm{g} m_\mathrm{H}}, \tag{1.10}$$

where $k_\mathrm{B} \simeq 1.38 \times 10^{-16}$ erg K^{-1} is the Boltzmann constant and $m_\mathrm{H} \simeq 1.66 \times 10^{-24}$ g is the proton mass.

Using the stability condition $\alpha > \frac{1}{2}$, one can determine that this cloud will be unstable against gravity if its mass is larger than the so-called *Jeans mass* M_J (Jeans, 1902) that writes

$$M_\mathrm{J} = \left(\frac{5 k_\mathrm{B} T_\mathrm{g}}{\mu_\mathrm{g} m_\mathrm{H} \mathcal{G}}\right)^{3/2} \left(\frac{3}{4\pi\rho_0}\right)^{-1/2}, \tag{1.11}$$

ρ_0 being the cloud density. Similarly, it is unstable when its radius is smaller than the so-called *Jeans length* λ_J given by

$$\lambda_\mathrm{J} = \left(\frac{3}{4\pi\rho_0} M_\mathrm{J}\right)^{1/3}. \tag{1.12}$$

To summarize, any isothermal cloud with a mass larger than its Jeans mass or, equivalently, a radius smaller than its Jeans length will undergo gravitational collapse. Interestingly, if the gas follows a polytropic equation of state such as $P_\mathrm{g} \propto \rho^{\gamma_\mathrm{eff}}$, one can show that $M_\mathrm{J} \propto \rho^{3\gamma_\mathrm{eff}/2-2}$. This means that for $\gamma_\mathrm{eff} > \gamma_\mathrm{crit} = 4/3$, the Jeans mass increases with density and the cloud is unconditionally stable against gravitational collapse. To understand the evolution of the polytropic index [9] is thus crucial to understand the protostellar collapse.

1.5.2 Free-fall timescale

The characteristic timescale of the gravitational collapse, the *free-fall* timescale t_ff, can be easily determined in the simplest case of a non-rotating cloud of uniform density ρ_0 only subject to gravity. As in Spitzer (1978), we study the collapse of a shell of initial radius r_0. We define r as its radius after a time t. Applying the second-law of Newton on the shell yields

$$\frac{\mathrm{d}^2 r}{\mathrm{d}t^2} = -\mathcal{G} \frac{4\pi\rho_0 r_0^3}{3r^2}, \tag{1.13}$$

[9] note to be confused with the adiabatic index $\gamma \equiv \frac{c_p}{c_v}$

after multiplying this equation by $\frac{\mathrm{d}r}{\mathrm{d}t}$ and integrating it over time we obtain

$$\frac{1}{2}\left(\frac{\mathrm{d}r}{\mathrm{d}t}\right)^2 = -\mathcal{G}\frac{4\pi\rho_0 r_0^3}{3}\left(\frac{1}{r} - \frac{1}{r_0}\right), \tag{1.14}$$

after taking the square-root of this equation one can show that

$$\frac{1}{\sqrt{\frac{r_0}{r} - 1}}\frac{\mathrm{d}r}{\mathrm{d}t} = -\sqrt{\mathcal{G}\frac{8\pi\rho_0 r_0^3}{3}}, \tag{1.15}$$

defining the dimensionless parameter β such as $\cos^2(\beta) = \frac{r}{r_0}$ and integrating the equation over time once again we obtain

$$\beta + \frac{1}{2}\sin^2(\beta) = \sqrt{\mathcal{G}\frac{8\pi\rho_0 r_0^3}{3}}t. \tag{1.16}$$

We can use this relation to estimate the free-fall timescale of the shell. We consider that the shell has entirely collapsed once $r = 0$, hence when $\beta = \frac{\pi}{2}$. This yields

$$t_{\mathrm{ff}} = \sqrt{\frac{3\pi}{32\mathcal{G}\rho_0}}. \tag{1.17}$$

1.5.3 Angular momentum conservation

As we already know, protoplanetary disks form around protostars through angular momentum conservation. It is therefore interesting to investigate the evolution of the angular velocity of a cloud during the gravitational collapse. The angular momentum of a system of volume $\mathcal{V}$, density ρ and velocity $\mathbf{v}$ is defined as

$$\mathbf{L} = \iiint_{\mathcal{V}} \rho\,[\mathbf{r} \times \mathbf{v}]\,\mathrm{d}\mathcal{V}, \tag{1.18}$$

$\mathrm{d}\mathcal{V}$ being the volume element at a position $\mathbf{r}$ and $\times$ denoting the cross product operation. This quantity must be conserved for an isolated system. Let us consider the simple case of an uniform and isolated cloud of initial radius r_0 and angular velocity Ω_0 and constant mass M_0, then the specific angular momentum $J = |\mathbf{L}|/M_0$ defined as $J = \Omega_0 r_0^2$ must also be conserved. This allows us to estimate its angular velocity at a time t as

$$\Omega(t) = \Omega_0\left(\frac{r_0}{r(t)}\right)^2. \tag{1.19}$$

As the cloud collapses, its angular velocity increases and the centrifugal force eventually dominates gravity leading to the formation of a disk. The typical radius of a prestellar core is about $\sim$ 500 AU (Andre et al., 1996) which is 10^5 times larger than a solar type star. Assuming the validity of equation (1.19), there should be approximately ten orders of magnitude increase in angular velocity during the protostellar collapse leading to velocities close to the speed of light which is far greater than what is observed or even physically acceptable.

In reality, there is at least a three orders of magnitude change in the specific angular momentum between prestellar cores and YSOs (Bodenheimer, 1995) which means that there is an efficient mechanism that transports or dissipates it during the protostellar collapse. This

angular momentum problem of star formation remains a fundamental issue in today's astrophysics as it requires to understand very precisely the angular momentum transport during star formation.

Early hydrodynamical calculations without magnetic field of protostellar collapse of rotating clouds led to very massive and extended disks (Bodenheimer & Tscharnuter, 1979; Boss, 1980). This was due to the absence of an efficient mechanism to eject the angular momentum such as wind, jet/outflows or magnetic braking. Since then, several solutions have been proposed. Among others, magnetic fields have long been investigated as a possible answer for the angular momentum problem with an ideal (Allen et al., 2003a; Hennebelle & Teyssier, 2008; Commerçon et al., 2010; Tomida, 2014) and non-ideal MHD (Tomida et al., 2015; Wurster et al., 2018; Vaytet et al., 2018b; Marchand et al., 2019) frameworks.

1.5.4 Magnetohydrodynamics

The dynamics of the gas during the protostellar collapse is well described by fluid equations (mass, momentum and energy conservation equations). In this context, the effects of gravitational acceleration, thermal pressure, magnetic fields and radiation are all important at different scales. For the sake of simplicity, I present the equations of radiation non-ideal magnetohydrodynamics (RNIMHD) considering a *barotropic* equation of state (EOS) to account for the effects of radiation.

Mass and momentum conservation

We define ρ as the density of the plasma and $\mathbf{v}$ as its velocity. $P_{\rm g}$ is the gas thermal pressure and ϕ is the gravitational potential. In addition, we consider a magnetic field $\mathbf{B}$, an electric field in the comoving frame $\mathbf{E}$. We also introduce the electric current $\mathbf{J}$. In the non-relativistic case[10], it writes $\mathbf{J} = \nabla \times \mathbf{B}$. Assuming local electroneutrality, the mass and momentum conservation equations write as

$$\begin{aligned} \frac{\partial \rho}{\partial t} + \nabla \cdot [\rho \mathbf{v}] &= 0, \\ \frac{\partial \rho \mathbf{v}}{\partial t} + \nabla \cdot \left[P_{\rm g} \mathbb{I} + \rho (\mathbf{v} \otimes \mathbf{v}) \right] &= -\rho \nabla \phi + \mathbf{J} \times \mathbf{B}. \end{aligned} \tag{1.20}$$

The Poisson equation

In order to determine the gravitational potential ϕ and deduce the gravitational force, one must solve the Poisson equation. It writes as follow

$$\triangle \phi = 4\pi \mathcal{G} \rho, \tag{1.21}$$

this equation shows that any distribution of mass generates a gravitational force.

The barotropic equation of state

As explained earlier, to account for radiative transfer we consider a simple barotropic EOS

$$P_{\rm g} = \rho c_{\rm s,iso}^2 \left[1 + \left(\frac{\rho}{\rho_{\rm ad}} \right)^{\gamma - 1} \right], \tag{1.22}$$

[10] in virtue of the *Maxwell-Ampère equation*

where $c_{s,iso}$ is this isothermal soundspeed at low densities, and $\gamma = 5/3$ to reproduce the monoatomic behavior of H_2 at low temperatures (Masunaga & Inutsuka, 2000).

The barotropic EOS is a convenient way to model the two thermal regimes of the first protostellar collapse, i.e. the isothermal regime at low density and the adiabatic regime when the radiation is trapped at $\rho > \rho_{ad}$.

- Where $\rho \ll \rho_{ad}$, $P_g \sim \rho c_{s,iso}^2$ and the cloud is merely isothermal. At these densities, the temperature is typically $\sim$ 10K, which yelds $c_{s,iso} \sim 0.2$ km s^{-1}. The thermal support is, by definition, not strong enough to prevent the collapse for a Jeans unstable cloud.
- Where $\rho > \rho_{ad}$, $P_g \propto \rho^\gamma$. In these regions, the gas becomes adiabatic as radiation is trapped, mostly because of the dust, and the temperature increases with density. As a consequence, the gas is thermally supported against gravity and is in slow contraction until H_2 starts to dissociate, which is not taken into account in this model.

Magnetic field

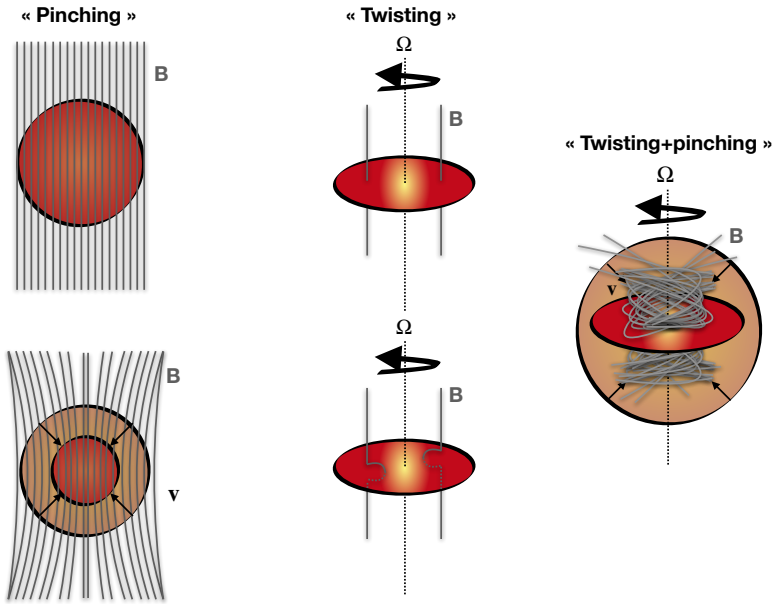

Figure 1.7: Schematic view of the twisting and pinching of the magnetic field lines in a collapsing cloud. Radial motions induce a pinch of the magnetic field lines while rotation twists them. In a rotating and collapsing cloud both effects can be observed.

The previous equations must be completed by the *induction equation* [11] and the *solenoidal constrain*, that prevents the formation of magnetic monopoles. These two equations, derived from *Maxwell's equations*, write as

$$\begin{aligned} \frac{\partial \mathbf{B}}{\partial t} + \nabla \times \mathbf{E} &= 0, \\ \nabla \cdot \mathbf{B} &= 0. \end{aligned} \tag{1.23}$$

Closure is then given by an Ohm's law, that relates the electric field $\mathbf{E}$ to the other hydrodynamical quantities. In the non-ideal MHD framework, which assumes a low ionization level,

[11] also known as the *Maxwell Faraday equation*

the Ohm's law is written as (Wardle & Ng, 1999)

$$\mathbf{E}_\mathrm{b} = \mathbf{v} \times \mathbf{B} + \mathbf{E}, \tag{1.24}$$

where $\mathbf{E}_\mathrm{b}$ the electric field in the rest frame of the fluid is given by

$$\mathbf{E}_\mathrm{b} = \eta_\mathrm{O}\mathbf{J} + \eta_\mathrm{H}\mathbf{J} \times \mathbf{b} + \eta_\mathrm{A}\mathbf{J}_\perp, \tag{1.25}$$

where η_O, η_H and η_A are Ohmic, Hall and Ambipolar resistivities, derived from the conductivity tensor. These quantities depend on the charge, density and cross section of the charged particles. More details on the Ohm's law can be found in Chapter 5 were I propose a more general derivation that includes dust dynamics.

It is interesting, in a first approach to consider only the effect of induction in the ideal MHD limit. In this limit, the gas is considered as fully ionized and the electric field $\mathbf{E} = \mathbf{v} \times \mathbf{B}$ is only induced by the fluid motion. To explain the induction equation in this framework, we place ourselves in cylindrical coordinates $(\mathbf{e_r}, \mathbf{e}_\theta, \mathbf{e_z})$. We now assume a cloud with a magnetic field $\mathbf{B} = B_z\mathbf{e_z}$ at a time $t = t_0$. The induction equation at $t = t_0$ is given by

$$\begin{aligned}
\frac{B_r}{\partial t}|_{t_0} &= \frac{1}{r}\frac{\partial v_r B_z}{\partial \theta}, \\
\frac{B_\theta}{\partial t}|_{t_0} &= \frac{\partial v_\theta B_z}{\partial z}, \\
\frac{B_z}{\partial t}|_{t_0} &= -\frac{1}{r}\left[\frac{\partial r v_r B_z}{\partial r} + \frac{\partial v_\theta B_z}{\partial \theta}\right].
\end{aligned} \tag{1.26}$$

It is quite clear that azimuthal motions in the cloud *twists* the field lines by generating a B_θ component while both the radial and toroïdal motions *pinches* them by generating a B_r and by affecting B_z. As there are no diffusive terms in the induction equation in the ideal case, the collapse of the cloud naturally strengthens the magnetic field in the central regions of a protostellar collapse. The *twisting* and *pinching* of the magnetic field is represented in a schematic way in figure 1.7 in this context.

Keeping in mind how the configuration of the magnetic field lines can evolve during the protostellar collapse, we now look at the magnetic force or *Lorentz force* $\mathbf{J} \times \mathbf{B}$. With some manipulation one can show that

$$\mathbf{J} \times \mathbf{B} = -\nabla \cdot \left[\frac{\mathbf{B}^2}{2}\mathbb{I} - \mathbf{B} \otimes \mathbf{B}\right], \tag{1.27}$$

$$\tag{1.28}$$

two terms can be identified, the magnetic pressure force $-\nabla \cdot \frac{\mathbf{B}^2}{2}$, that acts on the gas similarly to the thermal pressure force, and the magnetic tension $\nabla \cdot [\mathbf{B} \otimes \mathbf{B}]$. In a rotating cloud, the twisting of the field lines generates an azimuthal component in the magnetic field B_θ and thus an azimuthal magnetic tension $\nabla \cdot [B_\theta \mathbf{B}]\,\mathbf{e}_\theta$. This force then generates an azimuthal acceleration to counteract the twisting. This so-called *magnetic braking* is extremely efficient to transport angular momentum in the outer regions of the clouds. In the ideal MHD regime, the angular momentum removal due to the magnetic braking is actually so efficient that it actually prevents the disk formation (Allen et al., 2003a; Mellon & Li, 2008; Hennebelle & Fromang, 2008; Joos et al., 2012), this is the *magnetic braking catastrophe*.

According to Shu et al. (1987) a good estimate for the ionization fraction x_i in molecular cloud is

$$x_\mathrm{i} = \frac{C}{\sqrt{\rho}} \tag{1.29}$$

with $C = 3 \times 10^{-16}$ g$^{1/2}$ cm$^{-3/2}$. During the early phases of star formation the density ranges between $\sim 10^{-19}$ g cm^{-3} and $\sim 10^{-11}$ g cm^{-3}. The ionization is thus very low, typically ranging from $x_i \sim 10^{-11}$ to $x_i \sim 10^{-6}$. The ideal MHD approximation breaks and the resistive regime becomes relevant. Via diffusion, magnetic reconnection or drift between the charged species, the three resistive effects identified earlier can affect the topology of the magnetic field lines. In practice, both the Ohmic and Ambipolar diffusion can reduce the efficiency of the magnetic braking at different scales (Duffin & Pudritz, 2008; Mellon & Li, 2009; Kunz & Mouschovias, 2010; Tomida et al., 2015; Masson et al., 2016). The Hall effect is more complicated. Depending on the angle between the angular velocity and the magnetic field, it can either reduce or increase the strength of the braking (Tsukamoto et al., 2015; Marchand et al., 2018). Although non-ideal MHD is a good candidate to form realistic disks, its effects strongly rely on the values of magnetic resistivities that are still poorly constrained as they depend on a careful estimate of the ionization fraction which depends, among others, on the dust content of the clouds.

1.6 Towards gas and dust mixtures

1.6.1 Previous works

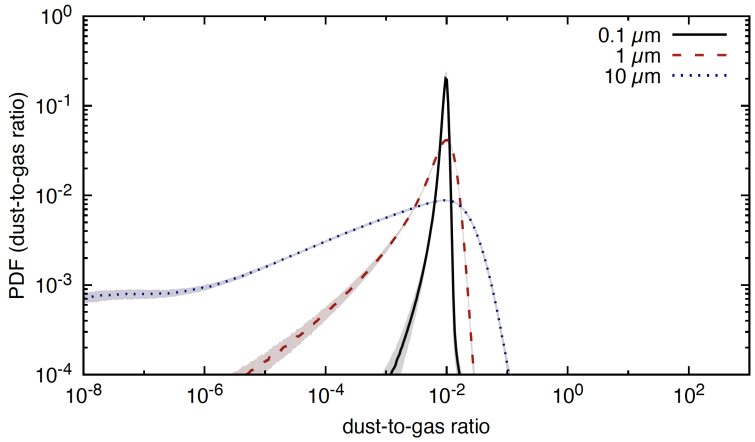

Figure 1.8: Taken from Tricco et al. (2017). Time averaged volume weighted probability density function of the dust-to-gas ratio in a SPH calculation of turbulent cloud in the typical conditions of molecular clouds. Grains smaller that 1 μm have a peaked PDF while for the 10 μm it is broad. This indicates that a significant decoupling occurs for those grains. For these grains, the dust-to-gas ratio can increase up to one order of magnitude.

All the aforementioned studies assumed a perfect collisional coupling between the gas and the dust with an uniform and constant *dust-to-gas ratio* $\theta_d \equiv \frac{\rho_d}{\rho_g}$. A few recent studies indicate that this might not be a legitimate approximation in the star formation context.

- At the scale of molecular clouds Hopkins & Lee (2016) found, using lagrangian particles for the dust, that a dynamical decoupling between the gas and the dust was occuring for dust grains with sizes larger than $\sim$ 1μm. Using *smoothed-particle-hydrodynamics* (SPH) and a monofluid approach for the gas and the dust [12], Tricco et al. (2017) found

[12] a detailled explanation of the monofluid formalism can be found in Chapter 2

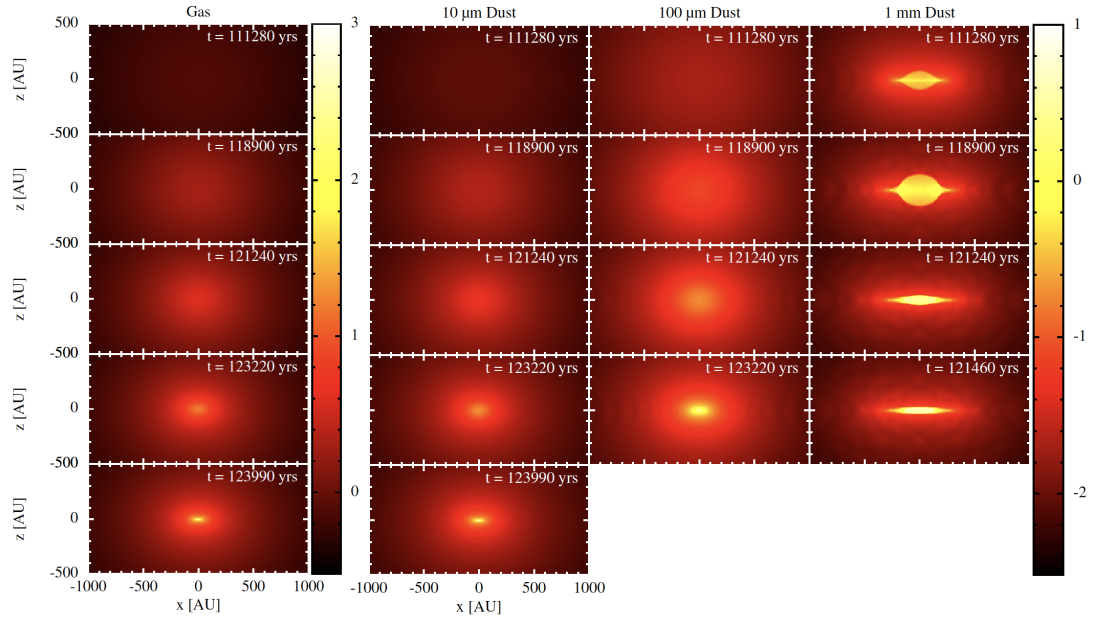

Figure 1.9: Taken from Bate & Lorén-Aguilar (2017). Edge-one view of the column density of gas and dust for three collapse simulations using the SPH approach with various grain sizes (10 µm,100 µm and 1 mm) at four different times. The colors are set so that the gas and dust maps match when the dust-to-gas ratio is at its initial value of 1%. A brighter dust map thus indicates a strong enrichment in dust grains. We observe that grains > 100 µm fall significantly faster than the gas enriching the central regions of the collapse.

that this effect was occurring for grains larger that $\sim$ 10 µm (see figure 1.8 for the probability density function of the dust-to-gas ratio obtained by Tricco et al., 2017).

- At the scale of the protostellar collapse, only Bate & Lorén-Aguilar (2017) has investigated the dynamical decoupling between gas and dust. They found that large dust grains with sizes $\gtrsim$ 100 µm could fall significantly faster than the gas enriching the inner regions at the cost of a depletion in the envelope (see figure 1.9 for the column density of gas and dust they obtained at various times). This work, although restrained in its exploration of the parameter space, sets a milestone for the study of dust dynamics in star formation.

All these works were carried out with single dust species simulations assuming a initial dust-to-gas ratio of 1% which means that they do not properly follow the evolution of the grain size distribution and that they might either under or over or under estimate the variations of dust-to-gas ratio by assuming a mean grain size.

1.6.2 This work

In this manuscript, I present the work that I carried out during my three years of PhD at the Centre de Recherche Astrophysique de Lyon under the supervision of Benoît Commerçon. This thesis aims to provide answers to modern questions of star and planet formation using theoretical and numerical tools. I mainly focus on the dynamics of the interstellar dust and its impact on stellar formation.

This manuscript is organized as follows

- In Chapter 2, I introduce the basic theoretical concepts required to study neutral dust dynamics in star forming regions. In that goal, I present the dynamics of a single neutral dust grain interacting with a surrounding gas. Then, I extend this view to a multifluid formalism. After this, I introduce the monofluid approach for gas and dust mixtures and the terminal velocity approximation useful when these mixtures are tightly coupled over a dynamical timescale. Finally, I extend the formalism to the dynamics of neutral dust grains in a weakly ionized plasma.

- In Chapter 3, I introduce my main numerical tool, the `RAMSES` code. After a technical description of main features of `RAMSES`, I detail the developments that I made to incorporate dust dynamics in its structure. Finally, I present multiple tests of implementation of my dust dynamics solver.

- In Chapter 4, I present protostellar collapse calculations of gas and dust mixtures, i.e. DUSTYCOLLAPSES, that I performed with my dust solver. After providing some details on my method of solution, I describe numerically and analytically the general properties of DUSTYCOLLAPSES. Finally, I discuss the caveats and prospects of this study.

- In Chapter 5, I extend the monofluid formalism in the terminal velocity approximation to the dynamics of mixtures composed of both neutral gas and charged solid particles. After a presentation of the formalism, I describe the main dynamical regimes that are implied by the additional decoupling terms it holds. Finally, I give some astrophysical prospect in the context of the protostellar collapse, protoplanetary and the interstellar medium.

- In Chapter 6, I present some preliminary work in which I explore a model of chondrule formation in weakly ionized protoplanetary disks. After an introduction of the essential theoretical knowledge of protoplanetary disks, I introduce unstratified and stratified shearing box calculations that include multiple dust species. These models are also computed with my dust solver and the `RAMSES` code.

- Finally, in Chapter 7, I summarize my thesis and present the most direct prospects of this work.

Chapter 2

Gas and dust hydrodynamics

Contents

Proximo

"We are nothing but dust and shadows. Dust and shadows!"

- Gladiator

In this chapter, I describe the dynamics of neutral dust grains. I first pay attention to the interaction between a single grain and a surrounding gas. After that, I review dust dynamics in a hydrodynamical context. Finally, I extend this formalism to the dynamics of neutral dust in a MHD frameworks. This chapter is mainly bibliographic although I use the notations and include additional terms that I introduced in my refereed paper Lebreuilly et al. (2019) and present some of my unpublished recent developments.

2.1 Single grain dynamics

2.1.1 Assumptions

Spherical compact grains To approach the dynamics of dust grains, I base myself on an approximation that considers the dust grains as small *spherical* and compact particles of radius $s_{\rm grain}$, mass $m_{\rm grain}$, and intrinsic density $\rho_{\rm grain}$. The spherical grain approximation is a first step toward a realistic treatment of dust dynamics and will be further questioned in future works.

Interaction with the gas particles The dust particles are colliding with the gas particles and couple to the mean flow. However, it is the imperfect nature of this decoupling that controls the differential gas and dust dynamics. We usually neglect grain-grain collisions.

Epstein regime Another important assumption is that the grain sizes are smaller than the gas mean free-path $\lambda_{\rm g}$, this will allow us to derive the so-called *Epstein drag-force* in section 2.1.3. More precisely, I consider that $s_{\rm grain} < \frac{4}{9}\lambda_{\rm g}$. The mean free-path of a gas is given by

$$\lambda_{\rm g} = \frac{1}{n_{\rm g}\sigma_{\rm coll}}, \tag{2.1}$$

where $n_{\rm g}$ is the number density of the gas and $\sigma_{\rm coll}$ its collision cross-section. Assuming a cross-section that is of typically the surface of a H_2 molecule, we get $\sigma_{\rm coll} = 2\times10^{-15}$ cm^{-2}. Typically, in the diffuse ISM, $n_{\rm g} \simeq 1$ cm^{-3} (Draine, 2011), assuming that the gas is mostly molecular hydrogen we obtain in these conditions $\lambda_{\rm g} \simeq 5\times10^{16}$ cm. In protoplanetary disk, the typical densities are $\simeq 10^{14}$ cm^{-3} which leads to $\lambda_{\rm g} \simeq 2$ cm. Star forming regions (molecular clouds, collapsing dense core) typically have intermediate densities between the diffuse ISM and the protoplanetary disk and therefore considering $s_{\rm grain} < \frac{4}{9}\lambda_{\rm g}$ is a valid hypothesis for the typical grains sizes I aim to consider ($s_{\rm grain} < 1-10$ mm).

2.1.2 Useful definitions

In the next sections, we consider mixtures made of gas and dust particles. Let us define, the gas density $\rho_{\rm g}$ and its velocity $\mathbf{v}_{\rm g}$. Similarly, I note $\rho_{\rm d}$ and $\mathbf{v}_{\rm d}$, the dust density and velocity. I emphasize that $\rho_{\rm d}$ is not the same quantity as the dust intrinsic density $\rho_{\rm grain}$ because of the large distances between two dust grains. I define $\mathbf{\Delta v} \equiv \mathbf{v}_{\rm d} - \mathbf{v}_{\rm g}$ as the differential velocity between the grain and the gas. I also define the gas sound speed $c_{\rm s}$, its thermal velocity $\omega_{\rm th} = \frac{2}{\sqrt{\pi\beta}}$ where $\beta = \frac{m_{\rm g}}{2k_{\rm B}T_{\rm g}}$, $m_{\rm g}$ being the mean mass of the gas particles and $T_{\rm g}$ its temperature. Note that $\omega_{\rm th} = \sqrt{\frac{8}{\pi\gamma}}c_{\rm s}$ where γ is the gas adiabatic index.

Grain coordinates

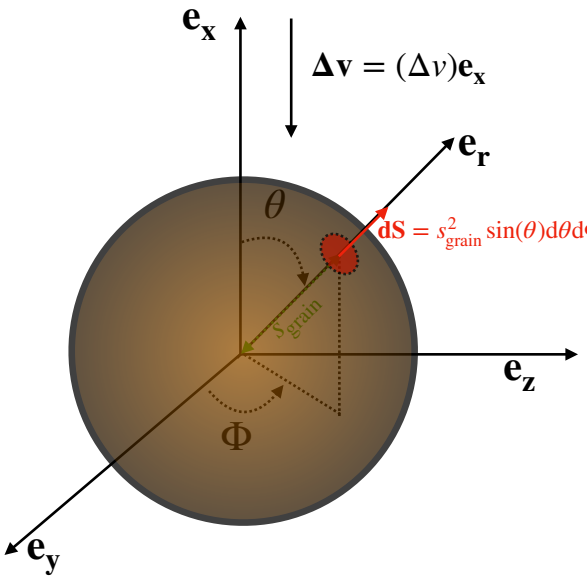

Figure 2.1: Cartoon representation of the grain coordinates. The polar axis $\mathbf{e_x}$ is chosen to be aligned with the differential velocity between the grain and the gas. θ is the angle between the surface element $\mathrm{d}\mathbf{S}$ and the polar axis and Φ the angle between the surface element and the y-axis. The grain radius is $s_{\rm grain}$.

2.1.3 Epstein drag force

First, let us examine the fate of a single grain within a gas of density $\rho_{\rm g}$. It exchanges momentum with the surrounding gas molecules through microscopic collisions. In this section, I demonstrate the Epstein law (Epstein, 1924). Let us assume that

- $m_{\rm grain} \gg m_{\rm g}$.
- The collision between the gas and the grain are specular, which means that the velocity of the gas particle after a gas-grain collision is orthogonal to the grain surface.
- Grain-grain collisions are neglected.
- The grains are small enough not to disturb the local Maxwellian distribution of the gas velocity, i.e. $s_{\rm grain} < \frac{4}{9}\lambda_{\rm g}$.

We place ourselves in the *grain coordinates* described in figure 2.1, the polar axis $\mathbf{e_x}$ is chosen to be aligned with the differential velocity between the grain and the gas. We assume that the gas velocity follows a Maxwell–Boltzmann distribution, the probability dP for a gas particle to have a velocity $u \in [u, u + \mathrm{d}u]$ writes as

$$\mathrm{dP} = \sqrt{\frac{\beta}{\pi}} e^{-\beta u^2} \mathrm{d}u, \tag{2.2}$$

if we define $\frac{\mathrm{d}N}{\mathrm{d}t}$ as the collision rate on the surface element $\mathrm{d}\mathbf{S}$ of particles with a velocity u, it writes as

$$\begin{aligned} \frac{\mathrm{d}N}{\mathrm{d}t} &= [u + \Delta v \cos(\theta)]\, n_{\rm g} \mathrm{dP} \mathrm{d}S \\ &= [u + \Delta v \cos(\theta)]\, n_{\rm g} \sqrt{\frac{\beta}{\pi}} e^{-\beta u^2} \mathrm{d}u \mathrm{d}S, \end{aligned} \tag{2.3}$$

under the assumption of specular collisions and if $m_{\rm grain} \gg m_{\rm g}$, the momentum transferred from a gas particle to a dust grain during one collision is given by

$$\mathbf{p} = -2m_{\rm g}(u + \Delta v \cos(\theta))\mathbf{e_r}. \tag{2.4}$$

Therefore, the momentum exchange rate between the gas and the dust grain $\frac{\mathrm{d}p}{\mathrm{d}t}$ is written as

$$\begin{aligned}\frac{\mathrm{d}p}{\mathrm{d}t} &= p\frac{\mathrm{d}N}{\mathrm{d}t} \\ &= -2m_{\mathrm{g}}(u+\Delta v\cos(\theta))^2 n_{\mathrm{g}}\sqrt{\frac{\beta}{\pi}}e^{-\beta u^2}\mathrm{d}u\mathrm{d}S. \end{aligned} \tag{2.5}$$

The effective drag force $\mathbf{F}_{\mathrm{drag}}$ generated by those collisions must be aligned with the polar axis, we can therefore write

$$\mathbf{F}_{\mathrm{drag}} = -2m_{\mathrm{g}}\sqrt{\frac{\beta}{\pi}}n_{\mathrm{g}}s_{\mathrm{grain}}^2\mathcal{I}\mathbf{e}_{\mathbf{x}}, \tag{2.6}$$

where

$$\mathcal{I} = \iiint (u+\Delta v\cos(\theta))^2 e^{-\beta u^2}\mathrm{d}u\cos\theta\sin\theta\mathrm{d}\theta\mathrm{d}\Phi. \tag{2.7}$$

We can the distinguish three different cases

- if $u \geq \Delta v$, collisions can occur for any angle θ.
- if $u < \Delta v$, collisions can occur only if $\Delta v\cos\theta > -u$.
- if $u \leq -\Delta v$, no collision is possible.

We can thus decompose $\mathcal{I}$ as

$$\begin{aligned}\mathcal{I} &= \int_0^{2\pi}\mathrm{d}\Phi\int_{\Delta v}^{+\infty}\mathrm{d}u\int_0^{\pi}(u+\Delta v\cos(\theta))^2 e^{-\beta u^2}\mathrm{d}u\cos\theta\sin\theta\mathrm{d}\theta \\ &+ \int_0^{2\pi}\mathrm{d}\Phi\int_{-\Delta v}^{\Delta v}\mathrm{d}u\int_0^{\cos^{-1}\left(\frac{-u}{\Delta v}\right)}(u+\Delta v\cos(\theta))^2 e^{-\beta u^2}\mathrm{d}u\cos\theta\sin\theta\mathrm{d}\theta. \end{aligned} \tag{2.8}$$

Computing these integrals yields (Laibe & Price, 2012b)

$$\mathbf{F}_{\mathrm{drag}} = -\sqrt{\pi}\frac{\rho_{\mathrm{g}}s_{\mathrm{grain}}^2}{\beta}\left[\left(\psi+\frac{1}{2\psi}\right)e^{-\psi^2}+\left(\psi^2+1-\frac{1}{4\psi^2}\right)\sqrt{\pi}\mathrm{erf}(\psi)\right]\mathbf{e}_{\mathbf{x}}, \tag{2.9}$$

where $\psi = \sqrt{\beta\Delta v}$. For $\psi \ll 1$, which means that the differential velocity is small compared to the thermal velocity, we obtain with a first-order Taylor expansion (Epstein, 1924)

$$\mathbf{F}_{\mathrm{drag}} = -\frac{4}{3}\pi\rho_{\mathrm{g}}s_{\mathrm{grain}}^2\omega_{\mathrm{th}}\mathbf{\Delta v}, \tag{2.10}$$

which can be rewritten as

$$\mathbf{F}_{\mathrm{drag}} = -\frac{m_{\mathrm{grain}}}{t_{\mathrm{s,grain}}}\mathbf{\Delta v}, \tag{2.11}$$

where we define the stopping time of the grain $t_{\mathrm{s,grain}}$. It is the typical time required by the dust grain to adjust its dynamics to a change in the gas velocity. The grain stopping time is given by

$$t_{\mathrm{s,grain}} \equiv \sqrt{\frac{\pi\gamma}{8}}\frac{\rho_{\mathrm{grain}}}{\rho_{\mathrm{g}}}\frac{s_{\mathrm{grain}}}{c_{\mathrm{s}}}, \tag{2.12}$$

where c_{s} and γ denote the sound speed and the adiabatic index of the gas, respectively. The Epstein regime is a particular case of a linear drag regime.

Large and dense grains are less coupled to the gas. If c_{s} and ρ_{g} increase, the coupling of the two phases becomes more important as the collision rate between gas and dust particles increases. The opposite drag force applies on the gas particles because of the total mixture momentum conservation.

2.1.4 Kwok correction

In star forming regions, the soundspeed can be very low because the gas is usually cold ($T_g \simeq 10$ K). It is thus interesting to investigate the Epstein drag force when $\psi \gg 1$. In this approximation, we can do a first-order Taylor expansion of equation (2.9) in $\frac{1}{\psi}$. We then obtain the following drag force

$$\mathbf{F}_{\text{drag}} = -\pi \rho_g s_{\text{grain}}^2 \Delta v \Delta \mathbf{v}. \tag{2.13}$$

By interpolating between the $\psi \gg 1$ and $\psi \ll 1$, Kwok (1975) has shown that a good approximation for the stopping time in supersonic regime is

$$t_{s,k} \equiv \sqrt{\frac{\pi\gamma}{8}} \frac{\rho_{\text{grain}}}{\rho_g} \frac{s_{\text{grain}}}{c_s} \left(1 + \frac{9}{128\pi} \mathcal{M}_d{}^2\right)^{-1/2}, \tag{2.14}$$

where $\mathcal{M}_d = \frac{|\Delta \mathbf{v}|}{c_s}$ is the differential velocity Mach number. For small values of $\mathcal{M}_d$ this stopping time converges to the value given by the Epstein regime, it is thus convenient to use it for any value of $\mathcal{M}_d$.

2.1.5 Stokes regime

If the dust grains are larger than $\frac{4}{9}\lambda_g$, they can perturb the local Maxwellian distribution of the gas and we enter in the so-called *Stokes regime* were

$$\mathbf{F}_{\text{drag}} = -\frac{1}{2} C_{\text{drag}} \pi s_{\text{grain}}^2 \Delta v \Delta \mathbf{v}, \tag{2.15}$$

C_{drag} being a piecewise function of the Reynolds number Rd, the ratio between the inertial and viscous forces. C_{drag} writes as

$$C_{\text{drag}} = \begin{cases} 24\text{Re}^{-1} \text{ if Rd} < 1, \\ 24\text{Re}^{-0.6} \text{ if } 1 < \text{Rd} < 800, \\ 0.44 \text{ if } 800 < \text{Rd}. \end{cases} \tag{2.16}$$

One can show that, for a highly turbulent media (Rd $\gg$ 1) [1], the Stokes drag force is equal to the Epstein drag force when $s_{\text{grain}} = \frac{4}{9}\lambda_g$. We note that in protoplanetary disk, as explained earlier, only grains larger than a centimeter have $s_{\text{grain}} > \frac{4}{9}\lambda_g$. Therefore in the remaining of the manuscript I will only place myself in the Epstein regime and, if needed, consider the Kwok correction.

2.2 Fluid approach

In the aim of modeling the collective effects of dust grains, I now introduce the fluid approach for gas and dust mixtures. A continuous fluid description of the dust being way more feasible than treating the grains independently with a N-body approach.

2.2.1 Continuous fluid approach

For a continuous fluid approach to be valid, one must be able to average the physical quantities such as the dust density, momentum, etc... over control volumes $V^* = L^{*3}$ that are sufficiently

[1] which is typically the case in astrophysical flows

large to be statistically meaningful, but still small compared to the macroscopic scale of the system $L_{\rm macro}^3$. The so-called *mesoscopic* scale L^* must verify the condition $L_{\rm micro} \ll L^* \ll L_{\rm macro}$ for the fluid approximation to stand. The microscopic scale is the typical scale at which particles interact. Dust grains are extremely massive compared to the gas molecule but much less numerous, so grain-grain collisions are extremely rare. Furthermore, the dust fluid, when it can be defined, can be considered as pressureless in most cases. The unfortunate consequence is that, without any gas, the microscopic scale of the dust is likely to be very large. Fortunately, gas-grain collisions are likely to be much more frequent than grain-grain collisions and they therefore set the microscopic scale when they damp the velocity spread of the dust quickly over a dynamical timescale. In the case of a moderately to strongly coupled gas and dust mixture one can then consider that $L_{\rm micro} = \lambda_{\rm g}$ which is the same scale as for the gas. It is therefore as legitimate to model the dust with a continuous approach as it is for the gas, provided that they couple via the drag force.

2.2.2 Bifluid formalism

A usual model for gas and dust mixtures consists of two fluids interacting via the drag term (Saffman, 1962). Although modeled as a pressureless fluid, the dust feels the forces exerted on the gas via the drag force. The bifluid formulation of gas and dust mass and momentum conservation writes

$$\begin{aligned}
\frac{{\rm d}_{\rm g}\rho_{\rm g}}{{\rm d}t} &= -\rho_{\rm g}(\nabla\cdot\mathbf{v}_{\rm g}),\\
\frac{{\rm d}_{\rm d}\rho_{\rm d}}{{\rm d}t} &= -\rho_{\rm d}(\nabla\cdot\mathbf{v}_{\rm d}),\\
\rho_{\rm g}\frac{{\rm d}_{\rm g}\mathbf{v}_{\rm g}}{{\rm d}t} &= -\nabla P_{\rm g} + \rho_{\rm g}\mathbf{f}_{\rm g} + \rho_{\rm g}\mathbf{f} + K\boldsymbol{\Delta}\mathbf{v},\\
\rho_{\rm d}\frac{{\rm d}_{\rm d}\mathbf{v}_{\rm d}}{{\rm d}t} &= \rho_{\rm d}\mathbf{f}_{\rm d} + \rho_{\rm d}\mathbf{f} - K\boldsymbol{\Delta}\mathbf{v},\\
\frac{{\rm d}_{\rm g}e_{\rm g}}{{\rm d}t} &= -\frac{P_{\rm g}}{\rho_{\rm g}}\nabla\cdot\mathbf{v}_{\rm g} + \frac{K}{\rho_{\rm g}}\boldsymbol{\Delta}\mathbf{v}\cdot\boldsymbol{\Delta}\mathbf{v},
\end{aligned} \tag{2.17}$$

where $\boldsymbol{\Delta}\mathbf{v} \equiv \mathbf{v}_{\rm d} - \mathbf{v}_{\rm g}$ is the differential velocity between the two fluids; $\mathbf{f}$ is the specific force acting on both gas and dust; and $\mathbf{f}_{\rm g}$ and $\mathbf{f}_{\rm d}$ are the specific forces, drag and pressure force excluded, affecting the gas or the dust, respectively. In the rest of this section, unless specified, I assume the hydrodynamical case where $\mathbf{f}_{\rm g}$ and $\mathbf{f}_{\rm d}$ are zero, and $\mathbf{f}$ is either zero or the gravity force. The gas pressure $P_{\rm g}$ is given by $P_{\rm g} = (\gamma - 1)\rho_{\rm g}e_{\rm g}$, $e_{\rm g}$ being the gas specific internal energy. The gas derivative $\frac{{\rm d}_{\rm g}}{{\rm d}t} \equiv \frac{\partial}{\partial t} + \left(\mathbf{v}_{\rm g}\cdot\nabla\right)$ differs from the dust derivative $\frac{{\rm d}_{\rm d}}{{\rm d}t} \equiv \frac{\partial}{\partial t} + (\mathbf{v}_{\rm d}\cdot\nabla)$. The drag force was obtained by integrating equation (2.11) over a mesoscopic control volume and assuming a locally homogeneous media. The drag coefficient K is defined as

$$K \equiv \frac{\rho_{\rm d}\rho_{\rm g}}{\rho t_{\rm s}}, \tag{2.18}$$

where the fluid stopping time, simply called stopping time hereafter, differs from the grain stopping time as the dust grains only represent a small fraction of the volume (Laibe & Price, 2012a). It is defined as

$$t_{\rm s} \equiv \frac{\rho_{\rm g}}{\rho} t_{\rm s,grain}, \tag{2.19}$$

$\rho \equiv \rho_{\rm d} + \rho_{\rm g}$ being the total density of the gas and dust mixture.

2.3 The monofluid formalism

Alternatively, it is possible to model the gas and dust mixture as a single fluid or *monofluid* made of multiple phases and with a total density ρ (Laibe & Price, 2014a,b). In this section, I first derive the full one-fluid/monofluid set of equations for one dust species.[2] Then, I present the diffusion and terminal velocity approximation which are ways to simplify the monofluid equations for strongly coupled gas and dust mixtures. Finally, I then present the extension of this formalism to multiple species that was first introduced in Laibe & Price (2014b).

2.3.1 Definition of the monofluid quantities

The monofluid is moving at the mixture barycentric velocity $\mathbf{v}$ defined as

$$\mathbf{v} \equiv \frac{\rho_{\rm g}\mathbf{v}_{\rm g} + \rho_{\rm d}\mathbf{v}_{\rm d}}{\rho_{\rm g} + \rho_{\rm d}}.$$

I also define the dust ratio

$$\epsilon \equiv \frac{\rho_{\rm d}}{\rho},$$

which must not be confused with the dust-to-gas ratio $\theta_{\rm d} = \frac{\rho_{\rm d}}{\rho_{\rm g}}$. Using these new monofluid quantities, it is straightforward to write

$$\mathbf{v}_{\rm g} = \mathbf{v} - \epsilon\boldsymbol{\Delta v};\ \mathbf{v}_{\rm d} = \mathbf{v} + (1-\epsilon)\boldsymbol{\Delta v};\ \rho_{\rm g} = (1-\epsilon)\rho;\ \rho_{\rm d} = \epsilon\rho.$$

A new Lagrangian derivative $\frac{\rm d}{{\rm d}t} \equiv \frac{\partial}{\partial t} + (\mathbf{v}\cdot\nabla)$ has to be defined to develop the monofluid set of equations

2.3.2 Monofluid formalism

Total mass conservation

Let us first focus on the total mass conservation equation. In their conservative formulation, the gas and dust mass conservation equations are written as

$$\begin{aligned} \frac{\partial\rho_{\rm g}}{\partial t} + \nabla\cdot(\rho_{\rm g}\mathbf{v}_{\rm g}) &= 0, \\ \frac{\partial\rho_{\rm d}}{\partial t} + \nabla\cdot(\rho_{\rm d}\mathbf{v}_{\rm d}) &= 0, \end{aligned} \tag{2.20}$$

using the new monfluid variables we can write these equations as

$$\begin{aligned} \frac{\partial\rho\,(1-\epsilon)}{\partial t} + \nabla\cdot\left[\rho\,(1-\epsilon)\,(\mathbf{v} - \epsilon\boldsymbol{\Delta v})\right] &= 0, \\ \frac{\partial\rho\epsilon}{\partial t} + \nabla\cdot\left[\rho\epsilon(\mathbf{v} + (1-\epsilon)\boldsymbol{\Delta v})\right] &= 0. \end{aligned} \tag{2.21}$$

Summing these two equations allows to straightforwardly obtain the mass conservation equation

$$\frac{\partial\rho}{\partial t} + \nabla\cdot\left[\rho\mathbf{v}\right] = 0, \tag{2.22}$$

[2] The demonstration are tedious, but relatively straightforward and can be left for a second reading, to emphasize on the results, the final equations are boxed.

which, with a Lagrangian formulation is written as

$$\boxed{\frac{\mathrm{d}\rho}{\mathrm{d}t} = -\rho(\nabla \cdot \mathbf{v}).} \tag{2.23}$$

Unsurprisingly, the total mass of the gas and dust mixture is strictly conserved.

Total momentum conservation

I now aim to derive the total momentum conservation equation. As for the mass conservation, it is easier to demonstrate it in the conservative form. In this form, the momentum conservation equations of the gas and dust fluids are written as

$$\begin{aligned} \frac{\partial \rho_\mathrm{g}\mathbf{v}_\mathrm{g}}{\partial t} + \nabla \cdot \left[\rho_\mathrm{g}\mathbf{v}_\mathrm{g} \otimes \mathbf{v}_\mathrm{g}\right] &= -\nabla P_\mathrm{g} + \rho_\mathrm{g}\mathbf{f} + K\boldsymbol{\Delta}\mathbf{v}, \\ \frac{\partial \rho_\mathrm{d}\mathbf{v}_\mathrm{d}}{\partial t} + \nabla \cdot \left[\rho_\mathrm{d}\mathbf{v}_\mathrm{d} \otimes \mathbf{v}_\mathrm{d}\right] &= \rho_\mathrm{d}\mathbf{f} - K\boldsymbol{\Delta}\mathbf{v}. \end{aligned} \tag{2.24}$$

Summing the two equation, we obtain

$$\frac{\partial \rho_\mathrm{g}\mathbf{v}_\mathrm{g} + \rho_\mathrm{d}\mathbf{v}_\mathrm{d}}{\partial t} + \nabla \cdot \left[\rho_\mathrm{g}\mathbf{v}_\mathrm{g} \otimes \mathbf{v}_\mathrm{g} + \rho_\mathrm{d}\mathbf{v}_\mathrm{d} \otimes \mathbf{v}_\mathrm{d}\right] = -\nabla P_\mathrm{g} + \rho\mathbf{f}, \tag{2.25}$$

switching to the monofluid variables and rearranging the order of the terms yields

$$\begin{aligned} \frac{\partial \rho\mathbf{v}}{\partial t} &+ \nabla \cdot [\rho(1-\epsilon)\mathbf{v} \otimes \mathbf{v} + \rho\epsilon\mathbf{v} \otimes \mathbf{v} + \rho(1-\epsilon)\epsilon^2\boldsymbol{\Delta}\mathbf{v} \otimes \boldsymbol{\Delta}\mathbf{v} + \rho\epsilon(1-\epsilon)^2\boldsymbol{\Delta}\mathbf{v} \otimes \boldsymbol{\Delta}\mathbf{v}] \\ &+ \nabla \cdot [-\rho\epsilon(1-\epsilon)(\mathbf{v} \otimes \boldsymbol{\Delta}\mathbf{v} + \boldsymbol{\Delta}\mathbf{v} \otimes \mathbf{v}) + \rho\epsilon(1-\epsilon)(\mathbf{v} \otimes \boldsymbol{\Delta}\mathbf{v} + \boldsymbol{\Delta}\mathbf{v} \otimes \mathbf{v})] \\ &= -\nabla P_\mathrm{g} + \rho\mathbf{f}. \end{aligned} \tag{2.26}$$

Simplifying all the terms, we get

$$\frac{\partial \rho\mathbf{v}}{\partial t} + \nabla \cdot [\rho\mathbf{v} \otimes \mathbf{v} + \rho\epsilon(1-\epsilon)\boldsymbol{\Delta}\mathbf{v} \otimes \boldsymbol{\Delta}\mathbf{v}] = -\nabla P_\mathrm{g} + \rho\mathbf{f}, \tag{2.27}$$

which using, the total mass conservation equation, yields the Lagrangian form

$$\boxed{\frac{\mathrm{d}\mathbf{v}}{\mathrm{d}t} = -\frac{\nabla P_\mathrm{g}}{\rho} + \mathbf{f} - \frac{1}{\rho}\nabla \cdot \left(\epsilon(1-\epsilon)\rho\boldsymbol{\Delta}\mathbf{v} \otimes \boldsymbol{\Delta}\mathbf{v}\right).} \tag{2.28}$$

Dust mass conservation/Dust ratio evolution

From equation (2.21), we can easily deduce the mass conservation equation from the dust. It is written as

$$\frac{\partial \rho\epsilon}{\partial t} + \nabla \cdot \left[\rho\epsilon(\mathbf{v} + (1-\epsilon)\boldsymbol{\Delta}\mathbf{v})\right] = 0. \tag{2.29}$$

To obtain the Lagrangian formulation of the dust ratio evolution equation, one has to develop the derivatives and linear operators of equation (2.29) in the following way

$$\epsilon\frac{\partial \rho}{\partial t} + \rho\frac{\partial \epsilon}{\partial t} + \rho\nabla \cdot \epsilon\mathbf{v} + \epsilon\nabla \cdot \rho\mathbf{v} = -\nabla \cdot \left[\rho\epsilon((1-\epsilon)\boldsymbol{\Delta}\mathbf{v})\right]. \tag{2.30}$$

Using equation (2.22), we easily get

$$\rho\frac{\partial \epsilon}{\partial t} + \rho\mathbf{v} \cdot \nabla\epsilon = -\nabla \cdot \left[\rho\epsilon((1-\epsilon)\boldsymbol{\Delta}\mathbf{v})\right]. \tag{2.31}$$

With a Lagrangian formulation, the former equation yields

$$\boxed{\frac{\mathrm{d}\epsilon}{\mathrm{d}t} = -\frac{1}{\rho}\nabla \cdot \left(\epsilon(1-\epsilon)\rho\boldsymbol{\Delta}\mathbf{v}\right).} \tag{2.32}$$

Differential velocity evolution

The total momentum equation is not sufficient to constrain the evolution of the gas and dust velocity as we also need to now how the differential velocity evolves. I now derive its evolution equation. No convenient conservative formulation has been found for this equation yet as the drag force constantly exchange momentum between the gas and the dust, I therefore demonstrate the evolution equation directly in its Lagrangian form. In this approach, we have

$$\begin{aligned}\frac{\mathrm{d}_\mathrm{g}\mathbf{v}_\mathrm{g}}{\mathrm{d}t} &= -\frac{\nabla P_\mathrm{g}}{\rho_\mathrm{g}} + \mathbf{f} + \frac{K}{\rho_\mathrm{g}}\mathbf{\Delta v},\\ \frac{\mathrm{d}_\mathrm{d}\mathbf{v}_\mathrm{d}}{\mathrm{d}t} &= \mathbf{f} - \frac{K}{\rho_\mathrm{d}}\mathbf{\Delta v}.\end{aligned} \tag{2.33}$$

By subtracting these two equations we get

$$\frac{\mathrm{d}_\mathrm{d}\mathbf{v}_\mathrm{d}}{\mathrm{d}t} - \frac{\mathrm{d}_\mathrm{g}\mathbf{v}_\mathrm{g}}{\mathrm{d}t} = \frac{\nabla P_\mathrm{g}}{\rho_\mathrm{g}} - K\frac{\rho_\mathrm{d}+\rho_\mathrm{g}}{\rho_\mathrm{d}\rho_\mathrm{g}}\mathbf{\Delta v}. \tag{2.34}$$

Switching to the monofluid variables leads to

$$\begin{aligned}\frac{\mathrm{d}\mathbf{v} + (1-\epsilon)\mathbf{\Delta v}}{\mathrm{d}t} &+ ((1-\epsilon)\mathbf{\Delta v}\cdot\nabla)(\mathbf{v}+(1-\epsilon)\mathbf{\Delta v}) - \frac{\mathrm{d}\mathbf{v}-\epsilon\mathbf{\Delta v}}{\mathrm{d}t} + (\epsilon\mathbf{\Delta v}\cdot\nabla)((\mathbf{v}-\epsilon)\mathbf{\Delta v})\\ &= \frac{\nabla P_\mathrm{g}}{\rho_\mathrm{g}} - K\frac{1}{\rho(1-\epsilon)\epsilon}\mathbf{\Delta v},\end{aligned} \tag{2.35}$$

this can be further simplified as

$$\begin{aligned}\frac{\mathrm{d}\mathbf{\Delta v}}{\mathrm{d}t} &+ (\mathbf{\Delta v}\cdot\nabla)\mathbf{v} + ((1-\epsilon)\mathbf{\Delta v}\cdot\nabla)((1-\epsilon)\mathbf{\Delta v}) - (\epsilon\mathbf{\Delta v}\cdot\nabla)(\epsilon\mathbf{\Delta v})\\ &= \frac{\nabla P_\mathrm{g}}{\rho_\mathrm{g}} - K\frac{1}{\rho(1-\epsilon)\epsilon}\mathbf{\Delta v},\end{aligned} \tag{2.36}$$

At this state, we already have an evolution equation for the differential velocity. It is however interesting to go further in the development. Let us thus work on the $(1-\epsilon)\mathbf{\Delta v}\cdot\nabla((1-\epsilon)\mathbf{\Delta v}) - \epsilon\mathbf{\Delta v}\nabla(\epsilon\mathbf{\Delta v})$ term that we call $\mathbf{X}$. Using the vector identity $(\mathbf{A}\cdot\nabla)\mathbf{A} = \frac{1}{2}\nabla(\mathbf{A}.\mathbf{A}) - \mathbf{A}\times(\nabla\times\mathbf{A})$, we find

$$\mathbf{X} = -\frac{1}{2}\nabla((2\epsilon-1)\mathbf{\Delta v}.\mathbf{\Delta v}) - (1-\epsilon)\mathbf{\Delta v}\times(\nabla\times((1-\epsilon)\mathbf{\Delta v})) + \epsilon\mathbf{\Delta v}\times(\nabla\times((\epsilon\mathbf{\Delta v})).$$

We can now, using the fact that $K = \frac{\rho\epsilon(1-\epsilon)}{t_\mathrm{s}}$, show that

$$\boxed{\frac{\mathrm{d}\mathbf{\Delta v}}{\mathrm{d}t} = \frac{\nabla P_\mathrm{g}}{(1-\epsilon)\rho} - \frac{\mathbf{\Delta v}}{t_\mathrm{s}} - (\mathbf{\Delta v}\cdot\nabla)\mathbf{v} + \mathbf{f}_\mathrm{frict} + \mathbf{\Delta}\omega.} \tag{2.37}$$

The term $\mathbf{\Delta}\omega$ was absent in the previous literature and I recovered it in Lebreuilly et al. (2019). The new and now complete formulation introduced here holds a physical meaning, it presents

- A friction force $\mathbf{f}_\mathrm{frict} = \frac{1}{2}\nabla\left((2\epsilon-1)\mathbf{\Delta v}\cdot\mathbf{\Delta v}\right)$.
- A differential vorticity term $\mathbf{\Delta}\omega = (1-\epsilon)\mathbf{\Delta v}\times(\nabla\times(1-\epsilon)\mathbf{\Delta v}) - \epsilon\mathbf{\Delta v}\times(\nabla\times\epsilon\mathbf{\Delta v})$.

Energy conservation

The last monofluid equation to derive is the gas energy conservation equation, which is the most straightforward to demonstrate. With a bifluid formalism, this equation writes as

$$\frac{\mathrm{d}_\mathrm{g} e_\mathrm{g}}{\mathrm{d}t} = -\frac{P_\mathrm{g}}{\rho_\mathrm{g}}\nabla\cdot\mathbf{v}_\mathrm{g} + \frac{K}{\rho_\mathrm{g}}\mathbf{\Delta v}\cdot\mathbf{\Delta v}, \tag{2.38}$$

the monofluid formulation is obtained simply by changing the variables as

$$\frac{\mathrm{d}e_\mathrm{g}}{\mathrm{d}t} - (\epsilon\mathbf{\Delta v}\cdot\nabla)e_\mathrm{g} = -\frac{P_\mathrm{g}}{\rho(1-\epsilon)}\nabla\cdot(\mathbf{v}-\epsilon\mathbf{\Delta v}) + \frac{\epsilon}{t_\mathrm{s}}\mathbf{\Delta v}\cdot\mathbf{\Delta v}, \tag{2.39}$$

and then rearranging the terms to finally obtain

$$\boxed{\frac{\mathrm{d}e_\mathrm{g}}{\mathrm{d}t} = -\frac{P_\mathrm{g}}{\rho(1-\epsilon)}\nabla\cdot(\mathbf{v}-\epsilon\mathbf{\Delta v}) + (\epsilon\mathbf{\Delta v}\cdot\nabla)e_\mathrm{g} + \epsilon\frac{\mathbf{\Delta v}\cdot\mathbf{\Delta v}}{t_\mathrm{s}}.} \tag{2.40}$$

In addition to the differential advection terms, this equation presents a heating term $\epsilon\frac{\mathbf{\Delta v}\cdot\mathbf{\Delta v}}{t_\mathrm{s}}$ due to the gas and dust friction.

Summary

Finally, in the Lagrangian form, the conservation of mass and momentum energy for the mixture and of the gas internal energy writes

$$\begin{aligned}
\frac{\mathrm{d}\rho}{\mathrm{d}t} &= -\rho(\nabla\cdot\mathbf{v}),\\
\frac{\mathrm{d}\mathbf{v}}{\mathrm{d}t} &= -\frac{\nabla P_\mathrm{g}}{\rho} + \mathbf{f} - \frac{1}{\rho}\nabla\cdot\left(\epsilon(1-\epsilon)\rho\mathbf{\Delta v}\otimes\mathbf{\Delta v}\right),\\
\frac{\mathrm{d}\epsilon}{\mathrm{d}t} &= -\frac{1}{\rho}\nabla\cdot\left(\epsilon(1-\epsilon)\rho\mathbf{\Delta v}\right),\\
\frac{\mathrm{d}\mathbf{\Delta v}}{\mathrm{d}t} &= \frac{\nabla P_\mathrm{g}}{(1-\epsilon)\rho} - \frac{\mathbf{\Delta v}}{t_\mathrm{s}} - (\mathbf{\Delta v}\cdot\nabla)\mathbf{v} + \frac{1}{2}\nabla\left((2\epsilon-1)\mathbf{\Delta v}\cdot\mathbf{\Delta v}\right)\\
&\quad +(1-\epsilon)\mathbf{\Delta v}\times(\nabla\times(1-\epsilon)\mathbf{\Delta v}) - \epsilon\mathbf{\Delta v}\times(\nabla\times\epsilon\mathbf{\Delta v}),\\
\frac{\mathrm{d}e_\mathrm{g}}{\mathrm{d}t} &= -\frac{P_\mathrm{g}}{\rho(1-\epsilon)}\nabla\cdot(\mathbf{v}-\epsilon\mathbf{\Delta v}) + (\epsilon\mathbf{\Delta v}\cdot\nabla)e_\mathrm{g} + \epsilon\frac{\mathbf{\Delta v}\cdot\mathbf{\Delta v}}{t_\mathrm{s}}.
\end{aligned} \tag{2.41}$$

At this point, the monofluid approach is a dual reformulation of the dust and gas fluid equations (2.17). However, it may be much more convenient for numerical simulations when using Lagrangian particles since it requires only one resolution scale (the mixture resolution) and it avoids the artificial trapping of dust particles (Laibe & Price, 2014a). Note that this system must be closed by a gas equation of state.

2.3.3 Stokes number

At this stage, it is necessary to introduce a very useful dimensionless quantity called the *Stokes number*. It is defined as

$$\mathrm{St} \equiv \left(t_\mathrm{s}/t_\mathrm{dyn}\right), \tag{2.42}$$

where t_dyn is the dynamical timescale of the system considered, e.g. the free-fall timescale during a protostellar collapse, the orbital time in a protoplanetary disk, or the crossing time in a molecular cloud. The Stokes number is useful to evaluate the strength of the coupling between the gas and the dust. Two limiting cases can be identified

- St $\ll 1$, the stopping time is very small compared to the dynamical timescale of the system and the dust fluid adjusts very quickly to the gas structure. The coupling between the gas and the dust is strong.
- St $\gg 1$, the dust grain does not have the time to feel the gas during a dynamical timescale and the coupling is weak.

I will now focus on the *strong coupling* (or *strong drag*) regime which is the most relevant regime in star formation (see Chapter 4 for the justification).

2.3.4 Diffusion approximation

Laibe & Price (2014a) have shown that, for a strong drag regime, two simplifications can be made. In the so-called *diffusion approximation*, $\left\|\boldsymbol{\Delta v}^2/\mathbf{v}^2\right\|$, $\left\|\boldsymbol{\Delta v}\otimes\boldsymbol{\Delta v}/\mathbf{v}^2\right\|$, $\left\|\boldsymbol{\Delta v}\times(\boldsymbol{\nabla}\times(1-\epsilon)\boldsymbol{\Delta v})/\mathbf{v}^2\right\|$ and $\left\|\boldsymbol{\Delta v}\times(\boldsymbol{\nabla}\times\epsilon\boldsymbol{\Delta v})/\mathbf{v}^2\right\|$ are second-order in Stokes number [3]. System (2.41) reduces to

$$\begin{aligned}
\frac{\mathrm{d}\rho}{\mathrm{d}t} &= -\rho(\boldsymbol{\nabla}\cdot\mathbf{v}),\\
\frac{\mathrm{d}\mathbf{v}}{\mathrm{d}t} &= -\frac{\boldsymbol{\nabla}P_{\mathrm{g}}}{\rho}+\mathbf{f},\\
\frac{\mathrm{d}\epsilon}{\mathrm{d}t} &= -\frac{1}{\rho}\boldsymbol{\nabla}\cdot\left(\rho\epsilon(\boldsymbol{\Delta v}-\epsilon\boldsymbol{\Delta v})\right),\\
\frac{\mathrm{d}\boldsymbol{\Delta v}}{\mathrm{d}t} &= \frac{\boldsymbol{\nabla}P_{\mathrm{g}}}{(1-\epsilon)\rho}-\frac{\boldsymbol{\Delta v}}{t_{\mathrm{s}}}-(\boldsymbol{\Delta v}\cdot\boldsymbol{\nabla})\mathbf{v},\\
\frac{\mathrm{d}e_{\mathrm{g}}}{\mathrm{d}t} &= -\frac{P_{\mathrm{g}}}{\rho(1-\epsilon)}\boldsymbol{\nabla}\cdot\mathbf{v}+(\epsilon\boldsymbol{\Delta v}\cdot\boldsymbol{\nabla})\,e_{\mathrm{g}}.
\end{aligned}\tag{2.43}$$

The errors caused by the diffusion approximation are marginal as long as St $\ll 1$. We note that the first-order term $-\frac{P_{\mathrm{g}}}{\rho(1-\epsilon)}\boldsymbol{\nabla}\cdot(\epsilon\boldsymbol{\Delta v})$ in the energy equation must also be simplified owing to energy conservation, as explained by Price & Laibe (2015) in their second footnote. Another approximation known as the terminal velocity approximation (Youdin & Goodman, 2005; Chiang, 2008) can be made when St $\ll 1$. In this case $\left\|\frac{\mathrm{d}\boldsymbol{\Delta v}}{\mathrm{d}t}/\left(\frac{\boldsymbol{\Delta v}}{t_{\mathrm{s}}}\right)\right\|$ and $\left\|(\boldsymbol{\Delta v}\cdot\boldsymbol{\nabla})\mathbf{v}/\left(\frac{\boldsymbol{\Delta v}}{t_{\mathrm{s}}}\right)\right\|$ are transitory terms, and are thus neglected. A consequence of the terminal velocity approximation for linear drag regimes is that the differential velocity directly depends on the force balance

$$\boldsymbol{\Delta v}=t_{\mathrm{s}}\frac{\boldsymbol{\nabla}P_{\mathrm{g}}}{(1-\epsilon)\rho}.$$

It should be noted that this expression can change if other forces apply on the dust or the gas, e.g., the radiation or the Lorentz forces (see section 2.3.8). In the terminal velocity approximation, we finally obtain

$$\begin{aligned}
\frac{\mathrm{d}\rho}{\mathrm{d}t} &= -\rho(\boldsymbol{\nabla}\cdot\mathbf{v}),\\
\frac{\mathrm{d}\mathbf{v}}{\mathrm{d}t} &= -\frac{\boldsymbol{\nabla}P_{\mathrm{g}}}{\rho}+\mathbf{f},\\
\frac{\mathrm{d}\epsilon}{\mathrm{d}t} &= -\frac{1}{\rho}\boldsymbol{\nabla}\cdot\left(\epsilon t_{\mathrm{s}}\boldsymbol{\nabla}P_{\mathrm{g}}\right),\\
\frac{\mathrm{d}e_{\mathrm{g}}}{\mathrm{d}t} &= -\frac{P_{\mathrm{g}}}{\rho(1-\epsilon)}\boldsymbol{\nabla}\cdot\mathbf{v}+\left(\epsilon t_{\mathrm{s}}\frac{\boldsymbol{\nabla}P_{\mathrm{g}}}{(1-\epsilon)\rho}\cdot\boldsymbol{\nabla}\right)e_{\mathrm{g}}.
\end{aligned}$$

[3] $\|.\|$ indicates the L2 norm of either a tensor or a vector

The two first equations are identical to pure hydrodynamics when only gas is involved. The third equation describes the evolution of the dust ratio. Using a conservative formulation, it can be expressed as an advection equation

$$\frac{\partial \rho\epsilon}{\partial t} + \nabla \cdot \left[\rho\epsilon\left(\mathbf{v} + \frac{t_\mathrm{s}\nabla P_\mathrm{g}}{\rho}\right)\right] = 0. \tag{2.44}$$

In this formulation, the equation is almost identical to mass conservation but with a different advection velocity due to the dephasing between the dust and the barycenter. The specific internal energy equation is similar to pure hydrodynamics with an additional term that accounts for the back-reaction of dust on the gas.

2.3.5 $(\mathcal{N}+1)$ phase mixtures

In the diffuse interstellar medium or in protoplanetary disks various grain sizes can coexist. It is therefore more realistic to simultaneously consider several dust species in order to reproduce the observed dust size distributions.

In this aim, the previous monofluid formalism has been extended to $(\mathcal{N}+1)$ phase mixtures with $\mathcal{N}$ distinct dust species and a gas phase (Laibe & Price, 2014c; Hutchison et al., 2018). They show that, in the diffusion approximation the monofluid set of equations writes

$$\begin{aligned}
\frac{\mathrm{d}\rho}{\mathrm{d}t} &= -\rho(\nabla\cdot\mathbf{v}),\\
\frac{\mathrm{d}\mathbf{v}}{\mathrm{d}t} &= -\frac{\nabla P_\mathrm{g}}{\rho} + \mathbf{f},\\
\frac{\mathrm{d}\epsilon_k}{\mathrm{d}t} &= -\frac{1}{\rho}\nabla\cdot\left(\epsilon_k T_{\mathrm{s},k}\nabla P_\mathrm{g}\right),\ \forall k\in[1,\mathcal{N}],\\
\frac{\mathrm{d}e_\mathrm{g}}{\mathrm{d}t} &= -\frac{P_\mathrm{g}}{\rho(1-\mathcal{E})}\nabla\cdot\mathbf{v} + \left(\mathcal{E}\mathcal{T}_\mathrm{s}\frac{\nabla P_\mathrm{g}}{(1-\mathcal{E})\rho}\cdot\nabla\right)e_\mathrm{g},
\end{aligned} \tag{2.45}$$

where ϵ_k is the dust ratio of the phase k and $T_{\mathrm{s},k}$ is the effective stopping time of the dust phase k defined as

$$T_{\mathrm{s},k} \equiv \frac{t_{\mathrm{s},k}}{1-\epsilon_k} - \sum_{l=1}^{\mathcal{N}}\frac{\epsilon_l}{1-\epsilon_l}t_{\mathrm{s},l},$$

where $t_{\mathrm{s},k}$ is the individual stopping time of the phase k. The $\sum_{l=1}^{\mathcal{N}}\frac{\epsilon_l}{1-\epsilon_l}t_{\mathrm{s},l}$ term accounts for the interaction between dust species that is due to their cumulative back-reaction on the gas. I also introduce the total dust ratio

$$\mathcal{E} \equiv \sum_{l=1}^{\mathcal{N}}\epsilon_l,$$

and the mean stopping time

$$\mathcal{T}_\mathrm{s} \equiv \frac{1}{\mathcal{E}}\sum_{l=1}^{\mathcal{N}}\epsilon_l T_{\mathrm{s},l}.$$

The gas and dust densities are simply given by

$$\begin{aligned}
\rho_\mathrm{g} &\equiv (1-\mathcal{E})\rho,\\
\rho_{\mathrm{d},k} &\equiv \epsilon_k\rho.
\end{aligned}$$

When $\mathcal{N}=1$, system (2.45) reduces to the formulation for a single dust phase.

2.3.6 Conservative formulation

Combining the different equations with mass conservation in the Lagrangian frame, co-moving with the barycenter, leads to the formulation of the system of equations in a conservative form

$$\begin{aligned}
\frac{\partial \rho}{\partial t} + \nabla \cdot [\rho \mathbf{v}] &= 0, \\
\frac{\partial \rho \mathbf{v}}{\partial t} + \nabla \cdot \left[P_{\rm g}\mathbb{I} + \rho(\mathbf{v}\otimes\mathbf{v})\right] &= \rho \mathbf{f}, \\
\frac{\partial \rho_{{\rm d},k}}{\partial t} + \nabla \cdot \left[\rho_{{\rm d},k}\left(\mathbf{v} + \frac{T_{{\rm s},k}\nabla P_{\rm g}}{\rho}\right)\right] &= 0, \\
\frac{\partial E}{\partial t} + \nabla \cdot \left[(E + P_{\rm g})\mathbf{v}\right] &= \nabla \cdot \left[\frac{\mathcal{E}\mathcal{T}_{\rm s}}{1-\mathcal{E}}\frac{\nabla P_{\rm g}}{\rho}\frac{P_{\rm g}}{\gamma - 1}\right],
\end{aligned} \tag{2.46}$$

where $\rho_{{\rm d},k}$ is the density of the dust phase k, $E \equiv \frac{1}{2}\rho\mathbf{v}^2 + \rho(1-\mathcal{E})e_{\rm g}$ is the total energy of the mixture and $\mathbb{I}$ is the identity matrix. We note the presence of a source term in the energy equation that comes from the fact that, if the kinetic energy flows at the mixture velocity, the gas internal energy is still advected at the gas velocity. This term is non-dissipative.

2.3.7 Gas and dust sound waves: dustywaves

At this stage, it is important to linearly perturb the equations in order to analyze the waves propagation in a gas and dust mixture (DUSTYWAVES from now on). This development was made in Laibe & Price (2011, 2014a) for one dust species and in Laibe & Price (2014b) for multiple species.

For simplicity, I demonstrate the dispersion relation in an isothermal 1D case without any exterior force ($\mathbf{f} = 0$). For any quantity A, we note A_0 its background value and δA its perturbed value. We suppose an uniform background state with an initial barycenter velocity set to zero. In this context, the perturbed conservation equations are written as

$$\begin{aligned}
\frac{\partial \delta\rho}{\partial t} + \rho_0 \frac{\partial \delta v_x}{\partial x} &= 0, \\
\rho_0 \frac{\partial \delta v_x}{\partial t} + c_{{\rm s},0}^2\left[(1-\mathcal{E}_0)\frac{\partial \delta\rho}{\partial x} - \rho_0 \frac{\partial \delta\mathcal{E}}{\partial x}\right] &= 0, \\
\rho_0 \frac{\partial \delta\epsilon_{{\rm k},0}}{\partial t} + c_{{\rm s},0}^2 T_{{\rm s},k,0}\epsilon_{{\rm k},0}\left[(1-\mathcal{E}_0)\frac{\partial^2 \delta\rho}{\partial x^2} - \rho_0 \frac{\partial^2 \delta\mathcal{E}}{\partial x^2}\right] &= 0.
\end{aligned} \tag{2.47}$$

Summing the last equation over all the dust species we get

$$\rho_0 \frac{\partial \delta\mathcal{E}}{\partial t} + c_{{\rm s},0}^2 T_{{\rm s},0}\mathcal{E}_0\left[(1-\mathcal{E}_0)\frac{\partial^2 \delta\rho}{\partial x^2} - \rho_0 \frac{\partial^2 \delta\mathcal{E}}{\partial x^2}\right] = 0. \tag{2.48}$$

The perturbation relation thus depends only on the mean properties of the dust fluid. Considering linear perturbations of the type $\delta A \propto e^{i[kx-\omega t]}$, we finally obtain the dispersion relation of the DUSTYWAVE

$$\omega^2 + i\mathcal{E}_0 T_{{\rm s},0} c_{{\rm s},0}^2 k^2 \omega - c_{{\rm s},0}^2 k^2 (1-\mathcal{E}_0) = 0. \tag{2.49}$$

A first-order development of the solution of this equation in $\omega T_{{\rm s},0}$ is particularly interesting and holds most of important effects for strongly coupled mixture (Laibe & Price, 2014a). We therefore approximate the dispersion relation as

$$\omega \simeq \pm k c_{{\rm s},0}\sqrt{1-\mathcal{E}_0} - \frac{i}{2}\mathcal{E}_0 T_{{\rm s},0} c_{{\rm s},0}^2 k^2. \tag{2.50}$$

The DUSTYWAVE can be interpreted as a modified soundwave that propagates at a modified sound speed $\tilde{c}_s = c_{s,0}\sqrt{1-\mathcal{E}_0}$ and is damped by the drag between the gas and the dust at a rate that increases with the stopping time, i.e. the grain size. This conclusion is valid only for strongly coupled mixture. If the initial Stokes number is large compared to 1, the coupling is poor and the damping disappears (Laibe & Price, 2011).

Solving exactly the perturbation relation for the full monofluid set of equations is not difficult, but tedious, as it requires to determine the roots of a cubic polynomial. The method was first presented in Laibe & Price (2011). In their work, they provided a numerical solver that I use in Chapter 3 to test my numerical implementation of dust dynamics.

2.3.8 A more general case: Individual forces

Let us now consider a more general case where individual forces apply on the gas and the different dust species. These forces are denoted as $\mathbf{f}_g$ and $\mathbf{f}_{d,k}$, respectively. The monofluid development and diffusion approximation can be made as in the previous section. Laibe & Price (2014a) have shown that in this case, the differential velocity between the dust species k and the gas is given by

$$\mathbf{\Delta v}_{d,k} = \frac{t_{s,k}}{1-\epsilon_k}\left[\mathbf{f}_{d,k} - \mathbf{f}_g - \sum_{j=1}^{\mathcal{N}} \epsilon_j(\mathbf{f}_{d,j} - \mathbf{f}_g)\right]. \tag{2.51}$$

considering that the dust velocity is written as

$$\mathbf{v}_{d,k} = \mathbf{v} + \mathbf{\Delta v}_{d,k} - \sum_{j=1}^{\mathcal{N}} \epsilon_j \mathbf{\Delta v}_{d,j}, \tag{2.52}$$

Let us now push further the derivation to get the set of hydrodynamical equations in this case. Using equation (2.52), defining the differential velocity with the barycenter $\mathbf{w_k} = \mathbf{v}_{d,k} - \mathbf{v}$, we easily find that

$$\begin{aligned}\mathbf{w_k} &= -T_{s,k}(1-\mathcal{E})\mathbf{f}_g \\ &+ \frac{t_{s,k}}{1-\epsilon_k}\left[\mathbf{f}_{d,k} - \sum_{i=1}^{\mathcal{N}}\epsilon_i\mathbf{f}_{d,i}\right] - \sum_{i=1}^{\mathcal{N}}\epsilon_i\frac{t_{s,i}}{1-\epsilon_i}\mathbf{f}_{d,i} + \sum_{i=1}^{\mathcal{N}}\sum_{j=1}^{\mathcal{N}} t_{s,i}\frac{\epsilon_i\epsilon_j}{1-\epsilon_i}\mathbf{f}_{d,j}.\end{aligned} \tag{2.53}$$

The dust mass conservation equation is given by

$$\frac{\partial \rho_{d,k}}{\partial t} + \nabla\cdot\left[\rho_{d,k}\left(\mathbf{v}+\mathbf{w_k}\right)\right] = 0. \tag{2.54}$$

The total momentum equation is also modified and is now written as

$$\frac{\partial \rho\mathbf{v}}{\partial t} + \nabla\cdot\left[\rho(\mathbf{v}\otimes\mathbf{v})\right] = \rho\mathbf{f} + \rho_g\mathbf{f}_g + \textstyle\sum_{j=1}^{\mathcal{N}}\rho_{d,j}\mathbf{f}_{d,j}. \tag{2.55}$$

The energy equation cannot be derived in the case because the energy E depends on the forces that operate, e.g. in the presence of a magnetic field $E = \frac{1}{2}\rho\mathbf{v}^2 + \rho(1-\mathcal{E})e_g + \frac{\mathbf{B}^2}{2}$ (see section 2.4.5 for the derivation with a magnetic field).

2.4 Non-ideal MHD with neutral dust grains

2.4.1 Introduction

In this section, I propose an extension of the monofluid formalism to include the dynamics of neutral dust grains in non-ideal magnetohydrodynamics (NdustyNIMHD), similar to what was presented by Fromang & Papaloizou (2006); Riols & Lesur (2018) with single dust species and without considering the cumulative dust back-reaction.

A new force, the Lorentz force must be introduced. As the dust grains are neutral, they are not sensitive the this force. However, as in the hydrodynamical case, they indirectly feel this force via collisions. The demonstration of this formalism is very similar to the hydrodynamical case and I therefore only present the equations with some indications on how to derive them.

2.4.2 Momentum equation

The plasma/gas now feels the Lorentz force and therefore the momentum conservation equation writes

$$\frac{\partial \rho \mathbf{v}}{\partial t} + \nabla \cdot \left[\left(P_\mathrm{g} + \frac{\mathbf{B}^2}{2} \right) \mathbb{I} + \rho (\mathbf{v} \otimes \mathbf{v}) - \mathbf{B} \otimes \mathbf{B} \right] = \rho \mathbf{f}. \tag{2.56}$$

This equation is exactly the same as the dust-free equation and is again simply obtained by summing all the momentum equation. By summing the Lorentz force of all the charged species, we find as in standard MHD that the barycenter feels a force $\mathbf{J} \times \mathbf{B}$. This force can still be decomposed in a magnetic pressure term and a magnetic tension. Note that the classical MHD equations already are monofluid equations (see the review by Teyssier & Commerçon, 2019), although they neglect the dynamics of any species in the barycenter frame. More detail on the subject can be found in Chapter 5.

2.4.3 Differential velocity

To determine the differential velocity between a dust species k and the barycenter, I use equation (2.53). The Lorentz force can be written as $\mathbf{f}_\mathrm{L} = \frac{\mathbf{J} \times \mathbf{B}}{\rho(1-\mathcal{E})}$ and thus $\mathbf{w_k}$ is given by

$$\mathbf{w_k} = T_{\mathrm{s},k} \frac{\nabla P_\mathrm{g} - \mathbf{J} \times \mathbf{B}}{\rho}, \tag{2.57}$$

which, in MHD, is equivalent to

$$\mathbf{w_k} = T_{\mathrm{s},k} \frac{\nabla P_\mathrm{g} - (\nabla \times \mathbf{B}) \times \mathbf{B}}{\rho}. \tag{2.58}$$

Contrary to the hydrodynamical case, the neutral dust grains in a magnetized environment do not simply drift toward pressure bumps but rather to regions where $(\nabla \times \mathbf{B}) \times \mathbf{B} = \nabla P_\mathrm{g}$.

2.4.4 Induction equation

The induction equation is written as

$$\frac{\partial \mathbf{B}}{\partial t} + \nabla \times \left[\mathbf{v}_\mathrm{g} \times \mathbf{B} \right] = -\nabla \times \mathbf{E}_\mathrm{b}, \tag{2.59}$$

where I recall that $\mathbf{E}_\mathrm{b} = \mathbf{E} - \mathbf{v}_\mathrm{g} \times \mathbf{B}$, here g refers to the neutral phase of the plasma (dust excluded). Accounting from the fact that the gas velocity differs from the barycenter velocity yields

$$\frac{\partial \mathbf{B}}{\partial t} + \nabla \times \left[\left(\mathbf{v} - \frac{1}{1-\mathcal{E}} \sum_{k=1}^{\mathcal{N}} \epsilon_k \mathbf{w_k} \right) \times \mathbf{B} \right] = -\nabla \times \mathbf{E}_\mathrm{b}. \tag{2.60}$$

We note that if the back-reaction is low, when $|\frac{1}{1-\mathcal{E}} \sum_k \epsilon_k \mathbf{w_k}| \ll |\mathbf{v}|$, we obtain again the non-ideal MHD induction equation

$$\frac{\partial \mathbf{B}}{\partial t} + \nabla \times [\mathbf{v} \times \mathbf{B}] = -\nabla \times \mathbf{E}_\mathrm{b}. \tag{2.61}$$

2.4.5 Energy equation

As said before, the derivation of the energy equation must be done specifically when a magnetic field is considered as the energy now writes $E \equiv \frac{1}{2}\rho \mathbf{v}^2 + \rho(1-\mathcal{E})e_\mathrm{g} + \frac{\mathbf{B}^2}{2}$. Without back-reaction the energy conservation equation is also the same as in non-ideal MHD and writes

$$\frac{\partial E}{\partial t} + \nabla \cdot \left[(E + P_\mathrm{n})\mathbf{v} - \mathbf{B}(\mathbf{B} \cdot \mathbf{v}) \right] = \rho \mathbf{f} \cdot \mathbf{v} + \rho \Lambda_\mathrm{res}, \tag{2.62}$$

where $\Lambda_\mathrm{res} = \mathbf{J} \cdot \mathbf{E}_\mathrm{b}$ is the non-ideal resistive heating source term.

If we now consider back-reaction, the derivation of the energy equation becomes more complicated. Energy conservation imposes that

$$\frac{\mathrm{d}E}{\mathrm{d}t} = 0. \tag{2.63}$$

We now define the kinetic energy $E_\mathrm{kin} = \frac{1}{2}\rho \mathbf{v}^2$, the internal energy $E_\mathrm{int} = \rho(1-\mathcal{E})e_\mathrm{g}$, and the magnetic energy $E_\mathrm{mag} = \frac{\mathbf{B}^2}{2}$. The three derivatives of the energies are given by

$$\begin{aligned}
\frac{\mathrm{d}E_\mathrm{kin}}{\mathrm{d}t} &= -\mathbf{v}\nabla P_\mathrm{g} + \rho \mathbf{v} \cdot \mathbf{f} + \mathbf{v} \cdot (\mathbf{J} \times \mathbf{B}) \\
\frac{\mathrm{d}E_\mathrm{int}}{\mathrm{d}t} &= -P_\mathrm{g} \nabla \cdot \mathbf{v} - (1-\mathcal{E}) e_\mathrm{g} \nabla \cdot \rho \mathbf{v} + \nabla \cdot \left(\frac{1}{1-\mathcal{E}} \sum_{k=1}^{\mathcal{N}} \epsilon_k \mathbf{w_k} e_\mathrm{g} \right) \\
\frac{\mathrm{d}E_\mathrm{mag}}{\mathrm{d}t} &= \mathbf{B} \cdot \left[(\mathbf{B} \cdot \nabla) \cdot \mathbf{v} - \mathbf{B}(\nabla \cdot \mathbf{v}) - \nabla \times \mathbf{E}_\mathrm{b} + \nabla \times \left(\frac{1}{1-\mathcal{E}} \sum_{k=1}^{\mathcal{N}} (\epsilon_k \mathbf{w_k}) \times \mathbf{B} \right) \right],
\end{aligned} \tag{2.64}$$

The magnetic energy can be further simplified as $\mathbf{B} \cdot \nabla \times (\frac{1}{1-\mathcal{E}} \sum_k (\epsilon_k \mathbf{w_k}) \times \mathbf{B}) = 0$. Summing all the terms, and using the same method to rearrange them as in standard MHD, we obtain the energy conservation equation. It writes as

$$\frac{\partial E}{\partial t} + \nabla \cdot \left[((E + P_\mathrm{n})\mathbf{v} - \mathbf{B}(\mathbf{B} \cdot \mathbf{v}) \right] = \nabla \cdot \left[\frac{P_\mathrm{g}}{\gamma - 1} \frac{1}{1-\mathcal{E}} \sum_{k=1}^{\mathcal{N}} \epsilon_k \mathbf{w_k} \right] + \rho \mathbf{f} \cdot \mathbf{v} + \rho \Lambda_\mathrm{res}. \tag{2.65}$$

2.4.6 NdustyNIMHD

Here, I summarize the equation of NdustyNIMHD, they write as follows

$$\begin{aligned}
\frac{\partial \rho}{\partial t} + \nabla \cdot [\rho \mathbf{v}] &= 0, \\
\frac{\partial \rho \mathbf{v}}{\partial t} + \nabla \cdot \left[\left(P_\mathrm{g} + \frac{\mathbf{B}^2}{2} \right) \mathbb{I} + \rho (\mathbf{v} \otimes \mathbf{v}) - \mathbf{B} \otimes \mathbf{B} \right] &= \rho \mathbf{f}, \\
\frac{\partial \rho_{\mathrm{d},k}}{\partial t} + \nabla \cdot \left[\rho_{\mathrm{d},k} \left(\mathbf{v} + \mathbf{w_k} \right) \right] &= 0, \\
\frac{\partial E}{\partial t} + \nabla \cdot \left[\left((E + P_\mathrm{n}) \mathbf{v} - \mathbf{B} (\mathbf{B} \cdot \mathbf{v}) \right] \right. &= \nabla \cdot \left[\frac{P_\mathrm{g}}{\gamma - 1} \frac{1}{1 - \mathcal{E}} \sum_{k=1}^{\mathcal{N}} \epsilon_k \mathbf{w_k} \right] + \rho \mathbf{f} \cdot \mathbf{v} + \rho \Lambda_\mathrm{res}, \\
\frac{\partial \mathbf{B}}{\partial t} + \nabla \times \left[\left(\mathbf{v} - \frac{1}{1 - \mathcal{E}} \sum_{k=1}^{\mathcal{N}} \epsilon_k \mathbf{w_k} \right) \times \mathbf{B} \right] &= -\nabla \times \mathbf{E}_\mathrm{b}, \\
\nabla \cdot \mathbf{B} &= 0.
\end{aligned} \tag{2.66}$$

where

$$\mathbf{w_k} = T_{\mathrm{s},k} \frac{\nabla P_\mathrm{g} - (\nabla \times \mathbf{B}) \times \mathbf{B}}{\rho}. \tag{2.67}$$

Fortunately, these equations are rather similar to the non-ideal MHD equations especially when we make the hypothesis that $|\frac{1}{1-\mathcal{E}} \sum_k \epsilon_k \mathbf{w_k}| \ll |\mathbf{v}|$.

As a first step toward correctly treating the dynamics of neutral grain in a magnetized environment it is interesting to only consider the modification in the differential velocity between the gas and dust show in equation (2.67). The additional terms of the induction equation are likely to be small compared to the others for strongly coupled mixtures. In this case, the differential velocity between the gas and the dust must be small compared to the barycenter velocity.

2.5 Summary

In this Chapter, I introduced the reader to gas and dust differential dynamics. In short:

1. I recalled the dynamics of a single dust grain embedded in a neutral gas.
2. I established that collective effects of dust grains could be well described with a multifluid approach.
3. I have later shown that this multifluid can be reformulated without approximation as a monofluid composed a gas and a dust phase.
4. I have shown that great simplifications could be made for tightly coupled gas and dust mixtures in the so-called diffusion and terminal velocity approximation.
5. I presented the extension of the previous formalism to multiple dust species.
6. I presented the monofluid set of equations in the case of neutral dust grains in a weakly ionized plasma (NdustyMHD).

Chapter 3

Numerical methods

Contents

Philoctetes

"Use your head!"

- Hercules

In this chapter, I introduce the RAMSES code (Teyssier, 2002). This code solves the self-gravitating radiation-magnetohydrodynamics equations and is a very popular tool for astrophysical or cosmological simulations. After introducing RAMSES main features, I present the RAMSES module that I developed in order to be able to treat dust dynamics with multiple grain species. In the last part of this chapter, I perform several tests to benchmark my implementation. This work was mostly presented in Lebreuilly et al. (2019).

3.1 The RAMSES code

3.1.1 RAMSES

The RAMSES code (Teyssier, 2002) is a finite-volume Eulerian code that integrates the equation of hydrodynamics in their conservative form on an AMR grid (Berger & Oliger, 1984).. Among others applications, it has been extended to magnetohydrodynamics (Teyssier et al., 2006; Fromang et al., 2006; Masson et al., 2012; Marchand et al., 2018), radiation hydrodynamics (Commerçon et al., 2011; Rosdahl et al., 2013; Commerçon et al., 2014; Rosdahl & Teyssier, 2015; González et al., 2015), and cosmic ray and anisotropic heat conduction (Dubois & Commerçon, 2016). I extended it to the treatment of dust dynamics in Lebreuilly et al. (2019).

3.1.2 Hyperbolic formulation of hydrodynamics

For simplicity, the hydrodynamical version of RAMSES is presented at first. It solves the Euler equations of a pure gas in their hyperbolic form

$$\frac{\partial \mathbb{U}}{\partial t} + \nabla \cdot \mathbb{F}(\mathbb{U}) = 0, \tag{3.1}$$

the state $\mathbb{U}$ vector and flux $\mathbb{F}$ vector being

$$\begin{aligned} \mathbb{U} &\equiv \left(\rho_g, \rho_g \mathbf{v}_g, E_g\right), \\ \mathbb{F}(\mathbb{U}) &\equiv \left(\rho_g \mathbf{v}_g, \rho_g \mathbf{v}_g \otimes \mathbf{v}_g + P_g \mathbb{I}, \mathbf{v}_g (E_g + P_g)\right), \end{aligned}$$

where $\mathbb{I}$ is the identity matrix and $E_g \equiv \frac{1}{2}\rho_g {\mathbf{v}_g}^2 + \rho_g e_g$ is the total energy of the gas. We note that the equations of hydrodynamics are hyperbolic only when there are no source terms such as the gravity. When introducing a non-hyperbolic source term, the former equation can be written as

$$\frac{\partial \mathbb{U}}{\partial t} + \nabla \cdot \mathbb{F}(\mathbb{U}) = \mathbb{S}(\mathbb{U}). \tag{3.2}$$

Let us now consider the case were $\mathbb{S}(\mathbb{U}) = 0$. For a 1D problem integrated over time (for $t \in [0, T]$) and space (for $x \in [x_{\rm left}, x_{\rm right}]$), the previous system is written as

$$\int_{x_{\rm left}}^{x_{\rm right}} (\mathbb{U}(T) - \mathbb{U}(0))\, \mathrm{d}x + \int_0^T \left(\mathbb{F}(x_{\rm right}) - \mathbb{F}(x_{\rm left})\right) \mathrm{d}t = 0. \tag{3.3}$$

3.1.3 Godunov scheme

Finite-volume methods are based on the estimation of the average of $\mathbb{U}$ over the cells. Equation (3.3) shows that, with this approach, the evolution of the state vector is constrained by the fluxes at the interfaces of the cells.

RAMSES uses a second-order predictor-corrector Godunov method (Godunov, 1959) to update $\mathbb{U}$. At the timestep n for a cell i, any physical quantity A is discretized as

$$A(x,t) \rightarrow A_i^n.$$

Cell interfaces are denoted with half integer subscripts, e.g, $i+1/2$ for the interface between the cell i and $i+1$. Similarly, half timesteps are also denoted with half integer superscripts, e.g, $n+1/2$. For a cell of length Δx and a timestep Δt, the scheme writes

$$\mathbb{U}_i^{n+1} = \mathbb{U}_i^n - \left(\mathbb{F}_{i+1/2}^{n+1/2} - \mathbb{F}_{i-1/2}^{n+1/2}\right)\frac{\Delta t}{\Delta x}, \tag{3.4}$$

where the discretized fluxes $\mathbb{F}_{i\pm1/2}^{n+1/2} = \mathbb{F}^\star\left(\mathbb{U}_i^n, \mathbb{U}_{i-1}^n\right)$ are the solutions of the so-called *Riemann problem* at the interfaces.

3.1.4 Riemann problems

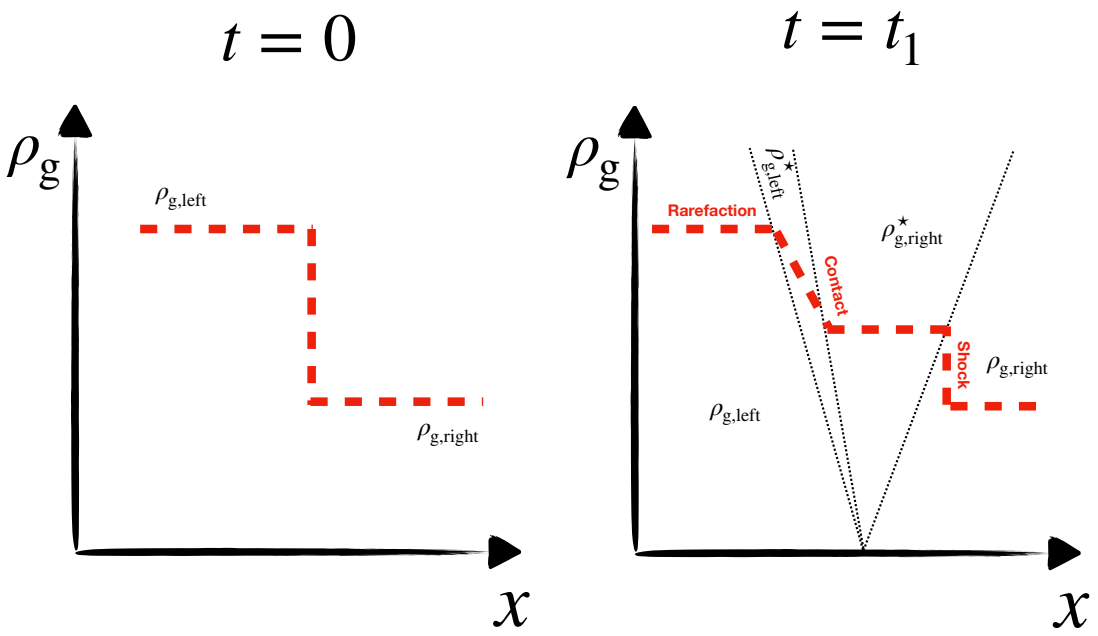

Figure 3.1: Cartoon illustration of a Riemann problem with a density discontinuity (*shock-tube*). (Left) initial state. (Right) Density after an arbitrary time, the three characteristic waves (rarefaction, contact and shock) propagate and two additional states are produced.

A Riemann problem occurs when there is a discontinuity of the hydrodynamical variables at the interface between two control volumes (see figure 3.1 for a cartoon illustration of a Riemann problem). Numerically, a Riemann problem is solved by determining the value of $\mathbb{F}^\star\left(\mathbb{U}_i^n, \mathbb{U}_{i-1}^n\right)$. One first needs to estimate the characteristic wave speeds of the system. In that goal, equation (3.1) can be reformulated as

$$\frac{\partial \mathbb{U}}{\partial t} + \mathbb{J}\nabla \cdot \mathbb{U} = 0, \tag{3.5}$$

where $\mathbb{J}$ is the *Jacobian* matrix of $\mathbb{F}(\mathbb{U})$, its eigenvalues are the characteristic wave speeds. In the hydrodynamical 1D case, it is written as

$$\mathbb{J} = \begin{bmatrix} 0 & 1 & 0 \\ \frac{\gamma-3}{2} v_{\mathrm{g},x}^2 & (3-\gamma) v_{\mathrm{g},x} & (\gamma-1) \\ \frac{\gamma-2}{2} v_{\mathrm{g},x}^3 - \frac{\gamma v_{\mathrm{g},x} P_\mathrm{g}}{\rho_\mathrm{g}(\gamma-1)} & \frac{3-2\gamma}{2} v_{\mathrm{g},x}^2 - \frac{\gamma P_\mathrm{g}}{\rho_\mathrm{g}(\gamma-1)} & \gamma v_{\mathrm{g},x} \end{bmatrix}, \tag{3.6}$$

this matrix is quite hard to handle as it is but, fortunately, equation (3.5) can be written in terms of so-called *primitive variables*[1] $\mathbb{V} = \left(\rho_\mathrm{g}, \mathbf{v}_\mathrm{g}, P_\mathrm{g}\right)$ as

$$\frac{\partial \mathbb{V}}{\partial t} + \mathbb{A}\nabla \cdot \mathbb{V} = 0, \tag{3.7}$$

where $\mathbb{A}$ is similar to $\mathbb{J}$ and therefore has the same eigenvalues. $\mathbb{A}$ is written

$$\mathbb{A} = \begin{bmatrix} v_{\mathrm{g},x} & \rho_\mathrm{g} & 0 \\ 0 & v_{\mathrm{g},x} & \frac{1}{\rho_\mathrm{g}} \\ 0 & \gamma P_\mathrm{g} & v_{\mathrm{g},x} \end{bmatrix}. \tag{3.8}$$

One then find that the three eigenvalues $\lambda_{i,i\in[1,3]}$ of $\mathbb{A}$ (and therefore $\mathbb{J}$) are

$$\lambda_{i,i\in[1,3]} = \begin{cases} v_{\mathrm{g},x} - c_\mathrm{s}, \\ v_{\mathrm{g},x}, \\ v_{\mathrm{g},x} + c_\mathrm{s}, \end{cases} \tag{3.9}$$

$c_\mathrm{s} = \sqrt{\frac{\gamma P_\mathrm{g}}{\rho_\mathrm{g}}}$ being the gas adiabatic soundspeed. In this simple hydrodynamical case, the information travels at three different wave speeds. There is an expansion wave at $v_{\mathrm{g},x} - c_\mathrm{s}$, a contact discontinuity wave at $v_{\mathrm{g},x}$ and a shock wave at $v_{\mathrm{g},x} + c_\mathrm{s}$. Assuming two initial states $\mathbb{U}_\mathrm{left}$ and $\mathbb{U}_\mathrm{right}$, two additional states $\mathbb{U}^\star_\mathrm{left}$ and $\mathbb{U}^\star_\mathrm{right}$ are expected to form while these three waves propagate (see figure 3.1). The second step to solve a Riemann problem consists in determining these additional step. Then one must estimate the flux at the interface between the control volumes $\mathbb{F}^\star\left(\mathbb{U}_\mathrm{left}, \mathbb{U}_\mathrm{right}, \mathbb{U}^\star_\mathrm{left}, \mathbb{U}^\star_\mathrm{right}\right)$.

3.1.5 Approximate Riemann solver : The HLL case

It is possible to numerically find an exact solution of a Riemann problem, however it comes with a great computational cost (Toro, 2013). A way to overcome this difficulty is to use an approximate Riemann solver such as

- The *Roe* solver that uses the linearized Jacobian matrix to estimate the states in each domain.
- The *Lax-Friedrich* solver that considers only two waves of opposite direction propagating at the highest of the three characteristic speeds. As a consequence, it also considers an intermediate state known as $\mathbb{U}_\mathrm{llf}$.
- The *HLL* solver also consider two waves but with different speeds. It thus also introduces an additional intermediate state which is $\mathbb{U}_\mathrm{hll}$.

[1] that can be expressed in term of the conservative variables

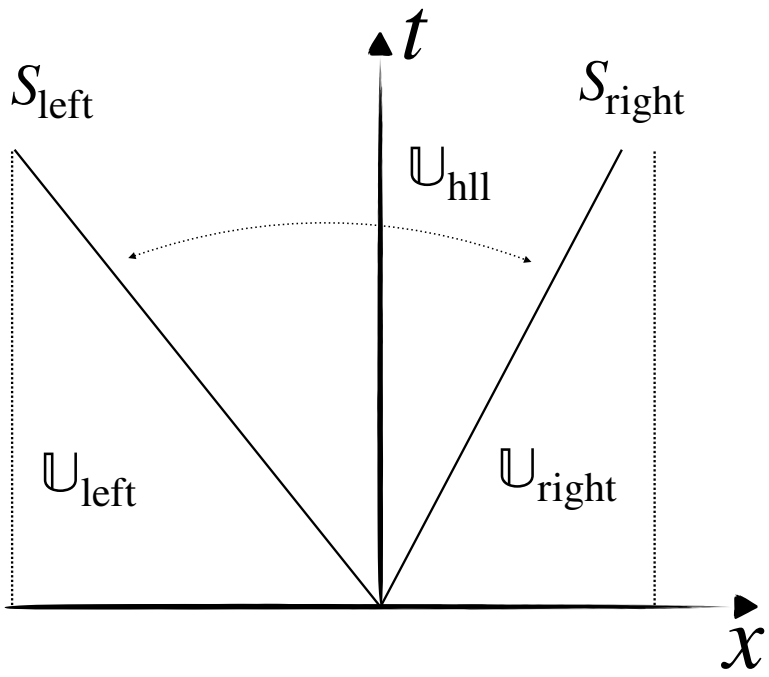

Figure 3.2: Space time diagram illustrating the Riemann problem in the HLL case. S_{left} and S_{right} are the two characteristic speeds of the problem. $\mathbb{U}_{\text{hll}}$ is the intermediate state. Note that with the HLL solver $S_{\text{left}} \neq S_{\text{right}}$ is possible, as illustrated here.

- The *HLLC* solver, a modification of HLL that restores the contact wave and therefore consider the four states presented above.

For simplicity, I explain here how the HLL solver works. In this approach the state vector is written as

$$\mathbb{U} = \begin{cases} \mathbb{U}_{\text{left}} \text{ if } \frac{x}{t} \leq S_{\text{left}}, \\ \mathbb{U}_{\text{hll}} \text{ if } S_{\text{left}} \leq \frac{x}{t} \leq S_{\text{right}}, \\ \mathbb{U}_{\text{right}} \text{ if } \frac{x}{t} \geq S_{\text{right}}, \end{cases} \tag{3.10}$$

where S_{left} and S_{right} are the two characteristic speeds of the problem[2] (see figure 3.2 for a space time diagram illustrating the HLL Riemann problem). It is easy to show that

$$\int_{x_{\text{left}}}^{x_{\text{right}}} \mathbb{U}(T)\mathrm{d}x = (TS_{\text{left}} - x_{\text{left}})\,\mathbb{U}_{\text{left}} + \left(TS_{\text{right}} - TS_{\text{left}}\right)\mathbb{U}_{\text{hll}} + \left(x_{\text{right}} - TS_{\text{right}}\right)\mathbb{U}_{\text{right}}, \tag{3.11}$$

which, using equation (3.3) yields

$$\mathbb{U}_{\text{hll}} = \frac{S_{\text{right}}\mathbb{U}_{\text{right}} - S_{\text{left}}\mathbb{U}_{\text{left}} + \mathbb{F}_{\text{left}} - \mathbb{F}_{\text{right}}}{S_{\text{right}} - S_{\text{left}}}, \tag{3.12}$$

where $\mathbb{F}_{\text{left}} = \mathbb{F}(\mathbb{U}_{\text{left}})$ and $\mathbb{F}_{\text{right}} = \mathbb{F}(\mathbb{U}_{\text{right}})$. Applying the Rankine-Hugoniot condition at the left-hll interface when $S_{\text{left}} \leq 0 \leq S_{\text{right}}$ one can show that

$$\mathbb{F}_{\text{hll}} = \mathbb{F}_{\text{left}} + S_{\text{left}}\left(\mathbb{U}_{\text{hll}} - \mathbb{U}_{\text{left}}\right), \tag{3.13}$$

which, using the expression of $\mathbb{U}_{\text{hll}}$, leads to

$$\mathbb{F}_{\text{hll}} = \frac{S_{\text{right}}\mathbb{F}_{\text{left}} - S_{\text{left}}\mathbb{F}_{\text{right}} + S_{\text{left}}S_{\text{right}}(\mathbb{U}_{\text{right}} - \mathbb{U}_{\text{left}})}{S_{\text{right}} - S_{\text{left}}}. \tag{3.14}$$

[2] not to be confused with the source terms $\mathbb{S}$

The final value of the flux at the interface of the control domain is then given by

$$\mathbb{F}^\star = \begin{cases} \mathbb{F}_{\text{left}} \text{ if } 0 \leq S_{\text{left}}, \\ \mathbb{F}_{\text{hll}} \text{ if } S_{\text{left}} \leq 0 \leq S_{\text{right}}, \\ \mathbb{F}_{\text{right}} \text{ if } 0 \geq S_{\text{right}}. \end{cases} \tag{3.15}$$

3.1.6 The MUSCL scheme

Once the interface fluxes are estimated, they can be used to update the state vector according to the Godunov method. In the first-order Godunov method, the state vector is considered constant in a cell, which constitutes a *piecewise constant approximation*. To gain an order of accuracy, one must adopt a *piecewise linear approximation*. The *MUSCL predictor-corrector* scheme (van Leer, 1979), used in `RAMSES`, has been developed in that perspective. This scheme consists in two successive steps

- *The predictor step*, during which the state vector is estimated at the left and right interfaces of the control domain using an estimate of its slopes in every direction and at half timestep using equation (3.7).
- *The corrector step*, when the predicted state vector is used to compute the flux using an approximate Riemann solver (e.g. HLL, HLLD, see section 3.1.5 for HLL)

Let us detail the predictor step (the corrector step simply follows section 3.1.5).

To perform the predictor step one can be tempted to use a central finite difference to estimate the slope $\Delta_x \mathbb{U}$ of the vector step. Unfortunately, there is no insurance of preserving the monotonicity with this estimate. To ensure its preservation, slope limiters must be employed. They are designed to preserve the so-called total variation diminishing property (TVD, Harten, 1983). Defining the total variation as

$$TV(\mathbb{U}^n) = \sum_i |\mathbb{U}^n_{i+1} - \mathbb{U}^n_i|, \tag{3.16}$$

the TVD condition is given by

$$TV(\mathbb{U}^{n+1}) \leq TV(\mathbb{U}^n). \tag{3.17}$$

A classical example of slope limiters is *MINMOD* that is written as

$$\Delta_x \mathbb{U}_{\text{MINMOD}} = \begin{cases} a \text{ if } |a| < |b| \text{ and } ab > 0 \\ b \text{ if } |a| > |b| \text{ and } ab > 0 \\ 0 \text{ otherwise }, \end{cases} \tag{3.18}$$

where $a = \mathbb{U}^n_i - \mathbb{U}^n_{i-1}$ and $b = \mathbb{U}^n_{i+1} - \mathbb{U}^n_i$.

Once the slope $\Delta_x \mathbb{U}$ is estimated using a slope limiter. $\mathbb{U}$, the MUSCL schemes uses equation (3.7) to perform the predictor step. In the simple case of mass conservation, this equation is given by

$$\frac{\partial \rho_{\text{g}}}{\partial t} = -\frac{\partial \rho_{\text{g}} v_{\text{g},x}}{\partial x}, \tag{3.19}$$

A discretization of this equation allows us to estimate ${\rho_{\text{g}}}^{n+1/2}_{i-1/2}$, which is the value at the left boundary of the cell i and therefore at the right of the interface between $i-1$ and i. It is written as

$${\rho_{\text{g}}}^{n+1/2}_{i-1/2} = {\rho_{\text{g}}}^n_i - \frac{1}{2}\Delta_x {\rho_{\text{g}}}^n_i - \frac{\Delta t}{2\Delta x}\left({\rho_{\text{g}}}^n_i \Delta_x {v_{\text{g},x}}^n_i + {v_{\text{g},x}}^n_i \Delta_x {\rho_{\text{g}}}^n_i\right). \tag{3.20}$$

All the other variables (momentum and energy in the hydrodynamical case) are updated similarly according to their evolution equation.

3.1.7 Gravity

As explained earlier, gravity adds non-hyperbolic source terms to the equation of hydrodynamics. In addition, the Poisson equation, that is not hyperbolic as well, must be solve to account for the interaction between the mass distribution and the gravitational potential. In RAMSES, the Poisson equation is solved either by the conjugate gradient algorithm or by a multigrid solver. I do not details their implementation which are explained in (Teyssier, 2002, for the conjugate gradient) and (Guillet & Teyssier, 2011, for the multigrid solver). Typically, the multigrid solver is more efficient than the conjugate gradient while the later is more robust.

Once the gravitational potential is determined at a time t by one of the two available solver one must add the source terms to the state vectors. In RAMSES, the gravity source term $\mathbb{S}^{n+1/2}_{\text{gravity}_i}$ is computed as

$$\mathbb{S}^{n+1/2}_{\text{gravity}_i} = \left(0, \frac{1}{2}\left({\rho_{\text{g}}}_i^n \nabla \phi_i^n + {\rho_{\text{g}}}_i^{n+1} \nabla \phi_i^{n+1}\right), \frac{1}{2}\left({\rho_{\text{g}}}_i^n {v_{\text{g},x_i}}^n \nabla \phi_i^n + {\rho_{\text{g}}}_i^{n+1} {v_{\text{g},x_i}}^{n+1} \nabla \phi_i^{n+1}\right)\right). \tag{3.21}$$

This method, called *the fractional step method* (detailled in Toro, 2013), ensure the preservation of the second-order accuracy of the Godunov method. The modified Godunov scheme in presence of gravity is

$$\mathbb{U}_i^{n+1} = \mathbb{U}_i^n - \left(\mathbb{F}_{i+1/2}^{n+1/2} - \mathbb{F}_{i-1/2}^{n+1/2}\right)\frac{\Delta t}{\Delta x} + \mathbb{S}^{n+1/2}_{\text{gravity}_i}\Delta t. \tag{3.22}$$

3.1.8 Magnetohydrodynamics

I explained in the previous section how the hydrodynamical conservation equations are solved in RAMSES. In star formation, magnetic fields are known to play an important role (Allen et al., 2003a; Hennebelle & Teyssier, 2008; Commerçon et al., 2010; Tomida, 2014; Tomida et al., 2015; Wurster et al., 2018; Vaytet et al., 2018b; Marchand et al., 2019). Besides adding new waves to the problem, MHD requires to solve the induction equation while ensuring that the solenoidal constraint is preserved.

In both non-ideal and ideal MHD, the induction equation can be written as

$$\frac{\partial \mathbf{B}}{\partial t} - \nabla \times \mathbf{E} = 0, \tag{3.23}$$

this equation is not hyperbolic. However, defining the magnetic flux over a surface S as $\phi_{\mathbf{B}} = \iint_S \mathbf{B}\mathbf{dS}$, equation (3.23) can be formulated as

$$\frac{\partial \phi_{\mathbf{B}}}{\partial t} = \oint_C \mathbf{E}\mathbf{dl}, \tag{3.24}$$

we note that this equation preserves the magnetic divergence during the magnetic field evolution.

The *finite-surface constrained transport method* (Evans & Hawley, 1988) have been implemented in RAMSES by Teyssier et al. (2006) to ensure the preservation of $\nabla \cdot \mathbf{B}$ even after discretisation. In that aim, the magnetic field is now defined at the cell interface while the time averaged electric field components are evaluated at the edges of the interfaces. With this

approach, equation (3.24) is discretized as follows

$$\begin{aligned}
\frac{B^{n+1}_{x,i-1/2,j,k} - B^{n}_{x,i-1/2,j,k}}{\Delta t} &= \frac{E^{n+1/2}_{z,i-1/2,j+1/2,k} - E^{n+1/2}_{z,i-1/2,j-1/2,k}}{\Delta y} - \frac{E^{n+1/2}_{y,i-1/2,j,k+1/2} - E^{n+1/2}_{y,i-1/2,j,k-1/2}}{\Delta z}, \\
\frac{B^{n+1}_{y,i,j-1/2,k} - B^{n}_{x,i,j,-1/2k}}{\Delta t} &= \frac{E^{n+1/2}_{x,i,j-1/2,k+1/2} - E^{n+1/2}_{x,i,j-1/2,k-1/2}}{\Delta z} - \frac{E^{n+1/2}_{z,i+1/2,j-1/2,k} - E^{n+1/2}_{z,i-1/2,j-1/2,k}}{\Delta x}, \\
\frac{B^{n+1}_{z,i,j,k-1/2} - B^{n}_{x,i,j,k-1/2}}{\Delta t} &= \frac{E^{n+1/2}_{y,i+1/2,j,k-1/2} - E^{n+1/2}_{y,i-1/2,j,k-1/2}}{\Delta x} - \frac{E^{n+1/2}_{x,i,j+1/2,k-1/2} - E^{n+1/2}_{x,i,j-1/2,k-1/2}}{\Delta y}.
\end{aligned} \tag{3.25}$$

By construction, this discretization imposes $\nabla \cdot \mathbf{B}^n = \nabla \cdot \mathbf{B}^{n+1}$. Hence to ensure the solenoidal constrant in *RAMSES*, having $\nabla \cdot \mathbf{B}^0 = 0$ is enough.

As the electric fields play a role that is equivalent to the fluxes in hydrodynamics, they must be estimated at the cell edges. A so-called *2D Riemann problem* at the junction between four states, left-bottom, left-top, right-bottom and right-top, must then be solved. For simplicity, I chose not to detail the 2D Riemann problem and the approximate 2D Riemann solver that follow the same principles, but with much heavier expressions, as the standard 1D case. In short, the procedure to update the magnetic field is executed as follows

1 The values of hydro variables are estimated at the cell corners using 2D slope limiters.

2 The electric fields at the corners are estimated using an *approximate 2D-Riemann solver*, e.g. HLL.

3 The magnetic fields are updated according to equations (3.25).

The induction equation is not the only change that is brought to the equation of hydrodynamics in MHD. In ideal MHD case seven characteristic wave must be considered

- 2 Alfvén waves that propagates at the speed $\lambda = \mathbf{v}_{\mathrm{g},x} \pm v_{\mathrm{a}}$,
- 4 fast/slow magneto-sonic waves with $\lambda = \mathbf{v}_{\mathrm{g},x} \pm \sqrt{\frac{1}{2}(c_{\mathrm{s}}^2 + v_{\mathrm{a}}^2) \pm \frac{1}{2}\sqrt{(c_{\mathrm{s}}^2 - v_{\mathrm{a}}^2)^2 - 4c_{\mathrm{s}}^2 v_{\mathrm{a},x}^2}}$,
- 1 contact discontinuity propagating at the speed $\lambda = \mathbf{v}_{\mathrm{g},x}$,

where $v_{\mathrm{a}} = \frac{B}{\sqrt{\rho}}$ is the Alfvén speed (Alfvén, 1942). The approximate Riemann solvers of `RAMSES` have been extended to take the additional ideal and non-ideal-MHD waves into accounts by (Teyssier et al., 2006; Fromang et al., 2006; Masson et al., 2012; Marchand et al., 2018).

3.1.9 AMR grid

The AMR grid enables an accurate description of the regions of interest in the simulation box. In `RAMSES`, the AMR grid is made of *otcs*. They are groups of 2^{ndim} cells, where ndim is the number of dimension of the simulation. Octs are tagged with a refinement level ℓ with a value between ℓ_{min} for the coarsest cells and ℓ_{max} for the finest. The length of a cell of level ℓ is

$$\Delta x_\ell = \frac{L_{\mathrm{box}}}{2^\ell},$$

where L_{box} is the size of the simulation box. For a uniform grid with an unique level ℓ, the effective resolution is simply 2^ℓ. As a consequence, in `RAMSES` $\Delta x = \Delta y = \Delta z$.

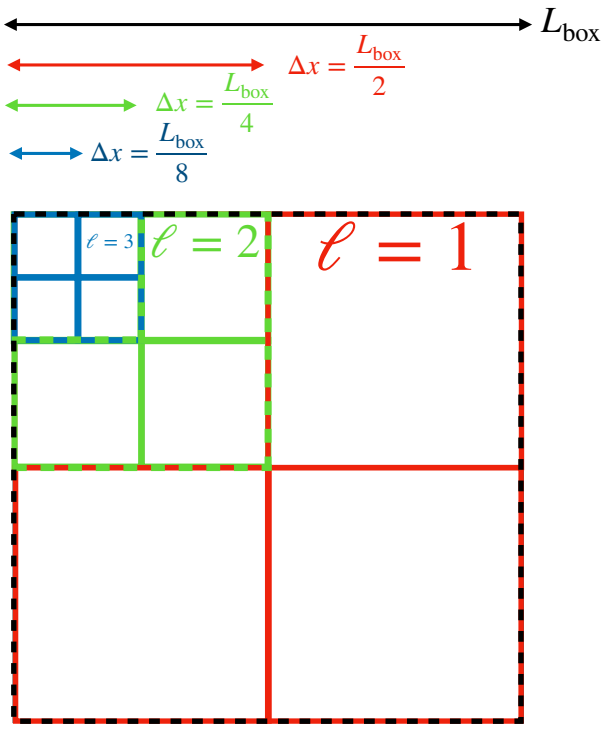

Figure 3.3: Cartoon illustration of an 2D AMR grid with $\ell_{\rm min} = 1$ and $\ell_{\rm min} = 3$ with a refinement strategy that imposes only one level difference between two adjacent cells. The AMR allows to increase the resolution in regions of interest using a relevant refinement criterion, e.g. the based on the Jeans-length in star formation simulations.

The AMR grid can be either refined or unrefined at each timestep to resolve regions of interest in the simulation box, it is however imposed that neighbor cells can only differ by one level. Figure 3.3 shows a cartoon illustration of an AMR grid in the simple case of a 2D simulation with a minimum level $\ell_{\rm min} = 1$ and a maximum level $\ell_{\rm min} = 3$. The minimum and maximum cell sizes are therefore $\frac{L_{\rm box}}{8}$ and $\frac{L_{\rm box}}{2}$.

3.1.10 Timestepping

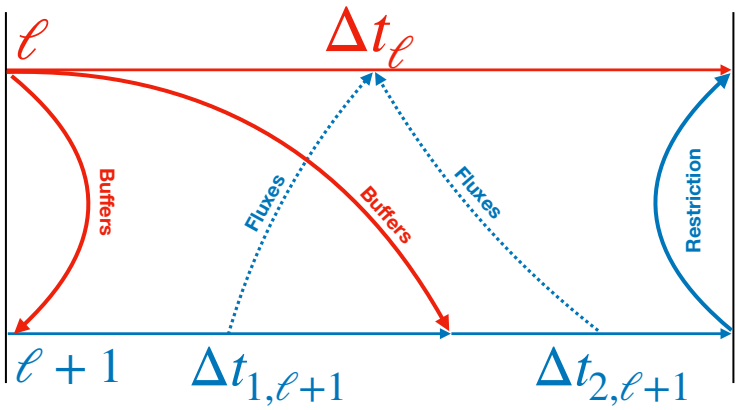

Figure 3.4: Cartoon illustration the adaptive timesteping strategy used by `RAMSES`. Inspired form Romain Teyssier's lecture.

Courant condition

RAMSES is an explicit code, which means that the timestep must be verifying the so-called *Courant–Friedrichs–Lewy condition* (Courant et al., 1928, hereafter CFL). If we consider a cell of length Δx in which the maximum wave speed is $c_{\max}$, then the CFL conditions typically imposes that

$$\Delta t = C_{\mathrm{CFL}} \frac{\Delta x}{c_{\max}}. \tag{3.26}$$

where $C_{\mathrm{CFL}} < 1$ is a safety factor. How $c_{\max}$ is determined depends on the numerical scheme used. RAMSES uses a *dimensionally split scheme* and the maximum waves speed must be chosen as $c_{\max} = c_{\mathrm{s}} + |v_{\mathrm{g},x}| + |v_{\mathrm{g},y}| + |v_{\mathrm{g},z}|$ in the hydrodynamical case. In the ideal MHD case, c_{s} is replaced by the fast magnetosonic wave.

Adaptive timestep

The RAMSES code uses an adaptive timestep to reduce the computation time while maintaining a good accuracy for the refined cells. When a level ℓ is updated with a timestep Δt_ℓ, the level $\ell + 1$ is updated twice with two timesteps, $\Delta t_{1,\ell+1}$ and $\Delta t_{2,\ell+1}$, each verifying the CFL. The two levels are synchronized with the following condition

$$\Delta t_\ell = \Delta t_{1,\ell+1} + \Delta t_{2,\ell+1}.$$

Time update

The state vector is updated level by level starting from the finer up to the coarser level. For a cell of level ℓ, three types of interfaces are possible

- The fine-to-coarse interfaces, when the neighbor cell is at level $\ell - 1$;
- the fine-fine interfaces, when the neighbor cell is also at level ℓ;
- the coarse-to-fine interfaces, when the neighbor cell is at level $\ell + 1$.

During the update of level $\ell + 1$, the fluxes at the interface with level ℓ are used to update the level $\ell + 1$ and stored for the later update of the level ℓ. During the update of the level, the state vector of the coarser levels is held constant. The fine-to-coarse and fine-fine fluxes are computed during the update of the level ℓ. The coarse neighbor cells at level $\ell - 1$ are virtually refined to compute the flux at the boundaries with level ℓ. The adaptive timesteping and flux update strategy is summarized in figure 3.4.

3.2 Implementation of the dust dynamics

3.2.1 Operator splitting

In the previous section, I explained how RAMSES solves the equations of hydrodynamics in their conservative form. The monofluid formalism in the diffusion approximation has the same structure for the mass, momentum and energy conservation equation. A total of $\mathcal{N}$ additional equations are however required when $\mathcal{N}$ dust species are included. The system is now written as

$$\frac{\partial \mathbb{U}}{\partial t} + \nabla \cdot \mathbb{F}_{\mathrm{H}}(\mathbb{U}) + \nabla \cdot \mathbb{F}_{\Delta}(\mathbb{U}) = 0. \tag{3.27}$$

The new state vector $\mathbb{U}$ is defined as

$$\mathbb{U} \equiv (\rho, \rho\mathbf{v}, E, \rho_{\mathrm{d},k})\,;$$

the flux $\mathbb{F}_{\mathrm{H}}$ is similar to the flux of pure hydrodynamics and is given by

$$\mathbb{F}_{\mathrm{H}}(\mathbb{U}) \equiv \left(\rho\mathbf{v}, \rho\mathbf{v}\otimes\mathbf{v} + P_{\mathrm{g}}\mathbb{I}, \mathbf{v}(E + P_{\mathrm{g}}), \rho_{\mathrm{d},k}\mathbf{v}\right),$$

the flux $\mathbb{F}_{\Delta}$ accounts for the dust drift and is given by

$$\mathbb{F}_{\Delta}(\mathbb{U}) \equiv \left(0, 0, \frac{P_{\mathrm{g}}}{\gamma - 1}\mathbf{w}_{\mathrm{g,b}}, \rho_{\mathrm{d},k}\mathbf{w}_{\mathbf{k}}\right),$$

where $\mathbf{w}_{\mathbf{k}}$, the differential advection velocity between the dust species k and the barycenter, is

$$\mathbf{w}_{\mathbf{k}} \equiv \frac{T_{\mathrm{s},k}\nabla P_{\mathrm{g}}}{\rho}; \tag{3.28}$$

and $\mathbf{w}_{\mathrm{g,b}}$ is the differential velocity between the gas and the barycenter is written as

$$\mathbf{w}_{\mathrm{g,b}} = -\frac{\mathcal{E}\mathcal{T}_{\mathrm{s}}}{1-\mathcal{E}}\frac{\nabla P_{\mathrm{g}}}{\rho} \tag{3.29}$$

or

$$\mathbf{w}_{\mathrm{g,b}} = -\sum_{k=1}^{\mathcal{N}} \frac{\rho_{\mathrm{d},k}}{\rho - \sum_j \rho_{\mathrm{d},j}}\mathbf{w}_{\mathbf{k}}. \tag{3.30}$$

The classical second-order Godunov method presented above is used to update the state vector. An operator splitting method is performed to solve the system in two steps. In the so-called hydrodynamical step, `RAMSES` only computes $\mathbb{F}_{\mathrm{H}}$ and update the state vector accordingly. An important difference between this step and the classical hydrodynamical version of `RAMSES` is that the fluid density ρ is different from the gas density. As a consequence, the pressure and the sound wave speeds must be computed using $\rho_{\mathrm{g}} = \rho(1-\mathcal{E})$ instead of ρ.

3.2.2 MUSCL scheme for dust diffusion/advection

The second step of the operator splitting consists in considering the contribution from the second flux vector $\mathbb{F}_{\Delta}$. For simplicity, let us now focus on the update of the dust density keeping in mind that the dust density and energy updates are done simultaneously. In this aim, the following equation is solved

$$\frac{\partial\tilde{\rho}_{\mathrm{d},k}}{\partial t} = -\nabla\cdot\left[\tilde{\rho}_{\mathrm{d},k}\mathbf{w}_k\right], \tag{3.31}$$

where $\tilde{\rho}_{\mathrm{d},k}$ refers to $\rho_{\mathrm{d},k}$ after its advection as a passive scalar at the velocity $\mathbf{v}$. In the remainder of the section, I omit this symbol and the k index. A MUSCL predictor-corrector scheme is used to compute the dust diffusion fluxes $\mathcal{F}(\rho_{\mathrm{d}}) \equiv \rho_{\mathrm{d}}\mathbf{w}$. The flux storage and the Godunov update are performed as in the hydrodynamical step.

Apart from the dust densities and the energy of the mixture, the variables are constant during this step. In particular, the total density ρ is constant.

Differential advection velocity: During the diffusion step, the aim is to compute the differential advection velocity $w^n_{i,j,k}$. To get its value, the pressure gradient is evaluated at the center of the cell i, j, k of length Δx. For example, its component in the x-direction, is

$$\nabla_x {P_{\mathrm{g}}}^n_{i,j,k} = \frac{{P_{\mathrm{g}}}^n_{i+1,j,k} - {P_{\mathrm{g}}}^n_{i-1,j,k}}{\Delta x_{i+1,j,k} + \Delta x_{i-1,j,k}}, \tag{3.32}$$

where $\Delta x_{i-1,j,k}$ and $\Delta x_{i+1,j,k}$ denote the distance in the x-direction from the center of the cell to the center of the left and right neighbor cells, respectively. They take into account the level of the neighbor cell.

If the neighbor cell is coarser, the pressure is interpolated at the fine level using a slope limiter to compute the gradient. This method is similar to what is used in the hydrodynamical solver of `RAMSES`, with a loss of one order of accuracy at level interface. In certain conditions this method maintains a second-order accuracy of the scheme in presence of AMR (see section 3.3.4). The case where the neighbor cell is at a finer level is never considered since fine-to-coarse fluxes are already computed during the update of the finer level. Finally, the expression of the x-component of $\mathbf{w}^n_{i,j,k}$ is given by

$${w_x}^n_{i,j,k} = \frac{{T_{\mathrm{s}}}^n_{i,j,k} \nabla_x {P_{\mathrm{g}}}^n_{i,j,k}}{\rho^n_{i,j,k}}. \tag{3.33}$$

Predictor step: During the predictor step, the dust density is estimated at the left and right interfaces with a simple finite difference method. It uses slope limiters to preserve the TVD property of the scheme. The centered value of the dust density is estimated at half timesteps as

$$\begin{aligned} {\rho_{\mathrm{d}}}^{n+1/2}_{i,j,k} &= {\rho_{\mathrm{d}}}^n_{i,j,k} \\ &- \frac{\Delta t}{2\Delta x} \sum_{\sigma=x,y,z} \left({w_\sigma}^n_{i,j,k} \Delta_\sigma {\rho_{\mathrm{d}}}^n_{i,j,k} + {\rho_{\mathrm{d}}}^n_{i,j,k} \Delta_\sigma {w_\sigma}^n_{i,j,k} \right), \end{aligned} \tag{3.34}$$

where $\Delta_\sigma {\rho_{\mathrm{d}}}^n_{i,j,k}$ and $\Delta_\sigma {w_\sigma}^n_{i,j,k}$ are the TVD variations of ρ_{d} and w_σ in the direction σ. After the prediction of ${\rho_{\mathrm{d}}}^{n+1/2}_{i,j,k}$, ρ_{d} and w_σ are interpolated at the interfaces.

Let us consider the interface in the x-direction. The left and right interface values, sill indicated by the left and right annotation, are given by

$$\begin{aligned} \rho_{\mathrm{left}_{i,j,k}} &= {\rho_{\mathrm{d}}}^{n+1/2}_{i,j,k} - \frac{\Delta_x {\rho_{\mathrm{d}}}^n_{i,j,k}}{2}. \\ \rho_{\mathrm{right}_{i,j,k}} &= {\rho_{\mathrm{d}}}^{n+1/2}_{i,j,k} + \frac{\Delta_x {\rho_{\mathrm{d}}}^n_{i,j,k}}{2}, \\ {w_x}_{\mathrm{left}_{i,j,k}} &= {w_x}^n_{i,j,k} - \frac{\Delta_x {w_x}^n_{i,j,k}}{2}, \\ {w_x}_{\mathrm{right}_{i,j,k}} &= {w_x}^n_{i,j,k} + \frac{\Delta_x {w_x}^n_{i,j,k}}{2}. \end{aligned} \tag{3.35}$$

The bottom, top, back, and front states are estimated in a similar way.

Corrective step: The correction operation consists in computing the fluxes at the interface using the left and right predicted values, respectively. Let us consider the left interface of the

cell i, j, k in the x-direction. To avoid issues with the velocity discontinuities at the interfaces (e.g., due to spurious pressure jumps, Sharma et al., 2009), I impose a unique advection velocity

$$w^{n+1/2}_{i-1/2,j,k} = \frac{{w_{\rm left}}^{n+1/2}_{i,j,k} + {w_{\rm right}}^{n+1/2}_{i-1,j,k}}{2}. \tag{3.36}$$

This average does not appear to be critical for the second-order accuracy of the scheme. Our scheme uses the upwind method (Courant et al., 1952) to estimate the flux, sufficient to get the second-order accuracy in space. It writes as

$$\begin{aligned} {\mathcal{F}_\Delta}^{n+1/2}_{i-1/2,j,k} &= \max\left(w^{n+1/2}_{i-1/2,j,k}{\rho_{\rm d,left}}^{n+1/2}_{i,j,k}, 0\right) \\ &+ \min\left(w^{n+1/2}_{i-1/2,j,k}{\rho_{\rm d,right}}^{n+1/2}_{i-1,j,k}, 0\right). \end{aligned} \tag{3.37}$$

Several other approximate Riemann solvers can be used in our implementation as well, such as Lax-Wendroff (Lax & Wendroff, 1960) or Harten-Lax-van Leer (Harten et al., 1983, hereafter HLL). The fluxes in the other directions $\mathcal{F}^{n+1/2}_{i,j-1/2,k}$ and $\mathcal{F}^{n+1/2}_{i,j,k-1/2}$ are estimated in a similar way. The dust density is finally updated according to

$$\begin{aligned} \rho_{{\rm d}\,i,j,k}^{n+1} = \rho_{{\rm d}\,i,j,k}^{n} &- \frac{\Delta t}{\Delta x}\left(\mathcal{F}^{n+1/2}_{i+1/2,j,k} - \mathcal{F}^{n+1/2}_{i-1/2,j,k}\right) \\ &- \frac{\Delta t}{\Delta x}\left(\mathcal{F}^{n+1/2}_{i,j+1/2,k} - \mathcal{F}^{n+1/2}_{i,j-1/2,k}\right) \\ &- \frac{\Delta t}{\Delta x}\left(\mathcal{F}^{n+1/2}_{i,j,k+1/2} - \mathcal{F}^{n+1/2}_{i,j,k-1/2}\right). \end{aligned} \tag{3.38}$$

The time update and flux storage strategy still follows section 3.1.10 when an AMR grid is employed.

Energy : Similarly and simultaneously with the dust diffusion step, the energy is updated after the hydrodynamical step to account for the energy component of $\mathbb{F}_\Delta$. It is computed using the same scheme as the dust density with the velocity computed with equation (3.30) and the internal energy instead of the dust density. The fluxes are then added to the state vector similarly to equation (3.38) with the total energy instead of the dust density.

3.2.3 Timestepping with dust

Since the dust diffusion step consists in solving an advection equation explicitly, the scheme stability is achieved if the timestep Δt verifies the split CFL condition

$$\Delta t < \Delta t_{\rm dust} \equiv C_{\rm CFL}\frac{\Delta x}{\sum_{\sigma=x,y,z}\left|\max(w_\sigma, w_{{\rm g,b}\sigma})\right|}, \tag{3.39}$$

where $C_{\rm CFL} < 1$ is a safety factor. In addition, the hydrodynamical step imposes another stability condition that writes

$$\Delta t < C_{\rm CFL}\frac{\Delta x}{|c_{\rm s}| + \sum_{\sigma=x,y,z}|v_\sigma|}, \tag{3.40}$$

where v_σ is the mixture velocity in the direction σ. Dust diffusion is stable without intervention on the timestep as long as

$$|c_{\rm s}| + \sum_{\sigma=x,y,z}|v_\sigma| > \sum_{\sigma=x,y,z}\left|\max(w_\sigma, w_{{\rm g,b}\sigma})\right|. \tag{3.41}$$

If the former condition is not verified, which is the case when the pressure gradient is steep, dust diffusion constrains the timestep. In this case, the dust timestep is imposed instead of the hydrodynamical one.

3.3 Tests

To benchmark the implementation of dust dynamics in RAMSES, I run the canonical tests for gas and dust mixtures, DUSTYDIFFUSE, DUSTYSHOCK, DUSTYWAVE and the SETTLING test. I also test this advection solver with the DUSTYADVECT test. These tests, of increasing complexity, intend to verify, separately, together and finally under realistic physical conditions, the implementation of the dust terms.

3.3.1 Dustyadvect

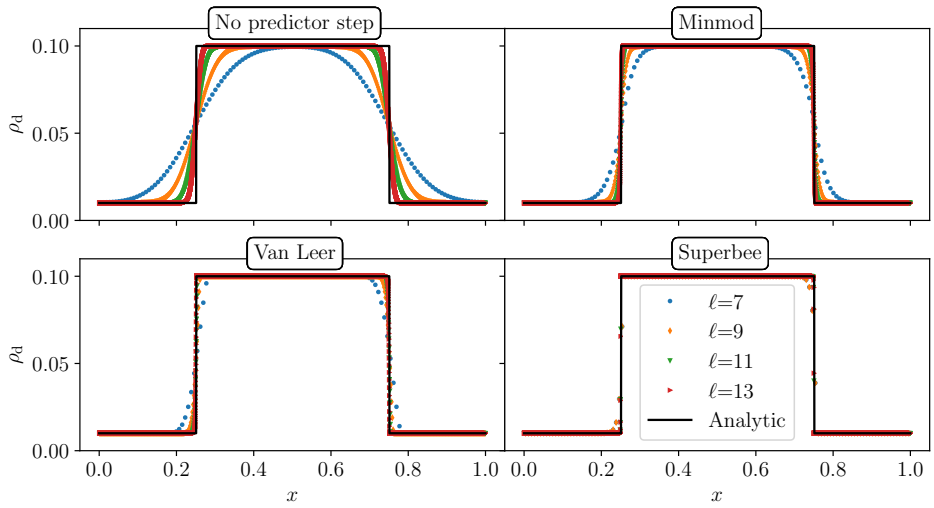

Figure 3.5: DUSTYADVECT tests using the function f_1 (equation (3.43)). Dust density after one period on various grids ($\ell = 7$ in blue, $\ell = 9$ in orange, $\ell = 11$ in green, $\ell = 13$ in red) as a function of the position compared with the analytic solution (black solid line). I present this test using four different slope limiters. (Top left) No predictor step. (Top right) Minmod slope limiter. (Bottom left) Van-Leer slope limiter. (Bottom right) Superbee slope limiter.

The scheme convergence and behavior at discontinuities is examined with 1D advection tests. These test are the simplest presented here and only verify the correct implementation of the advection scheme. In these DUSTYADVECT tests, the advection velocity w_x is set constant and the hydrodynamical update is deactivated. It consists in solving the following equation

$$\frac{\partial \rho_d}{\partial t} = -w_x \frac{\partial \rho_d}{\partial x}. \tag{3.42}$$

Considering an initial condition $\rho_d(x, 0) = f(x)$, $f(x)$ having a period of the size of the box $L = 1$, the analytic solution at time t is simply given by $\rho_d(x, t) = f(x - w_x t)$. In the remainder of the section, $w_x = 1$.

At first, four DUSTYADVECT tests are performed. I impose the initial function f_1, which writes $\forall x \in [0, L]$

$$f_1(x) = \begin{cases} 0.1 & \text{if } \frac{L}{4} < x < \frac{3L}{4}, \\ 0.01 & \text{otherwise.} \end{cases} \tag{3.43}$$

In the first test, no predictor step is operated. Different slope limiters are then used for the three other tests in the predictor step; Minmod (Roe, 1986), Van-Leer (van Leer, 1974), and Superbee

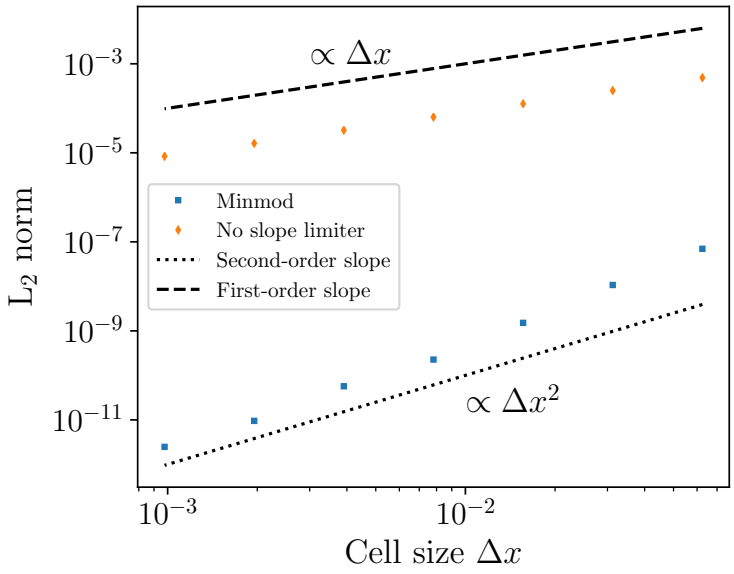

Figure 3.6: DUSTYADVECT tests with an initial condition given by the function f_2 (equation (3.44)). L_2 (equation (3.45)) norm as a function of the cell size for the scheme using the Minmod slope limiter (blue squares) and without predictor step (orange diamonds). The results are compared with a first-order slope (dashed line) and a second-order slope (dotted line).

(Roe, 1986). Uniform grids of resolutions ranging from $\ell = 7$ (128 cells) to $\ell = 13$ (8192 cells) are considered. Extremely small timesteps compared with the CFL condition $\Delta t = 8 \times 10^{-6}$ are imposed to ensure that the spatial error dominates.

Figure 3.5 shows the outcome of these tests after one period, at $t = 1$. As expected, the quality of the results strongly depends on the slope limiter. Without the predictor step (no slope limiter) the solver is simply a first-order centered upwind scheme. In this case a larger resolution is required to achieve the same accuracy as in the three other tests. As expected, the Van-Leer and Superbee slope limiters give more accurate results than the Minmod test but at the cost of a lack of symmetry. The Minmod slope limiter was therefore chosen as a good compromise to achieve a satisfying precision and to preserve symmetry.

Another series of DUSTYADVECT tests are performed for different resolutions, using the Minmod slope limiter and without a predictor step. A smooth initial Gaussian-like function f_2 is imposed to quantify the truncation error in space of the scheme which writes, $\forall x \in [0, L]$,

$$f_2(x) = 0.01 + 0.1 \exp\left[-\left(\frac{x - L/2}{L/4}\right)^2\right]. \tag{3.44}$$

I use a very small timestep $\Delta t = 10^{-8}$ to minimize the truncation errors in time compared with spatial errors. The results are compared at the same time $t = 0.01$ with the analytic solution using the L_2 norm

$$L_2 = \sqrt{\frac{\sum_{i=1}^{N_{\rm cell}} \left| \rho_{\rm d}{}^n_{{\rm RESULTS},i} - \rho_{\rm d}{}^n_{{\rm ANALYTIC},i} \right|^2}{N_{\rm cell}}}. \tag{3.45}$$

Figure 3.6 shows the evolution of the L_2 norm with (blue squares) and without (orange diamonds) a prediction step as a function of the size of the cells for the Gaussian-like test. As expected, without prediction, the scheme has only a first-order accuracy in space, while it is a second-order scheme when the full predictor-corrector scheme with slope limiters are used.

3.3.2 Dustydiffuse

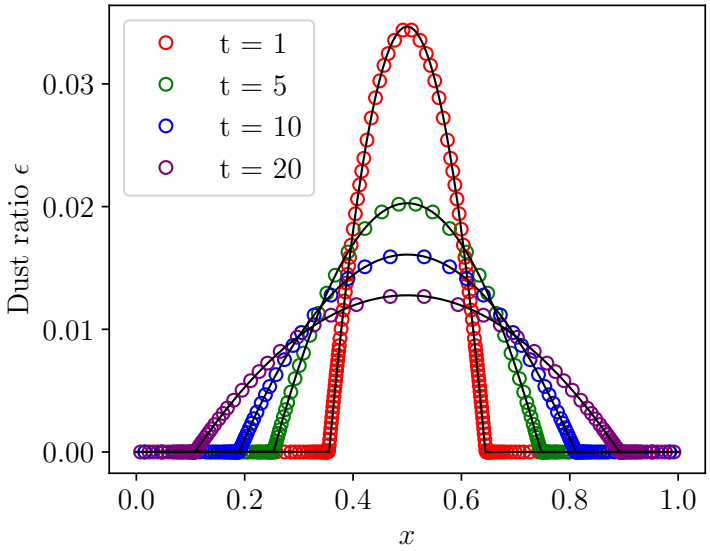

Figure 3.7: DUSTYDIFFUSE tests. Dust ratio as a function of the position at $t = 1$ (red), $t = 5$ (green), $t = 10$ (blue), $t = 20$ (purple) compared with the exact solution (black solid lines).

When the hydrodynamical variables (pressure and dust ratio excluded) remain constant, equation (2.44) behaves as a non-linear diffusion equation. Pure dust diffusion tests can thus be performed. The main goal of this test is to verify the correct implementation of the $\mathbb{F}_\Delta$ terms. In the DUSTYDIFFUSE tests (Price & Laibe, 2015), the hydrodynamical step is deactivated and t_s and c_s are set constant as well. Therefore, I only solve the following equation:

$$\frac{\partial \rho_d}{\partial t} = \frac{\partial \rho_d w_x}{\partial x}. \tag{3.46}$$

An isothermal equation of state $P_g = c_s^2(1-\epsilon)\rho$ is considered. The advection velocity is then given by

$$w_x = -t_s c_s^2 \frac{\partial \epsilon}{\partial x}; \tag{3.47}$$

ρ being constant, the equation can be written as the a non-linear diffusion equation

$$\frac{\partial \epsilon}{\partial t} = t_s c_s^2 \frac{\partial}{\partial x}\left(\epsilon \frac{\partial \epsilon}{\partial x}\right). \tag{3.48}$$

Equation (3.48) has a self similar solution known as the Barenblatt-Pattle solution (Barenblatt, 1952) that writes

$$\epsilon(t, x, C) = (t_s c_s^2 t)^{-1/3}\left(C - \frac{1}{6}\frac{x^2}{(t_s c_s^2 t)^{2/3}}\right), \tag{3.49}$$

where C is a constant depending on the initial conditions. I consider the following initial profile

$$\epsilon(t_0, x) = \epsilon_0\left(1 - \left(\frac{x}{x_c}\right)^2\right), \tag{3.50}$$

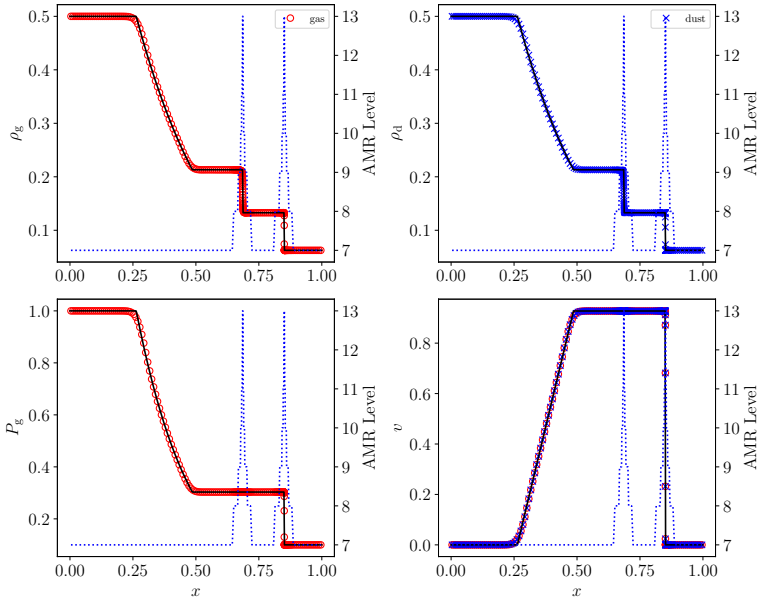

Figure 3.8: DUSTYSHOCK with $\epsilon = 0.5$. (Top left) Gas density as a function of position. (Top right) Same but for dust. (Bottom left) Gas pressure. (Bottom right) Gas and dust velocities. The AMR level (right axis) is represented with dotted blue lines. The analytic solution is given by the black solid lines. Red circles and blue crosses indicate gas and dust numerical quantities, respectively.

which is consistent with equation (3.49) if

$$t_0 = \frac{C^3}{t_s c_s^2 \epsilon_0^3},$$
$$C = \left(\frac{\epsilon_0 x_c}{\sqrt{6}}\right)^{2/3}.$$

I additionally set $\rho = 1$, $t_s = 0.1$, $\epsilon_0 = 0.1$ and $c_s = 1$ and an AMR grid of $\ell_{min} = 4$ and with $\ell_{max} = 10$. The refinement criterion, based on the dust density gradient, forbids a variation of more than 5% between two cells.

Figure 3.7 shows a comparison between the outcome of the tests and the analytic solutions at $t = 1$, $t = 5$, $t = 10$ and $t = 20$. At each time the numerical results agree with the exact solution to a precision of less then 1% in L_2 norm. Even though my scheme is fundamentally designed for advection, it is also efficient at handling diffusion problems.

3.3.3 Dustyshock

Another canonical test for gas and dust mixtures consists of 1D hydrodynamical shocks. For strongly coupled mixtures, these so-called DUSTYSHOCK tests are closely approximated by the same analytic solution as the usual Sod test (Sod, 1978), but with the modified sound speed $\tilde{c}_s$

$$\tilde{c}_s = c_s \sqrt{1 - \epsilon_0},$$

ϵ_0 being the initial dust ratio. The dust ratio ϵ remains almost constant through the shock; however, small pressure bumps must occur where there is either a pressure or density gradient. The goal of this test is to verify the impact of the dust in $\mathbb{F}_H$ since $\mathbb{F}_\Delta$ is almost negligible.

The same prescription as Laibe & Price (2014a) for the stopping time is used. It writes

$$t_s = \frac{\epsilon(1-\epsilon)\rho}{K},$$

where K is the drag coefficient defined previously. This prescription is consistent with the expression of the stopping time presented before is convenient for tests since it allows us simply parametrize the coupling between the gas and dust phase.

A DUSTYSHOCK test is performed on an AMR grid with $\ell_{\rm min} = 4$ and $\ell_{\rm max} = 13$ with a high initial dust ratio. The grid is refined with a criterion that forbids dust density variations of more than 5% between two neighbor cells. Two distinct regions, representing the left and right half of the box, are set with different initial conditions given by

$$\begin{aligned}\left(\rho_0, \mathbf{v}_0, P_{\rm g_0}, \epsilon_0\right)_{\rm left} &= (1, 0, 1, 0.5)\\ \left(\rho_0, \mathbf{v}_0, P_{\rm g_0}, \epsilon_0\right)_{\rm right} &= (0.125, 0, 0.1, 0.5)\,.\end{aligned}$$

Finally, a drag coefficient $K = 1000$ and an adiabatic index $\gamma = 1.4$ are imposed.

Figure 3.8 shows the gas and dust densities, the velocity, and the gas pressure as a function of the position at $t = 0.2$. The Sod solution with the modified sound speed is very well recovered.

3.3.4 Dustywave

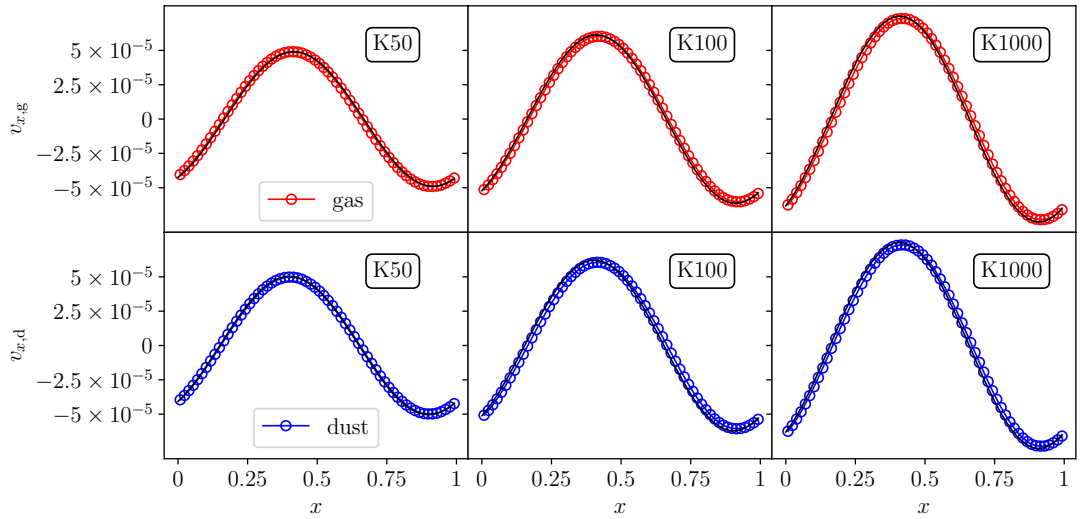

Figure 3.9: DUSTYWAVE test. Velocity of the gas (top) and dust (bottom) phase as a function of the position at $t = 4.5$ for the K50, K100 and K1000 tests (from left to right) compared with the analytical solution (black lines) given by Laibe & Price (2011).

The 1D DUSTYWAVE test (Laibe & Price, 2011) consists in following the evolution of an isothermal sound wave in a gas and dust mixture. The goal of this test is to verify the impact of the dust in both $\mathbb{F}_{\rm H}$ and $\mathbb{F}_{\Delta}$. Small periodic perturbations on the equations (2.41) on the density, the dust ratio, the pressure, and the velocity are imposed

$$\begin{aligned}\rho &= \rho_0 + \delta\rho_0,\\ \epsilon &= \epsilon_0 + \delta\epsilon_0,\\ P_{\rm g} &= P_{\rm g_0} + \delta P_{\rm g_0},\\ v_x &= 0 + \delta v_{x0},\end{aligned}$$

where the index 0 and the symbol δ indicate respectively the initial uniform quantities and the perturbations. As explained in chapter 2, Laibe & Price (2011) provide the analytic solution for this test in the full bifluid case. They find that the sound waves propagate with the modified sound speed $\tilde{c}_{\rm s}$ and are damped because of the dust inertia. Large grains damp these sound waves faster than small grains as they are more massive.

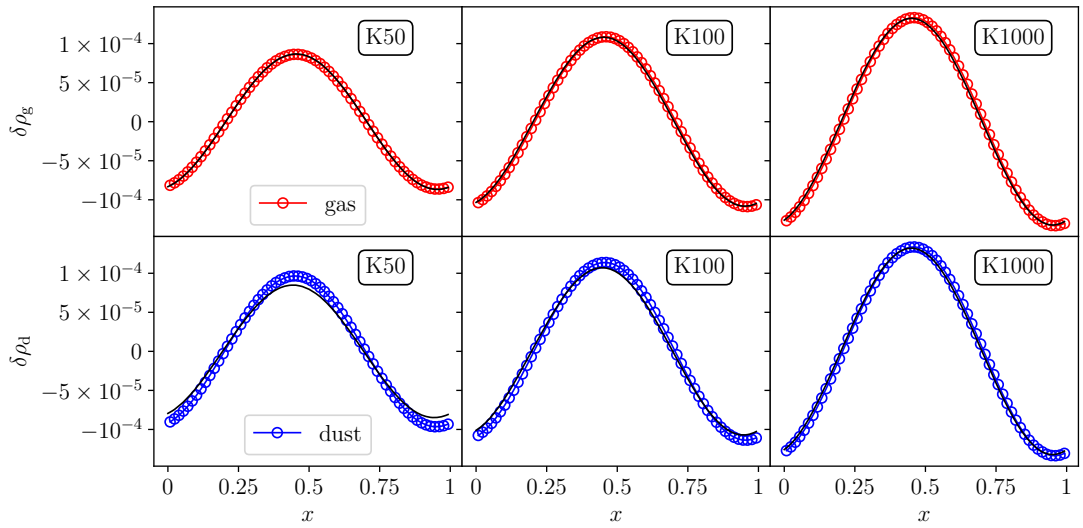

Figure 3.10: DUSTYWAVE test. Same as in figure 3.9 but for the density perturbations.

Three DUSTYWAVE tests are performed using different drag coefficients $K = 50$ (K50, strong back-reaction regime), $K = 100$ (K100) and $K = 1000$ (K1000,weak back-reaction regime). The initial perturbations are in the form

$$\begin{aligned}
\delta\rho_0 &= \rho_0 \delta \sin\left(2\pi \frac{x}{L}\right), \\
\delta v_{x0} &= v_0 \delta \sin\left(2\pi \frac{x}{L}\right), \\
\delta P_{g_0} &= (1-\epsilon_0)\, c_{s,0}^2 \delta\rho_0, \\
\delta\epsilon_0 &= 0,
\end{aligned}$$

where x is the position in the box, L is the box length, $c_{s,0}$ is the initial sound speed, and δ is a parameter that sets the amplitude of the perturbation. The initial uniform state is set such as that

$$\begin{aligned}
\rho_0 &= 2, \\
\epsilon_0 &= 0.5, \\
v_0 &= 1, \\
c_{s,0} &= 1.
\end{aligned}$$

The adiabatic index of the gas is $\gamma = 1.000001$[3] to simulate an isothermal soundwave propagation. The initial perturbation has a relative amplitude $\delta = 10^{-4}$. The simulation box has a size $L = 1.0$ and the grid is taken as uniform with 64 cells. The timestep $\Delta t = 10^{-4}$ is the same for the three tests and respects the stability condition for the considered drag coefficients.

Figures 3.9 and 3.10 show the velocity v_x and the perturbation density $\delta\rho = \rho - \rho_0$ for both gas and dust at $t = 4.5$ for these three tests. The amplitude of the damping increases with a decreasing K and the results are increasingly less accurate as the errors due to the diffusion approximation increase, consistently with the theory (Laibe & Price, 2011; Price & Laibe, 2015). Larger grains, i.e, with smaller K, have more inertia and allow an efficient damping of the gas.

[3] Taking exactly $\gamma = 1$ is not possible with RAMSES as the internal energy is computed as $\frac{P_g}{\gamma-1}$

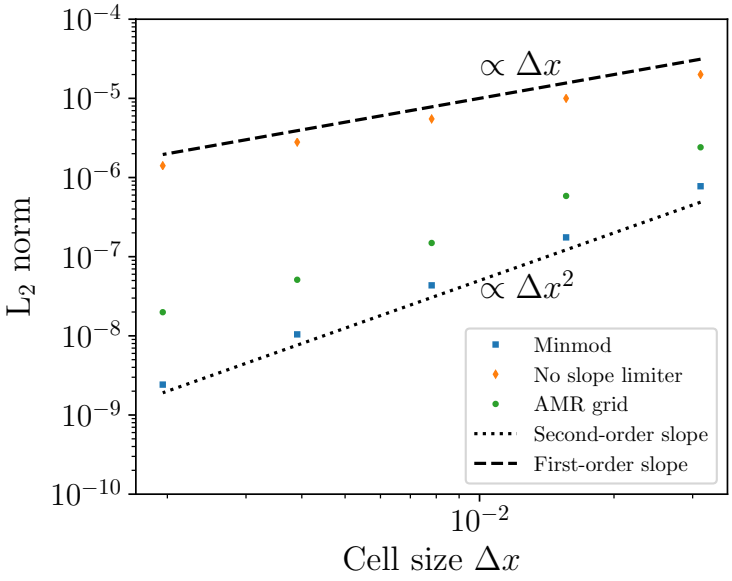

Figure 3.11: DUSTYWAVE numerical convergence tests. L_2 norm as a function of the minimum cell size for the scheme using the Minmod slope limiter (blue squares), without predictor step (orange diamonds) and with AMR (green circles) . The results are compared with a first-order slope (dashed line) and a second-order slope (dotted line).

I perform DUSTYWAVE tests on uniform grids with resolutions ranging from $\ell = 5$ to $\ell = 9$, with a small timestep $\Delta t = 10^{-5}$ and for $K = 50$. I also perform runs on AMR grids with coarse resolutions ranging from $\ell_{\rm min} = 4$ to $\ell_{\rm min} = 8$. For these tests, the cells for $x \in [0.25, 0.75]$ have a level of refinement $\ell_{\rm max} = \ell_{\rm min+1}$. I test the order of my scheme and measure the accuracy of numerical solution against a solution of reference obtained at very high resolution ($\ell = 11$) in both time and space ($\Delta t = 10^{-6}$). I do not compare the results with the analytic solution presented above as it not exact in the diffusion approximation. Figure 3.11 shows the L_2 errors obtained when increasing the number of cells. The scheme is first-order in space without correction and second-order when using the Minmod limiter. In the presence of AMR, the scheme keeps a second-order accuracy in space for low resolution but deteriorates at high resolutions. This is due to the estimate of the pressure gradient that is first-order at a refined interface. At high resolution, the error is smaller (almost two orders of magnitude) than the tests without a predictor step.

3.3.5 Disk settling

The SETTLING test, introduced by Price & Laibe (2015), is designed to test the algorithm in realistic astrophysical conditions and including gravity. It simulates the local settling of dust grains in a disk in hydrostatic equilibrium. As in Price & Laibe (2015), I set an analytic gravitational force

$$f_{\rm grav} = -\frac{\mathcal{G}M_\star y}{(y^2 + r^2)^{3/2}},$$

where $\mathcal{G}$ is the gravitational constant, $M_\star$ is the mass of the central star, y is the altitude and r the cylindrical radius at which the disk is simulated. The gas density at hydrostatic equilibrium

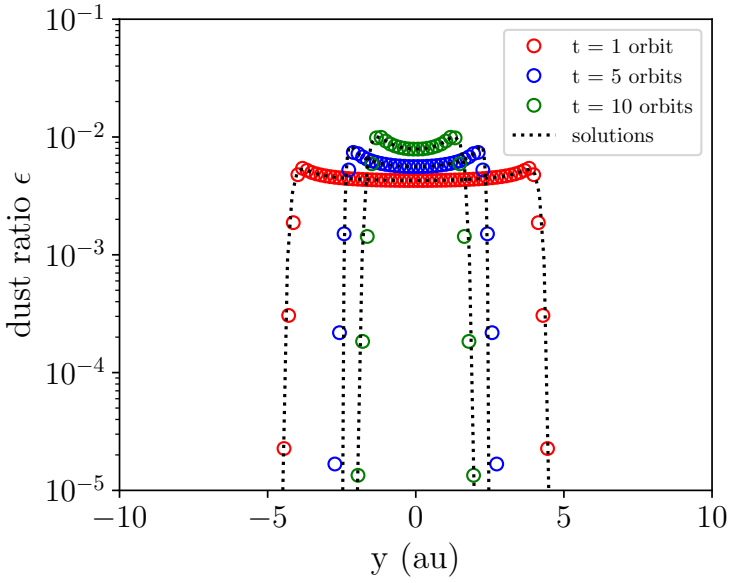

Figure 3.12: SETTLING test on a uniform grid at level $\ell = 8$ with millimeter-size dust grains. Dust ratio at t=1 (red circles), 5 (blue circles), and 10 orbits (green circles) as a function of the altitude.

for $|y| \ll r$ is

$$\rho_g = \rho_{g,0} e^{-\frac{y^2}{2\mathcal{H}^2}},$$

where $\mathcal{H}$ is the local scale height of the disk, which is determined by the ratio $\mathcal{H}/r = 0.05$. I then assume an isothermal equation of state where the imposed soundspeed c_s is

$$c_s = \mathcal{H}\Omega_k, \tag{3.51}$$

Ω_k being the Keplerian angular velocity at the radius r. Finally, a uniform initial dust ratio ϵ_0 is imposed.

In the terminal velocity approximation, the analytic solution for the dust velocity is directly set by the pressure gradient that compensates the gravitational force, hence

$$v_{d,y} = w_Y = -\mathrm{St}\Omega_k \frac{y}{(1 + (y/r)^2)^{3/2}}, \tag{3.52}$$

which is the limit at low Stokes number ($\mathrm{St} = \Omega_k t_s$ in this case) of the expression given by Hutchison et al. (2018). As the gas approximately remains in equilibrium, solving the settling problem consists in solving

$$\frac{\partial \rho_d}{\partial t} + \frac{\partial \rho_d w_y}{\partial y} = 0. \tag{3.53}$$

Even though the density can, in principle, be determined using the same method as the velocity, it relies on the hypothesis of an infinite dust reservoir that is inconsistent with my choice of boundaries. I choose to compare my results with a numerical solution as in Hutchison et al. (2018). I use a similar Crank-Nicholson scheme to get this solution, except that it only solves the dust density equation using the analytic dust velocity.

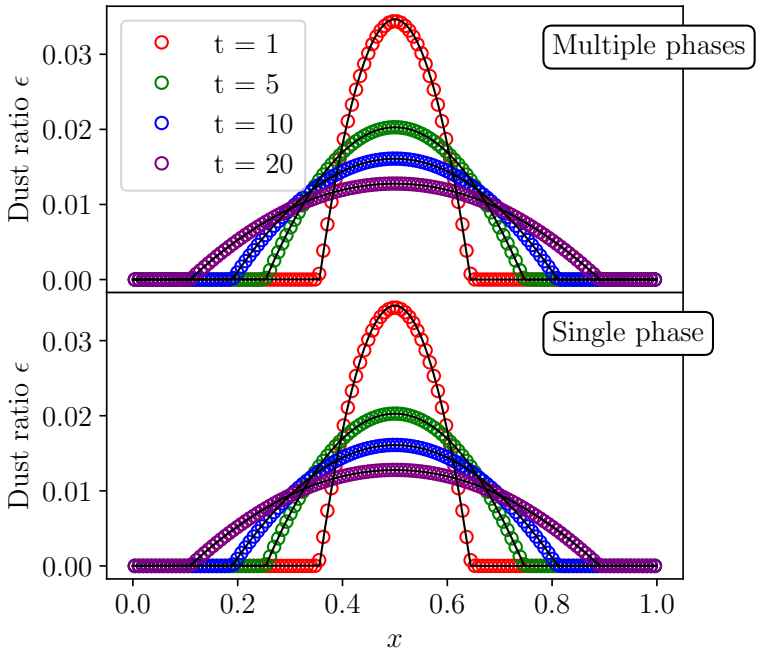

Figure 3.13: Comparison between multiple phase with $\mathcal{N} = 5$ (top) and an equivalent single phase (bottom) DUSTYDIFFUSE test. Dust ratio as a function of the position at $t = 1$ (red), $t = 5$ (green), $t = 10$ (blue) and $t = 20$ s (purple) compared with the exact solution (black solid lines).

I perform a 2D SETTLING test at a disk orbiting around a solar mass star at radius of 50 au. The simulation box has periodic boundary conditions and $L = 20$ au, which is approximately $8\mathcal{H}$. As in Price & Laibe (2015) and Hutchison et al. (2018), the initial mid-plane gas density $\rho_g \simeq 6 \times 10^{-13}$g cm^{-3}. I also set an initial dust ratio of 4.99×10^{-3} of millimeter grains with an intrinsic density of $\rho_{\text{grain}} = 3$ g cm^{-3}. The adiabatic index of the gas is $\gamma = 5/3$.

A first test with a uniform grid at level $\ell = 8$ is performed. Figure 3.12 shows the dust ratio as a function of y. As can be seen, the results are essentially similar to those obtained in Price & Laibe (2015) and Hutchison et al. (2018).

3.3.6 Multigrain

Example 1 : Dustydiffuse

To benchmark the implementation of the multiple dust species in the code, ten DUSTYDIFFUSE tests are performed on uniform grids of $\ell = 7$. They are operated with one dust phase and with this same phase split with $\mathcal{N} \in [2, 10]$ (MULTIGRAIN). All the dust bins have the same intrinsic properties. As all the tests are equivalent, it is expected that they give the same results. The parameters used are the same as in section 3.3.2.

Figure 3.13 shows the total dust density as a function of position with $\mathcal{N} = 5$ (top) and $\mathcal{N} = 1$ (bottom) at $t = 1$, $t = 5$, $t = 10$, and $t = 20$. The results agree for the MULTIGRAIN simulation and for the single phase simulation to machine precision.

Figure 3.14 shows the CPU time as a function of the number of species $\mathcal{N}$. We see that the MULTIGRAIN simulations are not very expensive. The CPU time agrees more with a square root scaling with $\mathcal{N}$ than a linear one. As discussed by Hutchison et al. (2018) with the MULTIGRAIN algorithm in the PHANTOM code (Price et al., 2017), the monofluid formalism is a highly computationally effective tool to treat multiple phases.

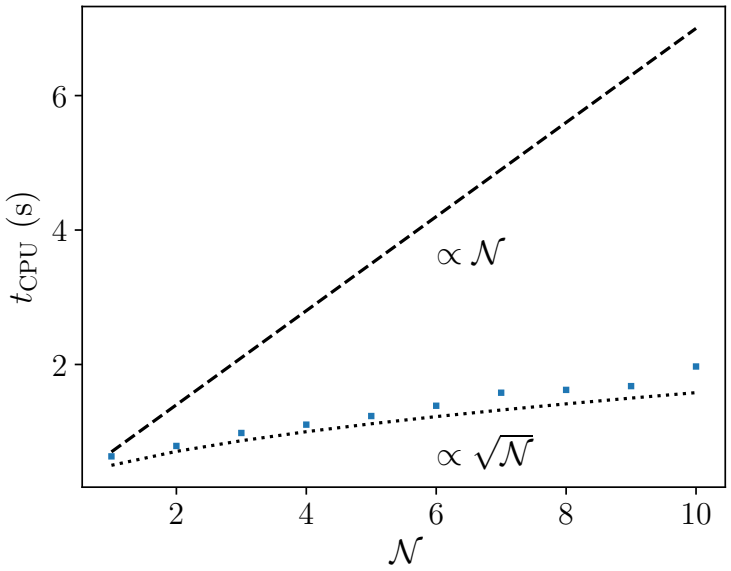

Figure 3.14: CPU time $t_{\rm CPU}$ of the ten equivalent DUSTYDIFFUSE tests as a function of the number of species $\mathcal{N}$.

Example 2 : Dustywave

In this section, I test the cumulative back-reaction of dust on the gas and the interaction between dust species. To benchmark my MULTIGRAIN implementation in a strong back-reaction regime I run a DUSTYWAVE simulation with two dust species. The initial barycentric velocity is a sinusoidal perturbation of amplitude 10^{-4}, the other variables are not initially perturbed. I numerically integrate the linearly perturbed equations of gas and dust mixtures assuming solutions of the type $A(t)\exp(ikx)$ as in Laibe & Price (2014c) to obtain my reference solution. The test is performed with a uniform grid of $\ell = 9$ and timesteps given by the CFL condition. In this test, I consider two dust phases and a total initial dust ratio of 0.5. The first bin has a drag coefficient $K = 50$ and an initial dust ratio of 0.4, the second has a drag coefficient $K = 1000$ and an initial dust ratio of 0.1. In this case, we expect the first dust species to damp the gas efficiently.

Figure 3.15 shows the amplitude of the density perturbations (gas and dust) and velocity (gas) compared with the reference solution. My results are in excellent agreement with the reference solution in terms of amplitude, period and damping rate. As expected the damping of the gas is significant. This emphasizes the fundamental role of the cumulative back-reaction on the dynamics of dust grains in presence of multiple species as the second phase $K = 1000$ could not damp the gas as efficiently (see section 3.3.4).

Example 3 : Disk settling

The disk SETTLING test presented in section 3.3.5 is nicely adapted to test my MULTIGRAIN solver in realistic conditions. Dust grains of various sizes are present in protoplanetary disks and they experience different dynamical evolutions. To test the solver in these conditions, a settling test with ten dust species is performed with a resolution of $\ell = 8$. As before, the intrinsic grain density is 3 g cm^{-3}, but every species is characterized by a proper dust ratio ϵ_j and grain size

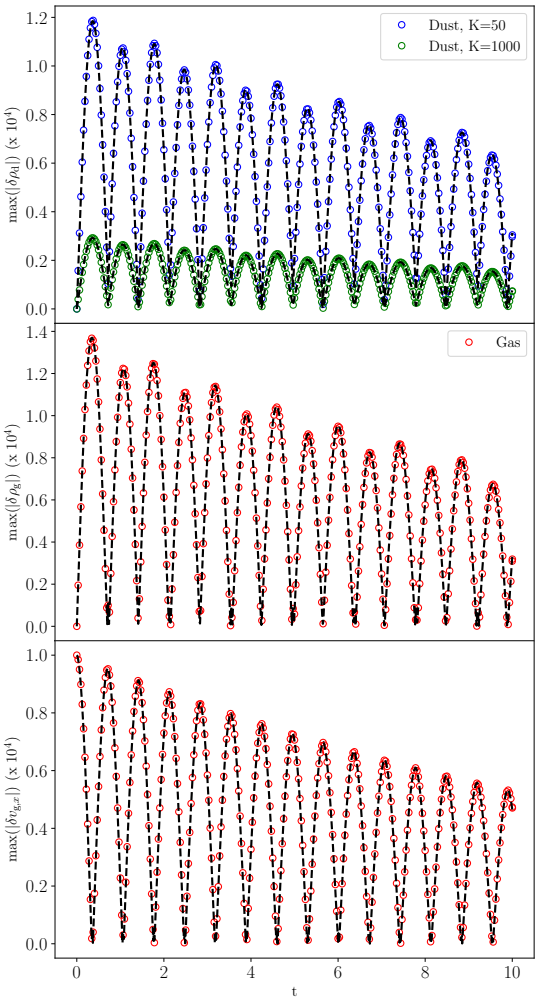

Figure 3.15: MULTIGRAIN DUSTYWAVE test. The three panels show the evolution of the maximum amplitude of the perturbation for the dust densities (top), the gas density (middle), and the gas velocity (bottom). The $K = 50$ and $K = 1000$ dust phases are shown with blue and green circles respectively. The red circles represent the gas. The semi-analytic solution is given by the dashed black line. The damping of the mixture is due to the cumulative back-reaction of dust on the gas and is mostly due to the grains with $K = 50$.

j	$s_{\mathrm{grain},j}$ (cm)	ϵ_j	t_{s} (s) at $z = 0$
1	1.0×10^{-5}	3.99×10^{-5}	40
2	2.78×10^{-5}	6.65×10^{-5}	111
3	7.74×10^{-5}	1.11×10^{-4}	310
4	2.15×10^{-4}	1.85×10^{-4}	860
5	5.99×10^{-4}	3.09×10^{-4}	2396
6	1.67×10^{-3}	5.15×10^{-4}	6680
7	4.64×10^{-3}	8.59×10^{-4}	18560
8	1.29×10^{-2}	1.43×10^{-3}	51600
9	3.59×10^{-2}	2.39×10^{-3}	143600
10	1.0×10^{-1}	3.99×10^{-3}	400000

Table 3.1: Dust distribution and stopping time at $z = 0$ for the MULTIGRAIN SETTLING test

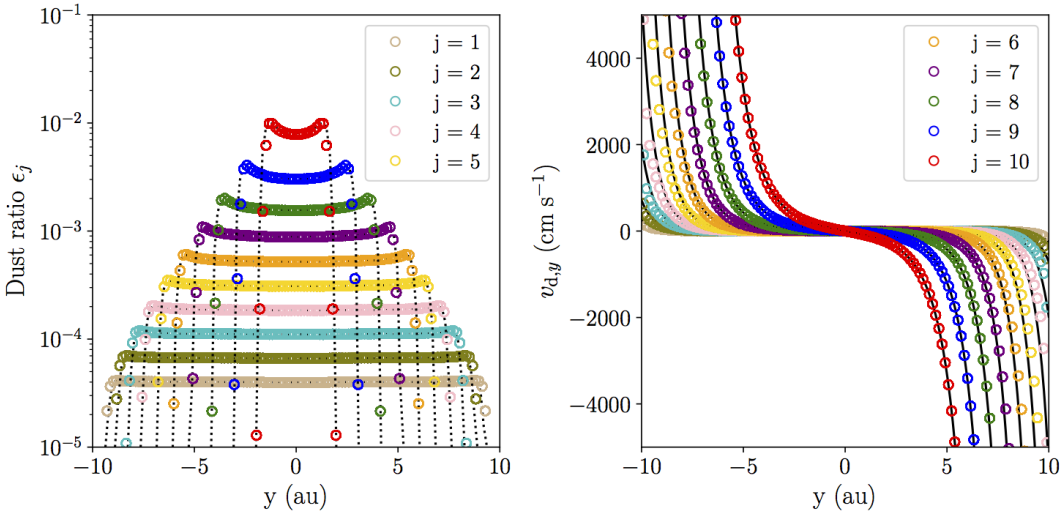

Figure 3.16: MULTIGRAIN SETTLING test. Dust ratios and dust velocities (circles) of the ten phases of the SETTLING test after ten orbits compared with the numerical (dotted black lines) and analytic (black lines) one-species solution.

$s_{\text{grain},j}$. These quantities are determined using a MRN-like distribution [4], I use the same values for the minimum and maximum grain size as in Hutchison et al. (2018). The details of the size distribution are summarized in table 3.1, which also shows the stopping time of each species in the mid-plane of the disk.

Figure 3.16 shows the dust ratio and velocity of every species after ten orbits compared with the one-species solution, which is a good approximation as long as the cumulative back-reaction on the gas is small. Again, the solution is very well captured by my solver.

Figure 3.17 shows the dust densities in the (xy)-plane. There is no dispersion of the values in the x-direction, and the initial symmetry of the problem is conserved to machine precision which originate from the Eulerian nature of the numerical scheme. As in previous studies, we see that ten orbits are enough to efficiently separate the dust phases. Note that an orbit at 50 au is approximately 353 years which is a few hundred times smaller than the free-fall timescale of a typical protostellar cloud of density $\simeq 10^{-19}$ g cm^{-3}(Andre et al., 2000) which is approximately $10^5 - 10^6$ years. An efficient settling is thus expected to happen during the collapse of this cloud, especially for large grains, e.g., $s_{\text{grain}} > 10^{-2}$cm here, for which the typical settling timescale is a few orbits.

As in Hutchison et al. (2018), I am interested in the effects of the interaction between different dust species. Figure 3.18 shows a zoom of the vertical profile of ϵ_1 as a function of y. The behavior of this phase is very similar to what was observed in Hutchison et al. (2018). The dashed black line shows the one-species solution. As can be seen, for this species, the discrepancies between the one-species solution and the MULTIGRAIN test are on the order of magnitude of the variations of ϵ_1 at the dust front, which emphasizes the fundamental character of the equivalent stopping time in MULTIGRAIN simulations.

[4] $\epsilon\left(s_{\text{grain}}\right) \propto s_{\text{grain}}^{4-m}$ with $m = 3.5$

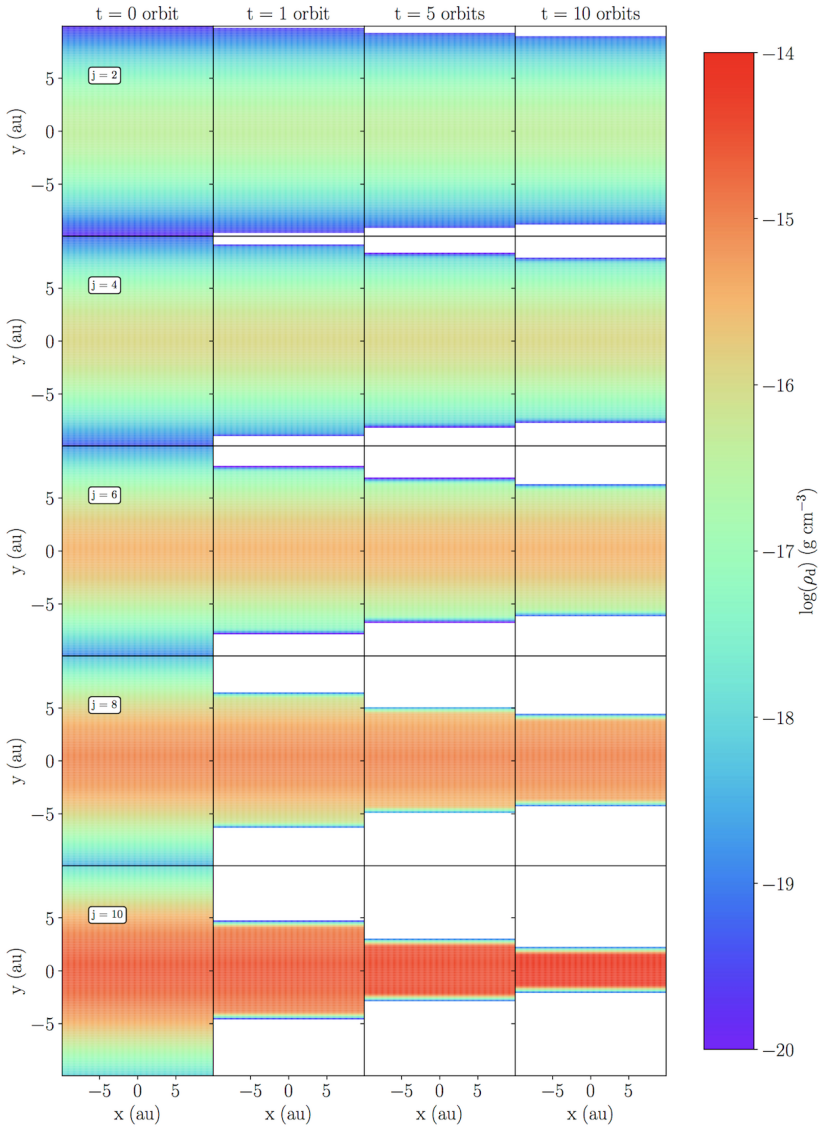

Figure 3.17: MULTIGRAIN SETTLING test. Dust density for the bin j = 2, 4, 6, 8, and 10 in the (xy)-plane at t = 0, 1, 5, and 10 orbits. The efficiency of the settling increases with the grain size and millimeter grains (10^{th} bin) are strongly settled after 10 orbits.

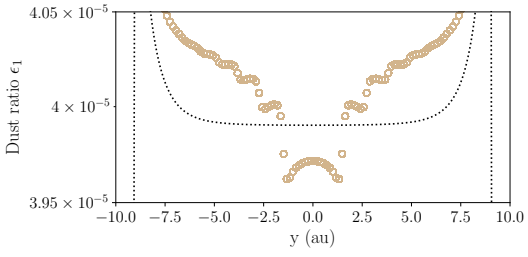

Figure 3.18: MULTIGRAIN SETTLING test. Magnification of the dust front as a function of y for the $j = 1$ dust species (brown circles) compared with the one-species solution (dotted line). These dust grains are dragged by the gas, which is itself submitted to the cumulative back-reaction of all the other dust species through the gas, hence the difference is the one-species solution.

3.4 Conclusion

In this Chapter, I have presented an Eulerian approach to treat the dynamics of small dust grains. It is efficient in the diffusion regime and can be employed to treat multiple dust species simultaneously and efficiently. After presenting the AMR code `RAMSES`, I described the numerical scheme that I implemented in it. It successfully passed the canonical validation tests for advection schemes and dust dynamics solvers.

- DUSTYADVECT, an advection test.
- DUSTYDIFFUSE, a diffusion test where the gas density and temperature are fixed.
- DUSTYSHOCK, a shock propagation test.
- DUSTYWAVE, a wave propagation test.
- SETTLING, that reproduces the settling of dust grains in a stratified protoplanetary disk.

I can draw the following conclusion

1. The scheme has a second-order accuracy in space on uniform grids and intermediate between first and second-order on AMR grids.
2. The method also appears to efficiently treat a non-linear diffusion problem (DUSTYDIFFUSE).
3. The DUSTYSHOCK, DUSTYWAVE and SETTLING tests show that the waves and shock propagate at the correct velocity and that the dust phase feels the common forces between gas and dust, e.g, gravity.
4. The MULTIGRAIN DUSTYDIFFUSE test operated with a split dust phase shows that my method is efficient to treat multiple dust species simultaneously as the computation time scales in $\sqrt{N}$.
5. Non-linear effects of the cumulative back-reaction on both the gas and the dust are well captured by the MULTIGRAIN DUSTYWAVE tests and the MULTIGRAIN SETTLING tests. In particular I retrieve similar behavior to the one that Hutchison et al. (2018) observed in the MULTIGRAIN SETTLING test.

Chapter 4

Dust dynamics during the first protostellar collapse

Contents

Puumba

"Oh, gee. I always thought they were balls of gas burning billions of miles away."

Simba

"Pumbaa, with you, everything's gas."

- The lion king

In this chapter, I present the dynamics of neutral dust during the early phases of the protostellar collapse (dustycollapse) with numerical models that were evolved in time with my multigrain dust dynamics solver in `RAMSES`. I shortly present the framework and the methods that I used to study the dustycollapse. Then, I briefly review the unrotating dustycollapses that were introduced in Lebreuilly et al. (2019). Finally, I focus on more advanced dustycollapse simulations that consider multiple dust species, initial solid body rotation and magnetic fields. The rotating dustycollapse simulations are the object of a recent submitted publication.

4.1 Context

Small dust grains are essential ingredients of star, disk and planet formation. They regulate the thermal budget of star forming regions through their opacity and thermal emission (McKee & Ostriker, 2007; Draine, 2004). In addition, they are thought to be the main formation site of H_2 at present days (Gould & Salpeter, 1963). It is widely accepted that planet formation is induced by dust growth within protoplanetary disks (see the recent review by Birnstiel et al., 2016). Finally, the dust grains are significant charge carriers (Marchand et al., 2016; Wurster et al., 2016; Zhao et al., 2016) and therefore regulate the evolution of magnetic fields during the protostellar collapse which can affect, among others, the disk formation (Masson et al., 2016; Hennebelle et al., 2020) and the fragmentation process (Commerçon et al., 2011).

Until recently, one paradigm was that dust of the interstellar medium (ISM) is usually composed of grains with sizes up to ~ 0.1 µm with a typical size distribution well modelled by the Mathis-Rumpl-Nordsieck distribution (MRN, Mathis et al., 1977). Recent observations seem to indicate that larger grains could exist in the denser regions of the ISM. Pagani et al. (2010) proposed that over-bright envelopes of prestellar cores (coreshine) could be explained by the presence of micrometer grains. In addition, it was suggested that recent observations

with ALMA of the polarised light at (sub)millimeter wavelengths in Class 0 and I objects could be interpreted as the self-scattering by grains with sizes up to ≈ 100 µm (Kataoka et al., 2015, 2016; Pohl et al., 2016; Sadavoy et al., 2018a,b, 2019). Galametz et al. (2019) has also shown that the low values of the dust emissivity in Class 0 objects could indicate the presence of these large grains in their envelope. Finally, Tychoniec et al. (2020) estimated that the mass of solids in Class 0 disks is sufficient to grow planets only if large grains are included in the opacity models, which might indicate dust growth in the early phases of protostar formation.

Over the past few years, significant improvements have been made in numerical models to better understand the early phases of the protostellar collapse that leads to the first Larson core formation (Larson, 1969). The angular momentum budget is a long-standing problem in star formation. Indeed, the specific angular momentum of prestellar cores differs to those of young stars by more than three orders of magnitude (Bodenheimer, 1995; Belloche, 2013). In numerous studies, the magnetic braking has been investigated as one of the possible solutions to address this issue (Allen et al., 2003b; Price & Bate, 2007; Hennebelle & Fromang, 2008; Commerçon et al., 2011; Masson et al., 2016). State-of-the-art simulations now account for the effect of magnetic fields both in a ideal (Commerçon et al., 2010) and non-ideal (Tomida et al., 2015; Vaytet et al., 2018a; Wurster et al., 2019) magnetohydrodynamics (MHD) framework, radiative feedback (Commerçon et al., 2010; González et al., 2015; Tomida et al., 2015) and other physical mechanisms. Only Bate & Lorén-Aguilar (2017) have investigated the dynamics of dust during the protostellar collapse (DUSTYCOLLAPSE). They report that ~ 100 µm grains can significantly decouple from the gas leading to large increase of dust-to-gas ratio in the disk and the first Larson core. In 2D, Vorobyov & Elbakyan (2019) have studied the gas and dust decoupling in gravitoviscous protoplanetry disks including dust growth and also report strong variations of dust-to-gas ratio. So far, no 3D DUSTYCOLLAPSE simulation has been performed in a MHD/non ideal MHD context or with multiple dust species.

In chapter 3, I presented a fast, accurate and robust implementation of dust dynamics for strongly coupled gas and dust mixtures that allows an efficient treatment of multiple grain species in `RAMSES`. I now present simulations of protostellar collapse of gas and dust mixtures and in particular the first simulations with multiple grain species. I investigate how the maximum grain size of the dust distribution, the ratio between the thermal and gravitational energy, i.e. the thermal support, and the magnetic fields may affect the decoupling between the gas and neutral dust grains.

4.2 Framework

4.2.1 Dusty hydrodynamics for the protostellar collapse

As explained in Chapter 2, a gas and dust mixture with $\mathcal{N}$ small grains species can be modeled as a monofluid in the diffusion approximation (Laibe & Price, 2014c; Price & Laibe, 2015; Hutchison et al., 2018; Lebreuilly et al., 2019). This fluid, of density ρ, flows at its barycenter velocity $\mathbf{v}$. The k-th dust phase, of density ρ_k, has the specific velocity $\mathbf{v_k} \equiv \mathbf{v} + \mathbf{w_k}$, where $\mathbf{w_k}$ is the differential velocity between the dust and the barycenter. In the context of the protostellar collapse and in the absence of magnetic fields, this mixture is well described by the following set of equations

$$\begin{aligned}
\frac{\partial \rho}{\partial t} + \nabla \cdot [\rho \mathbf{v}] &= 0, \\
\frac{\partial \rho_k}{\partial t} + \nabla \cdot [\rho_k (\mathbf{v} + \mathbf{w_k})] &= 0, \ \forall k \in [1, \mathcal{N}], \\
\frac{\partial \rho \mathbf{v}}{\partial t} + \nabla \cdot \left[P_{\rm g} \mathbb{I} + \rho (\mathbf{v} \otimes \mathbf{v}) \right] &= -\rho \nabla \phi,
\end{aligned} \tag{4.1}$$

where P_g is the thermal pressure of the gas and $\mathbb{I}$ the identity matrix. The gravitational potential ϕ is set by the Poisson equation

$$\triangle\phi = 4\pi\mathcal{G}\rho, \tag{4.2}$$

where $\mathcal{G}$ denotes the gravitational constant.

The previous equations are closed using a barotropic law that reproduces both the isothermal regime at low density and the adiabatic regime when the density reaches the critical value ρ_{ad} which corresponds to the density at which dust becomes opaque to its own radiation (Larson, 1969). Similarly to Commerçon et al. (2008), I express the gas pressure as

$$P_g = \rho_g c_{s,iso}^2 \left[1 + \left(\frac{\rho_g}{\rho_{ad}}\right)^{\gamma-1}\right], \tag{4.3}$$

The gas density ρ_g is $\rho_g = \rho - \sum_k \rho_k$. Regions of low densities are isothermal and have for sound speed $c_{s,iso}$.

I model a single dust grain k as a small compact and homogeneous sphere of radius $s_{grain,k}$ and intrinsic density $\rho_{grain,k}$ [1]. When the grain is smaller than the mean free path of the gas (the so-called Epstein drag regime, Epstein 1924), the drag stopping time $t_{s,k}$ is given by

$$t_{s,k} \equiv \sqrt{\frac{\pi\gamma}{8}} \frac{\rho_{grain,k}}{\rho} \frac{s_{grain,k}}{c_s}, \tag{4.4}$$

where ρ is the total density of the gas and dust mixture, c_s is the sound speed of the gas and γ its adiabatic index.

If the differential velocity $\Delta\mathbf{v}_k \equiv \mathbf{v}_k - \mathbf{v}_g$ between the gas and the dust is supersonic, a correction in the drag regime must be applied. In this case the stopping time is given by (Kwok, 1975)

$$t_{s,k} \equiv \sqrt{\frac{\pi\gamma}{8}} \frac{\rho_{grain,k}}{\rho} \frac{s_{grain,k}}{c_s} \left(1 + \frac{9}{128\pi}\mathcal{M}_d{}^2\right)^{-1/2}, \tag{4.5}$$

where $\mathcal{M}_d = \frac{|\Delta\mathbf{v}_k|}{c_s}$ is the differential velocity Mach number. In the remaining of this paper, unless specified, I consider this correction.

In the terminal velocity approximation, the differential velocity of the phase k is

$$\mathbf{w_k} = \left[\frac{\rho}{\rho - \rho_k} t_{s,k} - \sum_{l=1}^{\mathcal{N}} \frac{\rho_l}{\rho - \rho_l} t_{s,l}\right] \frac{\nabla P_g}{\rho}, \tag{4.6}$$

and the gas and dust velocities, $\mathbf{v}_g$ and $\mathbf{v_k}$ are given by

$$\begin{aligned} \mathbf{v}_g &= \mathbf{v} - \sum_{k=1}^{\mathcal{N}} \frac{\rho_k}{\rho - \rho_k} \mathbf{w_k}, \\ \mathbf{v_k} &= \mathbf{v} + \mathbf{w_k}. \end{aligned} \tag{4.7}$$

For later purposes, I still define the dust ratio $\epsilon_k \equiv \frac{\rho_k}{\rho}$, the total dust ratio $\epsilon \equiv \sum_k^{\mathcal{N}} \epsilon_k$, and the dust-to-gas ratio $\theta_d \equiv \frac{\sum_k^{\mathcal{N}} \rho_k}{\rho_g}$. For any quantity A, I define $\bar{A} \equiv A/A_0$ where A_0 is its initial value. $\bar{\epsilon}$ and $\bar{\theta}$ are called the dust-ratio and dust-to-gas ratio enrichment respectively. Further details about the monofluid formalism and its implementation in `RAMSES` can be found in Chapters 2 and 3.

[1] distinct from the dust density ρ_k

4.2.2 Dusty-MHD with neutral grains

In Chapter 2, I extended the above formalism to neutral grains embedded in a weakly ionized plasma. Here I only consider the resistive effect of ambipolar diffusion, i.e. the drift between ions and neutrals other than the dust. In this context, the equations of NdustyMHD can be expressed as

$$\begin{aligned}
\frac{\partial \rho}{\partial t} + \nabla \cdot [\rho \mathbf{v}] &= 0, \\
\frac{\partial \rho_k}{\partial t} + \nabla \cdot [\rho_k (\mathbf{v} + \mathbf{w_k})] &= 0, \ \forall k \in [1, \mathcal{N}], \\
\frac{\partial \rho \mathbf{v}}{\partial t} + \nabla \cdot \left[\left(P_\mathrm{g} + \frac{\mathbf{B}^2}{2} \right) \mathbb{I} + \rho(\mathbf{v} \otimes \mathbf{v}) - \mathbf{B} \otimes \mathbf{B} \right] &= -\rho \nabla \phi, \\
\frac{\partial \mathbf{B}}{\partial t} - \nabla \times \left[(\mathbf{v} - \sum_{k=1}^{\mathcal{N}} \frac{\rho_k}{\rho - \rho_k} \mathbf{w_k}) \times \mathbf{B} \right] & \\
+ \nabla \times \left[\frac{\eta_\mathrm{A}}{|\mathbf{B}|^2} [(\nabla \times \mathbf{B}) \times \mathbf{B}] \times \mathbf{B} \right] &= 0, \\
\nabla \cdot \mathbf{B} &= 0,
\end{aligned} \tag{4.8}$$

where $\mathbf{B}$ is the magnetic field and η_A is the ambipolar resistivity.

As in Chapter 2, I can express $\mathbf{w_k}$ as

$$\mathbf{w_k} = \left[\frac{\rho}{\rho - \rho_k} t_{\mathrm{s},k} - \sum_{l=1}^{\mathcal{N}} \frac{\rho_l}{\rho - \rho_l} t_{\mathrm{s},l} \right] \frac{\nabla P_\mathrm{g} - (\nabla \times \mathbf{B}) \times \mathbf{B}}{\rho}, \tag{4.9}$$

To further simplify equations (4.8), I assume in this chapter that the plasma velocity $\mathbf{v}$ is the barycenter velocity which is valid when $\epsilon_k \|\mathbf{w_k}\| \ll \|\mathbf{w_k}\| \ll |\mathbf{v}|$. In this case the induction equation is written as

$$\frac{\partial \mathbf{B}}{\partial t} - \nabla \times [\mathbf{v} \times \mathbf{B}] + \nabla \times \left[\frac{\eta_\mathrm{A}}{|\mathbf{B}|^2} [(\nabla \times \mathbf{B}) \times \mathbf{B}] \times \mathbf{B} \right] = 0. \tag{4.10}$$

4.3 Method

4.3.1 RAMSES

In this chapter, I take advantage of the `RAMSES` code presented in Chapter 3. In this same chapter (mostly based on Lebreuilly et al., 2019), I presented the extension of the code to the treatment of dust dynamics with multiple species in the diffusion approximation and terminal velocity regime that I also use here.

4.3.2 Boss and Bodenheimer test

I perform Boss and Bodenheimer tests (Boss & Bodenheimer, 1979) to follow the dynamics of the dust during the first collapse and first core formation. Boss and Bodenheimer tests consist in a gravitationally unstable uniform spherical cloud that we let collapse in a low density background. The parameters of the setup are the initial mass of the dense core M_0, the total dust ratio ϵ_0, the temperature of the gas T_g and a mean molecular weight μ_g. The ratio between the thermal and the gravitational energy α is

$$\alpha = \frac{5}{2} \frac{(1 - \epsilon_0) R_0}{\mathcal{G} M_0} \frac{k_\mathrm{B} T_\mathrm{g}}{\mu_\mathrm{g} m_\mathrm{H}}, \tag{4.11}$$

and sets the initial radius of the cloud R_0 and its density ρ_0. In addition, I impose an initial solid body rotation around the z-axis at the angular velocity Ω_0 by setting the ratio between the rotational and the gravitational energy β given by

$$\beta = \frac{1}{3}\frac{R_0^3\Omega_0^2}{\mathcal{G}M_0}. \tag{4.12}$$

Eventually, I apply an initial azimuthal density perturbation according to

$$\rho = \rho_0\left[1 + A\cos\left(m\theta\right)\right]. \tag{4.13}$$

In this chapter, I aim to investigate the impact of magnetic fields on the dynamics of neutral dust grains in two simulations, one with ideal MHD and one with ambipolar diffusion. For these runs, I impose an uniform magnetic field using the mass-to-flux-to-critical-mass-to-flux-ratio

$$\mu = \left(\frac{M_0}{\Phi}\right)/\left(\frac{M}{\Phi}\right)_{\rm c}, \tag{4.14}$$

the critical mass-to-flux ratio being given by $(M/\Phi)_{\rm c} = \frac{0.53}{3\pi}\sqrt{5/\mathcal{G}}$ (Mouschovias & Spitzer, 1976). I set an angle $\phi_{\rm mag}$ between the magnetic fields and the rotation axis to reduce the efficiency of the magnetic braking.

4.3.3 Dust grain size distributions

In my MULTIGRAIN simulations, $\mathcal{N} > 1$ dust bins are considered. The dust ratio of each bins is set from power-law distributions

$$\frac{{\rm d}\epsilon}{{\rm d}s} = \frac{\epsilon_0}{\int_{S_{\rm min}}^{S_{\rm max}} s^{3-m}{\rm d}s}s^{3-m}, \tag{4.15}$$

with ϵ_0 the total initial dust ratio and, $S_{\rm min}$ and $S_{\rm max}$ being the minimum and maximum sizes of the grains present in the medium, respectively. For the standard MRN distribution, $S_{\rm min}$ = 5 nm, $S_{\rm max}$ = 250 nm and m = 3.5.

The method described in Hutchison et al. (2018) is used to compute the initial dust ratio and typical grain size of each bin. A logarithmic grid is used to determine the edges S_k of the bins

$$\log(S_k) = \log\left(\frac{S_{\rm max}}{S_{\rm min}}\right)\frac{k}{\mathcal{N}} + \log\left(S_{\rm min}\right). \tag{4.16}$$

The typical grain size of a bin k required to compute the stopping time is

$$s_k = \sqrt{S_k S_{k+1}}. \tag{4.17}$$

$S_{\rm min}$ and $S_{\rm max}$ are the edges of the distribution and must not be confused with the minimum and maximum bin size that are averaged quantities. The initial dust ratios in each bin are computed according to

$$\epsilon_{0k} = \epsilon_0\left[\frac{S_{k+1}^{4-m} - S_k^{4-m}}{S_{\rm max}^{4-m} - S_{\rm min}^{4-m}}\right]. \tag{4.18}$$

4.3.4 Setup

Cloud setup

I impose initial conditions that are typical of the first protostellar collapse (Larson, 1969) with $T_g = 10$ K, $\mu_g = 2.31$ and a solar mass cloud. I also set $\gamma = 5/3$ since molecular hydrogen behaves as a monoatomic gas at low temperatures (Whitworth & Clarke, 1997). As explained in section 4.2.1, a barotropic law is used to close system (4.1) with $\rho_{ad} = 10^{-13}$g cm $^{-3}$ (Larson, 1969). Finally, I set $m = 2$ and $A = 0.1$ to favor fragmentation and the formation of two spiral arms in the rotating runs.

I impose an uniform initial total dust-to-gas ratio of $\theta_{d,0} = 0.01$ in all the models. For the MULTGRAIN rotating runs, I always consider 10 bins with grain sizes distributed according to section 4.3.3. Spherical collapses are however computed with only one dust species. In all the models $S_{min} = 5$ nm, and $m = 3.5$ and S_{max} is specified individually. I consider grains with $\rho_{grain} = 3$ g cm^{-3} for the spherical collapses and $\rho_{grain} = 1$ g cm^{-3} for the rotating models.

The two magnetic models have been computed with $\mu = 5$ and $\phi_{mag} = 40°$. For the non-ideal MHD model the ambipolar resistivity is computed similarly to the case of reference of Marchand et al. (2016).

Numerical setup

I use the HLLD Riemmann solver (Miyoshi & Kusano, 2005) for the barycenter part of the conservation equations with a MINMOD slope limiter (Roe, 1986) for both the gas and the dust. The Truelove criterion (at least 4 point per Jeans length, Truelove et al., 1997) must be satisfied to avoid artificial clump formation. I therefore enforce a refinement criteria that imposes at least 15 points per local Jeans length. The grid is initialized to the level $\ell_{min} = 5$ and allows refinement up to a maximum level $\ell_{max} = 16$[2] (which gives a resolution between 32^3 and 65536^3 cells).

Analysis of the models

I consider that the first hydrostatic core (FHSC) is fully formed when the peak density reaches 10^{-11} g cm^{-3} for the first time. I denote the corresponding time t_{core}, and use this definition to compare my models at similar evolutionary stages. I present here the different objects that are observed in my models and their definition in this work.

- The first hydrostatic core/the fragments are any object of density larger than $10^{-12.5}$ g cm^{-3}. The FHSC or $\mathcal{F}_0$ corresponds to the central fragment. $\mathcal{F}_1$ and $\mathcal{F}_2$ are the secondary fragments/FHSC

- The disk $\mathcal{D}$ is the region that satisfies Joos et al. (2012) criterion. For the analysis, we place ourselves in cylindrical coordinates (r, ϕ, z). A region is identified as a disk if it is Keplerian ($v_\phi > f_{thre} v_r$), in hydrostatic equilibrium ($v_\phi > f_{thre} v_z$), rotationally supported ($\frac{1}{2}\rho v_\phi^2 > f_{thre} P_g$) and dense $\rho > 3.9 \times 10^{-15}$ g cm^{-3}. As in Joos et al. (2012) , I choose $f_{thre} = 2$.

- The pseudo-disk $\mathcal{P}$ (Galli & Shu, 1993), for magnetic runs, is defined as the regions with $r < 5000$ AU and densities above 3.9×10^{-17} g cm^{-3} that are not in the disk and fragments. The criterion is similar to Hincelin et al. (2016). 5000 AU is an arbitrary distance that is sufficiently larger than the central objects while being smaller than the initial cloud.

[2] 17 for the spherical collapses, although this level is never reached

- Jets/outflows $\mathcal{O}$ correspond to any region with $r < 5000$ AU with $\mathbf{v} \cdot \frac{\mathbf{r}}{|\mathbf{r}|} > 0.2$ km sec^{-1}($\mathbf{r}$ is the position relative to the center of the box). The criterion is also similar as (Hincelin et al., 2016).

- The envelope $\mathcal{E}$ encompasses the regions with $r < 5000$ AU that exclude the fragments, the disk/pseudo-disk and the jets/outflows.

I consider two different weights for averaging a quantity A over a volume $\mathcal{V}$ in the computational box. Volume averaging is computed according to

$$\langle A \rangle_v = \frac{\sum_{i \in \mathcal{V}} \Delta x_i^3 A_i}{\sum_{i \in \mathcal{V}} \Delta x_i^3}. \tag{4.19}$$

Mass averaging is computed according to

$$\langle A \rangle_m = \frac{\sum_{i \in \mathcal{V}} \rho_i \Delta x_i^3 A_i}{\sum_{i \in \mathcal{V}} \rho_i \Delta x_i^3}, \tag{4.20}$$

where ρ_i and Δx_i are the total density and length of individual cells i in the averaged volume. Volume averages emphasize on regions of large spatial extension, i.e. the envelope, while mass averages emphasize on regions of high density, i.e. the core+disk and the denser regions of the envelope.

4.3.5 Regularization of the differential velocity and dust density

The terminal velocity approximation is unrealistic in low density regions or in shocked regions where the pressure is discontinuous (Lovascio & Paardekooper, 2019).

In the rotating models, I cap the differential velocities to $w_{\rm cap}$ in my models to avoid prohibitively small timesteps and unrealistically large variations in the dust ratio at strong shock fronts. I impose $w_{\rm cap} = 1$ km s^{-1}. To verify that this does not impact the results, I ran extra models with $w_{\rm cap} = 0.1$ km s^{-1}, $w_{\rm cap} = 0.5$ km s^{-1} and $w_{\rm cap} = 2$ km s^{-1}. A comparison between these models and my fiducial is given in Appendix 4.10.

In my models, the drift velocity can in some regions be supersonic. Unless specified, I account for the correction presented in equation (4.5). In that perspective, I use the drift velocity estimated at the previous timestep to estimate the differential velocity mach number.

Finally, I set the drift velocity to zero at densities lower than the ones of the initial cloud, i.e. the background. This is a way to ensure that the regions where the terminal velocity is not valid do not affect significantly the calculation.

4.3.6 Validity of the model

The diffusion approximation is valid as long as the ratio between the stopping time and the dynamical timescale of the gas is small compared to unity (Laibe & Price, 2014c). This ratio is called the Stokes number St.

During the first collapse, the dynamical timescale is the free-fall time $t_{\rm ff}$ (see section 4.4.1 or chapter 1). For an initial dust-to-gas ratio of 0.01 and a temperature of 10 K, the initial Stokes number St_0 of a spherical collapse is given by

$$\mathrm{St}_0 \sim 0.038 \left(\frac{M_0}{1 M_\odot}\right)\left(\frac{\rho_{\rm grain}}{1 \text{ g cm}^{-3}}\right)\left(\frac{s_{\rm grain}}{0.05 \text{ cm}}\right)\left(\frac{\alpha}{0.5}\right)^{3/2} < 1. \tag{4.21}$$

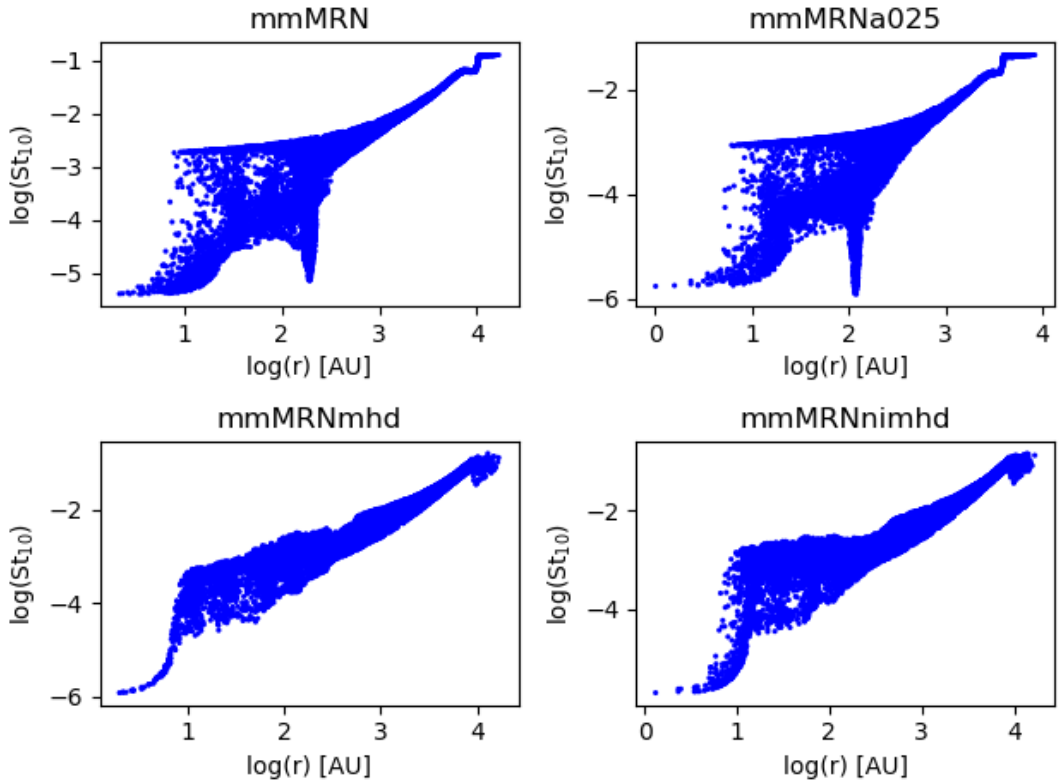

Figure 4.1: Logarithm of the maximum (10^{th} bin) Stokes number as a function of the spherical radius for the four models with the largest Stokes numbers at t_{core} + 2 kyr. (Top-left) mmMRN, (Top-right) mmMRNa0.25, (Bottom-left) mmMRNmhd , (Bottom-right) mmMRNnimhd.

The dynamics of grains smaller than 0.05 cm can be simulated using the diffusion approximation. Note that the Stokes number varies as $\propto \frac{1}{\sqrt{\rho}}$ (since $t_{\text{ff}} \propto \frac{1}{\sqrt{\rho}}$ and $t_{\text{s}} \propto \frac{1}{\rho}$) and hence can increases with a decreasing density. I show in figure 4.1 the values of the maximum Stokes number as a function of the radius for the four rotating models with the least coupled dust (see section 4.5 for a description of the models). The maximum value for St is smaller than ~ 0.15 in external regions of the collapse of the rotating models and it is typically smaller than 0.05 inside the collapsing regions for this models. Rotation provides an additional support to the collapse, which causes an increase of the free-fall timescale. Hence, as the initial angular velocity increases, the initial Stokes number decreases and the diffusion approximation is even more accurate. Similarly, magnetic fields increase the duration of the collapse which broadens the validity domain of the diffusion approximation. Finally, the Stokes number also decreases when α decreases, implying that the diffusion approximation remains valid for small values of α.

In the induction equation, I consider for simplicity that the plasma is moving at the barycenter velocity. This approximation is valid when $\epsilon \ll 1$, i.e. when the back-reaction from the dust onto the gas is negligible. Note that I investigate the impact of the back-reaction in Appendix 4.11.

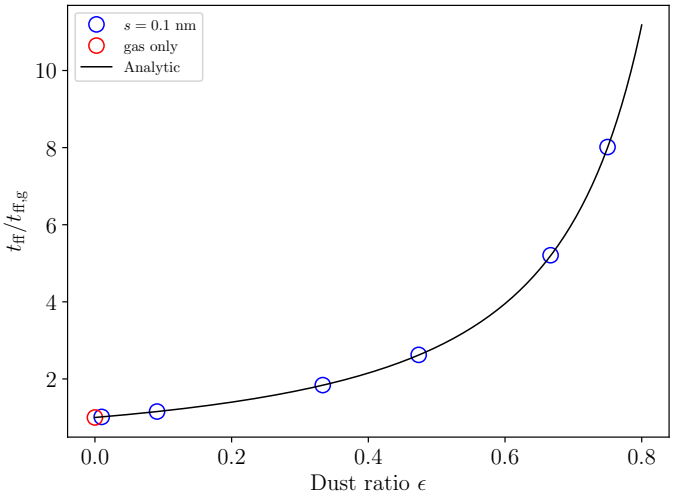

Figure 4.2: Ratio between the free-fall timescale of the mixture and the free-fall timescale of the gas. The red circle corresponds to the fiducial simulation with gas only, and the blue circles correspond to gas and dust mixtures for various dust ratios. The black solid line is the analytical solution.

4.4 Spherical dusty protostellar collapses

The final test of the algorithm verifies again that both gas and dust are sensitive to gravity and the 3D implementation of the solver. In all the models of this section, $\beta = 0$, $A = 0$ and the Kwok correction is not considered. All the collapse of this section are hydrodynamical and computed with single grain species. I presented these models in Lebreuilly et al. (2019).

4.4.1 Free-fall timescale for strongly coupled mixtures

A core only composed with gas would collapse at the following free-fall timescale

$$t_{\rm ff,g} \equiv \sqrt{\frac{3\pi}{32\mathcal{G}\rho_{\rm g}}}.$$

For a perfectly coupled gas and dust mixture ($t_{\rm s} \ll t_{\rm ff}$) it writes

$$t_{\rm ff} = \sqrt{\frac{3\pi}{32\mathcal{G}\rho}}.$$

In the context of the Boss and Bodenheimer test, this timescale indirectly depends on the initial dust ratio

$$t_{\rm ff} = \frac{\pi}{5\sqrt{5}}\mathcal{G}M_0\left(\frac{\alpha\mu m_{\rm H}}{k_{\rm b}T_{\rm g}(1-\epsilon_0)}\right)^{3/2}. \tag{4.22}$$

Physically, this is due to the fact that two cores with the same initial α but different ϵ_0 have different initial radius, hence free-fall timescale. Indeed, R_0 increases with ϵ_0 so that the gas provides the same thermal support against gravity.

To test this relation, non-rotating DUSTYCOLLAPSE with various dust ratios and the same $\alpha = 0.5$ are performed. The condition $t_{\rm s} \ll t_{\rm ff}$ is ensured by considering very small grains with $s = 10^{-7}$ cm.

Figure 4.2 shows the ratio between the free-fall timescale of a dusty cloud and the one of a pure-gas cloud compared with the analytical solution. I define the free-fall timescale as the time at which the peak density reaches $\rho_{\rm ad}$. The scaling relation is very well verified. As expected, the gas, but also the dust, are sensitive to gravity and fall at the mixture free-fall timescale.

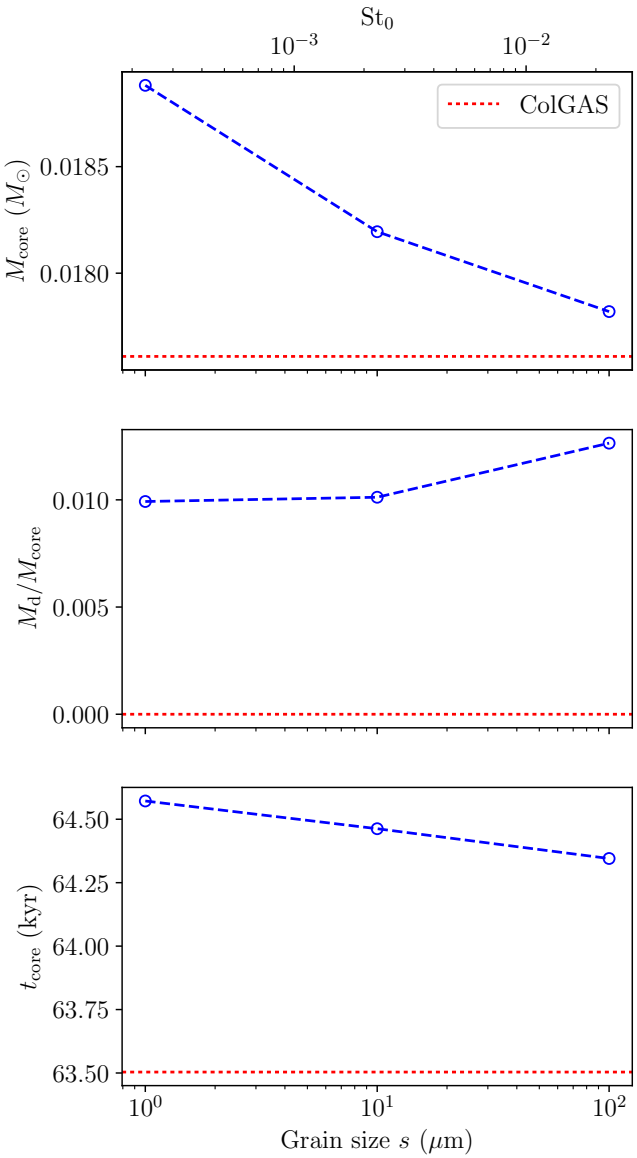

Figure 4.3: Properties of the first Larson core at $t_{\rm core}$ for the Col1, Col10, Col100. The core mass, the dust mass ratio and the formation time are shown as a function of the grain size (blue circles). The results are compared with the fiducial ColGAS simulation (dashed red lines). The top x-axis shows the initial Stokes number in the core St_0.

4.4.2 Core properties

Non-rotating DUSTYCOLLAPSE of $\alpha = 0.5$ are performed with an initial dust-to-gas ratio of 1%. Single grain species of size 1 µm (Col1), 10 µm (Col10) and 100 µm (Col100) are considered. The results are compared at at $t_{\rm core}$ with a fiducial collapse without any treatment of dust (ColGAS).

Figure 4.3 shows the total mass of the first hydrostatic core $M_{\rm core}$, the dust mass ratio $M_{\rm d}/M_{\rm core}$ and $t_{\rm core}$ as a function of the grain size (bottom x-axis) and the initial Stokes number (top x-axis). The first core properties depend on the amount of dust in the initial dense core. In the fiducial ColGAS test, the gas density is assimilated to the total density, as often in the literature. This results in a lower first-core mass and a shorter formation time. Note that

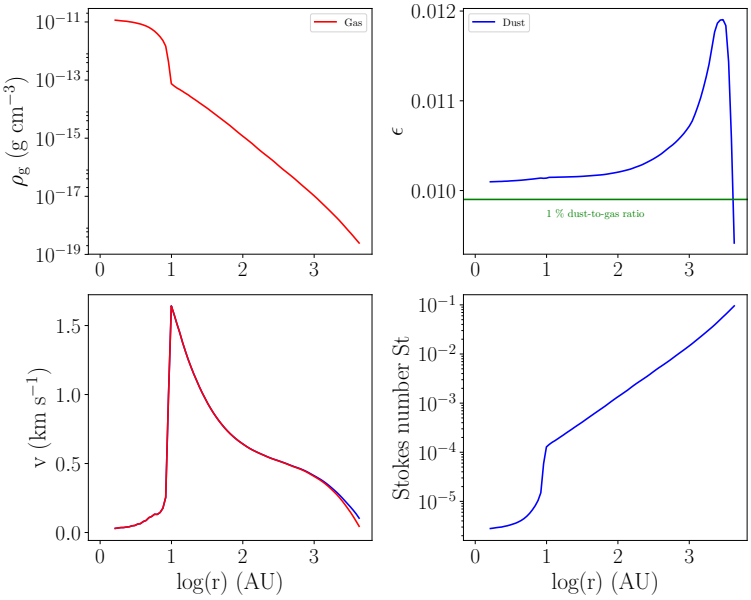

Figure 4.4: Radial profiles of the Col10 test. (Top-Left) Gas density. (Top-right) Dust ratio. (Bottom-Left) Gas and dust velocities. (Bottom-right) Stokes number. The horizontal green line corresponds to a dust-to-gas ratio of 1%

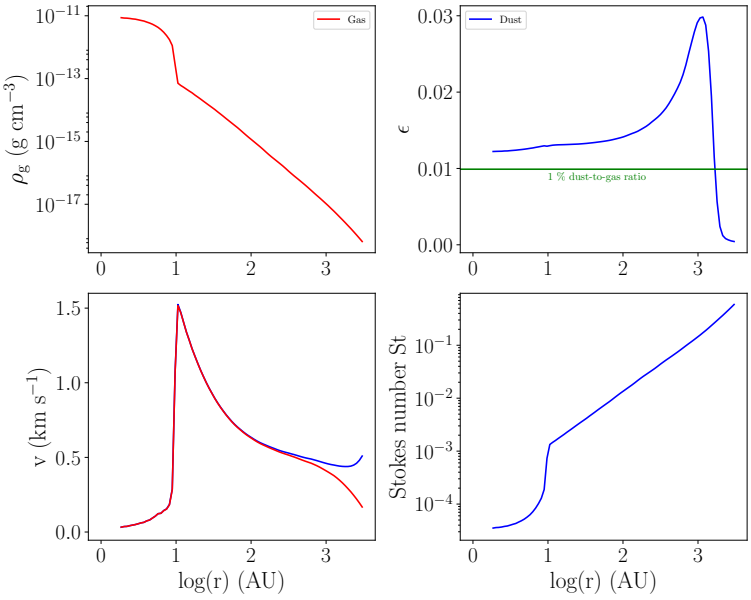

Figure 4.5: Same as Fig.4.4 for the Col100 test.

Model	α	$S_{\max}$ (cm)	μ	$\phi_{\rm mag}$ (°)	Ambipolar	$t_{\rm core}$ (kyr)	$\mathrm{St}_{0,10}$
MMMRN	0.5	0.1	-	-	-	72.84	1.22×10^{-2}
MRN	0.5	2.5×10^{-5}	-	-	-	73.6	1.06×10^{-5}
100MICMRN	0.5	0.01	-	-	-	72.9	1.72×10^{-3}
MMMRNA0.25	0.25	0.1	-	-	-	23	4.31×10^{-3}
MMMRNMHD	0.5	0.1	5	40	NO	81.1	1.22×10^{-2}
MMMRNNIMHD	0.5	0.1	5	40	YES	81.1	1.22×10^{-2}
Cloud mass	Number of bins						
$1 M_\odot$	10						

Table 4.1: Syllabus of the different simulations, with the thermal-to-gravitational energy ratios α, maximum grain sizes $S_{\max}$. The initial mass-to-flux ratio μ as well as the tilt between the magnetic field and the rotation axis $\phi_{\rm mag}$ are given for simulations with magnetic field. Additionally, I also provide the formation time of the FHSC $t_{\rm core}$ and and the initial Stokes number of the largest grains $\mathrm{St}_{0,10}$, the mass of the initial core and the number of dust bins.

the barotropic equation of state implicitly assumes a constant dust-to-gas ratio of 1% which is slightly inconsistent. Dust-to-gas ratios might be even larger in core forming regions (Hopkins & Lee, 2016; Tricco et al., 2017) which could lead to even more important discrepancies. In terms of dynamics, small grains ($s < 100$ µm) do not have a significant impact as they fall alongside the gas. However, the differential velocity between the gas and the dust is proportional to the stopping time, hence large grains ($s \geq 100$ µm) are prone to fall substantially faster than the gas. Their infall provokes a slight acceleration of the first core formation as it changes the balance between the gravity and the thermal support of the gas. The mass of the core decreases as the grain size increases because the gas has less time to be accreted during the collapse. The settling of dust in the central regions of the core, however, leads to an increase of the $M_{\rm d}/M_{\rm core}$.

Figures 4.4 and 4.5 show the radial profiles for the Col10 and Col100 tests, respectively, of the gas density, the dust ratio, the gas and dust velocities, and the Sotkes number. As can be seen, the strong dust depletion in the outer regions of the collapse provides the enrichment of the core. However, as the damping is more efficient in the high density regions (see the velocities $\mathbf{v}_{\rm g} \approx \mathbf{v}_{\rm d}$), the dust ratio increases at a slower rate in the inner regions of the collapse, i.e, the first core. If the maximum increase of dust ratio in the outer regions of the collapse is about $\sim 20\%$ for the Col10 test, it goes up to $\sim 300\%$ for the Col100 test.

4.5 Rotating models

The rotating models presented in this section are referenced in table 4.1. All of them have been evolved up to at least 2 kyr after the formation of the first core. My fiducial case MMMRN has been run over a longer time.

4.5.1 Fiducial simulation

In this section, I present my fiducial case MMMRN where $\alpha = 0.5$ and $\beta = 0.03$. The grain size distribution is extended up to $S_{\max} = 1$ mm. The value of $S_{\max}$ leads to an average size of the last and largest bin $s_{10} \sim 160$ µm. The total initial dust-to-gas ratio is $\theta_{\rm d,0} = 1\%$.

Figure 4.6 shows edge-on (four top figures) and mid-plane (four bottom figures) density cuts of the gas (left) and of the dust fluid with the largest grain size (160 µm, right) at 1 kyr and

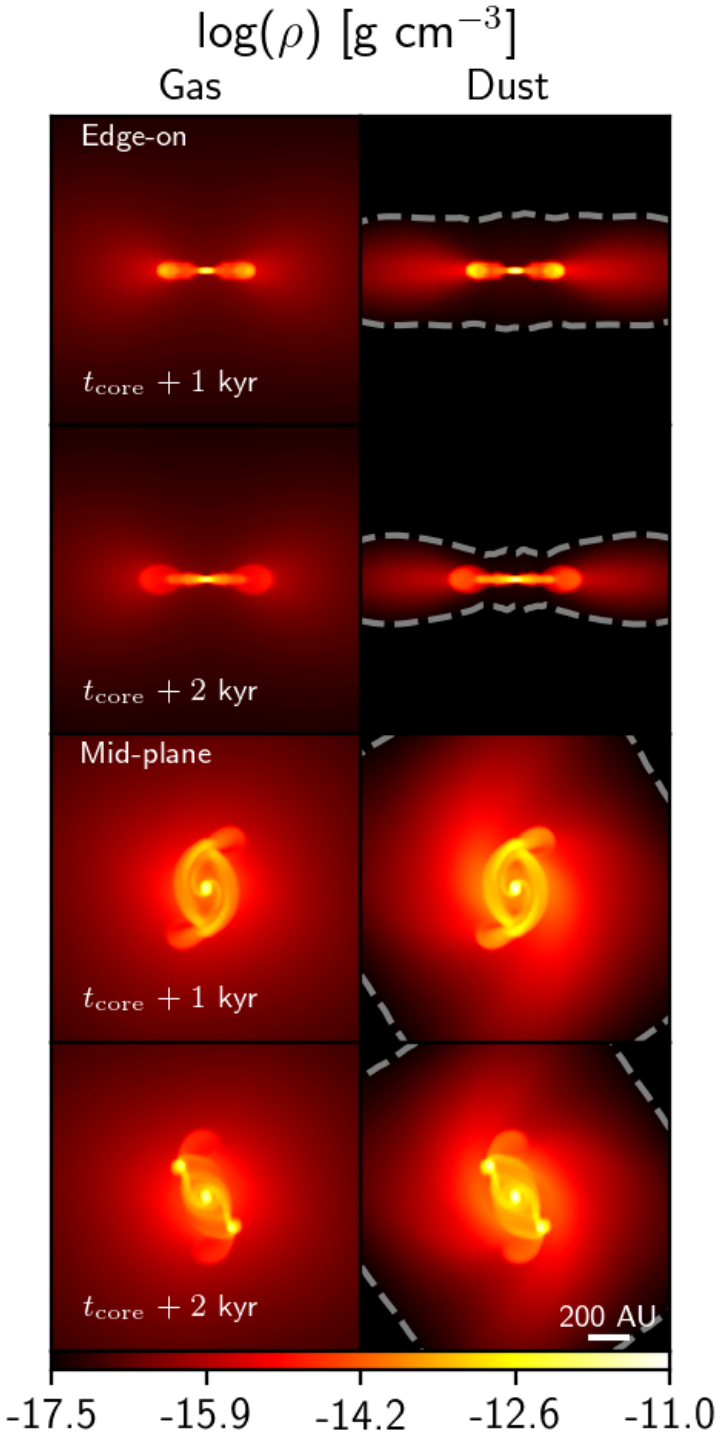

Figure 4.6: MMMRN test at $t_{\rm core}$ + 1 kyr and $t_{\rm core}$ + 2 kyr ($t_{\rm core}$ = 72.84 kyr). Edge-on and mid-plane cuts of the gas and the dust densities for the least coupled species are provided (left and right respectively). Values of the gas density are indicated by the colorbar on the bottom. Dust densities have been multiplied by a factor 100 to be represented on the same scale. Hence, colors of the gas and the dust maps match when the dust-to-gas ratio equals its initial value 0.01. Dust density variations in regions where $\epsilon_0\rho_{\rm d} < \min(\rho_{\rm g})$ have voluntarily not been displayed to highlight the enriched regions. These depleted regions are delimited by the dashed grey lines. This choice of colors applies for all density maps in this study. Gas and dust are clearly not perfectly coupled.

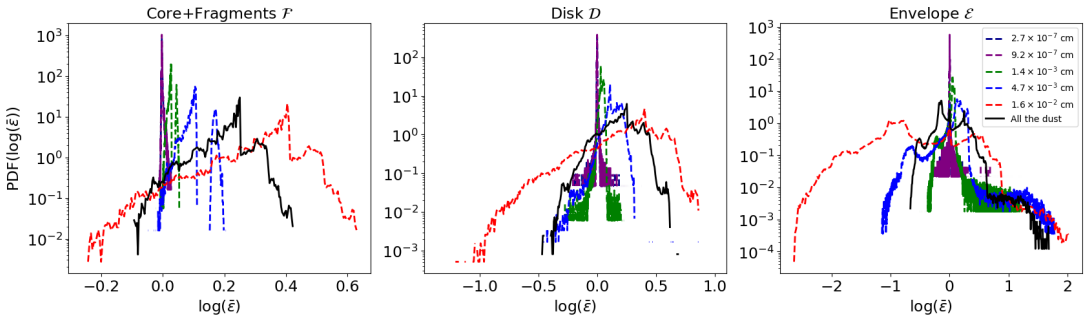

Figure 4.7: MMMRN test at $t_{\rm core}$ + 2 kyr. Probability density function (PDF) of the dust ratio enrichment $\log(\bar{\epsilon})$ for the two most coupled and three least coupled dust species (colored dashed lines) and for all the dust (black line) in the core+fragments(left), the disk (middle) and the envelope (right). Dust is not a good tracer for the gas here and the dust distribution is not uniform in the considered objects.

2 kyr after the formation of the first Larson core ($t_{\rm core}$ = 72.84 kyr for this model), respectively. The density distributions obtained for the gas and the dust are clearly different. This discrepancy originates from an imperfect coupling between the two phases which causes a drift of the dust toward the inner regions of the collapse. This general trend can be explained by a simple force budget on the gas and the dust. Although the gas is partially supported by pressure, dust grains are only subjected to gravity and gas drag. As such, the dust fluid collapses essentially faster than the gas. It therefore enriches the first core and the disk at the cost of a depletion of solids in the envelope. Figure 4.6 shows that these strong enrichment in the mid-plane and depletion in the envelope have already occurred at $t_{\rm core}$ + 1 kyr, and continues for more than 1 kyr. In the mid-plane, the envelope is enriched in large dust grains close to the central object and depleted further away. In the vertical direction, it is mostly depleted in large grains. In short, after the first core formation these grains are concentrated in a very thin layer of 10 − 100 AU above/under the mid-plane. At this stage, the envelope is mostly a reservoir of low dust densities for the large grains. Hence accretion of dust arising from the envelope does not enrich significantly the fragments and the disk in large grains and the dust-to-gas ratio in the disk even decreases. Note that the latter is still very enriched by the end of the calculation. Most of the enrichment of dust-to-gas ratio in the central objects is indeed actually taking place during the initial phases of the collapse, when the densities are low everywhere and the coupling between the gas and the dust is the weakest.

Figure 4.7 shows probability density functions (PDF) of the dust ratio enrichment, denoted $\log(\bar{\epsilon})$. It compares the distributions of the two most coupled and the three least coupled dust species (colored dashed lines) at $t_{\rm core}$ + 2 kyr. It also indicates the PDF integrated over the grain size distribution (black line). These PDF are displayed in three different regions, namely the core and the fragments (left), the disk (middle) and the envelope (right). Figure 4.7 shows that the dust enrichment in the inner regions is size-dependent. Small grains experience larger drag that reduces their differential velocity with respect to the gas.

Here, grains with sizes smaller than a few microns remain very well coupled with the gas in all the considered regions, whereas for larger grains the PDF of the dust ratio is broad. For 160 µm grains, the dust ratio increases by one order of magnitude in some regions of the disk and up to two orders of magnitude in the envelope. On average, the dust ratio is 1.8% in the core, 1.75% in the disk and ∼ 0.86% in the envelope. In addition, the dust has experienced a strong and local dynamical sorting. I indeed measure a typical standard deviation for the dust-ratio enrichment $\bar{\epsilon}$ of 0.072 in the core, 0.14 in the disk and 0.23 in the envelope. The

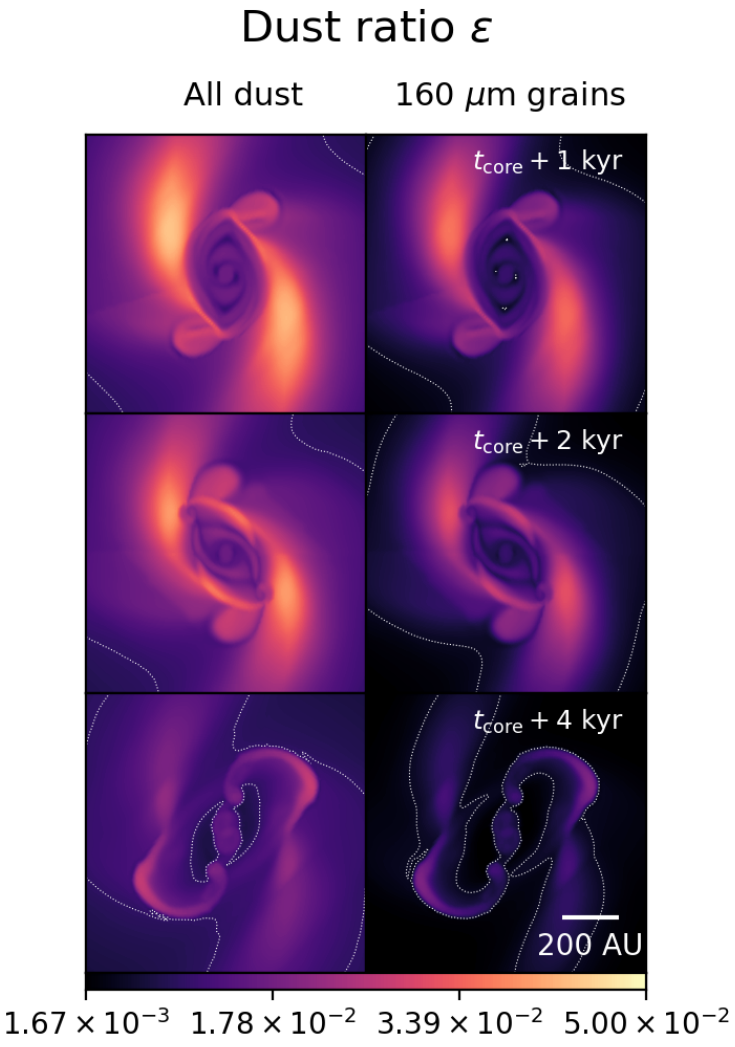

Figure 4.8: MMMRN test ~ 1 kyr (top), ~ 2 kyr (middle) and ~ 4 kyr (bottom) after the first core formation ($t_{\rm core}$ = 72.84 kyr). Mid-plane view of the total dust ratio (left) and the dust ratio of the least coupled species (right). The colorbar is the same for both figures. The dotted white lines represent the regions where the total (left) or 160 µm grains (right) dust-to-gas ratio is at its initial value, which can also be regarded as a dust enrichment line.

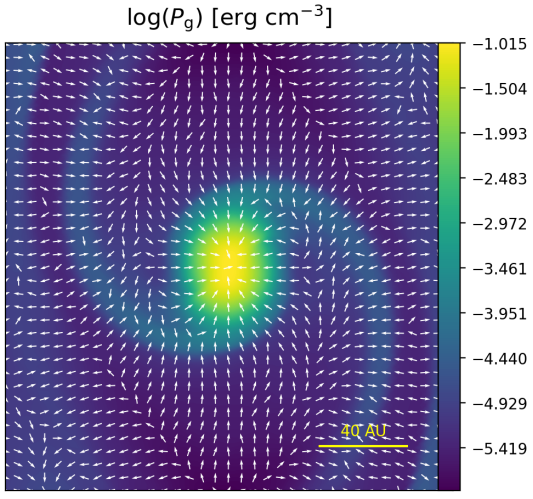

Figure 4.9: MMMRN test at $t_{\rm core}$ + 1 kyr ($t_{\rm core}$ = 72.84 kyr). Mid-plane view of the gas pressure (up-close). The white arrows represent the direction of the differential velocity $\mathbf{w_{10}}$.

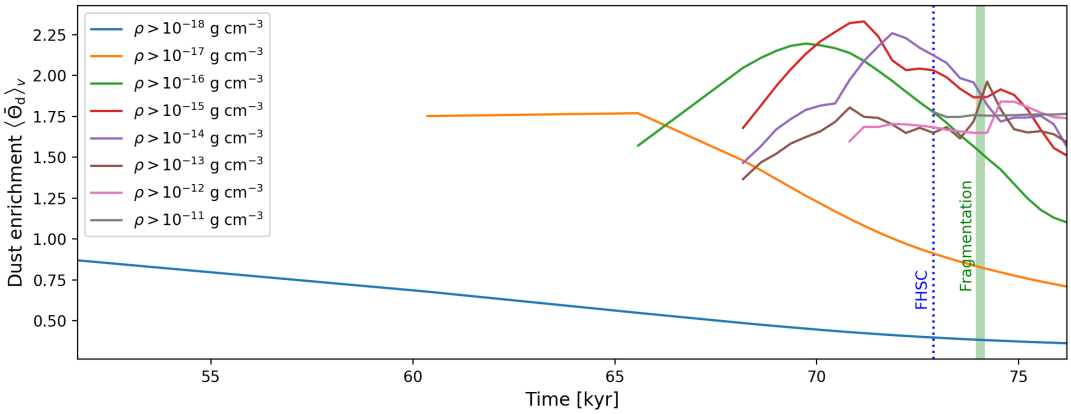

Figure 4.10: MMMRN test. Volume averaged total dust-to-gas ratio enrichment as a function of time for different density thresholds. The FHSC formation can be identified by the dotted vertical blue line while fragmentation occurs during a time delimited by the green area. We observe a slow decrease of the dust-to-gas ratio at low density at the benefit of an enrichment of high density regions. Cores and fragments at $\rho > 10^{-11}$ g cm^{-3} are formed in a dust rich environment. The dust-to-gas ratio is almost constant for $\rho > 10^{-11}$ g cm^{-3} because the increase of temperature due to the adiabatic contraction strengthen the coupling between the gas and the dust.

standard deviation is the largest in the envelope, a region which is depleted in dust in the outer regions and enriched close to the disk and fragments. The disk experiences larger variations of dust-to-gas ratio compared to the core. Indeed, the latter is in adiabatic contraction. This induces high temperatures, which in return causes a strong decrease of the Stokes number. Hence, dust is essentially frozen with the gas in the core and $\mathbf{v}_d \approx \mathbf{v}_g$. Figure 4.8 shows the dust ratio for the total dust distribution (left) and for the 10^{th} species (right) in the mid-plane of the collapse, at 1 kyr (top), 2 kyr (middle) and 4 kyr (bottom) after the formation of the first Larson core respectively. The maps on the left and on the right are very similar as most of the evolution of the dust ratio is due to the dynamics of the least coupled species, which represents a large fraction of the dust mass (see also the PDF). The structures in the dust ratio observed in figure 4.8 can be interpreted by looking at the thermal pressure distribution shown in figure 4.9. Dust grains tend to drift toward local pressure maxima (see figure 4.8, top panel) where the differential velocity is zeroed (see equation (4.6)). The essential of the variations of the total dust ratio are due to the largest grains, since they represent most of the dust mass and have the largest drift velocities. Hence, a significant fraction of the dust mass in the inner regions is composed with large grains. Finally, note that 4 kyr after the first core formation, the average value for the total dust-to-gas ratio is roughly unchanged but generally increasing (of about 1%) in the core and fragments since their formation. For the disk, I note a decrease of dust ratio of $\sim$ 30% for the largest grains ($\sim$ 22% in total) in the disk since the first core formation. In addition, the total dust-to-gas ratio continues to diminish in the envelope at this time as settling goes on, with a final average value of $\sim$ 0.83%.

Figure 4.10 shows the evolution of the dust-to-gas ratio enrichment averaged in volume for different density threshold in the regions where $R < 5000$ AU. The dust depletion at large scales in the envelope at low densities is a relatively slow process, which occurs during the entire collapse. Once regions with larger densities are formed, they usually experience a relatively quick enrichment from the dust content of the low density regions, and then a quick depletion in favor of even denser regions. Figure 4.10 shows that fragmentation occurs in a dust-rich

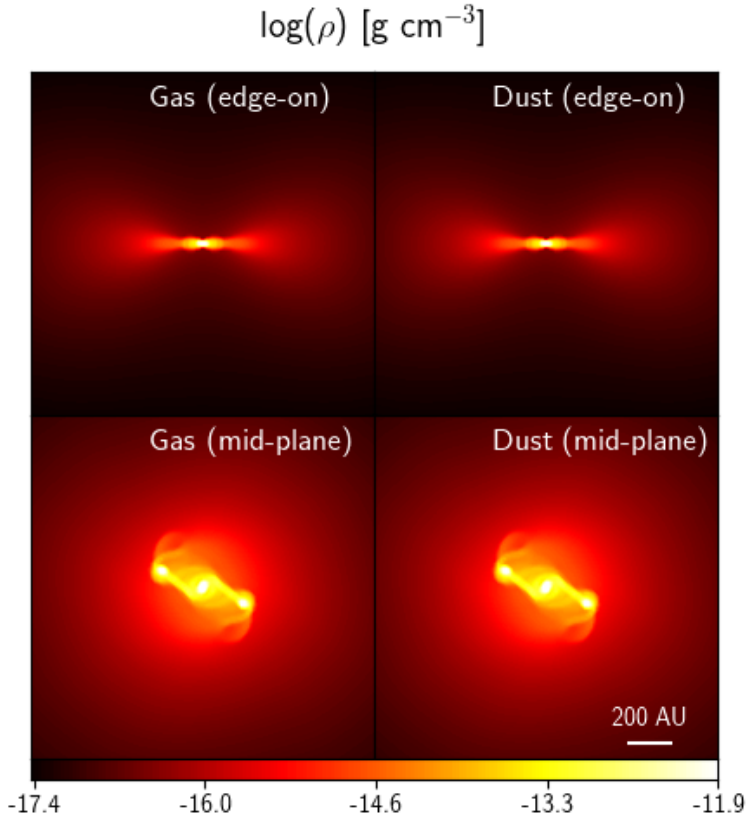

Figure 4.11: MRN test at $t_{\rm core} + 2$ kyr ($t_{\rm core} = 73.6$ kyr). Edge-on (top) and mid-plane (bottom) cuts of the gas density (left) and dust density of the least coupled species (right). The two maps are almost indistinguishable due to the very strong coupling between gas and all dust species.

environment. A strong enrichment of the volume where $\rho > 10^{-13}$ g cm^{-3} delimited by the brown line indeed happens exactly when fragments form. This explains why these fragment tend to be more dust-rich than the first hydrostatic core. Interestingly, the dust-to-gas ratio does not vary significantly in the volume where $\rho > 10^{-11}$ g cm^{-3} which is in adiabatic contraction. Again, the temperatures in this region are high and therefore the Stokes numbers are very low, which significantly slows down the differential dynamics of the gas and the dust. Note that this volume is already dust enriched by the time of its formation by almost a factor of two.

4.5.2 Parameter exploration

Maximum grain size

As seen in section 4.5.1 for the MMMRN model, the differential dynamics between gas and dust during the protostellar collapse depends critically on the grain sizes. Therefore, I perform two simulations 100MICMRN and MRN with the same set of parameters as in MMMRN, but where I vary the maximum grain size. I choose $S_{\rm max} = 100$ µm for the 100MICMRN model (which yields $s_{10} \sim 22.6$ µm) and $S_{\rm max} = 250$ nm for the MRN model (which yields $s_{10} \sim 139$ nm).

Let us first consider MRN, which is the model that has the smallest $S_{\rm max}$. Figure 4.11 shows the density of the gas (left) of the least coupled dust species (right) at $t_{\rm core} + 2$ kyr. Because the coupling between gas and dust is almost perfect, the two maps are indistinguishable by eye. This is expected because the maximum grain size is $\approx 10^{-5}$ cm which corresponds to an initial Stokes number ${\rm St}_{0,10} \sim 1.06 \times 10^{-5} \ll 1$(see section 4.3.4 for a theoretical justification). As

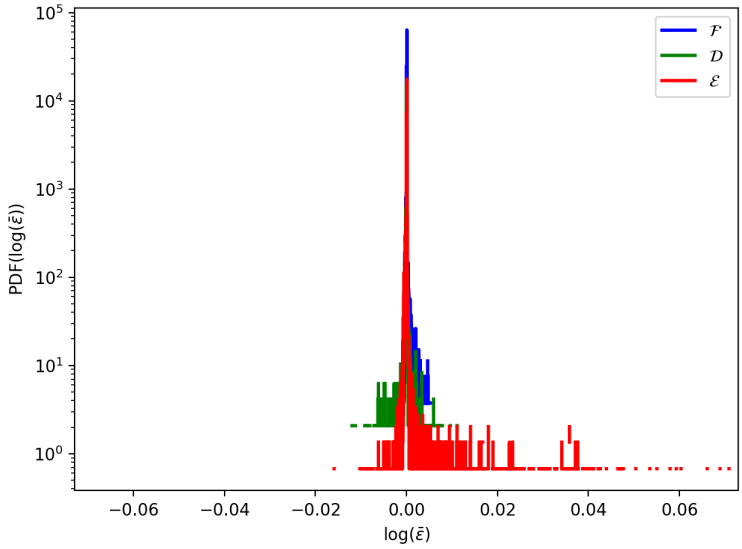

Figure 4.12: MRN test at $t_{\rm core} + 2$ kyr. Probability density function (PDF) of the total dust ratio enrichment $\log(\bar{\epsilon})$ in the core and the fragments, the disk and the envelope. Dust is a very good tracer for the mass here and the dust distribution is almost uniform in the objects considered.

a result, dust is a excellent tracer of the gas in this model. This is illustrated by figure 4.12 that shows the probability density function of the dust ratio enrichment $\log(\bar{\epsilon})$ in the core and fragments, the disk and the envelope at $t_{\rm core}+2$ kyr. Contrary to the MMMRN model, these PDFs are strongly peaked. The average dust-to-gas ratio integrated over the total dust distribution is $\approx$ 1% in the core and the fragments, the disk and the envelope. The standard deviation for the dust ratio enrichment ranges between 2×10^{-4}%(in the core) and 1.4×10^{-2}% (in the envelope). For this model, the variations of the dust ratio are very small. Therefore, in absence of coagulation, one may expect that a standard MRN distribution appears to remain extremely well preserved during the protostellar collapse at all scales.

To investigate an intermediate scenario, I now focus on the 100MICMRN model. I do not show the density maps in this case due to their strong resemblance with the MRN case. The PDFs of the dust ratio enrichment $\log(\bar{\epsilon})$ in the core and fragments, the disk and the envelope at $t_{\rm core}$ + 2 kyr are shown in figure 4.13. In this case, the variations of dust ratio are more significant than in MRN. However, compared to the MMMRN case, these variations still remain quite small. The average dust-to-gas ratio is 1.06% in the core and the disk and 0.99% in the envelope. The typical standard deviation for the dust-ratio enrichment are 7×10^{-3} in the core, 2.2×10^{-2} in the disk and 7.8×10^{-2} in the envelope. This confirms that the larger the grains are, the more significant the decoupling with the gas is. Note that, for 100MICMRN, it is reasonable to infer the gas density from the dust.

Thermal-to-gravitational energy ratio

The free-fall timescale depends on the ratio between the thermal and the gravitational energy. I therefore present in this section MMMRNA0.25, a model similar to the reference case but with $\alpha = 0.25$. This parameter is expected to affect strongly the dust dynamics. A lower value of α produces faster protostellar collapses prior to the first core formation due to the smaller thermal support. It thus develops faster high densities regions where dust strongly couples. In addition, a cloud with a smaller α has a smaller initial Stokes number, which means that the dust is also

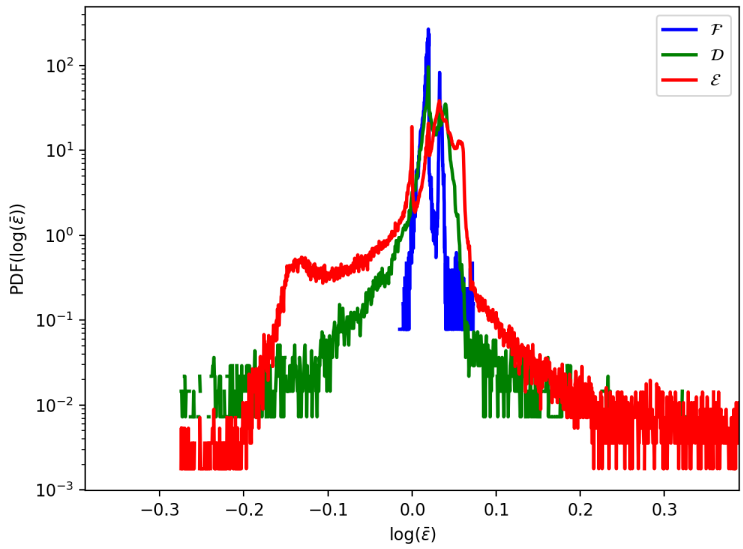

Figure 4.13: 100MICMRN test at $t_{\rm core}$ + 2 kyr. Probability density function (PDF) of the total dust ratio enrichment $\log(\bar{\epsilon})$ in the core and the fragments, the disk and the envelope. Dust is a relatively good tracer for the gas although significant variations of the dust-to-gas are observed.

initially better coupled with the gas. The post-core evolution of MMMRNA0.25 is different than in MMMRN in virtue of a smaller initial disk radius. Smaller disk with a smaller initial value of α are expected as shown by Hennebelle et al. (2016) (their equation (14)).

Figure 4.14 shows the densities of the gas (left) and the least coupled dust species (right) at $t_{\rm core}$ + 2 kyr for MMMRNA0.25. Apart from the outer regions that are quite depleted in dust content, we do not see any significant difference between gas and dust. Indeed, the core forms quickly, leaving no time for the differential motion between gas and dust to develop. For a comparison with the fiducial case, I show in figure 4.15 the probability density function of the dust ratio enrichment $\log(\bar{\epsilon})$ in the core and the fragments, the disk and the envelope at $t_{\rm core}$ + 2 kyr. The PDFs are much more peaked in MMMRNA0.25 than in MMMRN. The values of the standard deviation of the dust-ratio enrichment are 2×10^{-2} in the FHSC and fragments, 3×10^{-2} in the disk and 0.1 in the envelope. This was actually expected as the initial Stokes number scales as $\alpha^{2/3}$ and is thus ≈ 0.6 times smaller in MMMRNA0.25 than in MMMRN.

Magnetic fields

I now consider the dynamics of neutral grains in collapsing magnetized clouds. The two models are performed with the same parameters as MMMRN but with an initial magnetic field given by $\mu = 5$ and a tilt of 40°. For MMMRNMHD I use an ideal MHD solver and for MMMRNNIMHD I consider ambipolar diffusion.

Figures 4.16 and 4.17 show the densities for the gas (left) and the least coupled dust species (right) at $t_{\rm core}$ + 2 kyr for the two models MMMRNMHD and MMMRNNIMHD respectively. For both models, the dust is significantly decoupled from the gas and the settling in the core/disk/pseudo-disk is very efficient. As in MMMRN, dense regions (disk, core, pseudo-disk and high density regions of the outflow) are prone to be enriched in solid particles while low density regions are depleted (envelope and low density regions of the outflow). I note that the decoupling is slightly more efficient in these models than in MMMRN. This is mostly due to the 10 kyr difference in free-fall timescale. Although additional decoupling terms due to the magnetic field appear in

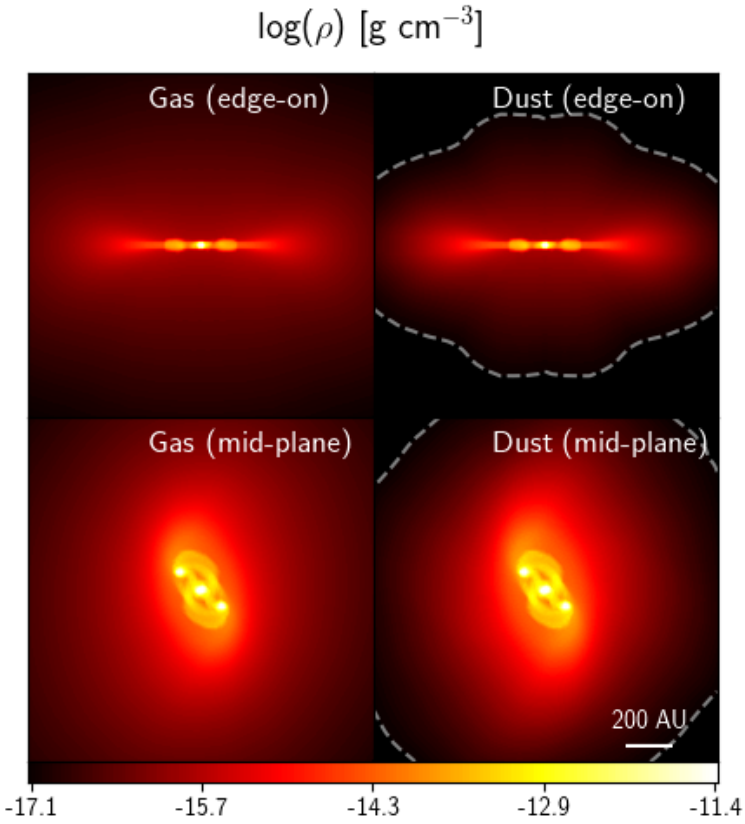

Figure 4.14: MMMRNA0.25 test at $t_{\rm core}$ + 2 kyr ($t_{\rm core}$ = 23 kyr). Edge-on (top) and mid-plane (bottom) cuts of the gas density (left) and dust density of the least coupled species (right). Dust has less time to significantly decouple from the gas than in the MMMRN case. A strong dust depletion is observed in the envelope.

the dust differential velocity ($\propto \mathbf{J} \times \mathbf{B}$) those are negligible compared to the hydrodynamical terms ($\propto \nabla P_{\rm g}$) in the decoupling of gas and dust in my magnetised collapse models.

I show in figure 4.18 and 4.19 the PDF of the dust ratio enrichment for the different objects at $t_{\rm core}$ + 2 kyr for the MMMRNMHD and MMMRNNIMHD runs, respectively. Although the shapes of the distributions are different from my fiducial case, I essentially reach to the same conclusion that is a peaked distribution with a significantly large average, indicating a strong initial enrichment, in the [core+disk] system and a broad distribution in the envelope. Note that the average dust-to-gas ratio in the disk and the core are higher in these two models than in the fiducial case. I indeed measure an average dust-to-gas ratio of $\sim 2.2 - 2.3\%$ in the disk and the first hydrostatic core for these models. In these magnetic runs, the pinching of the magnetic field lines during the collapse produces a pseudo-disk, which is a dense but not rotationally supported regions. These pseudo-disks have a very broad PDF and show enriched and depleted regions in both the ideal and non-ideal cases. A similar behavior is observed in the magnetically driven outflow for the ideal case, that are dust-rich in dense regions and depleted at low densities. In the MMMRNNIMHD, the outflow is less evolved and is mostly dust-depleted similarly to the envelope.

In summary, neutral dust dynamics in the presence of magnetic fields seems to follow the same general trend as in the hydrodynamical case. Dust collapses faster than the gas and is enriched in the inner regions of the collapse a few thousand years after the first core formation. This enrichment is mainly located in the pseudo-disk (only observed in the magnetized

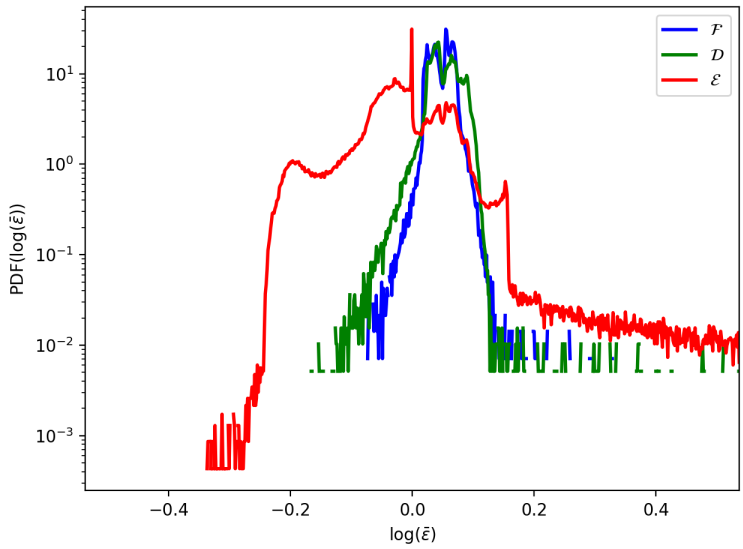

Figure 4.15: MMMRNA0.25 test at $t_{\rm core}$ + 2 kyr. Probability density function (PDF) of the total dust ratio enrichment $\log(\bar{\epsilon})$ in the core+fragments, the disk and the envelope. Dust is a relatively good tracer for the gas in the dense object although a notable depletion is observed in the envelope.

models), the disk, the first hydrostatic core. and the high density regions of the outflow.

4.6 Features of dusty collapses

I summarize here the properties of the dusty collapse in its different regions. Figure 4.20 shows the dust-to-gas ratio enrichment averaged in mass as a function of the grain size for all the models and all the objects defined in section 4.3.4. I refer to the dashed horizontal line as the enrichment line. If an object lies above it, it is enriched in dust during the collapse. If it lies under, it is dust depleted. This information is collected in table 4.3.

4.6.1 Core and fragments

Here, I detail the dust and gas properties in the first hydrostatic core and the fragments. In every model, we observe a value of $\langle \Theta_{d,k\leq 6} \rangle_m$ that remains unchanged for all the cores and fragments. Indeed, small grains have short stopping times and remain very well coupled to the gas all along the collapse. Simulations with the largest maximum grain size ($S_{\rm max}$ = 0.1 µm) have the largest dust enrichment. On the contrary, for the MRN model, the dust-to-gas ratio preserves its initial value in all the fragments. Moreover, the dust distribution itself remains extremely well preserved. In the MMMRNA0.25 case, the enrichment of the largest dust grains is much less efficient than in MMMRN. This is explained by a shorter free-fall timescale and higher initial densities, which implies smaller initial Stokes numbers. In MMMRN MMMRNA0.25 and 100MICMRN, the fragments have larger enrichment in large grains ($k > 6$, see table 4.2 for the corresponding grain sizes) . For example, in the MMMRN case, the dust-to-gas ratio of the 160 µm grains is enriched by a factor of ≈ 2.6 in the central object, and ≈ 3 in the fragments. Note that the dust-to-gas ratio enrichment of the first hydrostatic core is stronger in simulations that include magnetic fields than in MMMRN. As explained before, magnetic fields bring an additional decoupling in the case of neutral grains which explains in part why the dust enrich-

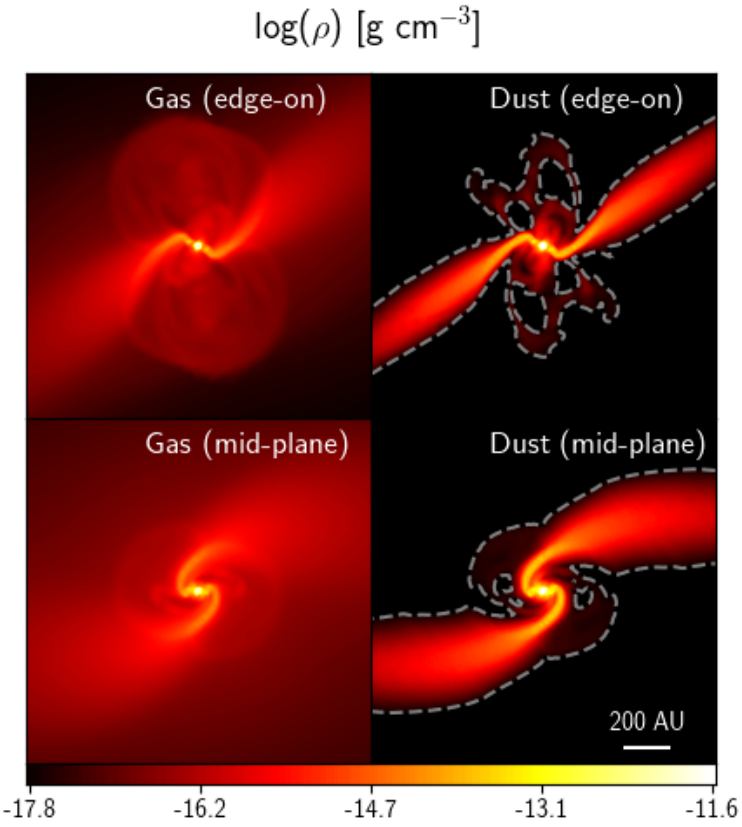

Figure 4.16: MMMRNMHD at $t_{\rm core}$ + 2 kyr ($t_{\rm core}$ = 81.1 kyr). Edge-on (top) and mid-plane (bottom) cuts of the gas density (left) and dust density of the least coupled species (right). Dust is significantly decoupled from the gas and concentrate in the high density regions such as the core, the disk, the pseudo-disk and the inner regions of the outflow.

ment is even stronger in MMMRNMHD and MMMRNNIMHD than in MMMRN. More importantly, the collapse is longer for these models due to the magnetic support. This leaves more time for dust grains to enrich the central regions. For the fragmenting cases, I note a preferred concentration of dust in the fragments that can be explained by two mechanisms. First, fragments form after the central object and thus stay a longer time in the isothermal phase where dust is less coupled since the temperature is smaller. Second, the dust-rich spiral arms developing through the envelope (see figures 4.8) are mainly accreted by the fragments (see figure 4.10). This provides an additional channel to enrich the fragments in solids.

4.6.2 Disks

I review the disk properties of all the models at $t_{\rm core}$ + 2 kyr . Essentially, the values are similar to what is measured in the cores. This is essentially caused by the fact that the dust enrichment happens prior to core formation at low densities (see figure 4.10). I measure a total dust-to-gas ratio enrichment of $\sim$ 1.75 in MMMRN, $\sim$ 1 in MRN, $\sim$ 1.1 in 100MICMRN, $\sim$ 1.1 in MMMRNA0.25, $\sim$ 2.3 in MMMRNMHD and $\sim$ 2.1 in MMMRNNIMHD. I emphasize once again that the decoupling between the gas and the dust depends strongly on the initial properties of the cloud. Note that in MMMRN the dust ratio is highly non-uniform in the disk (see figures 4.7 and 4.8 for the MMMRN case) or even constant (see figure 4.10). As explained in section 4.5.1, there is a decrease of $\sim$ 22% of dust-to-gas ratio in MMMRN between $t_{\rm core}$ and $t_{\rm core}$ + 4 kyr.

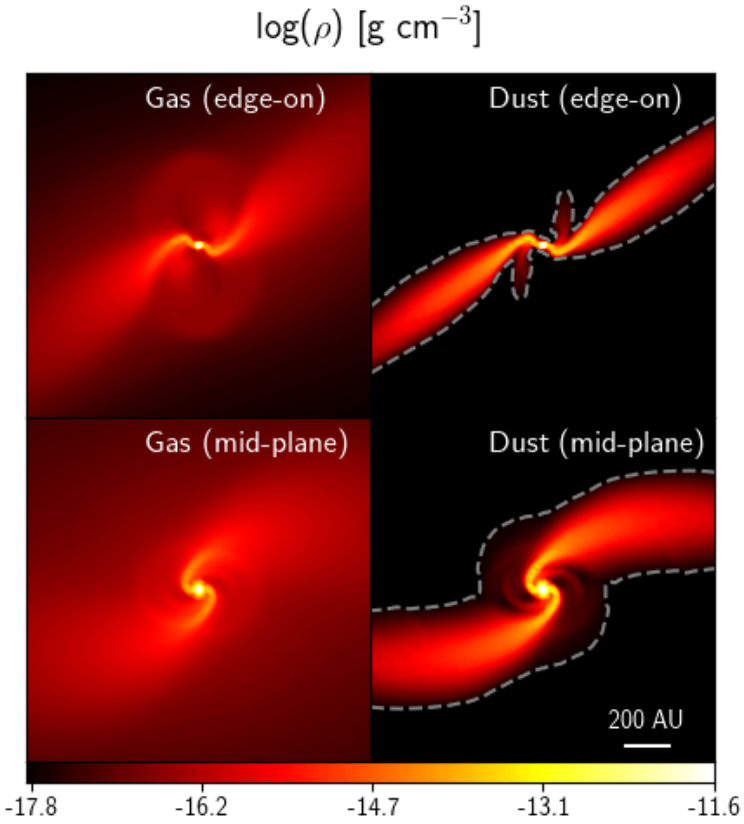

Figure 4.17: MMMRNNIMHD at $t_{\rm core}$ + 2 kyr ($t_{\rm core}$ = 81.1 kyr). Edge-on (top) and mid-plane (bottom) cuts of the gas density (left) and dust density of the least coupled species (right). As in the ideal case, dust is significantly decoupled from the gas and concentrate in the high density regions such as the core, the disk, the pseudo-disk and the inner regions of the outflow
.

This is most likely due to the fact that the disk is accreting dust depleted material from the envelope. In addition, since dust drifts toward pressure bumps – or regions where $\mathbf{J}\times\mathbf{B} \sim \nabla P_{\rm g}$ for magnetic runs – dust cannot always be used as a direct proxy to trace the gas density. Although, as shown in figure 4.9, the sub-structures seen in the dust originate from the ones in the gas, they may have very distinct morphologies. This is similar to what is found for T-Tauri disks, where gaps could be opened in the dust only (Dipierro & Laibe, 2017). Once again, simulations with magnetic fields show a more significant dust enrichment because of the longer timescale of the collapse. Note that the disk masses are however much smaller in the two models where magnetic braking occurs. Indeed, longer integration time is required for the disk to grow significantly (Hennebelle et al., 2020).

4.6.3 Pseudo-disks

In this section, I describe the principal features of the dusty pseudo-disks that are observed in the two magnetic runs MMMRNMHD and MMMRNNIMHD. These pseudo-disks are strongly enriched with a total dust-to-gas ratio enrichment of ∼ 2 for both cases (see values in table 4.3). Interestingly, the pseudo-disk is generally more enriched in smaller grains (up to 47 µm grains) than the other objects. This is due to two effects. First, the pseudo-disk is less dense than the central regions of the collapse, namely the disk and the core. This explains why smaller grains

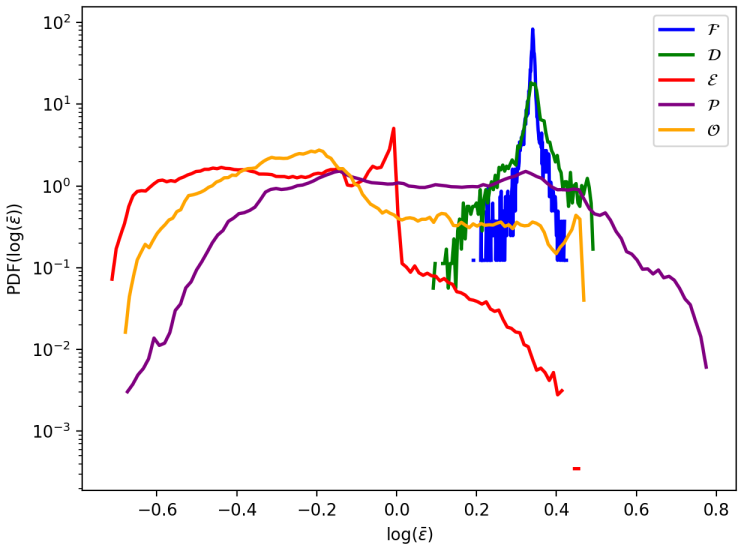

Figure 4.18: MMMRNMHD test at t_{core} + 2 kyr. Probability density function (PDF) of the dust ratio enrichment log($\bar{\epsilon}$) in the core (blue), the disk (green) the pseudo-disk (purple), the outflow (orange) and the envelope (red). Dust is not a good tracer for the gas here and the dust distribution is not uniform in the considered objects.

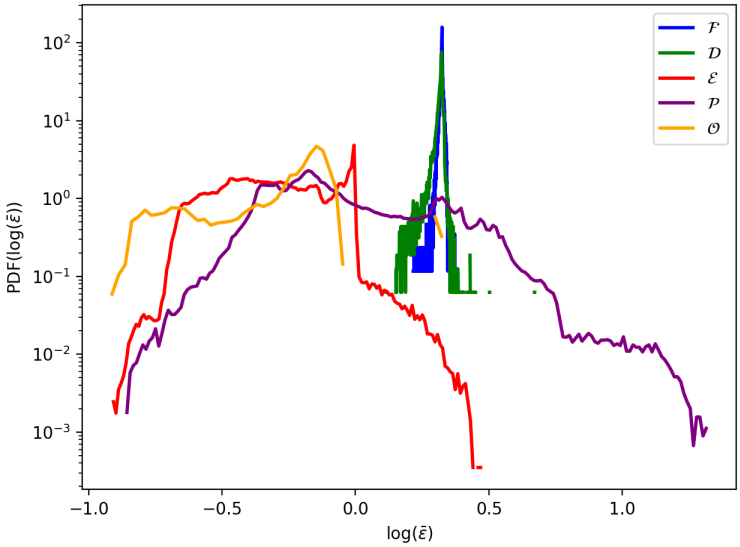

Figure 4.19: MMMRNNIMHD test at t_{core} + 2 kyr. Probability density function (PDF) of the dust ratio enrichment log($\bar{\epsilon}$) in the core (blue), the disk (green) the pseudo-disk (purple), the outflow (orange) and the envelope (red). Dust is not a good tracer for the gas here and the dust distribution is not uniform in the considered objects.

are more easily drifting towards it. Second, the strong pressure gradient orthogonal to the pseudo-disk generates a drift from the envelope towards it, even for small grains. Once these grains have reached the pseudo-disk, they couple strongly to the gas while larger grains are able to drift to even deeper regions such as the disk and the core.

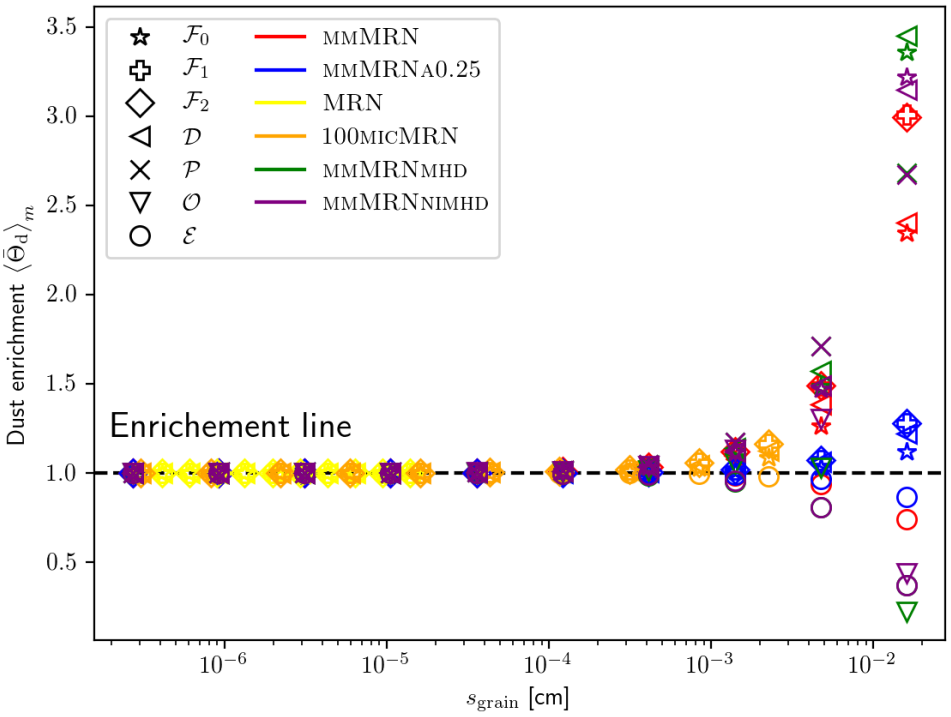

Figure 4.20: All the models at $t_{core}+2$ kyr. The dust-to-gas ratio enrichment averaged in mass is shown as a function of the grain size for all the objects. Grain with sizes smaller than 10^{-4} cm are almost always perfectly coupled with the gas. For larger sizes, the enrichment is model dependent. Grains with typical sizes larger than 10^{-3} cm decouple from the gas. Dense objects such as the fragments $\mathcal{F}$ or the disk $\mathcal{D}$ and pseudo-disk $\mathcal{P}$ are enriched in dust. Low density objects such as the envelope $\mathcal{E}$ or the outflows $\mathcal{O}$ are depleted in dust. Magnetized models exhibit the stronger decoupling between the gas and the dust.

4.6.4 Outflows

I now describe the major features of the dusty outflows that can be observed in the two magnetic runs MMMRNMHD and MMMRNNIMHD. For MMMRNMHD, figure 4.21 shows the relative variations of the dust ratio at three different times, for the 47 µm (left) and 160 µm (right) grains (9th and 10th bins), respectively. The magenta arrows represent the differential velocity with the barycenter. These two dust species have a completely different evolution. Indeed, the outflow does not carry a significant quantity of 160 µm grains at t_{core} + 2 kyr because they are already strongly depleted in low density regions. Subsequently, the outflow is strongly depleted in these species with $\left\langle \bar{\Theta}_{d,10} \right\rangle_m \sim 0.22$ for MMMRNMHD and $\left\langle \bar{\Theta}_{d,10} \right\rangle_m \sim 0.44$ for MMMRNNIMHD. On the contrary, 47 µm grains are significantly enriched by a factor 1.04-1.28 at that time. Initially, the outflow is not powerful enough to eject matter from then inner regions and rather collects the grains from the envelope. This explains why the enrichment measured in the outflow are similar to those measured in the envelope. Interestingly at t_{core} + 2 kyr, we see that the outflow is well established and starts to carry the inner regions that are denser and more enriched in 160 µm grains. This indicates that outflows provide a channel to re-enrich the envelope in large grains.

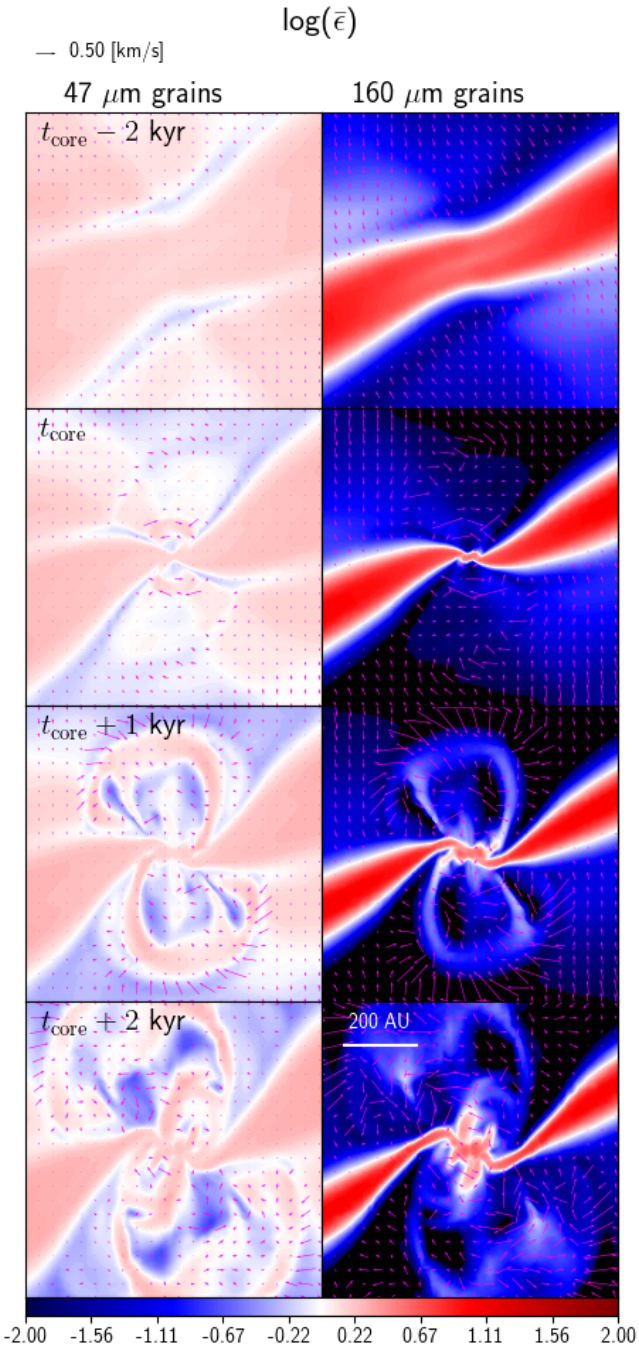

Figure 4.21: mmMRNmhd. Edge-on view of the relative variations of the dust ratio at four different times for the 47 µm (left) 160 µm grains (right). The magenta arrows represent the differential velocity with the barycenter. Regions that are dust depleted of more than two orders of magnitude are not displayed (black background).

4.6.5 Envelope

In general, the envelope is dust depleted owing to mass conservation since the inner part are enriched. For all the models, the small dust grains (with $k \leq 6$) do not experience significant dust-to-gas ratio variations. Larger grains can however show significant dust-to-gas ratio variations. I measure a value of $\langle \Theta_{d,10} \rangle_m$ as low as 0.38 for mmMRNnimhd and mmMRNmhd, and 0.73 for mmMRN. This values are averaged over all the envelope, but contrary to the core and fragments, the envelope is very contrasted in terms of density. Among all objects (pseudo-disk excluded), the envelope is experiencing the larger dust-to-gas ratio variations (see for example figures 4.7 and 4.19). This is expected since the density in the envelope is lower than in the other objects. Typically, the depletion in large grain of the envelope increases with a decreasing density and have a larger dust content in their inner regions (see figure 4.21 for both behavior).

I have shown that dust is not necessarily a good tracer for the gas density, i.e. I find important local variations in the dust distribution in mmMRN, mmMRNmhd, mmMRNnimhd. This has strong consequences for observations, since dust continuum radiation fluxes depend on densities integrated along the line of sight. It is therefore interesting to estimate error that arises when the total column density is estimated from the mass of a single dust bin k. I compute this error Err_k from the total column density and the dust column density $\Sigma_{\mathrm{d},k}$ according to

$$\mathrm{Err}_k \equiv \frac{\Sigma - \Sigma_{\mathrm{d},k}/\epsilon_{k,0}}{\Sigma}. \tag{4.23}$$

The total error Err is defined the same way but using the total dust column density and initial dust ratio.

Figure 4.22 shows an edge-on view of the total column density Σ (top), the total error Err (middle) and the error estimated by using the largest grains only – 160 µm in this case (bottom) for the mmMRNnimhd model 2 kyr after the formation of the first core. The error is large when considering either all the grains (middle) or only the largest ones (bottom). Note that the total column density inferred from the total dust mass would be underestimated in the upper layers and overestimated in the inner regions because dust drifts toward the center of the collapse. The effect is maximal for the largest grains, where the error can reach values as high as $\sim 250\%$ in the inner envelope.

4.7 Estimate of the dust enrichment

Here, I provide a semi-analytic estimate of the dust enrichment occurring during the protostellar collapse. I use it to infer the typical minimal Stokes number above which a given dust enrichment can be reached.

4.7.1 Enrichment equation

In the terminal velocity approximation, and making the assumption that the collapse is is isothermal and purely hydrodynamical, the evolution of the dust ratio for a species k is given by

$$\frac{\mathrm{d}\epsilon_k}{\mathrm{d}t} = -\frac{1}{\rho}\nabla \cdot \left[\epsilon_k \left(\frac{t_{\mathrm{s},k}}{1-\epsilon_k} - \sum_{j=1}^{\mathcal{N}} \epsilon_j \frac{t_{\mathrm{s},j}}{1-\epsilon_j} \right) c_{\mathrm{s}}^2 \nabla\rho \left(1 - \sum_{i=1}^{\mathcal{N}} \epsilon_i \right) \right]. \tag{4.24}$$

To provide analytical estimates of dust-ratio enrichment during the collapse, I now neglect the cumulative back-reaction of dust onto the gas. When the cumulative back-reaction is negligible,

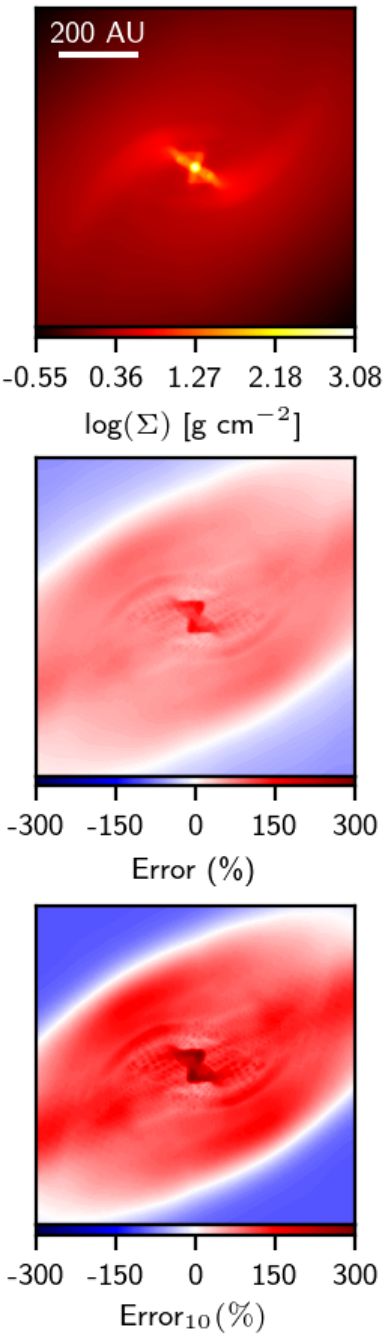

Figure 4.22: MMMRNMHD at $t_{\rm core}$ + 2 kyr. Edge-on view of the total column density log(Σ) (top), the total error Err (middle) and the error when using the largest grains only – 160 μm in this case (bottom).

the evolution of $\bar{\epsilon} = \frac{\epsilon}{\epsilon_0}$ and ϵ are constrained by the same equation, i.e. $\bar{\epsilon}$ does not depend on ϵ_0. The dust ratio enrichment is described by the equation

$$\frac{\mathrm{d}\bar{\epsilon_k}}{\mathrm{d}t} = -\frac{1}{\rho}\nabla \cdot \left[\bar{\epsilon_k} t_\mathrm{s} c_\mathrm{s}^2 \nabla\rho\right]. \tag{4.25}$$

where $\frac{\mathrm{d}}{\mathrm{d}t} \equiv \frac{\partial}{\partial t} + \mathbf{v}\cdot\nabla$. I now use the dimensionless variables

$$\tau = \frac{t}{\tau_{\mathrm{ff},0}} \text{ and } x = \frac{r}{\lambda_{\mathrm{J},0}},$$

where $\tau_{\mathrm{ff},0} = \sqrt{\frac{1}{\mathcal{G}\rho_0}}$ and $\lambda_{\mathrm{J},0} = c_\mathrm{s}\tau_{\mathrm{ff},0}$. Equation (4.25) becomes

$$\frac{\mathrm{d}\bar{\epsilon_k}}{\mathrm{d}\tau} = -\mathrm{St}_{k,0}\frac{1}{\bar{\rho}}\nabla_x \cdot \left[\bar{\epsilon_k}\bar{\rho}^{-1}\nabla_x\bar{\rho}\right], \tag{4.26}$$

where $\bar{\rho} = \frac{\rho}{\rho_0}$. The term $\bar{\rho}^{-1}$ appears in the divergence owing to $t_{\mathrm{s},k} \propto \frac{1}{\rho}$.

4.7.2 Semi-analytical model

Neglecting local variations of $\bar{\epsilon}$ in comparison with local density variations yields

$$\frac{\mathrm{d}\bar{\epsilon_k}}{\mathrm{d}\tau} \simeq -\mathrm{St}_{k,0}\bar{\epsilon_k}\frac{1}{\bar{\rho}}\nabla_x \cdot \left[\bar{\rho}^{-1}\nabla_x\bar{\rho}\right]. \tag{4.27}$$

I then obtain

$$\bar{\epsilon}\,(x,\tau) = \chi^{\mathrm{St}_{k,0}}, \tag{4.28}$$

where $\chi \equiv e^{-\int_0^\tau \nabla_x(\bar{\rho}^{-1}\nabla_x\bar{\rho})/\bar{\rho}\mathrm{d}\tau}$ is independent of the dust properties. Hence, at a given time and position, the dust enrichment varies essentially exponentially with the initial Stokes number. A proper mathematical estimate of the integral quantity will be investigated in the future.

4.7.3 Estimate in the core

We can roughly approximate χ in the core and after a free-fall time $t_{\mathrm{ff},0} = \sqrt{\frac{3\pi}{32}}\tau_{\mathrm{ff},0}$. An order of magnitude estimate provides

$$|\ln(\chi)| \approx \sqrt{\frac{3\pi}{32}}\frac{c_\mathrm{s}^2}{\mathcal{G}\rho_\mathrm{ad} r_\mathrm{var}^2}, \tag{4.29}$$

where r_var is the typical length at which variations of density become significant. Above ρ_ad, the temperature are high and the gas and dust differential dynamics is negligible. A reasonable choice for $\bar{\rho}$ is therefore $\bar{\rho} = \frac{\rho_\mathrm{ad}}{\rho_0}$. In the typical condition of a protostellar collapse, one obtains

$$|\ln(\chi)| \approx 126\left(\frac{r_\mathrm{var}}{1\ \mathrm{AU}}\right)^{-2}\left(\frac{T_\mathrm{gas}}{10\ \mathrm{K}}\right). \tag{4.30}$$

Taking $r_\mathrm{var} = 1$ AU seems reasonable as it is about a tenth of the first-core radius in my models. For $r_\mathrm{var} \approx 5$ AU, I find that $|\ln(\chi)| \approx 5$. The value of χ strongly depends on the steepness of the pressure gradients, hence on r_var. This model only provides an rough estimate of $\bar{\epsilon}$ and should not replace either a numerical treatment of the dust or a proper estimate of χ during the collapse.

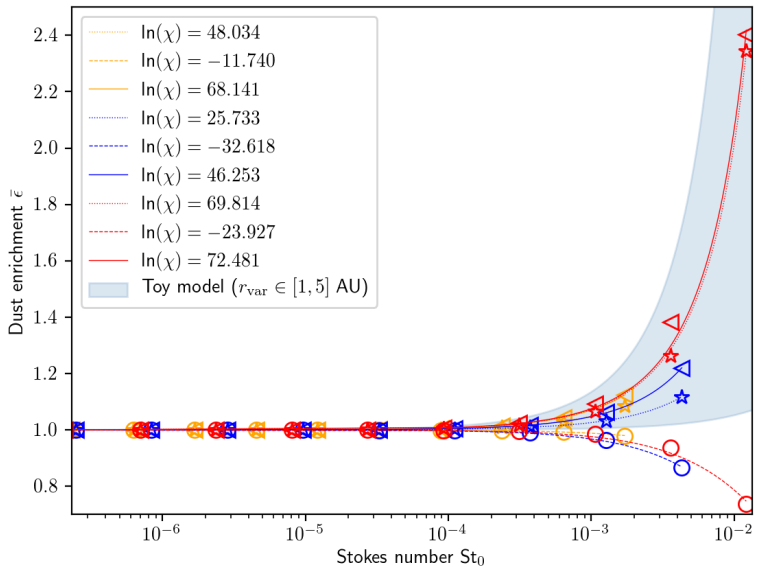

Figure 4.23: Semi-analytic and measured enrichment in my hydrodynamical models (MRN excluded) against the initial Stokes number. The lines represent the semi-analytical development using a best fit of χ for the FHSC (dotted), disk (solid) and envelope (dashed), respectively. The extreme values of the enrichment given by my toy model are delimited by the blue areas. The color coding and choice of markers is the same as in figure 4.20.

4.7.4 Comparison with the models

Figure 4.23 shows the dust ratio enrichment as a function of the initial Stokes number for MMMRN, MMMRNA0.25 and 100MICMRN for the first core, the disk and the envelope. The dashed, dotted and solid lines represent the values obtained with equation (4.28) by fitting the values of χ. Finally, the blue area represents the range of dust enrichment obtained with the two extreme values of χ estimated in the previous section. I do not show the dust enrichment for MRN as it is clearly negligible (see figure 4.20). In addition, I do not display the enrichment in the secondary fragments for the sake of readability.

A fairly good agreement between the fits and the measured dust ratio enrichment is observed in all the regions, especially in the cores. This suggests that the enrichment indeed mostly varies exponentially with the initial Stokes number. We do observe small deviations in the disk and the envelope for MMMRN. The non-linear behaviour of equation (4.24), either due to local variations of ϵ or the cumulative back-reaction of dust on the gas is therefore not completely negligible. In appendix 4.11, I show that the dust-to-gas variations induced by the dust back-reaction are almost negligible and that the discrepancy with the exponential increase of the dust ratio observed is most likely caused by local variation of dust-to-gas ratio, e.g the mixing between depleted material of the envelope and dust rich material from the disk.

Finally, I emphasize that the dust enrichment in all the cores is comprised between the lowest and highest value estimated with my toy-model. This model being quite crude, I acknowledge that it cannot compete with an eventual model based on an accurate estimate of χ.

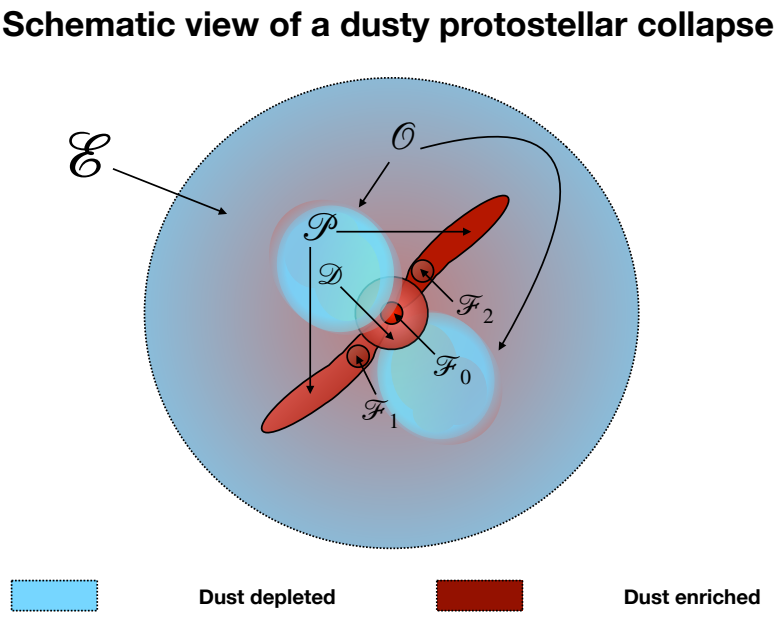

Figure 4.24: Schematic view of a dusty protostellar collapse. Blue regions are dust depleted and red regions are dust enriched. Typically, the outer regions of the envelope is depleted. The outflow, only observed in magnetic runs, is enriched on its surface and depleted elsewhere. Dense regions, such as the core and fragments $\mathcal{F}$ (the fragments are observed only in the hydrodynamical case), the pseudo-disk $\mathcal{P}$ (only in magnetic runs) and the disk $\mathcal{D}$ are generally enriched. The strength of dust decoupling depends on the initial choice of parameters such as the maximum grain size, the thermal-to-gravitational energy ratio or the presence of a magnetic field. This view of a dusty protostellar collapse is simplified and provides only a global sketch of the evolution.

4.7.5 Critical Stokes number

Assuming that the value of χ is known, it can be used to determine the critical Stokes number $\mathrm{St}_{\mathrm{crit},\bar{\epsilon}}$ above which some regions can reach a given enrichment $\bar{\epsilon}$. Equation (4.28) can indeed by inverted as

$$\mathrm{St}_{\mathrm{crit},\bar{\epsilon}} = \frac{\ln\bar{\epsilon}}{\ln\chi}. \tag{4.31}$$

Using the value of χ obtained by fitting my models (figure 4.23), we can estimate the typical Stokes numbers needed to get a dust enrichment by a factor of 2 in the core and the disk is approximately $\mathrm{St}_{\mathrm{crit},2} \sim 0.01 - 0.027$. With my toy model, I find $\mathrm{St}_{\mathrm{crit},2} \sim 0.006 - 0.13$. It is a significantly wider range but it contains what is measured with my models. Similarly, we can estimate that to get a dust ratio depletion of 50%, the grains must typically have $\mathrm{St}_{\mathrm{crit},1/2} \sim 0.027-0.11$. In short, it is easier to enrich the disk and the core than it is to deplete the envelope.

4.8 Discussion

4.8.1 Summary of the models

I investigated the effect of several parameters on the dust dynamics during the protostellar collapse such as the thermal-to-gravitational energy ratio α, the maximum grain size of the

dust distribution and the presence of magnetic fields. It appears that the first two parameters are critical for the development of a significant differential dynamics between the gas and the dust during the early phases of the collapse.

From MMMRN, MRN and 100MICMRN, I established that the maximum grain size is a critical parameter for the differential gas and dust dynamics. Typically, if the maximum grain size in the core is smaller than a few microns (see figure 4.20), I do not observe significant variations of the dust ratio. On the contrary, when larger grains are considered, the total dust ratio can increase by a factor of $2-3$, even in the very first thousands of years of the protostellar collapse (see MMMRN, MMMRNMHD or MMMRNNIMHD). Hence, in order to understand the initial dust and gas content of protoplanetary disks, it is crucial to measure accurately the dust size distribution in early prestellar cores. This conclusion is reinforced by recent observations (Galametz et al., 2019) or synthetic observations (Valdivia et al., 2019) that seem to probe the existence of ~ 100 µm exist in Class 0 objects.

For small initial values of α, e.g. in MMMRNA0.25, the collapse is fast and large grains do not have the time to significantly enrich the core and the disk in one free-fall timescale. Besides, as MMMRNA0.25 is set with a higher initial density, dust is initially more coupled with the gas in this particular model. I point out that the efficiency of the dust enrichment relies strongly on the lifetime of low densities regions (see figure 4.10) and on the range of densities experienced during the collapse (see section 4.3.4). Hence, although 100MICMRN has a smaller maximum grain size as MMMRNA0.25, both models have a similar total dust content by the end of the simulation as the free-fall timescale in 100MICMRN is longer. The initially properties of the cloud appear to be extremely important to quantify the evolution of the dust distribution during the protostellar collapse. It would be therefore interesting to study the dust collapse of a Bonor-Ebert sphere, since its free-fall timescale is usually longer than the one of the Boss and Bodenheimer test (Machida et al., 2014). I leave this proper comparison to further works.

With MMMRNMHD and MMMRNNIMHD, I investigated the effect of a magnetic field on the dynamics of dust during the protostellar collapse. I qualitatively find similar results as in my fiducial case. Quantitatively, the decoupling between the gas and the dust does however produce more significant variations of the dust-to-gas ratio in the magnetic case. The presence of a dense and stratified pseudo-disk strengthens the envelope and the outflow depletion. This pseudo-disk is consequently strongly enriched in solids. It is in fact almost as enriched as the disk and the first hydrostatic core. However it is much more massive than the disk by the end of the calculation. Therefore, understanding how the pseudo-disk is accreted by the core and the disk is of particular interest and future studies should focus on its long time evolution.

For the sake of summarizing, I show in figure 4.24 a schematic view of a dusty protostellar collapse a few kyr after the formation of the first hydrostatic core. The blue areas depict the dust depleted regions (low density regions of the envelope and outflow) and the red areas represent the regions enriched in dust (cores, disk high density regions of the envelope and outflow, and pseudo-disk). The intensity of the gas and dust decoupling depends naturally of the parameters that I presented earlier in this chapter. I emphasize that this cartoon illustration is only a simplified picture of a dusty protostellar collapse that does not account for the variability between the models and were I do not quantitatively show the local variations of the dust-to-gas ratio.

4.8.2 Comparison with previous works

My results are in qualitative agreement with the previous study of Bate & Lorén-Aguilar (2017), where a decoupling between gas and dust for grains larger than ≈ 100 µm was also identified. A main difference is that I do not obtain as large dust-to-gas ratio enhancements. Indeed, in Bate & Lorén-Aguilar (2017), the dust mass is distributed in a single bin of dust with mass of 1% of the mass of the gas. In my MULTIGRAIN simulations, only a fraction of the

dust mass lies in the largest grains, which provides, less significant dust-to-gas ratio variations as in Bate & Lorén-Aguilar (2017). This effect was predicted in Bate & Lorén-Aguilar (2017). I note that $\bar{\epsilon}$ only depends on the initial dust content via the cumulative back-reaction of the dust on the gas. If this back-reaction is neglected as in equation (4.25), the enrichment is independent from the initial value of the dust-to-gas ratio. This allows us a more direct comparison with Bate & Lorén-Aguilar (2017). In their study, they observe an increase of dust-to-gas ratio of about one order of magnitude for the 100 µm grains, which is about 3 times larger than what I observe in MMMRN for example. Using the calibrated value of χ and equation (4.28), we can estimate that the dust ratio enrichment of 100 µm for grains with $\rho_{\rm grain} = 3$g cm^{-3} would be ~ 2.27 in the first hydrostatic core. The difference with Bate & Lorén-Aguilar (2017) is likely due to their use of Bonor-Ebert spheres as initial conditions that have a longer free-fall timescale ($\sim$ 120 kyr) and because they have lower initial densities ($\sim 10^{-20}$ g cm^{-3})and therefore larger initial Stokes numbers (~ 1 for 100 µm grains). In 2D simulation of collapsing gravitoviscous protoplanetary disks, Vorobyov et al. (2019); Vorobyov & Elbakyan (2019); Elbakyan et al. (2020) have focused on the evolution of dust including grain growth and fragmentation. Similarly to my models, they observe local variations of the dust-to-gas ratio in the disks. They also found larger dust-to-gas ratios in the inner regions of the collapse and smaller dust-to-gas ratios a few hundreds of AU away from the core. In their high density clumps, they find dust-to-gas ratios between 1.7% and 2.3% which is quite similar to my findings. Locally, Vorobyov & Elbakyan (2019) observe particularly large increase of dust-to-gas ratio in density clumps, which is typically to what we observe in my secondary fragments.

In section 4.4, I performed three collapse simulations of non-rotating gas and dust mixture, considering only single dust species (1 µm, 10 µm and 100 µm). In this work, I already observed a significant decoupling occurring for 100 µm grains. However the increase of dust-to-gas ratio in the core was strong only in the outer regions of the collapse. As previously said, we can estimate that in MMMRN the dust-to-gas ratio enrichment of 100 µm would be about 2.27 for grains with $\rho_{\rm grain} = 3$ g cm^{-3}. It was only ~ 1.2 in my first non-rotating spherical collapse calculation, although both models have the same initial α. I interpret this result as an effect of rotation. Firstly, because it slows down the collapse (by a factor ~ 0.87 here), which leaves more time for the central regions to be enriched in dust. Secondly, because it generates steeper vertical pressure gradients which allows a more efficient settling of the dust grains. I do not aim to investigate the effect of the initial angular velocity in details since this was done by Bate & Lorén-Aguilar (2017). The initial angular velocity was found to simply enhance the differential gas and dust dynamics similarly to what the thermal-to-gravitational energy ratio would do. I choose not to explore the impact of grain density because the dependence of the Stokes number in this quantity is the same as for the grain size.

4.8.3 Possible implications for planet formation

The simulations presented in this study consolidate the idea that protostellar collapses may form protoplanetary disks containing $\epsilon_0 \gtrsim 2-3\%$ of their mass under the form of solids.

When the dust ratio ϵ_0 is larger than the square of the aspect ratio of the disk $\left(\frac{H}{r}\right)^2$ – even by a tiny amount, grain growth is expected to occur so efficiently that pebbles can decouple from the gas before drifting and falling onto the central star (Laibe, 2014). This condition is likely to be fulfilled as protoplanetary disks typically have $\left(\frac{H}{r}\right)^2 \simeq 0.01$ (Andrews et al., 2010). The former condition is strengthened by the fact that back-reaction may also inhibit radial-drift and vertical settling (e.g. Kanagawa et al. 2017; Dipierro et al. 2018a; Lin 2019), and holds until grains fragment. Two scenarios have been debated when fragmentation occurs. In the first scenario, grains may fall onto the central star if the disk does not contain a pressure trap

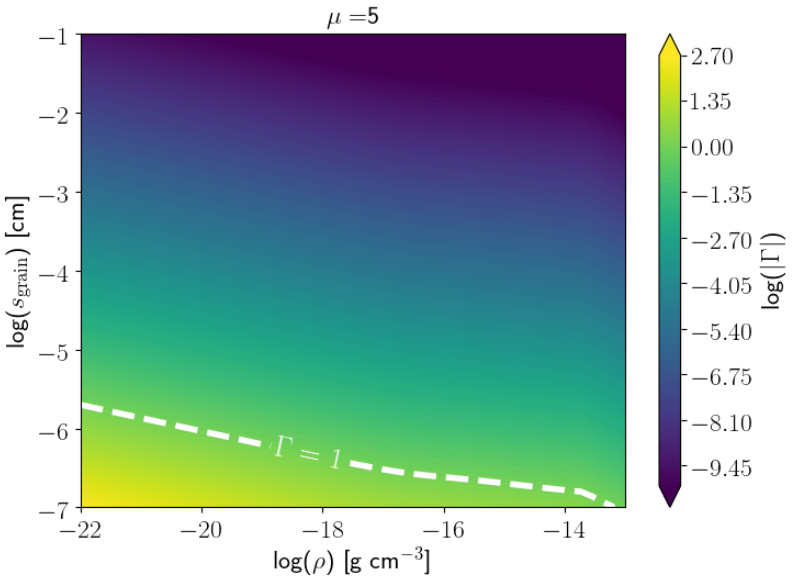

Figure 4.25: Hall factor as a function of the density and the grain size for $\mu = 5$ for negatively charged grains. The dashed line denotes the equality between the gyration and the stopping time.

(e.g. Brauer et al. 2008; Birnstiel et al. 2009). In the second one, dust may exert strong drag onto the gas and powers the development of self-induced dust traps (Gonzalez et al., 2017). The formation of these traps occurs when back-reaction dominates locally over gas viscosity, and may be extremely effective for $\epsilon_0 \gtrsim 2-3\%$. In any case, large dust contents favour the formation of planetesimals through the development of the streaming instability (e.g. Johansen et al. 2007, 2009; Drążkowska et al. 2016). This instability may be even more effective when it develops through unstable epicyclic modes (Jaupart & Laibe, 2020), although peculiar dust distributions may quench it (Krapp et al., 2019). As argued by Vorobyov & Elbakyan (2019), dust-rich density clumps, similar to the secondary cores in my fragmenting models, could be a favored locus of giant planet formation. They indeed noted both the piling-up of large grains and important growth in these clumps.

In short, a larger initial dust content always favour planet formation in disks, and this may be in a dramatic manner. A quantitative knowledge of the differential dynamics of gas and dust during the protostellar collapse and the initial dust size distribution in prestellar cores therefore appears essential to understand the early stages of planet formation. In that perspective, an extensive study of dust dynamics and coagulation/fragmentation should be done from the scales of molecular clouds and, through the protostellar collapse, up to protoplanetary disks.

4.8.4 Neutral grains approximation

Grains are likely to be significant or even the main charge carriers during the protostellar collapse (Umebayashi & Nakano, 1990; Marchand et al., 2016). Charged dust fluids feel the Lorentz drag $\mathbf{f}_{\mathrm{L},k}$ in addition to the Epstein drag. The expression of this force is

$$\mathbf{f}_{\mathrm{L},k} \equiv \frac{3Z_k e}{4\pi\rho_{\mathrm{grain},k} s_{\mathrm{grain},k}^3} \left(\mathbf{E} + \mathbf{v}_k \times \mathbf{B}\right), \tag{4.32}$$

where Z_k is the number of charges on the dust grain k, e the electron charge and $\mathbf{E}$ is the electric field. The gyration time of a grain is expressed as

$$t_{\mathrm{gyr},k} = \frac{4\pi\rho_{\mathrm{grain},k}\, s_{\mathrm{grain},k}^3}{3Z_k e|\mathbf{B}|}. \tag{4.33}$$

A grain subject to a significant Lorentz drag could preferentially couple to the magnetic field rather than the gas. In addition, by controlling the Ohmic, ambipolar and Hall resistivities (Kunz & Mouschovias, 2009), charged grains most likely affect the magnetic and electric fields evolution. To compare the magnetic and neutral drags strength, it is interesting to compare the stopping-to-gyration time ratio also known as Hall factor Γ_k. In the Epstein regime, this ratio writes

$$\Gamma_k \equiv \sqrt{\frac{9\gamma}{128\pi}} \frac{Z_k e|\mathbf{B}|}{\rho c_\mathrm{s} s_{\mathrm{grain},k}^2}. \tag{4.34}$$

To model the Hall factor in a collapsing core, I consider a gas with a barotropic equation of state with $T_\mathrm{g} = 10$ K, an adiabatic index $\gamma = 5/3$ and negatively charged grains. The grain charge computation follows Wurster et al. (2016) and is detailed in Appendix 4.A. I use simple assumptions for the magnetic field, stating that

$$|\mathbf{B}| = \min\left(B_0\left(\frac{\rho}{\rho_0}\right)^{2/3}, 0.1\mathrm{G}\right), \tag{4.35}$$

where B_0 is the initial magnetic field, given by μ and ρ_0 the initial core density. The magnetic threshold at 0.1 G is imposed to reproduce the plateau systematically observed when considering ambipolar diffusion Masson et al. (2016); Hennebelle et al. (2016); Vaytet et al. (2018a). One can then show that

$$\Gamma_k = \sqrt{\frac{9\gamma}{128\pi}} \frac{Z_k e}{\rho c_\mathrm{s} s_{\mathrm{grain},k}^2} \min\left(\frac{{M_0}^{1/3}}{\mu\left(\frac{M_0}{\Phi}\right)_\mathrm{c}}\left(\frac{4\pi\rho}{3}\right)^{2/3}, 0.1\mathrm{G}\right). \tag{4.36}$$

Figure 4.25 shows the absolute value of the Hall factor as a function of the density and the grain size. For a wide range of grain sizes, the Hall factor is always much smaller than unity. These grains can therefore be considered neutral at least dynamically. I note that Γ_k is larger than unity for very small grain ($s_{\mathrm{grain},k} \lessapprox 10^{-6}$cm). These grains are very well coupled the the gas in the neutral case but, when charged, could experience a strong decoupling with the neutrals. This would occur if the latter are decoupled from the magnetic field e.g., in the non-ideal regime. The Lorentz drag might play a crucial role for the dynamics of very small grains in star formation but is probably not very important for the large grains that I observe to decouple in my models. Efforts to study the dynamics of such grains have been made in the past (Guillet et al., 2007; Hopkins & Squire, 2018) and should be extended to dusty collapses in future studies. I emphasize that the electromotive term in the Lorentz force applies only on the charged species and not the barycenter and might play a very important role in the decoupling between the charged grains and the neutrals (barycenter) even when $\Gamma_k < 1$.

4.8.5 Caveat: Coagulation/fragmentation during the collapse

Dust coagulation has been neglected during this study. It may however affect strongly dust evolution during the collapse since dust decoupling depend on grain sizes. Following Draine

(1985), one can estimate the coagulation timescale $t_{\mathrm{coag},i,j}$ between two dust phases i and j due to their relative motion within the collapsing clouds as

$$t_{\mathrm{coag},i,j} = \left[\frac{3}{4} \rho_i \frac{(s_{\mathrm{grain},i} + s_{\mathrm{grain},j})^2}{\rho_{\mathrm{grain},i} s_{\mathrm{grain},i}^3} |\mathbf{v}_i - \mathbf{v}_j| \right]^{-1}. \tag{4.37}$$

Assuming the same density for all the grains, neglecting cumulative back-reaction effects and magnetic fields, and considering an isothermal collapse, differential velocities can be estimated from the diffusion approximation as

$$|\mathbf{v}_i - \mathbf{v}_j| \sim \rho_{\mathrm{grain}} |s_{\mathrm{grain},i} - s_{\mathrm{grain},j}| c_{\mathrm{s}} \frac{|\nabla \rho|}{\rho^2}. \tag{4.38}$$

As said in section 4.3.4, the density profile of the free-falling material can be approximated as a power law with an exponent $\zeta = -2$ (Larson, 1969). In this case, one obtains at a distance r from the central region

$$t_{\mathrm{coag},i,j} = \left[\frac{3|\zeta|}{4r} \epsilon_i (1 + q_{i,j})(1 - q_{i,j}^2) c_{\mathrm{s}} \right]^{-1}. \tag{4.39}$$

where $q_{i,j} \equiv \frac{s_{\mathrm{grain},j}}{s_{\mathrm{grain},i}}$ is the ratio between the grain sizes. In the limit $q_{i,j} \ll 1$, I find

$$t_{\mathrm{coag},i,j} \sim 170 \text{ kyr} \left(\frac{\epsilon_j}{10^{-2}} \right)^{-1} \left(\frac{r}{100 \text{ AU}} \right) \left(\frac{c_{\mathrm{s}}}{0.19 \text{ km s}^{-1}} \right)^{-1}. \tag{4.40}$$

Growth induced by the relative dynamics between dust grains is therefore expected to be not very efficient during protostellar collapse away from the core but could be non-negligible in the inner regions. At $r = 10$ AU, $t_{\mathrm{coag},i,j} \sim 17$ kyr, which is quite smaller than the typical free-fall timescale of a prestellar core.

I note that growth could also be enhanced by the turbulence, the Brownian motions of dust grains or focalization due to grain charges (Blum & Wurm, 2008). In the case of Brownian motions, for example, assuming that the grain temperature is equal to the gas temperature, the differential velocity for two grains of different mass can be expressed as (Birnstiel et al., 2016)

$$|\mathbf{v}_i - \mathbf{v}_j| = \sqrt{\frac{8 k_{\mathrm{B}} T_{\mathrm{g}}}{\pi}} \sqrt{\frac{m_{\mathrm{grain},i} + m_{\mathrm{grain},j}}{m_{\mathrm{grain},i} m_{\mathrm{grain},j}}}, \tag{4.41}$$

hence, assuming again that $q_{i,j} \ll 1$ the coagulation timescale writes as

$$t_{\mathrm{coag},i,j} = \left[\frac{3}{4} \rho_i \frac{1}{\rho_{\mathrm{grain},i} s_{\mathrm{grain},i}} \sqrt{\frac{8 k_{\mathrm{B}} T_{\mathrm{g}}}{\pi m_{\mathrm{grain},j}}} \right]^{-1}, \tag{4.42}$$

I now consider a region of density 10^{-12} g cm^{-3} and temperature of 10 K. Assuming $s_{\mathrm{grain},j} = 0.1$ µm and $s_{\mathrm{grain},i} = 100$ µm, I get $t_{\mathrm{coag},i,j} \sim 240$ kyr. I note that, in the case of the Brownian motions, the coagulation timescale depends on the grains size of both species. If we now consider $s_{\mathrm{grain},j} = 0.01$ µm, $t_{\mathrm{coag},i,j} \sim 7$ kyr.

In short, I am tempted to say that in the presence of large grains, very small grain could be efficiently removed during the collapse in high density regions. Coagulation should therefore be included in future studies. I admit however that the presence of such large grains during the early phases of the protostellar collapse is still under debate. It is indeed unclear how these large dust grains can overcome the fragmentation barrier, as the differential velocities

between two dust species is typically quite large, e.g up to a few $\approx 0.1\text{kms}^{-1}$ in the envelope of MMMRN in the case of the two least coupled species. Typically, the velocity above which fragmentation can occur is thought to be about a few 10 ms^{-1} (Blum & Wurm, 2008) although it could be higher (Yamamoto et al., 2014). Large grains could overcome the fragmentation barrier because the fragmentation timescale is typically equivalent to coagulation timescale (e.g. Gonzalez et al., 2017). Fragmentation could simply not have the time to occur during the collapse, especially considering that large grains quickly drift toward regions of high density where their drift velocity is typically around a few meter per seconds.

4.9 Conclusion and perspective

In this study, I presented the first MULTIGRAIN and non-ideal MHD simulations of dusty protostellar collapses using the new dust dynamics solver of `RAMSES`. I presented six rotating and three non-rotating DUSTYCOLLAPSE simulations. The rotating models were carried out with a simultaneous treatment of 10 dust species with different sizes. In these simulations, I investigate the impact of the maximum grain size, the thermal-to-gravitational energy ratio and the presence of magnetic fields on the dynamics of the DUSTYCOLLAPSE. I summarize below my principal findings

1. Small grains with sizes less than a few 10 μm are strongly coupled to the gas during the protostellar collapse. On the contrary, grains larger than ∼ 100 μm tend to decouple significantly.

2. When the first hydrostatic core forms, high density regions – the core, the fragments, the disk and the pseudo-disk – are enriched in dust by a typical factor of two, whereas low density regions – the envelope and the outflow – are dust-depleted.

3. Dust is not necessarily a proxy for gas during the collapse. Inferring gas densities from dust is found to potentially lead to extremely large errors (up to ∼ 250%).

4. A standard MRN grain size distribution with a maximum grain size of 250nm is however extremely well preserved during the protostellar collapse in absence of coagulation.

5. Dust dynamics is strongly affected by the initial cloud properties. Variations of the dust-to-gas ratio reach the largest values when the free-fall is long and the initial density is low. An additional decoupling occurs for neutral grains in the presence of magnetic fields because collapse proceeds over longer timescales.

6. With a semi-analytical model, I show that the dust-ratio varies exponentially with the initial Stokes number during the collapse. More precisely, I have shown that it can be expressed as $\epsilon_0 \chi^{\text{St}_0}$ where χ is a dimensionless function of the time independent on the dust properties. Fitting the values of χ gives a very good agreement between the semi-analytical model and the measured dust-ratios in the range of Stokes number considered in my simulations.

7. Using the calibration of χ with the results of my model, I show that a Stokes number of at least 0.01 is required to enrich the core and the disk in a dust species by a factor of 2. Similarly I show that grains with $\text{St}_0 \gtrapprox 0.0027$ can potentially be depleted by a factor of 2 in the envelope after the first core formation.

Dust evolution during the protostellar collapse could have serious consequences on the initial state of protoplanetary disks and the further formation of the planets. In the future,

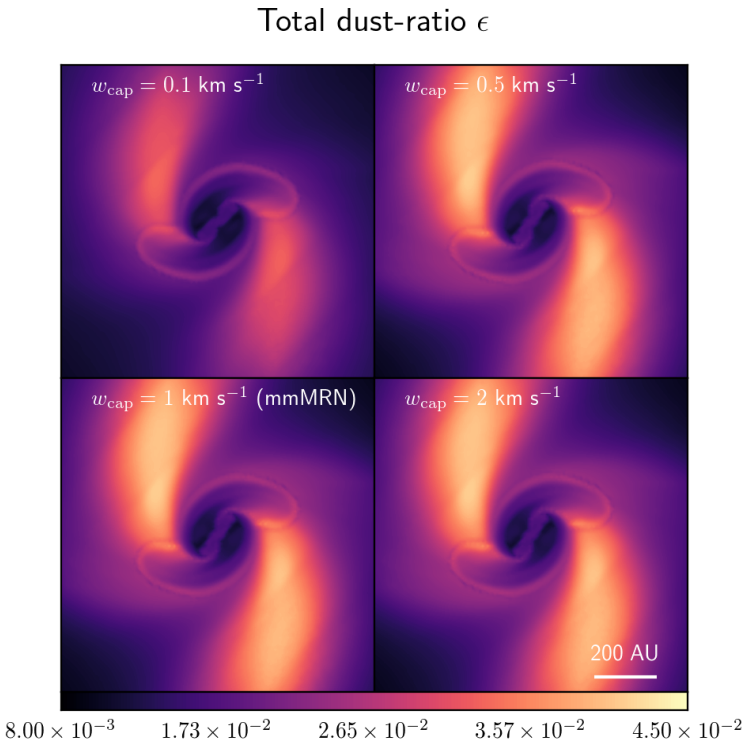

Figure 4.26: Fiducial model for various maximum dust differential velocity $w_{\rm cap}$. Mid-plane view of the total dust-ratio at the FHSC formation. (Top-left) $w_{\rm cap} = 0.1$ kms^{-1}, (Top-right) $w_{\rm cap} = 0.5$ km s^{-1}, (Bottom-left) $w_{\rm cap} = 1$ km s^{-1}, (Bottom-right) $w_{\rm cap} = 2$ km s^{-1}.

substantial efforts should be made to include the dynamics of charged dust grains during the protostellar collapse, since the Lorentz drag cannot necessarilly be neglected for small grains. Coagulation and fragmentation of dust grains should also be considered to investigate more realistically dust evolution during the star formation process.

4.10 Impact of velocity regularization

As explained in section 4.3.5, the simulations of my fiducial model have been performed with various values for the maximum gas and dust differential velocity $w_{\rm cap}$. I investigated the effect of varying w_{cap} by performing complementary simulations with $w_{\rm cap} = 0.1$, 0.5, 1 and 2 km s^{-1}. I attempted to simulate an additional model with $w_{\rm cap} = 10$ km s^{-1} but this led to numerical instabilities due to unrealistically large dust velocities at the accretion shock, where the diffusion approximation is not valid.

In figure 4.26, I show a face-one view of the dust-ratio at the time of the FHSC formation for these 4 models. With $w_{\rm cap} = 0.5 - 2$ km s^{-1} I essentially find the same results as in the fiducial case that has $w_{\rm cap} = 1$ km s^{-1}. Having $w_{\rm cap} = 0.1$ km s^{-1} however appears to be a too extreme choice. It indeed suppresses most of the initial dust enrichment that is due to the decoupling between the gas and the dust in the envelope. Having $w_{\rm cap} = 1$ km s^{-1} appeared to be a reasonable choice to cope with time stepping and physical constraints.

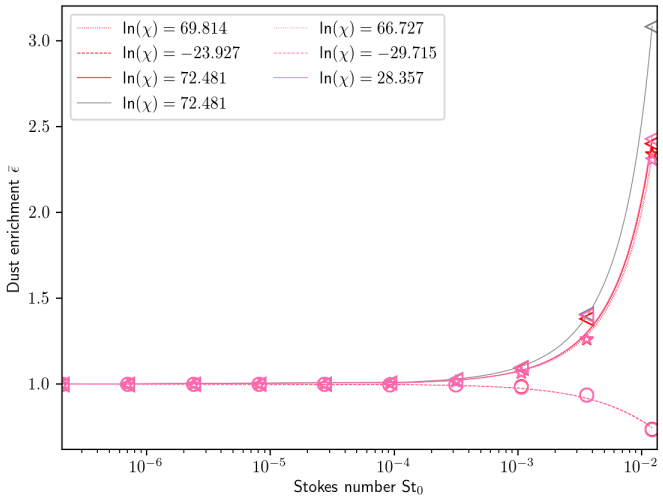

Figure 4.27: Semi-analytic and measured dust-ratio enrichment in MMMRN (red) and MMMRNEPS1E-7 (pink) in the core (stars), disk (triangles) and envelope (circles) at $t_{\rm core}+2$ kyr against the initial Stokes number. The lines represent the semi-analytical development using a best fit of χ for the FHSC (dotted), disk (solid) and envelope (dashed), respectively. I display the same information for MMMRN at $t_{\rm core}$+kyr in the disk (grey).

4.11 Non-linear dust enrichment: neglecting back-reaction

As stated in section 4.3.4, equation (4.26) is valid as long as local dust-ratio variations and the cumulative back-reaction of the dust can be neglected. In this approximation, the dust ratio enrichment increases exponentially with the Stokes number. As pointed out in section 4.3.4, I observe deviations from the exponential law in the disk and the envelope in MMMRN, while it is very well verified in the core.

To ascertain whether these deviations are due to back-reaction or not, I perform an additional simulation similar to the fiducial one, but with $\theta_{\rm d,0} = 10^{-7}$ (MMMRNEPS1E-7). For MMMRNEPS1E-7, we expect the back-reaction to be definitely negligible as $\theta_{\rm d,0} \ll 1$.

Figure 4.27 shows the dust ratio enrichment as a function of the initial Stokes number for MMMRN (red) and MMMRNEPS1E-7 (pink) in the core, disk and envelope at $t_{\rm core}+2$ kyr. On top of this, the dust ratio in the disk but at $t_{\rm core}$ is plotted for MMMRN (grey). As can be seen, the differences between the models at $t_{\rm core}+2$ kyr have similar dust-ratio enrichment. This indicates that the cumulative back-reaction of dust is negligible when $\mathrm{St}_{k,0} < 10^{-2}$ and only corrective above that. I am also confident that the mixing between dust enriched and dust depleted content, i.e. a non-negligible $\nabla\epsilon$, are the source of discrepancy between a pure exponential enrichment and the values measured in my models in the disk. We indeed observe a very good agreement with the exponential law for MMMRN at $t_{\rm core}$. At this time the disk has just formed from the dense and dust enriched material of the inner envelope. Later at $t_{\rm core}+2$ kyr, the disk has been accreting material from the envelope that is significantly depleted in large grains which causes a diminution of the average dust enrichment.

4.A Charges on dust grains

One can crudely estimate the charges on the grains during the collapse similarly to Wurster et al. (2016), to compare the relative intensities of the Lorentz and the Epstein drags. For simplicity, I assume that all the grains have the same negative charge Z_d (for all k, $Z_k = Z_\mathrm{d}$) and the ions to have a charge $Z_\mathrm{ions} = 1$. I consider 100 dust bins distributed as an MRN extended to millimeter-in-size grains, with a dust-to-gas ratio of 1%. Local electroneutrality ensures that

$$n_\mathrm{ions} - n_\mathrm{e} + Z_\mathrm{d} n_\mathrm{d} = 0, \tag{4.43}$$

n_ions, n_e and n_d being the number density of the ions, electrons and dust, the latter being given by

$$n_\mathrm{d} \equiv \frac{\mu_\mathrm{g} m_\mathrm{H}}{m_\mathrm{grain}} \epsilon n, \tag{4.44}$$

where m_grain is the average mass of a dust grain.

Two additional constrains are provided by the evolution equations for the ions and electrons charge density (Umebayashi & Nakano, 1980; Fujii et al., 2011). Assuming steady state and only considering charge capture by the grains (Keith & Wardle, 2014), they give

$$\begin{aligned} n_\mathrm{ions} &= \frac{\zeta n}{k_\mathrm{ions,grains} n_\mathrm{d}}, \\ n_\mathrm{e} &= \frac{\zeta n}{k_\mathrm{e,grains} n_\mathrm{d}}, \end{aligned} \tag{4.45}$$

where ζ is the cosmic-ray ionization rate. Similarly to Wurster et al. (2016), I adopt the typical value $\zeta = 10^{-17}\mathrm{s}^{-1}$. I also express $k_\mathrm{ions,grains}$ and $k_\mathrm{e,grains}$, the charge capture rates on neutral grains, as in (Fujii et al., 2011) as

$$\begin{aligned} k_\mathrm{ions,grains} &\equiv \pi s_\mathrm{grain}^2 \sqrt{\frac{8 k_\mathrm{b} T_\mathrm{g}}{\pi m_\mathrm{ions}}} \left(1 - \frac{e^2 Z_\mathrm{d}}{s_\mathrm{grain} k_\mathrm{b} T_\mathrm{g}}\right), \\ k_\mathrm{e,grains} &\equiv \pi s_\mathrm{grain}^2 \sqrt{\frac{8 k_\mathrm{b} T_\mathrm{g}}{\pi m_\mathrm{e}}} \exp\left[\frac{e^2 Z_\mathrm{d}}{s_\mathrm{grain} k_\mathrm{b} T_\mathrm{g}}\right]. \end{aligned} \tag{4.46}$$

where s_grain is the average grain size, m_e is the electron mass and m_ions the ions mass, assumed to be 24.3 proton masses. Using the previous equations, one obtains

$$Z_\mathrm{d} = \frac{\zeta}{n} \left(\frac{m_\mathrm{grain}}{\epsilon \mu_\mathrm{g} m_\mathrm{H}}\right)^2 \left[\frac{1}{k_\mathrm{ions,grains}(Z_\mathrm{d})} - \frac{1}{k_\mathrm{e,grains}(Z_\mathrm{d})}\right], \tag{4.47}$$

that I invert using the Newton-Raphson method to get Z_d.

4.B Distributions

In table 4.2, I provide the initial dust distributions, rounded quantities for the three maximum grain size used in my models (the exact calculation can be made using the method presented in 4.3.3). Table 4.3 shows $\langle \Theta_{\mathrm{d},k} \rangle_m$ (in %), the dust-to-gas ratio averaged in mass, along with its corresponding dust enrichment and the gas mass (in units of $M_\odot$) for all runs t_core + 2 kyr and all the different objects.

S_{max}	s (cm), θ :	1	2	3	4	5	6	7	8	9	10
2.5(-5)	s (cm)	4.11(-7)	6.08(-7)	8.99(-7)	1.33(-6)	1.97(-6)	2.91(-6)	4.3(-6)	6.36(-6)	9.4(-6)	1.39(-5)
	θ	3.56(-4)	4.33(-4)	5.26(-4)	6.40(-4)	7.78(-4)	9.46(-4)	1.15(-3)	1.4(-3)	1.7(-3)	2.1(-3)
0.01	s (cm)	3.05(-7)	8.2(-7)	2.21(-6)	5.95(-6)	1.6(-5)	4.31(-5)	1.16(-4)	3.12(-4)	8.41(-4)	2.26(-3)
	θ	4.56(-5)	7.49(-5)	1.223(-4)	2.02(-4)	3.31(-4)	5.43(-4)	8.9(-4)	1.46(-3)	2.40(-3)	3.93(-3)
0.1	s (cm)	2.72(-7)	9.2(-7)	3.12(-6)	1.05(-5)	3.58(-5)	1.21(-4)	4.12(-4)	1.4(-3)	4.73(-3)	1.6(-2)
	θ	1.88(-5)	3.47(-5)	6.39(-5)	1.18(-4)	2.16(-4)	3.99(-4)	7.34(-4)	1.35(-3)	2.49(-3)	4.58(-3)

Table 4.2: Initial dust distributions, rounded quantities for the three maximum grain size used in my models (the exact calculation can be made using the method presented in 4.3.3) . For each S_{max}, the first line represent the grain size in cm and the second the initial dust-to-gas ratio. The exponents are given by the parenthesis and the integers from 1 to 10 correspond to bins of increasing sizes.

Model	j	$\langle\Theta_{d,k\leq6}\rangle_m$	$\langle\Theta_{d,7}\rangle_m$	$\langle\Theta_{d,8}\rangle_m$	$\langle\Theta_{d,9}\rangle_m$	$\langle\Theta_{d,10}\rangle_m$	m_g
MMMRN	$\mathcal{F}_0$	0.085[1]	0.075[1.03]	0.14[1.03]	0.31[1.24]	1.17[2.6]	0.082
	$\mathcal{F}_1$	0.085[1]	0.076[1.04]	0.15[1.1]	0.37[1.54]	1.38[3]	0.024
	$\mathcal{F}_2$	0.085[1]	0.076[1.04]	0.15[1.1]	0.37[1.54]	1.37[2.98]	0.024
	$\mathcal{D}$	0.085[1]	0.075[1.03]	0.15[1.1]	0.34[1.41]	1.1[2.4]	0.096
	$\mathcal{E}$	0.085[1]	0.073[1]	0.13[0.96]	0.23[0.95]	0.34[0.73]	1.0
MRN	$\mathcal{F}_0$	0.37[1]	0.12[1]	0.14[1]	0.17[1]	0.21[1]	0.088
	$\mathcal{F}_1$	0.37[1]	0.12[1]	0.14[1]	0.17[1]	0.21[1]	0.033
	$\mathcal{F}_2$	0.37[1]	0.12[1]	0.14[1]	0.17[1]	0.21[1]	0.033
	$\mathcal{D}$	0.37[1]	0.12[1]	0.14[1]	0.17[1]	0.21[1]	0.091
	$\mathcal{E}$	0.37[1]	0.12[1]	0.14[1]	0.17[1]	0.21[1]	0.98
100MICMRN	$\mathcal{F}_0$	0.13[1]	0.09[1]	0.15[1]	0.25[1.04]	0.43[1.1]	0.086
	$\mathcal{F}_1$	0.13[1]	0.09[1]	0.15[1]	0.25[1.04]	0.46[1.17]	0.023
	$\mathcal{F}_2$	0.13[1]	0.09[1]	0.15[1]	0.25[1.04]	0.46[1.17]	0.023
	$\mathcal{D}$	0.13[1]	0.09[1]	0.15[1]	0.25[1.04]	0.44[1.13]	0.097
	$\mathcal{E}$	0.13[1]	0.09[1]	0.15[1]	0.24[1]	0.38[0.97]	0.99
MMMRNA0.25	$\mathcal{F}_0$	0.085[1]	0.074[1.01]	0.14[1.03]	0.26[1.04]	0.51[1.12]	0.20
	$\mathcal{F}_1$	0.085[1]	0.074[1.01]	0.14[1.03]	0.27[1.08]	0.58[1.29]	0.10
	$\mathcal{F}_2$	0.085[1]	0.074[1.01]	0.14[1.03]	0.27[1.08]	0.58[1.29]	0.10
	$\mathcal{D}$	0.085[1]	0.074[1.01]	0.14[1.03]	0.26[1.04]	0.56[1.24]	0.16
	$\mathcal{E}$	0.085[1]	0.073[1]	0.13[0.96]	0.24[0.96]	0.4[0.89]	0.7
MMMRNMHD	$\mathcal{F}_0$	0.085[1]	0.076[1.04]	0.15[1.1]	0.37[1.48]	1.5[3.33]	0.075
	$\mathcal{D}$	0.085[1]	0.076[1.04]	0.15[1.1]	0.39[1.56]	1.58[3.58]	0.0012
	$\mathcal{P}$	0.086[1.01]	0.077[1.05]	0.16[1.19]	0.43[1.72]	1.23[2.73]	0.1
	$\mathcal{O}$	0.085[1]	0.074[1.01]	0.14[1.03]	0.26[1.04]	0.1[0.22]	0.0082
	$\mathcal{E}$	0.085[1]	0.072[0.98]	0.13[0.96]	0.2[0.8]	0.17[0.38]	0.5
MMMRNNIMHD	$\mathcal{F}_0$	0.085[1]	0.077[1.5]	0.15[1.1]	0.37[1.48]	1.5[3.33]	0.081
	$\mathcal{D}$	0.085[1]	0.076[1.04]	0.15[1.1]	0.37[1.48]	1.44[3.2]	0.011
	$\mathcal{P}$	0.086[1.01]	0.077[1.05]	0.16[1.19]	0.43[1.72]	1.22[2.71]	0.1
	$\mathcal{O}$	0.086[1.01]	0.076[1.04]	0.15[1.1]	0.32[1.28]	0.2[0.44]	0.0018
	$\mathcal{E}$	0.085[1]	0.072[0.98]	0.13[0.96]	0.2[0.8]	0.17[0.38]	0.5

Table 4.3: Mass averaged dust-to-gas ratio $\langle\Theta_{d,k}\rangle_m$ (in %) and gas mass (in units of $M_\odot$) for all runs $t_{\rm core}$ + 2 kyr and all the objects, the number inside the brackets is the corresponding mass averaged dust enrichment. When $\left\langle\bar{\Theta}_{\rm d}\right\rangle_m > 1$, the enrichment is referenced in red while it is referenced in blue when $\left\langle\bar{\Theta}_{\rm d}\right\rangle_m \leq 1$. I denote the different objects as follows, $\mathcal{F}_j$ represent the fragments ($\mathcal{F}_0$ being the FHSC), $\mathcal{D}$ the disks, $\mathcal{O}$ the outflow, $\mathcal{P}$ the pseudo-disks and $\mathcal{E}$ the envelope.

Chapter 5

Gas and dust magnetohydrodynamics

Contents

Robert Muldoon

"Quiet, all of you! They're approaching the Tyrannosaur paddock."

- Jurassic Park

In this chapter, I present a set of equations for magnetohydrodynamics with multiple charged grains species that I recently derived in collaboration with Pr. Daniel Price at the Monash university. This visit in Australia was possible thanks to the DUSTBUSTERS consortium. This work is also carried out in collaboration with Vincent Guillet (IAS). This chapter is the most technical of this manuscript and I encourage the reader to be read Chapter 2 before this one.

5.1 Introduction

Growing number of studies have investigated the dynamics of neutral dust grains in various regions of the interstellar medium (ISM). When large enough, these grains are expected to decouple from the gas. The size at which the decoupling occurs typically depends on the environment, it goes from $1 - 10$ µm in molecular clouds (Lee et al., 2017; Tricco et al., 2017) to $1 - 10$ mm in protoplanetary disks (e.g. Dipierro et al., 2015, 2018a; Riols & Lesur, 2018; Lin, 2019). During the protostellar collapse the typical grain size for the decoupling is intermediate ($\sim 10 - 100$ µm, see Bate & Lorén-Aguilar, 2017, or see Chapter 4).

One of the missing ingredients in these studies is the impact of the grain charge. These studies indeed all consider the grains to be dynamically neutral. In the diffuse ISM and up to the densities of molecular clouds, dust grains are typically negatively charged, approximately carrying one elementary charge per grain (Draine & Sutin, 1987; Guillet et al., 2007). During the protostellar collapse, they might even be the main charge carriers. In this case the value of magnetic resistivities would be controlled by the shape of the grain size distribution (Umebayashi & Nakano, 1990; Marchand et al., 2016; Wurster et al., 2016). This is important because the coupling between the magnetic fields and the neutral gas, regulated by the resistivity, probably controls the early disk properties (Masson et al., 2016; Hennebelle et al., 2016; Vaytet et al., 2018b; Hennebelle et al., 2020).

Sub-micrometer grains are believed to be extremely important for the coupling between the gas and the magnetic fields. Small grains tend to strongly couple to the magnetic field. This happens because their gyration time is shorter than their stopping time (see Guillet et al., 2007; Hopkins & Squire, 2018, or Chapter 4). As a consequence, their presence reduce the values of the resistivities and hence increase the magnetic braking efficiency. It was shown by Zhao et al. (2016) that the smallest grain size in the dust size distribution is a critical parameter that controls the angular momentum transport during disk formation. In particular, they have shown that including very small grains in the dust distribution could prevent the formation of a rotationally supported disks. A key question of disk formation might thus be: what is the fate of the very small grains from the diffuse ISM to collapsing regions? Another potential consequence of the strong coupling between the magnetic field and the very small grains is that they might decouple with the gas when the latter is poorly coupled with magnetic fields (Guillet et al., 2007). This potential decoupling might lead to a size sorting even for small grains and enhance the effect of grain growth in low density regions. To investigate this hypothesis, the drift velocity of dust grains needs to be determined in a full set of MHD equations that includes their dynamics whether if they are charged or neutral.

The charged dust grain dynamics has been investigated in the ideal MHD limit with a multifluid approach by Hopkins & Squire (2018); Squire & Hopkins (2018); Hopkins et al. (2020). In the non-ideal case, monofluid approaches have been proposed by Wardle (1998); Guillet et al. (2007); Kunz & Mouschovias (2009). These studies however neglected the impact of the hydrodynamical drift (see Chapters 2 and 4) due to the imperfect coupling between the grains and the neutral gas and that remains when the grain charge goes to zero. In this chapter, I present a new set of non-ideal MHD eqution for neutral gas + charged particles mixtures in section 5.2. In section 5.3, I show that this set of equations recovers the expected drift velocities in the main limiting cases, e.g. non-ideal MHD, ideal MHD and hydrodynamics. In section 5.4, I discuss the potential astrophysical objects where this new formalism could prove useful. Finally I present my conclusions and perspectives in section 5.5

5.2 Dynamical equations

The aim of this section is to provide a new set of non-ideal MHD equations (dusty-MHD hereafter) that includes the drift of several distinct charged species, i.e. the dust, ions and electrons and one neutral gas. For simplicity, I consider that the collisions with the neutral gas are dominant over charged-charged collisions. It is important to keep in mind that, although I put the emphasize on dust grains, ions and electrons have the same treatment.

5.2.1 Definitions and useful relations

Before introduce the dynamical equation, I re-define here the multi- and mono-fluid quantities. The new notations aim to be as general as possible. In this work, I consider $\mathcal{N}$ charged species. The species n, represented by the $\mathcal{N}+1$ index in sums, is the neutral gas. The total density of the fluid ρ writes

$$\rho \equiv \sum_{j=1}^{\mathcal{N}+1} \rho_j, \tag{5.1}$$

ρ_j is the density of the fluid j, q_j its typical charge and n_j its number density . For a fluid k, the mass fraction x_k is defined as

$$x_k \equiv \frac{\rho_k}{\rho}. \tag{5.2}$$

In the case of the dust, the mass fraction is exactly the same quantity as the dust-ratio. Each fluid k has a velocity $\mathbf{v}_k$. The barycenter of the total mixture has a velocity $\mathbf{v}$ that is expressed as

$$\mathbf{v} \equiv \sum_{j=1}^{\mathcal{N}+1} x_j \mathbf{v}_j, \tag{5.3}$$

$\mathbf{w_k} \equiv \mathbf{v}_k - \mathbf{v}$ is the drift of the species k with respect to the barycenter. The neutral gas differential velocity is then directly given by

$$\mathbf{w}_n = -\sum_{j=1}^{\mathcal{N}} \frac{x_j}{x_n} \mathbf{w}_j, \tag{5.4}$$

as $\sum_{j=1}^{\mathcal{N}+1} x_j \mathbf{w}_j = 0$.

$\mathbf{f}$ are the specific forces that apply on all the fluids, e.g. the gravitational force. $\mathbf{F}_\mathrm{k}$ the forces that apply only on the fluid k, drag and Lorentz force excluded. I define again $K_k \equiv \frac{x_k \rho_n}{t_k}$ as the drag coefficient between k and the neutral gas, t_k being the timescale of coupling with the neutral gas, e.g. the stopping time for the dust.

Finally, $\mathbf{E}$ and $\mathbf{B}$ are the electric and magnetic field, respectively.

5.2.2 Multifluid: Mass and momentum conservation

In the multifluid approach, the mass and momentum conservation equations of the charged+neutral gas mixture are written as

$$\begin{aligned}
\frac{\partial \rho_{\rm n}}{\partial t} + \nabla \cdot \rho_{\rm n} \mathbf{v}_{\rm n} &= 0, \\
\frac{\partial \rho_{\rm k}}{\partial t} + \nabla \cdot \rho_{\rm k} \mathbf{v}_{\rm k} &= 0, \\
\frac{\partial \rho_{\rm n} \mathbf{v}_{\rm n}}{\partial t} + \nabla \cdot [\rho_{\rm n} \mathbf{v}_{\rm n} \otimes \mathbf{v}_{\rm n}] &= \rho_{\rm n} \mathbf{f} + \mathbf{F}_{\rm n} + \sum_{j=1}^{\mathcal{N}} K_j \Delta \mathbf{v}_j, \\
\frac{\partial \rho_{\rm k} \mathbf{v}_{\rm k}}{\partial t} + \nabla \cdot [\rho_{\rm k} \mathbf{v}_{\rm k} \otimes \mathbf{v}_{\rm k}] &= \rho_{\rm k} \mathbf{f} + \mathbf{F}_{\rm k} + n_k q_k (\mathbf{E} + \mathbf{v}_{\rm k} \times \mathbf{B}) \\
&- K_k \Delta \mathbf{v}_k.
\end{aligned} \tag{5.5}$$

The electric fields need to be constrained by an Ohm's law, derived from the momentum equation, while the magnetic field evolution is constrained by the induction equation. This set of equations must also be completed with an energy conservation equation and an equation of state when thermal pressure forces are significant.

5.2.3 Monofluid: Mass and momentum conservation

As explained in details in Chapter 2 or in the previous works of Laibe & Price (2014a,b,c); Hutchison et al. (2018), the mass and barycenter momentum conservation equations can be rewritten without any approximation using a monofluid approach. In the case of the dusty-MHD equations are given by

$$\begin{aligned}
\frac{\partial \rho}{\partial t} + \nabla \cdot \rho \mathbf{v} &= 0, \\
\frac{\partial \rho_k}{\partial t} + \nabla \cdot \rho_k (\mathbf{v} + \mathbf{w}_k) &= 0, \\
\frac{\partial \rho \mathbf{v}}{\partial t} + \nabla \cdot [\rho \mathbf{v} \otimes \mathbf{v}] &= -\sum_{j=1}^{\mathcal{N}} \nabla \cdot (\rho_j \mathbf{w}_j \otimes \mathbf{w}_j) \\
&+ \mathbf{F} + \bar{\mathbf{F}} + \mathbf{J} \times \mathbf{B},
\end{aligned} \tag{5.6}$$

where $\mathbf{F} \equiv \rho \mathbf{f}$ and $\bar{\mathbf{F}} \equiv \sum_{j=1}^{\mathcal{N}+1} \mathbf{F}_j$. Note that we do not need to solve a similar equation for the neutral gas in virtue of equation (5.4). Let us recall that, it virtue of the Maxwell-Ampère equation, the current is defined as $\mathbf{J} \equiv \nabla \times \mathbf{B}$ in the non-relativistic magnetic regime. No electric force applies to the barycenter in virtue of local electroneutrality.

On top of this, the drift velocities of the charged particles are constrained by the following equation

$$\begin{aligned}
\frac{\partial \mathbf{w}_k}{\partial t} + (\mathbf{v} \cdot \nabla) \mathbf{w}_k &= (\mathbf{w}_k \cdot \nabla) \mathbf{v} + -(\mathbf{w}_k \cdot \nabla) \mathbf{w}_k \\
&+ \frac{1}{\rho} \sum_{j=1}^{\mathcal{N}} \nabla \cdot (\rho_j \mathbf{w}_j \otimes \mathbf{w}_j) \\
&+ \frac{\mathbf{F}_{\rm k}}{\rho_k} + \frac{q_k}{m_k} (\mathbf{E}_{\rm b} + \mathbf{w}_{\rm k} \times \mathbf{B}) - \frac{K_k}{\rho_k} (\mathbf{w}_k - \mathbf{w}_{\mathbf{n}}) \\
&- \frac{\bar{\mathbf{F}}}{\rho} - \frac{\mathbf{J} \times \mathbf{B}}{\rho},
\end{aligned} \tag{5.7}$$

where $\mathbf{E}_\mathrm{b} \equiv \mathbf{v} \times \mathbf{B} + \mathbf{E}$ is the electric field in the rest frame of the barycenter. This equation is obtained similarly as the evolution equation of $\Delta\mathbf{v}$ (see chapter 2) but subtracting the evolution equation of $\mathbf{v}$ instead of $\mathbf{v}_\mathrm{n}$ to the one of $\mathbf{v}_\mathbf{k}$.

5.2.4 Approximations

In strong coupling regimes, one can neglect neglect the quadratic and inertial terms in equations (5.6) and (5.7) : this is the terminal velocity approximation and the diffusion approximation (see Chapter 2 or Laibe & Price, 2014a,b,c; Price & Laibe, 2015, for a complete study).

In this formalism, equation (5.7) becomes

$$0 = \frac{\mathbf{F}_\mathrm{k}}{\rho_k} + \frac{q_k}{m_k}(\mathbf{E}_\mathrm{b} + \mathbf{w}_\mathrm{k} \times \mathbf{B}) - \frac{K_k}{\rho_k}(\mathbf{w}_k - \mathbf{w}_\mathbf{n}) - \frac{\bar{\mathbf{F}}}{\rho} - \frac{\mathbf{J} \times \mathbf{B}}{\rho}. \tag{5.8}$$

We can further neglect the cumulative back-reaction of the dust on the gas when $x_n \sim 1 \gg x_{j\neq n}$ which gives $\|\mathbf{w_n}\| \ll \|\mathbf{w}_k\|$ as $\sum_{j=1}^{\mathcal{N}+1} x_j \mathbf{v}_j \simeq x_n \mathbf{v}_n \simeq \mathbf{v}$ and also $\rho_n \simeq \rho$. This leads to

$$\frac{K_k}{\rho_k}\mathbf{w}_k - \frac{q_k}{m_k}\mathbf{w}_\mathrm{k} \times \mathbf{B} = \frac{\mathbf{F}_\mathrm{k}}{\rho_k} + \frac{q_k}{m_k}\mathbf{E}_\mathrm{b} - \frac{\bar{\mathbf{F}}}{\rho} - \frac{\mathbf{J} \times \mathbf{B}}{\rho}, \tag{5.9}$$

which, after rearranging the terms yields

$$\mathbf{w}_k - \Gamma_k \mathbf{w}_k \times \mathbf{b} = \frac{\Gamma_k}{|\mathbf{B}|}\mathbf{E_b} + \frac{\mathbf{F}_\mathrm{k} - x_k(\bar{\mathbf{F}} + \mathbf{J} \times \mathbf{B})}{K_k}, \tag{5.10}$$

where I define the Hall factor as $\Gamma_k \equiv \frac{\rho_k q_k |\mathbf{B}|}{m_k K_k}$. It is the ratio between the coupling time t_k and the gyration time $t_{\mathrm{gyr},k} \equiv \frac{q_k|\mathbf{B}|}{m_k}$. The Hall factor quantifies the relative importance of the coupling with the neutral gas to the one with the magnetic field. I also define the magnetic field unit vector as $\mathbf{b} \equiv \frac{\mathbf{B}}{|\mathbf{B}|}$.

We can rewrite the former equation as

$$\mathbf{w}_k - \Gamma_k \mathbf{w}_k \times \mathbf{b} = \frac{\Gamma_k}{|\mathbf{B}|}\mathbf{E_b} + \mathcal{W}_{\mathcal{H},k}, \tag{5.11}$$

where $\mathcal{W}_{\mathcal{H},k}$ is the drift velocity of k in the limit $\Gamma_k \to 0$. In other words, $\mathcal{W}_{\mathcal{H},k}$ is the drift velocity of neutral grains. It is defined as

$$\mathcal{W}_{\mathcal{H},k} \equiv \frac{\mathbf{F}_k - x_k(\bar{\mathbf{F}} + \mathbf{J} \times \mathbf{B})}{K_k}, \tag{5.12}$$

Equation (5.11) can be inverted straightforwardly to obtain $\mathbf{w}_k$, as long as the forces $\mathbf{F}_k$ do not depend on the drift velocities, to obtain

$$\mathbf{w}_k \quad = \quad \mathbf{w}_{\mathrm{MH},k} + \mathbf{w}_{\mathrm{EM},k}, \tag{5.13}$$

where I distinguish the magneto-hydro drift [1]

$$\mathbf{w}_{\mathrm{MH},k} \equiv \frac{\Gamma_k}{1+\Gamma_k^2}\mathcal{W}_{\mathcal{H},k} \times \mathbf{b} + \frac{1}{1+\Gamma_k^2}\mathcal{W}_{\mathcal{H},k,\perp} + \mathcal{W}_{\mathcal{H},k_{//}} \tag{5.14}$$

[1] see chapter 2 for the hydrodynamical limit of this drift

and the electromotive drift due to the imperfect coupling between the neutral gas and the magnetic field

$$\mathbf{w}_{\mathrm{EM},k} \equiv \frac{1}{|\mathbf{B}|}\left[\frac{\Gamma_k^2}{1+\Gamma_k^2}\mathbf{E}_b \times \mathbf{b} + \frac{\Gamma_k}{1+\Gamma_k^2}\mathbf{E}_{b,\perp} + \Gamma_k \mathbf{E}_{b//}\right], \tag{5.15}$$

where // and $\perp$ denote the parallel and perpendicular component of a vector, respectively. Equation (5.13) shows strong similarities with the form proposed by the previous studies of Wardle (1998) and Guillet et al. (2007). They were however neglecting the neutral drift $\mathcal{W}_{\mathcal{H},k}$ due to the differential forces between the neutral gas and the charged species. As explained earlier, in this study, a drift between the neutral gas and the charged species remains when $\Gamma_k \to 0$. More precisely, in this limit $\mathbf{w}_{\mathrm{EM},k} \to 0$ and the magneto-hydro drift tends to the hydro drift $\mathbf{w}_{\mathrm{MH},k} \to \mathcal{W}_{\mathcal{H},k}$.

5.2.5 Full Ohm's law

As previously mentioned, the evolution of the magnetic field is constrained by the induction equation that writes as follows

$$\frac{\partial \mathbf{B}}{\partial t} = -\nabla \times \mathbf{E}. \tag{5.16}$$

An Ohm's law is then required to constrain the electric field. Using the local electroneutrality we can show that

$$\mathbf{J} \equiv \sum_{j=1}^{\mathcal{N}} n_j\, q_j(\mathbf{v}+\mathbf{w}_j) = (\sum_{j=1}^{\mathcal{N}} n_j\, q_j)\mathbf{v} + \sum_{j=1}^{\mathcal{N}} n_j\, q_j \mathbf{w}_j = \sum_{j=1}^{\mathcal{N}} n_j\, q_j \mathbf{w}_j, \tag{5.17}$$

using equation (5.13) and defining the magneto-hydro drift current

$$\mathbf{J}_{\mathrm{MH}} \equiv \sum_{j=1}^{\mathcal{N}} n_j\, q_j \mathbf{w}_{\mathrm{MH},j}, \tag{5.18}$$

we can show that

$$\mathbf{J} = \mathbf{J}_{\mathrm{MH}} + \sigma_{\mathrm{O}}\mathbf{E}_{b//} + \sigma_{\mathrm{p}}\mathbf{E}_{b,\perp} + \sigma_{\mathrm{H}}\mathbf{E}_b \times \mathbf{b}, \tag{5.19}$$

where we define

- the Ohm conductivity

$$\sigma_{\mathrm{O}} \equiv \sum_{j=1}^{\mathcal{N}} \frac{n_j\, q_j}{|\mathbf{B}|}\Gamma_j, \tag{5.20}$$

- the Peterson conductivity

$$\sigma_{\mathrm{p}} \equiv \sum_{j=1}^{\mathcal{N}} \frac{n_j\, q_j}{|\mathbf{B}|}\frac{\Gamma_j}{1+\Gamma_j^2}, \tag{5.21}$$

- the Hall conductivity

$$\sigma_{\mathrm{H}} \equiv \sum_{j=1}^{\mathcal{N}} \frac{n_j\, q_j}{|\mathbf{B}|}\frac{\Gamma_j^2}{1+\Gamma_j^2}. \tag{5.22}$$

Apart from the term $\mathbf{J}_{\rm MH}$, equation (5.19) is the same a in usual non-ideal MHD (e.g., Wardle & Ng, 1999). Writing $\Delta\mathbf{J} = \mathbf{J} - \mathbf{J}_{\rm MH}$, it is then easy to demonstrate that the Ohm's law writes

$$\mathbf{E}_b = \eta_{\rm O}\Delta\mathbf{J} + \eta_{\rm H}\Delta\mathbf{J}\times\mathbf{b} + \eta_{\rm A}\Delta\mathbf{J}_\perp, \tag{5.23}$$

where we define

- the Hall resistivity

$$\eta_{\rm H} \equiv \frac{\sigma_{\rm H}}{\sigma_{\rm p}^2 + \sigma_{\rm H}^2}, \tag{5.24}$$

- the Ohm resistivity

$$\eta_{\rm O} \equiv \frac{1}{\sigma_{\rm O}}, \tag{5.25}$$

- the ambipolar resistivity

$$\eta_{\rm A} \equiv \frac{\sigma_{\rm p}}{\sigma_{\rm p}^2 + \sigma_{\rm H}^2} - \frac{1}{\sigma_{\rm O}}. \tag{5.26}$$

We note that, in the limit $|\mathbf{J}_{\rm MH}| \ll |\mathbf{J}|$, equation (5.23) reduces to the standard Ohm's law in non-ideal MHD.

5.2.6 Energy conservation

In the terminal velocity approximation, we neglect the internal energy of the charged particles, assuming the total energy of the mixture is defined as $E \equiv \frac{1}{2}\rho\mathbf{v}^2 + \frac{\mathbf{B}^2}{2} + \rho u$, where u is the neutral gas internal energy. The energy conservation equation is thus written as

$$\begin{aligned} \frac{\partial E}{\partial t} &+ \nabla\cdot\left[\left((E + P_{\rm n})\mathbf{v} - \mathbf{B}(\mathbf{B}\cdot\mathbf{v})\right]\right. \\ &= (\mathbf{F} + \bar{\mathbf{F}})\cdot\mathbf{v} + \Lambda_{\rm res}, \end{aligned} \tag{5.27}$$

where the resistive heating source term $\Lambda_{\rm res}$ writes

$$\Lambda_{\rm res} = \mathbf{E}_b\cdot\mathbf{J}. \tag{5.28}$$

Contrary to the standard non-ideal MHD case there is no constrain on the positivity of $\Delta\mathbf{J}\cdot\mathbf{J}$ even though that must be intrinsically the case to verify the second principle of thermodynamics. This means that $\|\mathbf{J}_{\rm MH}\|$ must be smaller than $\|\mathbf{J}\|$ for the terminal velocity approximation to hold. As a precaution, I choose to neglect the magneto-hydro drift current in the induction equation and assume a standard non-ideal MHD Ohm law (see Wardle & Ng, 1999; Kunz & Mouschovias, 2009, for detailed works on the matter). We therefore have

$$\mathbf{E}_b = \eta_{\rm O}\mathbf{J} + \eta_{\rm H}\mathbf{J}\times\mathbf{b} + \eta_A\mathbf{J}_\perp. \tag{5.29}$$

5.2.7 Summary

Using the previous derivation we can now write down the expression of multispecies MHD in the first-order terminal velocity approximation with neglected back-reaction and magneto-hydro drift current as

$$\begin{aligned}
\frac{\partial \rho}{\partial t} + \nabla \cdot \rho \mathbf{v} &= 0 \\
\frac{\partial \rho_k}{\partial t} + \nabla \cdot \rho_k (\mathbf{v} + \mathbf{w}_k) &= 0 \\
\frac{\partial \rho \mathbf{v}}{\partial t} + \nabla \cdot [\rho \mathbf{v} \otimes \mathbf{v}] &= -\sum_{j=1}^{\mathcal{N}} \nabla \cdot (\rho_j \mathbf{w}_j \otimes \mathbf{w}_j) \\
&+ \mathbf{F} + \bar{\mathbf{F}} + \mathbf{J} \times \mathbf{B}, \\
\frac{\partial \mathbf{B}}{\partial t} - \nabla \times (\mathbf{v} \times \mathbf{B}) &= -\nabla \times \mathbf{E}_b, \\
\frac{\partial E}{\partial t} + \nabla \cdot [((E + P_\mathrm{n})\mathbf{v} - \mathbf{B}(\mathbf{B} \cdot \mathbf{v})] &= (\mathbf{F} + \bar{\mathbf{F}}) \cdot \mathbf{v} + \Lambda_\mathrm{res},
\end{aligned} \tag{5.30}$$

with the drift velocity and electric field given by

$$\begin{aligned}
\mathbf{w}_k &= \mathbf{w}_{\mathrm{MH},k} + \mathbf{w}_{\mathrm{EM},k}, \\
\mathbf{E}_b &= \eta_\mathrm{O} \mathbf{J} + \eta_\mathrm{H} \mathbf{J} \times \mathbf{b} + \eta_A \mathbf{J}_\perp.
\end{aligned} \tag{5.31}$$

We note that $\mathbf{E}_{b//} = 0$ as $\mathbf{J} = \nabla \times \mathbf{B}$, which is why there is now only three terms in the drift velocity. For energy conservation reasons, we neglected $\mathbf{J}_\mathrm{MH}$ in the induction equation but one should keep in mind that this term exists. The set equations that includes $\mathbf{J}_\mathrm{MH}$ can be straightforwardly obtained by performing the transformation $\mathbf{J} \rightarrow \Delta\mathbf{J}$ except in Λ_res that remains unchanged.

5.2.8 On the back-reaction

I neglected the cumulative back-reaction of charged species onto neutral gas particles, but this is only valid in the low ionisation regime and when the dust ratio is small compared to unity. During the protostellar collapse phase neglecting the back-reaction for the dust is likely to be valid (see Chapter 4). In addition, the ionization fraction of the most abundant charged species remains between $x_i \simeq 10^{-25} - 10^{-5}$ in dense cores (Marchand et al., 2016) which is significantly smaller than unity. We note however that in certain objects, such as the protoplanetary disks, the back-reaction of dust is not negligible (Dipierro et al., 2018b). A simple solution to approximate the back-reaction consists in a first order development in terms of $x = \sum_{j=1}^{\mathcal{N}} x_j$ such as

$$\mathbf{w}_k^\mathrm{back} = \mathbf{w}_k^\mathrm{no-back} + x \delta \mathbf{w}_k + O(x^2 \mathbf{w}_k^\mathrm{no-back}), \tag{5.32}$$

where $\mathbf{w}_k^\mathrm{back}$ and and $\mathbf{w}_k^\mathrm{no-back}$ are the drift velocity of the species k when the back-reaction is not neglected and neglected, respectively. We note that $\mathbf{w}_k^\mathrm{no-back}$ is given by equation (5.31). When the back reaction is considered, we must solve equation (5.8), it now becomes

$$\mathbf{w}_k^\mathrm{back} - \Gamma_k \mathbf{w}_k^\mathrm{back} \times \mathbf{b} = \frac{\Gamma_k}{|\mathbf{B}|} \mathbf{E}_\mathbf{b} + \frac{\mathbf{F}_\mathrm{k} - x_k (\bar{\mathbf{F}} + \mathbf{J} \times \mathbf{B})}{K_k} - \sum_{j=1}^{\mathcal{N}} \frac{x_j}{x_n} \mathbf{w}_j^\mathrm{back}, \tag{5.33}$$

substituting $\mathbf{w}_k^{\text{back}}$ in equation (5.33) with the expression given by equation (5.32) yields

$$x\delta\mathbf{w}_k - x\Gamma_k\delta\mathbf{w}_k \times \mathbf{b} = -\sum_{j=1}^{\mathcal{N}} \frac{x_j}{x_n}\mathbf{w}_j^{\text{no-back}}, \tag{5.34}$$

which eventually gives

$$x\delta\mathbf{w}_k = -\frac{\Gamma_k}{1+\Gamma_k^2}\sum_{j=1}^{\mathcal{N}} \frac{x_j}{x_n}\mathbf{w}_j^{\text{no-back}} \times \mathbf{b} - \frac{1}{1+\Gamma_k^2}\sum_{j=1}^{\mathcal{N}} \frac{x_j}{x_n}\mathbf{w}_{j,\perp}^{\text{no-back}} - \sum_{j=1}^{\mathcal{N}} \frac{x_j}{x_n}\mathbf{w}_{j,//}^{\text{no-back}}. \tag{5.35}$$

To determine the new Ohm's law, we need to separate the expression into a magneto-hydro drift and electromotive drift as in the back-reaction free case. We will thus obtain additional terms in the three resistivities. I choose not to go any further on this question yet.

5.2.9 Dimensionless numbers

Before reviewing the different regimes of dusty-MHD mixtures, it is convenient to define certain dimensionless quantities. Let us re-define the Stokes number as

$$\text{St}_k \equiv \frac{t_k}{t_{\text{dyn}}}, \tag{5.36}$$

where t_{dyn} is the dynamical timescale of the system studied. e.g. the free-fall timescale during the protostellar collapse. When $\text{St}_k \ll 1$, the coupling between the species k and the neutral gas is strong. Similarly we can also define a magnetic Stokes number as

$$\text{Stm}_k \equiv \frac{t_{\text{gyr},k}}{t_{\text{dyn}}}. \tag{5.37}$$

When $\text{Stm}_k \ll 1$, the coupling between the species k and the magnetic field is strong. If $\text{Stm}_k \ll \text{St}_k$, then the species k preferentially couples to the magnetic field rather than with the neutral gas. This corresponds exactly to the condition $\Gamma_k \gg 1$ because $\Gamma_k = \frac{\text{St}_k}{\text{Stm}_k}$.

For each resistive effect r we define the magnetic Reynolds number as

$$\text{Rm}_r \equiv \frac{|\mathbf{v}|^2 t_{\text{dyn}}}{\eta_r}. \tag{5.38}$$

When any of the magnetic Reynolds number is smaller than unity, the resistivity of the mixture potentially causes a decoupling from the magnetic field. If both Rm_r and $\Gamma_k \ll 1$, then the species k can decouple from the neutral gas by coupling with the magnetic field even when $\text{St}_k \ll 1$.

We also define the β plasma parameter as

$$\beta \equiv \frac{2P}{|\mathbf{B}|^2}, \tag{5.39}$$

this parameter quantifies the relative importance of the thermal and magnetic pressure forces. The magnetic force dominates over the pressure force when $\beta \ll 1$.

The last dimensionless numbers that we define quantifies the relative the importance of the magneto-hydro drift velocity compared to the electromotive drift. This magneto-hydro-to-electromotive-drift ratio writes as

$$\Phi_k \equiv \frac{|\mathbf{w}_{\text{MH},k}|}{|\mathbf{w}_{\text{EM},k}|}. \tag{5.40}$$

5.3 Dynamical regimes

In these section, I introduce the main dynamical regimes that can be explored by our formalism (see table 5.1 for a summary). For simplicity, and as it is the most usual case, I consider in this section that $\mathbf{F}_k = 0$ and $\mathbf{F}_n = -\nabla P_\mathrm{n}$, where P_n is the thermal pressure. Therefore

$$\mathcal{W}_{\mathcal{H},k} = \frac{t_k}{\rho}(\nabla P_\mathrm{n} - \mathbf{J}\times\mathbf{B}).$$

Regime	$\lvert\Gamma_k\rvert$	Φ_k	$\mathbf{w}_k$
Neutral	$\ll 1$	$\gg 1$	$\mathcal{W}_{\mathcal{H},k}$
Resistive	$-$	$\ll 1$	$\mathbf{w}_k \simeq \frac{1}{\lvert\mathbf{B}\rvert}\mathbf{E}_b \times \mathbf{b}$
Ideal MHD	$\gg 1$	$\gg 1$	$\mathcal{W}_{\mathcal{H},k_{//}}$
Guiding Center	$\simeq 1$	$\gg 1$	$\frac{1}{2}\mathcal{W}_{\mathcal{H},k}\times\mathbf{b} + \frac{1}{2}\mathcal{W}_{\mathcal{H},k,\perp} + \mathcal{W}_{\mathcal{H},k_{//}}$

Table 5.1: Summary the different coupling regimes for a phase k. Name of the regime and expression of the terminal drift velocity depending on the Hall factor Γ_k and of Φ_k ($-$ means that the regime is valid for any value of the quantity) .

5.3.1 Neutral regime

When $\Gamma_k \ll 1$ and $\Phi_k \gg 1$ it is easy to show that $\mathbf{w}_k \simeq \mathcal{W}_{\mathcal{H},k}$ which is exactly the expression that one would obtain in the case of neutral grains dynamics when back-reaction is neglected (Laibe & Price, 2014a, or see Chapter 2).

It is interesting to note that since $\mathcal{W}_{\mathcal{H},k} = \frac{t_{\mathrm{s},k}}{\rho_\mathrm{n}}(\nabla P_\mathrm{n} - \mathbf{J}\times\mathbf{B})$, even neutral grains will not preferentially drift toward pressure bumps but rather towards regions where $\nabla P_\mathrm{n} = \mathbf{J}\times\mathbf{B}$. Which can be substantially different in the case where the plasma parameter is of the order of unity or less (e.g. see the next chapter).

5.3.2 Ideal regime

When $\Gamma_k \gg 1$ for all the charged particles, then the electric field writes $\mathbf{E} \simeq \mathbf{v}\times\mathbf{B}$ and ideal MHD becomes a correct approximation. In this case we expect that $\Phi_k \gg 1$ and $\mathbf{w}_k \simeq \mathcal{W}_{\mathcal{H},k_{//}}$, the drift between the charged particles and the neutral gas can only occur along the field lines. Interestingly, $\mathcal{W}_{\mathcal{H},k_{//}} = \frac{t_{\mathrm{s},k}}{\rho}(\nabla P_\mathrm{n}\cdot\mathbf{b})\mathbf{b}$ as the current is orthogonal to the magnetic field. Contrary to neutral grains, that drift toward $\nabla P_\mathrm{n} = \mathbf{J}\times\mathbf{B}$ regions, perfectly coupled magnetized grains do drift toward pressure bumps. However, they only do so along the magnetic field lines.

5.3.3 Resistive regime

Let us now consider the resistive regime for a charged species k that has $\phi_k \ll 1$. In this case, $\mathbf{w}_k \simeq \frac{1}{\lvert\mathbf{B}\rvert}\mathbf{E}_b\times\mathbf{b}$. The resistive regime contains three sub-regimes depending on which resistive effect dominates.

- Ambipolar regime. When $\lvert\sigma_\mathrm{H}\rvert \ll \sigma_\mathrm{P} \ll \sigma_\mathrm{O}$, the ambipolar diffusion dominates over the other resistive effects, then $\mathbf{w}_k \simeq \frac{\eta_\mathrm{A}}{\lvert\mathbf{B}\rvert}\mathbf{J}\times\mathbf{b}$.
- Ohmic regime. If $\sigma_\mathrm{O} \sim \sigma_\mathrm{P} \gg \lvert\sigma_\mathrm{H}\rvert$ we enter the Ohmic regime. In this regime $\mathbf{w}_k \simeq \frac{\eta_\mathrm{O}}{\lvert\mathbf{B}\rvert}\mathbf{J}$.
- Hall regime. If the Hall effect is the dominant resistive effect then we enter the Hall regime where $\mathbf{w}_k \simeq \frac{\eta_\mathrm{H}}{\lvert\mathbf{B}\rvert}(\mathbf{J}\times\mathbf{b})\times\mathbf{b}$.

5.3.4 Guiding center regime

Another interesting regime occurs when $|\Gamma_k| \simeq 1$ and $\Phi_k \gg 1$. In this case, we obtain $\mathbf{w}_k \simeq \frac{1}{2}\mathcal{W}_{\mathcal{H},k} \times \mathbf{b} + \frac{1}{2}\mathcal{W}_{\mathcal{H},k,\perp} + \mathcal{W}_{\mathcal{H},k_{//}}$. $\mathbf{w}_k$, although similar in norm as $\mathcal{W}_{\mathcal{H},k}$ does not have the same direction as in the case of neutral grains. This regime might be of particular interest when grains of $\mathrm{St}_k \sim 0.01 - 0.1$ also have $|\Gamma_k| \simeq 1$ as it significantly alters the dynamics of dust species that typically decouple from the gas in the neutral case.

5.3.5 Critical grain size

A particularly interesting quantity is the maximum grain size s_{crit} for which $|\Gamma_k| > 1$. Assuming the Epstein regime

$$t_k \equiv \sqrt{\frac{\pi\gamma}{8}} \frac{\rho_{\mathrm{grain},k}}{\rho} \frac{s_{\mathrm{grain},k}}{c_{\mathrm{s}}}, \tag{5.41}$$

the condition $|\Gamma_k| > 1$ is expressed as

$$s_{\mathrm{crit}}^2 = \frac{3}{8}\sqrt{\frac{\gamma}{2\pi}} \frac{|Z_{\mathrm{crit}}|e|\mathbf{B}|}{\rho c_{\mathrm{s}}}, \tag{5.42}$$

where Z_{crit}, the average number of charges for a grain of size s_{crit}, need to be determined to find s_{crit} [2] . According to Spitzer (1941); Simpson (1978) a simple estimate of the charge of a grains with a size s_{crit} is

$$|Z_{\mathrm{crit}}| \simeq \frac{k_{\mathrm{B}} T_{\mathrm{g}} s_{\mathrm{crit}}}{e^2 c^2}. \tag{5.43}$$

Combining equations (5.42) and (5.43) yields

$$s_{\mathrm{crit}} \simeq \frac{3}{8}\sqrt{\frac{\gamma}{2\pi}} \frac{k_{\mathrm{B}} T_{\mathrm{g}}}{ec^2} \frac{|\mathbf{B}|}{\rho c_{\mathrm{s}}}, \tag{5.44}$$

which can be further simplified as $c_{\mathrm{s}} = \sqrt{\frac{\gamma k_{\mathrm{B}} T_{\mathrm{g}}}{\mu_{\mathrm{gas}} m_{\mathrm{H}}}}$. We thus obtain

$$s_{\mathrm{crit}} \simeq \frac{3}{8\sqrt{2\pi}} \frac{1}{ec^2} \sqrt{\frac{k_b T_{\mathrm{g}}}{\mu_{\mathrm{gas}} m_{\mathrm{H}}}} \frac{|\mathbf{B}|}{n}, \tag{5.45}$$

where n is the neutral gas number density.

5.4 Discussion

In this section, I review the critical grain size in various astrophysical objects to have a first idea of the dynamical regime that applies to them. We note however that to clearly identify the regime in which a grain stands, an estimate of Φ_k is essential although it is not as trivial as determining s_{crit} because it requires a precise knowledge of the charge distribution and current intensity.

[2] note that in this system of units $e \simeq 1.602 \times 10^{-20}$ abC

5.4.1 Protostellar collapse

During the protostellar collapse, a typical estimate of the magnetic field is (Li et al., 2011)

$$|\mathbf{B}| \simeq 1.43 \times 10^{-7} \sqrt{n}\ \mathrm{G}. \tag{5.46}$$

Considering that during the collapse $\mu_{\rm gas} = 2.31$ and assuming isothermality (which is valid in low density regions) , we can estimate $s_{\rm crit}$ as

$$s_{\rm crit} \simeq 8.8 \times 10^{-6}\ \mathrm{cm} \left(\frac{T_{\rm g}}{10\ \mathrm{K}}\right)^{1/2} \left(\frac{n}{10\ \mathrm{cm}^{-3}}\right)^{-1/2}, \tag{5.47}$$

this size is smaller than most of the grains present in the ISM, which seems to indicate that during the protostellar collapse most grains are well described in the neutral regime. Small sub-nanometer grains such as the Polycyclic Aromatic Hydrocarbons (PaHs) will probably only couple to the magnetic field in low density regions (typically with $n < 10^4 - 10^5\ \mathrm{cm}^{-3}$). Ions, that have a typical size of $\simeq 10^{-8}$ cm could potentially couple to magnetic field up to higher densities.

I refer to Chapter 4 for more detail on the charge during the collapse with another model of magnetic field and grain charging. The main picture is relatively unchanged with the simplified model that I use in this chapter.

5.4.2 Protoplanetary disks

I now aim to estimate $s_{\rm crit}$ in protoplanetary disks (see the next chapter for details on protoplanetary disks). In that perspective, I consider a simple magnetic field configuration where the magnetic field intensity is given by the β parameter such as

$$\frac{|\mathbf{B}|}{n} \simeq 2\sqrt{2\pi}\sqrt{\mu_{\rm gas} m_{\rm H}}\sqrt{\gamma k_{\rm b} T_{\rm g}}\frac{1}{\sqrt{\beta\rho}}. \tag{5.48}$$

Let us now assume a disk density profile (Hayashi, 1981, see the next chapter for the details) such as

$$\rho = \rho_0 e^{-\frac{N_z^2}{2}}, \tag{5.49}$$

where $\rho_0 = 9 \times 10^{-10}\mathrm{g\ cm}^{-3}$ is the disk density at a radius of 1 AU and N_z is the altitude in terms on scale height (typically smaller than $5-6$). Combining the disk equilibrium density with equations (5.45) and (5.48) and considering $\gamma = 1.4$ and $\mu_{\rm gas} = 2.38$ (Bai & Stone, 2013, e.g. as in), we get

$$s_{\rm crit} \simeq 4.73 \times 10^{-12}\mathrm{cm} \left(\frac{T_{\rm g}}{280\ \mathrm{K}}\right)\frac{1}{\sqrt{\beta}} e^{\frac{N_z^2}{4}}, \tag{5.50}$$

this length is extremely small (even compared to the size of an hydrogen atom). β being probably rarely smaller than 10^{-1} within less than $5-6$ scale heights (Lesur et al., 2014), we thus expect dust grains to behave dynamically as is they where neutral in the innermost regions of protoplanetary disks even where the temperature is high. This is consistent with the presence of the dead zones (and the domination of the Ohmic dissipation) in the mid-plane of protoplanetary disks. We note that the mid-plane density ρ_0 decreases with R. In the Hayashi (1981) model for example, $\rho_0 \propto R^{-5/2}$ and $T_{\rm g} \propto R^{-1/2}$. At the disk edge $R \simeq 150$ AU, at $N_z = 5$ and $\beta = 0.1$, we therefore have

$$s_{\rm crit} \simeq 3.3 \times 10^{-7}\mathrm{cm}, \tag{5.51}$$

this is still a very small grain size, especially in the context of protoplanetary disks.

5.4.3 Interstellar medium

Let us now focus on dust in the interstellar medium, where the density is significantly lower than during the protostellar collapse or in protoplanetary disks. I will investigate three different regions, i.e the warm neutral medium (WNM), the cold neutral medium (CNM) and the Giant molecular clouds (GMC). Some key properties of these regions are

- WNM. It is also composed of atomic gas but with temperatures of $T \simeq 10^4$ K and densities of ~ 0.6 cm^{-3} (Draine, 2011).
- CNM. These regions are composed of atomic gas, have temperature of the order of $T \simeq 10^2$ K and densities of ~ 30 cm^{-3} (Draine, 2011).
- GMC. They are large clouds composed of molecular hydrogen and the locus of prestellar cores. They have typical temperatures of $\sim 10 - 50$ K and densities typically larger than 10^3 cm^{-3} (Draine, 2011).

These three regions are intrinsically connected. The thermal instability (Field, 1965; Parker, 1966), occuring at the boundaries of the CNM and the WNM, is one of the most common mechanism to explain molecular cloud formation. These three environment have completely different temperatures. Since they are low density regions and we can expect a strong coupling between the magnetic fields and the grains. In the following, I estimate the critical grain size in the three regions.

WNM

We now place ourselves in the typical WNM conditions, assuming a temperature between 500 K and 7000 K, a density of ~ 0.6 cm^{-3}, $\mu_{\rm gas} = 1$ and a magnetic field between 2 µG and 8 µG (Draine, 2011). We find that typically $s_{\rm crit} \in [0.028, 0.1]$ cm, these values are even largen than what we obtain for the CNM (see next section). They are typically much higher than the maximum grain size expected in the diffuse ISM. This indicates that, in the WNM, all the dust grains strongly couple to the magnetic field and quite possibly decouple with the gas. If the gas is however coupled to the magnetic field the dust might couple to it even better than if they were neutral as they would be in the ideal MHD drift regime ($\mathbf{w}_k \simeq \mathcal{W}_{\mathcal{H},k_{//}}$).

CNM

In the CNM, the temperature is typically 100 K, assuming a density of ~ 30 cm^{-3} and a magnetic field between 2 µG and 8 µG (Draine, 2011) we find $s_{\rm crit} \in \left[6.3 \times 10^{-5}, 2.5 \times 10^{-4}\right]$ cm. Both values are larger than the expected maximum grain size of the diffuse ISM (typically 0.1 µm Mathis et al., 1977). In the CNM, all the dust distribution might thus couple to the magnetic field when the latter is large. In regions of low magnetic fields, the largest grains ~ 0.1 µm might only be marginally coupled with the field.

Molecular clouds

Molecular clouds are the locus of the protostellar collapse and hence star and planet formation. They are typically denser and colder than the CNM and WNM but less dense than collapsing regions. Assuming a typical cloud density of ~ 100 cm^{-3}, temperatures of $\sim 10-50$ K and $\mu_{\rm gas} = 2.31$ and magnetic fields between 2 µG and 8 µG, we obtain $s_{\rm crit} \in \left[3.8 \times 10^{-6}, 3.5 \times 10^{-5}\right]$ cm. The bulk of the grain size distribution [3] is still coupled to the magnetic fields in molecular

[3] in terms of abundance and not in terms of mass

clouds if there is no dust growth in GMC. If grains larger than a micron are already formed in this clouds (Pagani et al., 2010), they will rather couple to the neutral gas than to the magnetic fields although it was shown by Tricco et al. (2017) that this coupling is not perfect either and leads to strong dust-to-gas ratio variations.

5.5 Conclusion

In this chapter, I introduced a monofluid formalism in the terminal velocity approximation useful to model simultaneously several neutral and charged fluids. This formalism allows to follow simultaneously the decoupling of charged particles with the neutral gas or with the magnetic field under the approximation that neutral gas-charged collisions are the most frequent and that the cumulative back-reaction of dust on the neutral gas is negligible. I proposed a solution to extend this formalism including the back-reaction with a first-order Taylor expansion in terms of charged particle concentration. In the near future, I aim to use this method to include the impact of charged-charged collisions.

After a presentation of the derivation of the monofluid in section 5.2, I described the dynamical regimes that can be treated with this formalism in section 5.3. These regimes are:

1. The neutral regime. Whatever their charge, the grains are not coupled to the magnetic field.

2. The ambipolar, Ohmic and Hall regimes, that are the three non-ideal MHD regimes where the drift between the charged particles and the neutral depends on which non-ideal effect dominates.

3. The ideal MHD regime, where all the charged particles are strongly coupled with the magnetic fields and with the neutral gas, only a drift parallel to the magnetic field lines remains.

4. The guiding center regime, where the charged are marginally coupled to the magnetic field. In this regime the drift velocity is typically of the same order of magnitude as if they were neutral but its direction is changed.

After presenting the dynamical regimes, I introduced the maximum grain size for a grains to couple more to the magnetic field than to the neutral gas. The study of this critical grain size in protoplanetary disks and during the protostellar collapse indicates that when the density is high enough (typically larger than 100 cm^3), the grains are more prone to behave as if they were neutral no matter how many charges they hold. I have however shown that the smallest grains of the size distribution might still be marginally coupled to the magnetic fields in low density regions and that it is worth investigating their dynamics. In low density parts of the star forming ISM such as the cold neutral medium, the warm neutral medium and giant molecular cloud, I have shown that most grains are significantly coupled to the magnetic field. I have yet to determine if this strong coupling with the magnetic field weakens or strengthens the coupling between the grains and the neutral gas.

Chapter 6

Chondrule formation in protoplanetary disks

Contents

Samwise Gamgee

"Come on, Mr. Frodo ! I can't carry it for you, but I can carry you."

- The Lord of the Rings (The Return of the King)

In this final chapter, I focus on evolved protoplanetary disks around T-Tauri stars. More specifically, I investigate a possible formation mechanism for chondrules in resistive current sheets. After drawing some of the essential context, I introduce my preliminary results and current issues. This work is carried out in collaboration with Pr. Mordecai-Mark Mac Low. I got the pleasure to work with him at the American Museum of Natural History (AMNH) in New York City. This visit took place in 2018 and was allowed by the Kade Fellowship[1].

6.1 Context

The dust content of the solar system originates from interstellar dust. All the dust collected on earth is highly reprocessed either during the early solar system evolution or during the entry in earth's atmosphere. This is especially the case in chondrites. They are the most often found type of meteorites (around 80% mass). In these meteorites, the chondrules represent the 20 – 80% the mass. They are surrounded by a matrix of fine grains that are more numerous than chondrules. The chondrules are spherical silicate grains of 0.1 – 1 mm with a glassy texture (Jones et al., 2005). To constrain the physical conditions at play in protoplanetary disks, it is essential to find a common mechanism that explains chondrule formation and is able to reproduce their abundance in the solar system.

Chondrule properties indicate that they might form during rapid heating and cooling events called flashes (see Boss, 1996, for a short review of chondrule formation theories). The abundance of chondrules is an evidence that these flashes, no matter how and where they occur, are common enough to turn a large fraction of the dust into chondrules. Nevertheless, a chondrule forming flash must meet at least three prerequisites. They must have extremely short timescales (less than a few minutes, Connolly & Love, 1998), be very localized so that the chondrule can exit them rapidly (Hubbard & Ebel, 2015) while being energetic enough to increase the grain temperature up to $\approx$ 1700 – 2000 K (Lofgren & Lanier, 1990; Radomsky & Hewins, 1990; Hewins & Connolly, 1996). Compared to the free-space cooling time of chondrule-sized objects of a few seconds, the cooling rate must be relatively slow ($\approx 10^2 - 10^3$ K h^{-1} Radomsky & Hewins, 1990). Chondrules are most likely formed in repeated heating events which suggest that they must experience several flashes during their heating (Barosch et al., 2020). Chondrule formation theories must also be able to reproduce their narrow range of size (0.1 – 1 mm, Jacquet, 2014; Friedrich et al., 2015), their diversity of composition and must explain the presence of the matrix. The evidence for complementarity suggests a reservoir of common origin for chondrules and matrix. Nevertheless, the matrix grains are clearly different from chondrules in term of composition and size. They contain a substantial abundance of volatiles that would evaporate at temperatures higher than 500 – 800 K, which indicates that they do not experience any dramatic heating event. In addition, the matrix is mostly composed of fine grains (less than $\lesssim 5\mu$m). Whether it is a by-product of chondrule formation (Huss et al., 2005) or a population that experiences a totally different evolution, the question of the matrix formation is intrinsically related to chondrule formation.

Magnetic fields in protoplanetary disks have been widely studied as a possible source of angular momentum transport via the so-called *magnetorotational instability* (hereafter MRI,

[1] I was granted a total of 9,500 $ by the Richard Gilder Graduate School for a three month stay

Balbus & Hawley, 1991; Stone et al., 1996; Sano et al., 2000, among others). As disks are in fact poorly ionised, the importance of the MRI has later been downward revised as mid-plane dead zones have been theorized (Gammie, 1996; Fleming et al., 2000). Some studies have shown that it might even be suppressed entirely in disks, with the angular momentum carried away instead by magnetocentrifugal winds (Bai & Stone, 2013; Lesur et al., 2014). An imperfect coupling between the neutral and the magnetic field however might give birth to interesting dissipative structures (Brandenburg & Zweibel, 1994). An interesting theory of chondrule formation states that it could happen it in narrow current sheets (Joung et al., 2004). These dissipative structures are believed to occur because of the finite electric conductivity (Parker, 1972, 1994; Joung et al., 2004). The resistive heating might be efficient enough in current sheets so that dust grains reach their melting temperatures (McNally et al., 2014). In addition, it was shown by Hubbard et al. (2012), that the increase of the temperature could theoretically reduce the sheets spatial extension making them a favoured place for chondrule formation. Current sheet formation has been investigated in the unstratified shearing box models of McNally et al. (2014) with Ohmic dissipation only and observed in global (Gressel et al., 2015) simulations of protoplanetary disks as well. In parallel, recent studies have started to investigate dust dynamics in resistive disks (Riols & Lesur, 2018; Riols et al., 2020) however the dust behaviour near the current sheets and in presence of dissipation essentially remains unexplored.

In this chapter, I investigate the theory of chondrule formation in current sheet simulations with the help of both unstratified and stratified shearing box simulations including the dynamics of multiple neutral dust species. After a recall of the theoretical framework, I present the early results of my simulations and the perspectives to improve my models.

6.2 Theoretical framework

In this section, I review the essential properties of resistive dusty protoplanetary disks.

6.2.1 NdustyNIMHD for protoplanetary disks

Around T-Tauri stars, the disk mass is much smaller than the mass of the star, it is usual to neglect the self gravity of the disk. In this context the equations of MHD with multiple neutral dust grains species write as

$$\begin{aligned}
\frac{\partial \rho}{\partial t} + \nabla \cdot [\rho \mathbf{v}] &= 0, \\
\frac{\partial \rho_k}{\partial t} + \nabla \cdot [\rho_k (\mathbf{v} + \mathbf{w_k})] &= 0, \ \forall k \in [1, \mathcal{N}], \\
\frac{\partial \rho \mathbf{v}}{\partial t} + \nabla \cdot \left[\left(P_\mathrm{g} + \frac{\mathbf{B}^2}{2} \right) \mathbb{I} + \rho (\mathbf{v} \otimes \mathbf{v}) - \mathbf{B} \otimes \mathbf{B} \right] &= -\rho \mathbf{g}, \\
\frac{\partial \mathbf{B}}{\partial t} - \nabla \times \left[(\mathbf{v} - \sum_{k=1}^{\mathcal{N}} \frac{\rho_k}{\rho - \rho_k} \mathbf{w_k}) \times \mathbf{B} \right] &= -\nabla \times \mathbf{E_b}, \\
\nabla \cdot \mathbf{B} &= 0,
\end{aligned} \tag{6.1}$$

where I still model the dust differential velocity as

$$\mathbf{w_k} = \left[\frac{\rho}{\rho - \rho_k} t_{\mathrm{s},k} - \sum_{l=1}^{\mathcal{N}} \frac{\rho_l}{\rho - \rho_l} t_{\mathrm{s},l} \right] \frac{\nabla P_\mathrm{g} - (\nabla \times \mathbf{B}) \times \mathbf{B}}{\rho}. \tag{6.2}$$

This set of equations is essentially the same as in Chapter 4 but without self-gravity. The gravitational acceleration is $\mathbf{g}$ is now simply given by

$$\mathbf{g} = -\frac{\mathcal{G}M_*}{|\mathbf{r}-\mathbf{r}_*|^3}(\mathbf{r}-\mathbf{r}_*) \tag{6.3}$$

where M_* is the mass of the central star and $\mathbf{r}_*$ is its position. At this point, let us recall the definition of the plasma parameter

$$\beta \equiv \frac{2P_\mathrm{g}}{|\mathbf{B}|^2}. \tag{6.4}$$

6.2.2 Thin-disk approximation

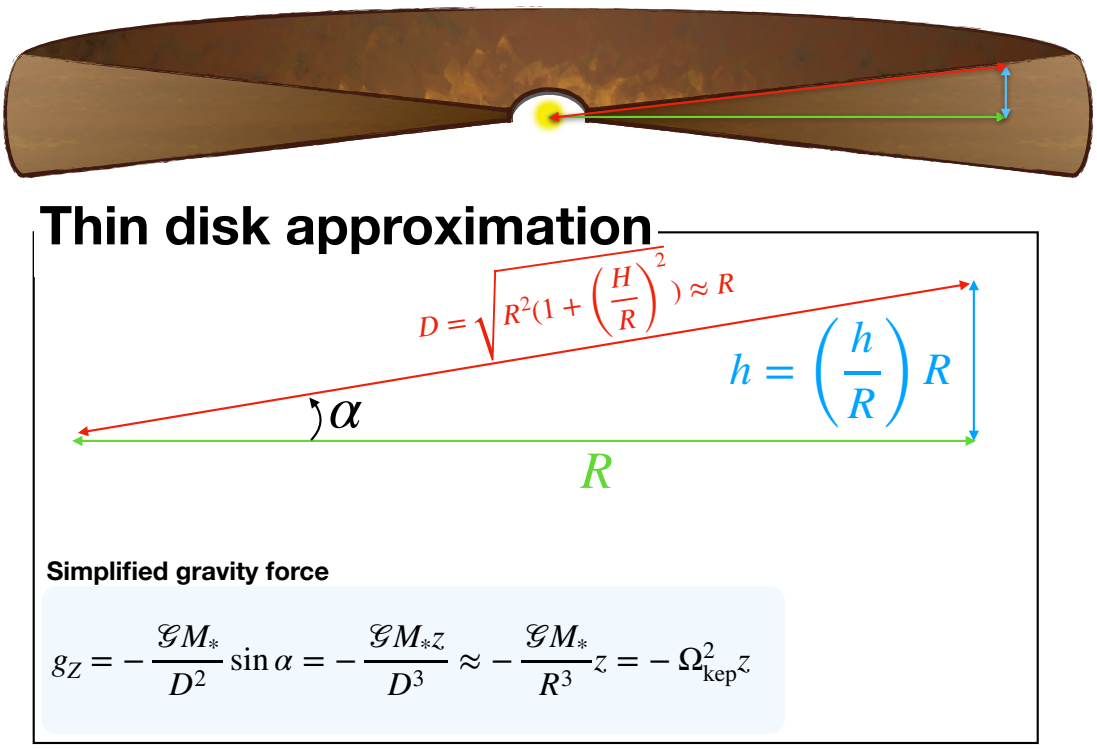

Figure 6.1: Cartoon illustration of an edge-on cut of a protoplanetary disk explaining the principle of the thin-disk approximation. As $H/R \ll 1$, the distance to the star can be approximated by the cylindrical radius. As a consequence, the gravitational force is simplified and an analytical solution for the hydrostatic equilibrium can be found.

We now place ourselves in a cylindrical set of coordinates where R is the cylindrical radius, z is the altitude and θ is the azimuthal angle. At equilibrium and neglecting magnetic fields or dust, we find

$$\frac{\partial P_\mathrm{g}}{\partial z} = \rho_\mathrm{g} g_Z, \tag{6.5}$$

$$\frac{\partial P_\mathrm{g}}{\partial R} = \rho_\mathrm{g} g_R + \frac{\rho_\mathrm{g} v_\theta^2}{R}, \tag{6.6}$$

If we assume that the protoplanetary disk is vertically thin, which constitutes the *thin disk approximation*, then the gravity can be simplified (see figure 6.1 for the justification)

$$\mathbf{g} \equiv (g_R, 0, g_Z) = \left(-\Omega_{\text{kep}}^2 z, 0, -\Omega_{\text{kep}}^2 R\right), \tag{6.7}$$

where $\Omega_{\text{kep}} \equiv \sqrt{\frac{\mathcal{G}M_*}{R^3}}$ is the Keplerian orbital velocity.

Vertical equilibrium

At first, we place ourselves at a radius R and focus on the vertical equilibrium. With the simplified gravitational acceleration, equation (6.5) becomes

$$\frac{\partial P_{\text{g}}}{\partial z} = \rho_{\text{g}} g_Z. \tag{6.8}$$

As the disk is very thin $z \ll R$, it is reasonable to assume vertical isothermality ($\frac{\partial c_{\text{s}}}{\partial z} = 0$, c_{s} being the gas sound speed). We can re-write equation (6.8) for a perfect gas as

$$\frac{1}{\rho_{\text{g}}} \frac{\partial \rho_{\text{g}}}{\partial z} = -\frac{z}{H^2}, \tag{6.9}$$

H, the disk *scale-height*, is defined as

$$H = \frac{c_{\text{s}}}{\Omega_{\text{kep}}}. \tag{6.10}$$

Solving equation (6.8) yields

$$\rho_{\text{g}}(R, z) = \rho_{\text{g},0}(R)\, e^{-\frac{z^2}{2H^2}}, \tag{6.11}$$

where $\rho_{\text{g},0}(R)$, the mid-plane density, is an integration constant for z that only depends on the cylindrical radius. The mid-plane density is a free-function of R modeled as

$$\rho_{\text{g},0}(R) = \rho_0 \left(\frac{R}{R_0}\right)^{-n}, \tag{6.12}$$

where ρ_0, R_0 and n can be chosen to best reproduce observed disks.

Radial equilibrium

If we now assume that the temperature also has as a power law radial dependency such as

$$T_{\text{g}} = T_{\text{g},0} \left(\frac{R}{R_0}\right)^{-\alpha}, \tag{6.13}$$

then

$$c_{\text{s}} = c_{\text{s},0} \left(\frac{R}{R_0}\right)^{-\alpha/2}, \tag{6.14}$$

and

$$\frac{1}{\rho_{\text{g}}} \frac{\partial c_{\text{s}}^2 \rho_{\text{g}}}{\partial R} = -\frac{(n+\alpha)\, c_{\text{s}}^2}{R}. \tag{6.15}$$

Which yields

$$v_\theta = R\Omega_{\rm kep}\sqrt{1-(n+\alpha)\left(\frac{H}{R}\right)^2}. \tag{6.16}$$

In thin disks, the gas is almost Keplerian with a small deviation of the order of H/R. If H/R is large then the pressure force starts to act on the rotation velocity and this deviation must be considered. To simplify the model, I now assume that $v_\theta = R\Omega_{\rm kep}$.

Thin disk model

In summary,thin disks equilibrium can be approximated as

$$\begin{aligned} \rho_{\rm g}(R,z) &= \rho_0\left(\frac{R}{R_0}\right)^{-n} e^{-\frac{z^2}{2H^2}} \\ v_\theta(R,z) &= R\Omega_{\rm kep}. \end{aligned} \tag{6.17}$$

6.2.3 Shearing box approximation

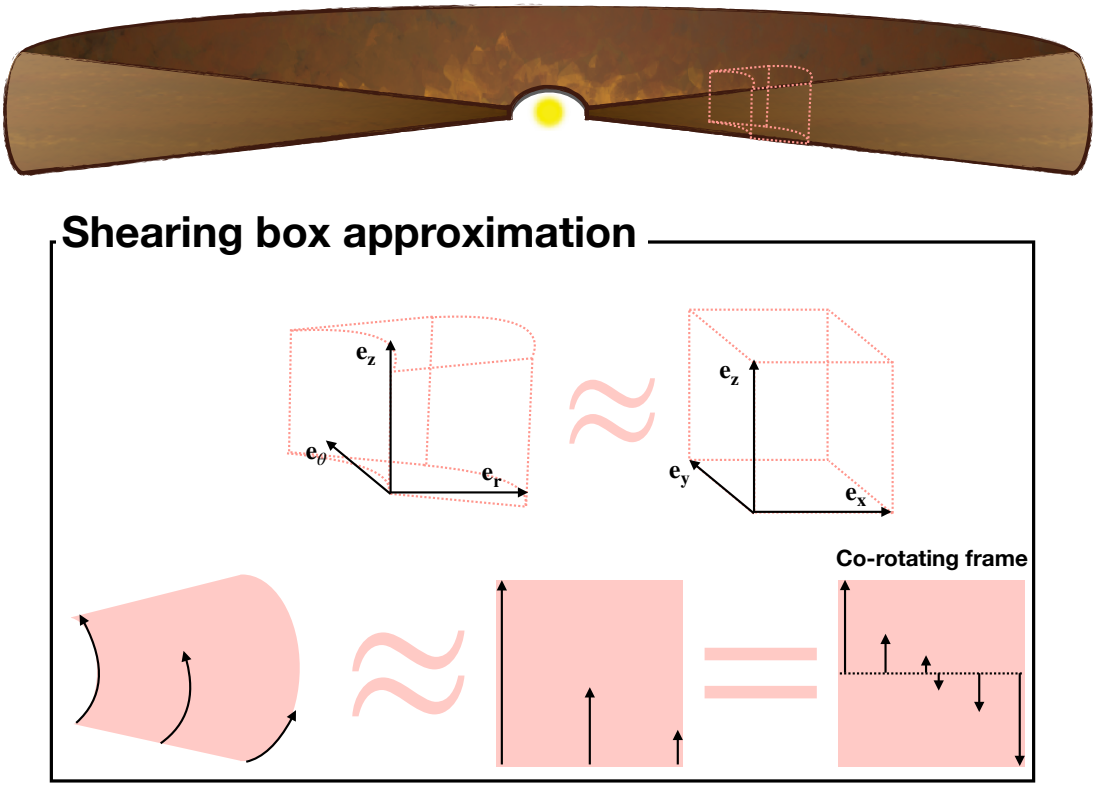

Figure 6.2: Cartoon illustration of an edge-on cut of a protoplanetary disk explaining the principle of the shearing box approximation. In the shearing box, we neglect both the curvature terms and the radial dependency of the hydrodynamical quantities.

Modeling the protoplanetary disk as a whole is computationally expensive, especially when attempting to resolve the current sheets. Fortunately, a simple approximation can be made when considering only a small part of the disk. In this so-called *vertically stratified shearing*

box approximation (VSBA, Hawley et al., 1995), we only model a small volume of the disk at a radius R_0 called the shearing box, with a length $L_0 \ll R_0$ typically of a few H and in rotation at the Keplerian velocity $\Omega_{\rm kep}|_{R_0}$. We then neglect any radial variations of the quantities within the shearing box (as shown is the cartoon illustration of figure 6.2). Neglecting locally the curvature of the disk (Hill, 1878), we can approximate the shearing box as a Cartesian box where $e_x = e_r$ and $e_y \approx e_\theta$. In the Keplerian case $\Omega \propto R^{-3/2}$ hence

$$\frac{\partial \Omega_{\rm kep}}{\partial R}|_{R_0} = -\frac{3}{2}\frac{\Omega_{\rm kep}|_{R_0}}{R_0}, \tag{6.18}$$

for simplicity we now write $\Omega_{\rm kep}|_{R_0} \equiv \Omega$. In the co-rotating frame, and in absence of any perturbation, the disk material flows at the shear velocity $v_{\rm shear}$ in the x direction. It is expressed as

$$v_{\rm shear} = -q\frac{x}{R_0}\Omega. \tag{6.19}$$

Out of equilibrium, the total momentum conservation equation becomes (Hawley et al., 1995)

$$\frac{\partial \rho \mathbf{v}}{\partial t} + \nabla \cdot \left[\rho \mathbf{v} \otimes \mathbf{v} + (P_{\rm g} + \frac{\mathbf{B^2}}{2})\mathbb{I} + \mathbf{B} \otimes \mathbf{B}\right] = -2\rho\Omega \times \mathbf{v} + \rho \mathbf{g}, \tag{6.20}$$

where the gravitational acceleration $\mathbf{g}$ is given by $\mathbf{g} = -2q\Omega^2\mathbf{x} - \Omega^2\mathbf{z}$. The term $-2\rho q\Omega^2\mathbf{x}$ represents the centrifugal pseudo-force and $-2\rho\Omega\times\mathbf{v}$ is the Coriolis force. The vertical gravitational acceleration, $-\Omega^2\mathbf{z}$, is often neglected in what is called *unstratified shearing boxes*.

6.2.4 Ionization fraction

Protoplanetary disks are poorly ionized (Fromang et al., 2002; Lesur et al., 2014). The *electron fraction* x_e (equal to the ionization fraction in the dust free case) needs to be determined in order to quantify the impact of the non-ideal resistivities on the disk evolution (essentially on the gas and dust motions). The ionization fraction is defined as

$$x_e \equiv \frac{n_e}{n_n}, \tag{6.21}$$

where n_e and n_n are number densities of the electrons and the neutrals, respectively. The ionization model follows Lesur et al. (2014) and Béthune et al. (2017). In a metal free environment Gammie (1996) and Fromang et al. (2002) have shown that

$$x_e \simeq \sqrt{\frac{\zeta}{k_r n_n}}, \tag{6.22}$$

where ζ is the ionization rate and k_r is the dissociative recombination rate coefficient of molecular ions that is estimated as (Leu et al., 1973)

$$k_r \simeq 3 \times 10^{-6} T_{\rm g}^{-1/2} {\rm cm}^3 {\rm s}^{-1}. \tag{6.23}$$

In addition, as in Lesur et al. (2014), I also consider the ionization from far-ultraviolet (FUV) radiation $x_{\rm FUV} = 2 \times 10^{-5} e^{-(\Sigma/0.03 \text{ g cm}^{-2})^4}$ such as

$$x_e \simeq \sqrt{\frac{\zeta}{k_r n_n}} + x_{\rm FUV}. \tag{6.24}$$

To compute x_e, one must evaluate the ionization rate ζ. As in Lesur et al. (2014)

$$\zeta = \zeta_{\rm cr} + \zeta_{\rm rad} + \zeta_{\rm x-rays}, \tag{6.25}$$

where

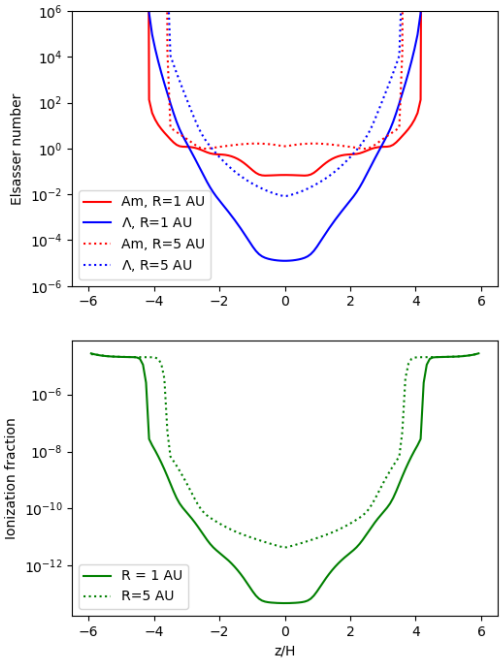

Figure 6.3: Elsasser number (top) and ionization fraction (bottom) profiles of the stratified models at $R = 1$ AU (solid lines) and $R = 5$ AU (dashed lines).

- The ionization rate by the cosmic rays is given by $\zeta_{\rm cr} = \zeta_{\rm cr,0} e^{-(\Sigma/96\ {\rm gcm}^{-2})}$ where $\zeta_{\rm cr,0} = 10^{-16}$ s^{-1} (see for example Umebayashi & Nakano, 1981).

- The radioactive decay of ^{26} Al is given by $\zeta_{\rm rad} = 10^{-19}$ s^{-1} (Umebayashi & Nakano, 2009).

- The ionization from x-ray photons at 3 kev (Igea & Glassgold, 1999; Bai & Goodman, 2009) is given by

$$\begin{aligned}\frac{\zeta_{\rm x-rays}}{L_{x,29}}\left(\frac{R}{1{\rm AU}}\right)^{2.2} &= \zeta_1\left(e^{-\frac{N_+}{1.5\times10^{21}{\rm cm}^{-2}}^{0.4}} + e^{-\frac{N_-}{1.5\times10^{21}{\rm cm}^{-2}}^{0.4}}\right)\\ &+ \zeta_2\left(e^{-\frac{N_+}{7\times10^{23}{\rm cm}^{-2}}^{0.65}} + e^{-\frac{N_-}{7\times10^{23}{\rm cm}^{-2}}^{0.65}}\right),\end{aligned}$$

  where $L_{x,29} = \frac{L_x}{10^{29}{\rm erg}}$, L_x being the x-ray luminosity of the star. As in Béthune et al. (2017), I consider the case $L_x = 10^{30}$erg s^{-1} which is typical of T-Tauri stars. N_+ and N_- are the number column density above and bellow the considered point. Finally, we have $\zeta_1 = 6 \times 10^{-12}$ s^{-1} and $\zeta_2 = 10^{-15}$ s^{-1}. The first two terms represent the attenuation of x-rays by absorption and the two last terms represent the contribution from scattering.

This estimate of the ionization fraction, although simplified, considers most of the effects at play in protoplanetary disk. It however lacks an essential ingredient which is the dust. It could play an essential role in the ionization level by capturing the free-electrons becoming the main charge carriers in the disk (Marchand et al., 2016).

6.2.5 Resistivities

The ionization fraction allows us to directly infer the value of the resistivities assuming only one ion species (potassium K^+ of mass $m_i = 39\, m_H$, Balbus & Terquem, 2001) we have

$$\begin{aligned} \eta_O &= \frac{c^2 m_e}{4\pi e^2}\frac{1}{x_e}\langle\sigma v\rangle_e\,, \\ \eta_A &= \frac{|\mathbf{B}|^2}{\gamma_i \rho_i \rho}. \end{aligned} \tag{6.26}$$

where $\langle\sigma v\rangle_e = 8.28\times10^{-9}\sqrt{\frac{T_g}{100\ \mathrm{K}}}\mathrm{cm^3 s^{-1}}$ is the electron-neutral collision rate (Draine et al., 1983) and $\gamma_i = \frac{\langle\sigma v\rangle_i}{\mu_g m_H + m_i}$ where the ion-neutral collision rate (Draine, 2011), writes as $\langle\sigma v\rangle_i = 1.3\times10^{-9}\mathrm{cm^3 s^{-1}}$. As a first step, I do not consider yet any effect of the Hall resistivity which constitutes one of the caveats of this study.

At this stage it is interesting to define the ambipolar and Ohmic Elsasser numbers Am and Λ, that quantify the relative importance of the resistivity and the Alfven wave propagation and are defined as

$$\begin{aligned} \mathrm{Am} &\equiv \frac{v_A^2}{\eta_A \Omega}, \\ \Lambda &\equiv \frac{v_A^2}{\eta_O \Omega}, \end{aligned} \tag{6.27}$$

where $v_A \equiv |\mathbf{B}|/\sqrt{\rho}$ is still the Alfven speed.

Figure 6.3 shows the Elsasser number (top) and ionization fraction (bottom) profiles of the stratified models at $R = 1$ AU (solid lines) and $R = 5$ AU (dashed lines). As can be seen, the impact resistivities is expected to be significant in the inner 2 to 4 scale heights above the mid-plane. Typically Ohmic dissipation is dominant in the close to the mid-plane while ambipolar diffusion takes over at around $2-3H$. At these scale heights, the Elsasser numbers are typically of the order of 1-100.

6.2.6 Resistive heating

The Ohmic and ambipolar resistivities both introduce a heating term in the energy equation, Λ_O and Λ_A respectively (see chapter 5). These two heating terms can be written as

$$\begin{aligned} \Lambda_O &\equiv \eta_O \|\mathbf{J}\|^2, \\ \Lambda_A &\equiv \eta_A \frac{\|\mathbf{J}\times\mathbf{B}\|^2}{\|\mathbf{B}\|^2}. \end{aligned} \tag{6.28}$$

In this preliminary study, I do not introduce these terms in the energy equation and assume isothermality because including them would require an accurate treatment of the cooling terms as well.

6.2.7 Useful quantities

Several quantities need to be defined in order to properly analyze magnetized disks. First let us define the spatial horizontal average of any quantity A as

$$\langle A\rangle_S = \frac{1}{L^2}\iint A\mathrm{d}x\mathrm{d}y, \tag{6.29}$$

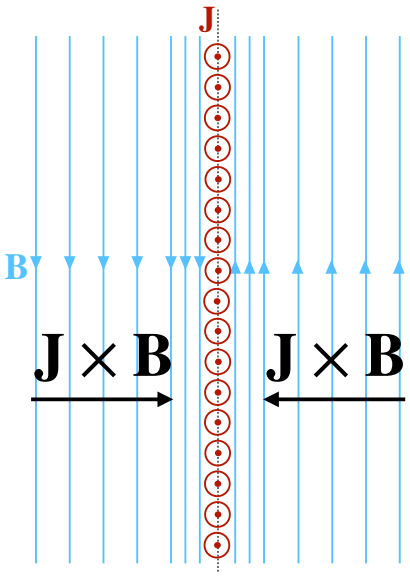

Figure 6.4: Illustration of a current sheet near a magnetic null (black dotted line). The magnetic field lines are displayed in blue, while the current direction is given by the red symbols.

where L is the box size. I also define the time average as

$$\langle A \rangle_{\mathcal{T}} = \frac{1}{T_2 - T_1} \int A \mathrm{d}t, \tag{6.30}$$

where T_1 is the time at which the average starts and T_2 the time at which it ends, both are specified in the text. Naturally the horizontal space-time average then is defined as

$$\langle A \rangle_{\mathcal{S},\mathcal{T}} = \frac{1}{T_2 - T_1} \frac{1}{L^2} \iiint A \mathrm{d}x\mathrm{d}y\mathrm{d}t, \tag{6.31}$$

There are two source of angular momentum transport in my models.

- the Maxwell stress tensor, defined as $M = -\mathbf{B} \otimes \mathbf{B}$. It quantifies the amount of momentum transported by the magnetic field.
- the Reynolds stress tensor, defined as $R = \rho \mathbf{v} \otimes \mathbf{v}$. It quantifies the amount of momentum transported by the fluid motions.

Using these two quantities, we can define the effective radial transport parameter (Shakura & Sunyaev, 1976)

$$\alpha = \frac{\int \left(\left\langle M_{xy} \right\rangle_{\mathcal{S},\mathcal{T}} + \left\langle R_{xy} \right\rangle_{\mathcal{S},\mathcal{T}} \right) \mathrm{d}z}{\int P_{\mathrm{g}} \mathrm{d}z}, \tag{6.32}$$

it quantifies the efficiency of angular momentum transport in the disk is typically smaller than 1.

6.2.8 Current sheets generation

To understand the basic principle of current sheet formation, let us place ourselves in a simple one dimensional case as in Joung et al. (2004) with a magnetic field in the y direction and varying with x. This simple configuration is illustrated in figure 6.4. Similarly to Joung et al.

(2004), I assume that the resistive part of the induction equation rapidly dominates over the $\nabla \times (\mathbf{v} \times \mathbf{B})$ term and that the Ohmic resistivity is locally uniform. When a steady state is reached, the induction equation of B_y simplifies as

$$(B_0^2 + B_y^2)\frac{\mathrm{d}^2 B_y}{\mathrm{d}x^2} + 2B_y\left(\frac{\mathrm{d}B_y}{\mathrm{d}x}\right)^2 = 0, \tag{6.33}$$

where $B_0 = \sqrt{\eta_O \gamma_i \rho_i \rho}$. The solution of this equation satisfies the condition

$$\frac{1}{3}B_y^3 + B_0^2 B_y = Cx, \tag{6.34}$$

where C is an integration constant. It can be determined by estimating the value of the magnetic field at $x = \frac{1}{2}\lambda_{\mathrm{MRI}}$, $\lambda_{\mathrm{MRI}} = \frac{2\pi}{\sqrt{3}}(v_A/\Omega)$ being the distance between two magnetic nulls (or current sheets), but also the wavelength of the most MRI unstable mode (Balbus & Hawley, 1991).

Naturally, we expect the magnetic field to be close to its maximum value $B_{\max}$ at $x = \frac{1}{2}\lambda_{\mathrm{MRI}}$, hence we have

$$C = \frac{2B_{\max}(B_0^2 + \frac{1}{3}B_{\max}^2)}{\lambda_{\mathrm{MRI}}}, \tag{6.35}$$

where $B_{\max}$ is inferred from the remnant magnetic field in chondrites which is typically a few Gauss (Desch & Connolly, 2002; Fu et al., 2014). When $B_0^2 \ll \frac{1}{3}B_y^2$, this model retrieves the expected behavior of ideal where $B_y \propto x^{1/3}$ or $J_z \propto x^{-2/3}$ (Brandenburg & Zweibel, 1994). We note that here the peak of the current is obtained at $x = 0$. As stated in Joung et al. (2004), we can define the typical current sheet thickness L_{CS} as the value of x where there is a transition between the resistive and ideal regime, i.e where $B_0^2 \sim \frac{1}{3}B_y^2$. This yields

$$L_{\mathrm{CS}} \approx \frac{2\sqrt{3}B_0^3}{C}. \tag{6.36}$$

With a simplified resistivity profile Joung et al. (2004) obtained

$$L_{\mathrm{CS}} \sim 1.5 \times 10^5 \left(\frac{n}{10^{13}\mathrm{cm}^3}\right)\left(\frac{T_g}{1000\mathrm{K}}\right)\left(\frac{B}{1\mathrm{G}}\right)\left(\frac{B_{\max}}{3\mathrm{G}}\right)^{-3}\left(\frac{R}{3\ \mathrm{AU}}\right)^{3/2}\ \mathrm{km}. \tag{6.37}$$

6.3 Numerical Model

In this work, I still take advantage of my implementation of the dust dynamics in the RAMSES code (see Chapter 3 for more details). My new tool is indeed well suited to study dust dynamics in the context of protoplanetary disks. I present, in this chapter, two types of shearing box models, the unstratified and stratified models. In this manuscript, I emphasize more on the unstratified models. I also present the setup of the stratified models that are described in sectio 6.5. Although they are less advanced, they represent the next goal of this study and its interesting to discuss them.

6.3.1 Numerical scheme

In all the models, I integrate equations (6.1) replacing the momentum equation by equation (6.20). I use the MUSCL scheme of RAMSES with the HLLD Riemann solver for the barycenter part of the MHD equations and for the induction equation (Miyoshi & Kusano,

2005). For stability and similarly to Fromang et al. (2013), the solver automatically switches to a Lax–Friedrichs solver where $\beta < 10^{-3}$. As in Fromang et al. (2013) and again for stability issues, I use the multidimensional slope limiter of Suresh (2000) for the barycenter part of the conservation equations. Similarly to Colling et al. (2018), I use an operator-splitting and an implicit Crank-Nicholson scheme to take into account the shear source terms in equation (6.20) without adding any constrain on the scheme stability.

For the dust source term, I use the upwind MUSCL solver that I implemented in RAMSES and I use the MINMOD slope limiter (see Chapter 2 for the details on the implementation). I found that using this slope limiter for the differential dust advection source term is significantly faster as it does not require the computation of any transverse derivatives.

6.3.2 Regularization of the scheme

When regions of very small density form in a model, they can lead to very large Alfven velocities and hence very small timesteps. When this happens, to evolve significantly the model in a reasonable time is impossible. To circumvent this issue, I impose an adaptive density floor that prevents β to be smaller than the value $\beta_{\rm min} = 10^{-4}$. In other words, I impose

$$\rho = \max\left(\rho, \beta_{\rm min}\frac{|\mathbf{B}|^2}{2c_{\rm s}^2}\right). \tag{6.38}$$

I noticed that this floor is enough to get tractable timesteps and is actually less restrictive than density floors used in the previous studies of Bai & Stone (2013); Bai (2013) and simpler than implementing a source term in the density as in Fromang et al. (2013). I point out that this method is strictly equivalent to imposing a maximum Alfvenic Mach number.

In low density regions, the terminal velocity approximation no longer holds. I impose a maximum dust differential velocity of 5 km s^{-1} everywhere in the box to avoid unphysically large dust velocities or new constraint on the timestep. This value is typically only reached in regions of very low densities. For safety, I also enforce the maximum Stokes number to be 0.3 by setting

$$t_{{\rm s},k} = \min\left(t_{{\rm s},k}, \frac{0.3}{\Omega}\right). \tag{6.39}$$

This last regularization is similar to what was used in Ballabio et al. (2018).

6.3.3 Boundary conditions

Radial boundaries

In shearing box simulations, the shear must be imposed at the ghost cells of the radial boundaries. I adapted the previous implementation of the shearing box in RAMSES by Colling et al. (2018) used in galactic disk simulations to Keplerian rotation. At the upper boundary, the shear requires replacement of the value of the conservative variables in the ghost cell (at the exception of the magnetic field and the radial velocity) by the value in the lower domain shifted by $-q\Omega\frac{L}{2}t$ (modulo half the box size). Similarly, the hydrodynamical variables of the lower boundary are estimated by applying the shear $q\Omega\frac{L}{2}t$ on the upper domain. In addition, the shear is added to the radial velocity so that $v_{r,\rm ghost} = v_r + q\Omega\frac{L}{2}$. At each timestep, the length at which ghost zones are displaced is not an integer multiple of the grid size, hence a linear interpolation between two adjacent cells is required to get the exact value of the shear at the ghost zone. Figure 6.5 shows a simplified cartoon illustration of the shearing box radial boundary conditions for the hydrodynamical variable when ghost cells are exactly moved one cell size during a timestep.

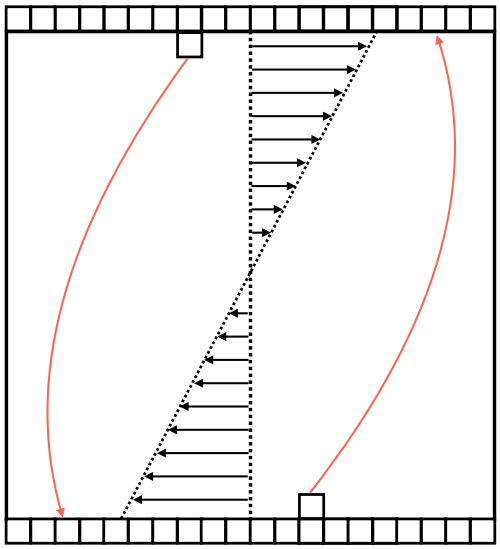

Figure 6.5: Cartoon illustration of the shearing boundary conditions (inspired from Colling et al., 2018). Values in the ghost zone are obtained by the advection of the variables of the corresponding cells at the opposite side of the domain.

The magnetic field is treated differently because one must ensure the preservation of the solenoidal constrain. I first impose the continuity of the tangential magnetic fields (B_y and B_z) by setting a zero-gradient between the ghost zone and the extremity of the computational domain. Then, I also enforce the continuity of B_x in the face of the ghost cell neighboring the domain by copying its value from the last cell of the computational domain. Finally the value of B_x in the remaining face of the ghost cell is deduced by enforcing a zero divergence in the cell.

Azimuthal and vertical boundaries

In all the models, azimuthal boundaries are treated as simple periodic boundaries. For the unstratified models, the vertical boundaries are also periodic. They however require a special treatment in the stratified case. To avoid any odd symmetry in the wind solution (Bai & Stone, 2013), to gain in resolution at a cheap cost and to partly circumvent the cubical box of `RAMSES`, I model only the upper half of the disk, hence the lower vertical boundary is treated as a reflective boundary, which is similar to a zero gradient boundary but with a flip of the vertical component of the velocity. The upper boundary is a zero-gradient boundary where I forbid any inflow by imposing a positive vertical component of the velocity. As for the shearing boundaries, the magnetic fields also require a special treatment. At the lower boundary, the magnetic field is treated exactly as for the shear boundary. At the upper boundary, I impose the continuity of the vertical component of the magnetic field and set the horizontal component to zero as in previous studies (Fromang et al., 2013; Bai & Stone, 2013; Lesur et al., 2014).

6.3.4 Initial conditions

Equilibrium

- **Unstratified models**. I impose a constant initial density and a temperature of 300K. The initial magnetic field is vertical with $\beta_0 = 750$. In addition, the effect of vertical gravity is neglected. Although the vertical gravity is neglected, the Coriolis and Centrifugal force are kept. These models have a box length of one scale height, i.e 0.05 AU as all the unstratified models are computed at $R_0 = 1$ AU. The models are all isothermal, however future models will explore the impact of heating and cooling.

- **Stratified models**. The disk equilibrium is computed according to the Hayashi (1981) model where the initial column density and temperatures are given by

$$\begin{aligned} \Sigma &= \Sigma_0 \left(\frac{R}{R_0}\right)^{-3/2} \\ T_g &= T_{g,0} \left(\frac{R}{R_0}\right)^{-1/2} . \end{aligned} \tag{6.40}$$

As in Hayashi (1981), $\Sigma_0 = 1700$ g cm^{-2}, $T_{g,0} = 280$ K and $R_0 = 1$ AU. The initial density ρ is determined by equation (6.17) where

$$\rho = \frac{\Sigma}{2\pi R H} e^{-\frac{z^2}{2H^2}}, \tag{6.41}$$

The initial magnetic field is vertical with mid-plane value for β_0 of 10^5. During the disk evolution, a magneto-centrifugal wind is quickly triggered. As there is no way for accretion to proceed in local disk simulation, the mass of the box decreases significantly if one does not replenish it as it would naturally occur in a global accretion disk. To mimic the steady state implied by the replenishment of the disk, I multiply the density by an uniform factor at each timestep to ensure the total mass conservation (Ogilvie, 2012)[2].

Dust

In all the runs, I consider three dust species of size 10 µm,100 µm and 1 mm with initial dust-to-gas ratios of 1/3%. I choose not to explore the behavior of grains smaller than a micron because they are probably strongly coupled with the gas (as 10 µm grains). All the dust species have an intrinsic grain density of 3 g cm^{-3}. In this model, I did not considered the Kwok correction of the stopping time as the gas soundspeed is significantly higher than during the first protostellar collapse.

Resitivities

- **Unstratified models** The initial ambipolar and Ohmic resistivity are initially uniform and imposed by setting the value of the Elsasser number. Through the run, the Ohmic resistivity stays constant. The ambipolar resistivity however varies as it scales as $\propto |\mathbf{B}^2|$. To avoid very small timesteps, I cap the value of the resistivies by the value $10\Omega H^2$ as Lesur et al. (2014). This safety threshold has not yet been reached in the stratified models.

- **Stratified models** The ambipolar and Ohmic resistivities are set according to the model presented in sections 6.2.4 and 6.2.5. For simplicity, the column density used to get the ionization profile is considered constant and matches the initial conditions during the run. I indeed assume that it does not vary significantly during the evolution of the models. I aim to reproduce the strong ionization in high altitudes where the vertical isothermal approximation breaks down (Aresu et al., 2011). I therefore multiply the resistivity by a factor $e^{-(x_e/10^{-8})}$ as in Béthune et al. (2017). I still cap the values of the resistivity to $10\Omega H^2$ to avoid very small timesteps.

[2] I do not do this for unstratifed runs since they use periodic conditions at $z = \pm L/2$ and mass is better conserved

6.4 Results

In this section, I present some of the preliminary results in the unstratified case. I briefly discuss the stratified models in section 6.5.

6.4.1 Models

The naming of the models follows simple rules. Each unstratified model name starts with the label UNSTR while stratified model names start with STR. When either the Ohmic dissipation of the ampibolar diffusion is activated, the letter O and A are included in the name respectively. For the unstratified models the number following O and A refers to the initial value of the Elsasser number of the Ohmic dissipation and ambipolar diffusion. For the stratified models no Elsasser number is specified because the resistivity is computed according to the model presented above. If a non-ideal effect is not activated then its corresponding letter is absent in the model name. The initial mixture density is specified by the number after the letter D. For the unstratified models, it refers to the density according to $\rho_0 = 10^{-\text{D}}$g cm^{-3}, while, for the stratified models, it refers to the column density such as $\Sigma_0 =$ D g cm^{-2} . Finally the radius at which the model is computed is given after the letter R.

I show in table 6.1 the main properties of each model including their name, the presence of stratification, the box size, the radial distance from the star, information on which non-ideal effect is considered, the initial density (of the mid-plane for stratified runs), α and the current final time of the model t_{end} expressed in units of Ω^{-1}. In addition, I provide the resolution and the initial plasma parameter β. In the future, I will run these models further in time until they all reach at least $t = 100\ \Omega^{-1}$ in the unstratified case and $t = 1000\ \Omega^{-1}$ in the stratified case.

6.4.2 Fiducial run

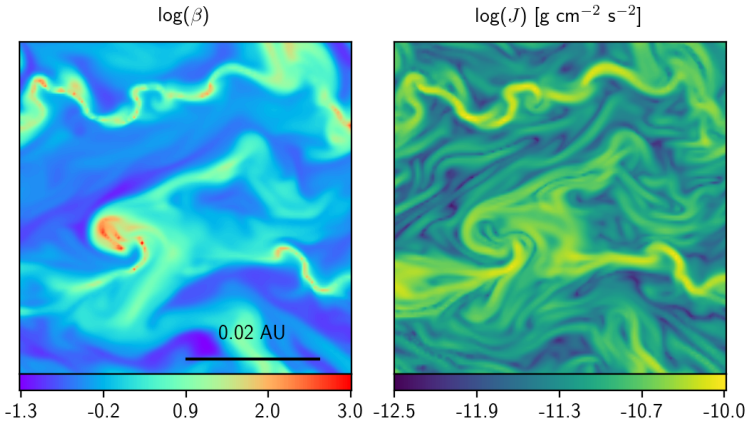

Figure 6.6: Edge-on slices (x-z cuts) of the beta plasma (left) and the current (right) at $t = 5$ years ($\sim 31\Omega^{-1}$) for the UNSTR-O10A10D11R1 model.

In this section, I introduce my fiducial model UNSTR-O10A10D11R1 which is an unstratified model at $R = 1$ AU. In this model, both the ambipolar diffusion and the Ohmic dissipation are activated. The ambipolar and Ohmic initial Elsasser numbers are both set equal to 10.

Figure 6.6 shows a slice of the β plasma (left) and the current (right) at $t = 5$ years which corresponds approximately to $\sim 31\Omega^{-1}$. As can be seen, some MRI turbulence has developed in this model. There are strong local variations of β ranging between ~ 0.05 and ~ 1000. I

Model	Strat.	L (AU)	R (AU)	Ambip.	Ohmic	ρ_0 (g cm^{-3})	α	Am	Λ	$t_{\rm end}$ (Ω^{-1})
UNSTR-O10A10D11R1	No	0.05	1	Yes	Yes	10^{-11}	0.66	10	10	38.6
UNSTR-O1A1D11R1	No	0.05	1	Yes	Yes	10^{-11}	0.28	1	1	33.1
UNSTR-O10A10D10R1	No	0.05	1	Yes	Yes	10^{-10}	0.75	10	10	34.4
UNSTR-D11R1	No	0.05	1	No	No	10^{-11}	0.88	∞	∞	56
STR-OAD1700R1	Yes	0.3	1	Yes	Yes	$\sim 9\times10^{-10}$	6.3×10^{-3}	N/A	N/A	443
STR-OAD1700R5	Yes	1.5	5	Yes	Yes	$\sim 1.8\times10^{-10}$	1.34×10^{-2}	N/A	N/A	464.25
	Resolution	β	Hall							
Unstratified runs	128^3	750	No							
Stratified runs	64^3	10^5	No							

Table 6.1: Summary of the different simulations, with the name of the model, the presence of stratification, the box size, the radial distance from the star, information on which non-ideal effect is considered, the initial density (of the mid-plane for stratified runs), α (averaged up to the end of the calculation) and the current final time of the model $t_{\rm end}$. In addition, I provide the resolution and the initial plasma parameter β.

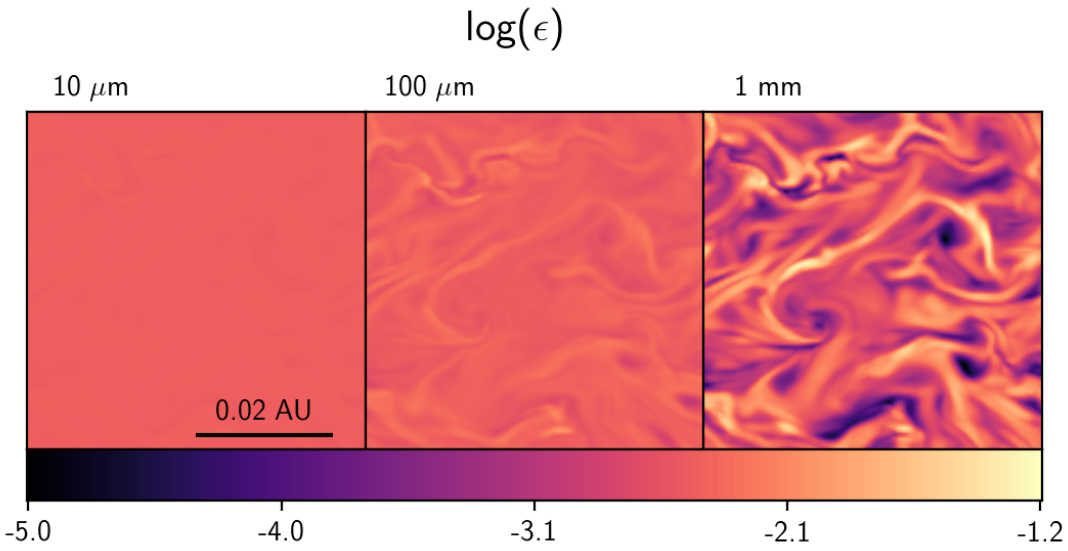

Figure 6.7: Edge-on slices (x-z cuts) of the dust ratio at $t = 5$ years ($\sim 31\Omega^{-1}$) for the UNSTR-O10A10D11R1 model. The dust grain size increases from left to right. The unique colorbar has been chosen to display at best the dust ratio variations for the millimeter grains.

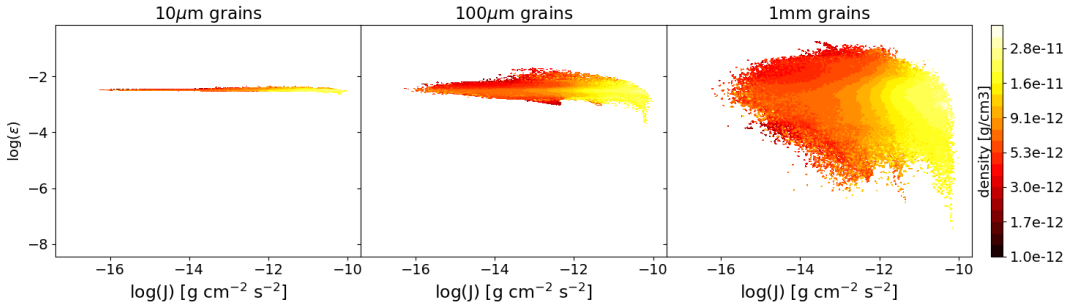

Figure 6.8: Histogram of the dust ratio ϵ of the 10 μm (left), 100 μm (middle) and 1 mm grains (right) as a function of the current $\|\mathbf{J}\|$ at $t = 5$ years for the UNSTR-O10A10D11R1 model. The colors represent the averaged total density (the colorbar is log-scaled).

verified, by looking at parallel slices, that the complex structures in the current are made of sheets rather than filaments although they might re-organize themselves after a longer integration time. These sheets have a typical width of $\approx 10^{-3}$ AU $\approx 1.5 \times 10^5$ km which is about the same order of magnitude as our previous estimate but it also of the order of $4\Delta x$. We can thus wonder if the current structures are resolved yet. I am currently running the same model with twice the resolution to confirm this.

In figure 6.7, I show a slice of the dust ratio for the 10 μm (left), 100 μm (middle) and 1 mm grains (right) at $t = 5$ years. The colorbar of these three slices is unique and aims to display at best the variation of dust ratio of the 1 mm grains. As can be seen, these grains experience a strong dynamical sorting. Their dust ratio indeed increases up to two order of magnitude in a significant fraction of the volume. Smaller 100 μm grains also experience significant, although less important, dust ratio variations (up to an order of magnitude). The dust ratio variations of 10 μm are much smaller (about ±10% at most). Dust grains tend to be more depleted in current maxima. This is actually not unexpected, if we consider a magnetically dominated

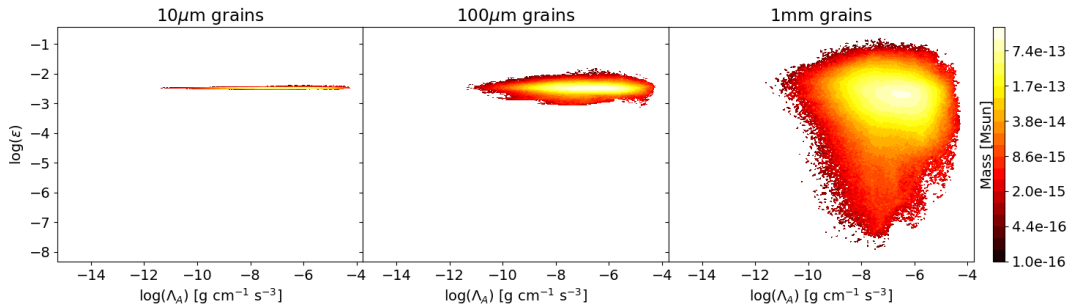

Figure 6.9: Histogram of the dust ratio ϵ of the 10 µm (left), 100 µm (middle) and 1 mm grains (right) as a function ambipolar heating source Λ_A term at t $t = 5$ years for the UNSTR-O10A10D11R1 model. The colors represent the integrated total mass (the colorbar is log-scaled).

plasma ($\beta < 1$), the differential dust velocity can be approximated as $\mathbf{w}_k \approx -t_{s,k}\frac{\mathbf{J}\times\mathbf{B}}{\rho}$, and dust thus tends to be repelled from current sheets (see figure 6.4 for the structure of $\mathbf{J}\times\mathbf{B}$ in current sheets). This correlation between strong currents and low dust ratio is clearly visible in figure 6.8 that shows the histogram of the dust ratio as a function of the current for the three dust species. We note, however, that a significant proportion of the dust is still observed in high current regions.

The heating source term $\Lambda_A = \eta_A \frac{||\mathbf{J}\times\mathbf{B}||^2}{||\mathbf{B}||^2}$ due to ambipolar diffusion dominates strongly over the Ohmic source term $\eta_O||\mathbf{J}||^2$ in this model. The ambipolar term $\frac{||\mathbf{J}\times\mathbf{B}||^2}{||\mathbf{B}||^2}$ does not have the same morphology as $||\mathbf{J}||^2$. The strongly heated regions are thus not necessarily where the peaks of the current sheets are. In figure 6.9, I display the histogram of the dust ratios as a function of Λ_A, the color represents the integrated mass. In the right panel, we see that the bulk of the mass for the millimeter dust grains resides in regions of moderate heating although large dust ratio can be noted in a wide range of Λ_A. As explained earlier, the dust ratio variations of small 10 µm grains are much less important. There is no significant preferential sorting of these grains.

6.4.3 Impact of the resistivity

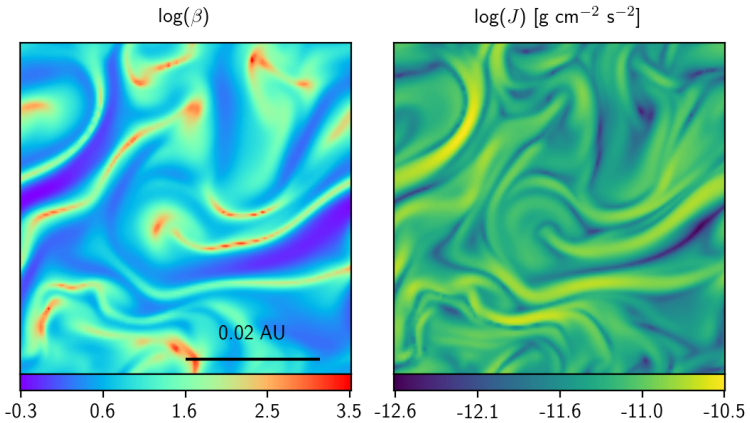

Figure 6.10: Same as figure 6.6 for the UNSTR-O1A1D11R1 model.

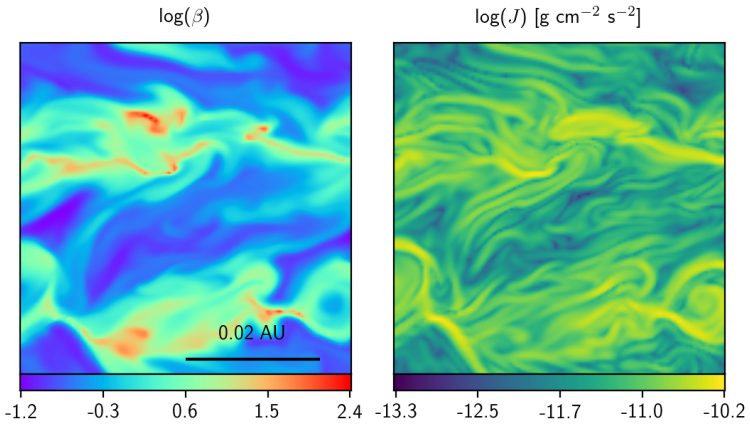

Figure 6.11: Same as figure 6.8 for the UNSTR-D11R1 model.

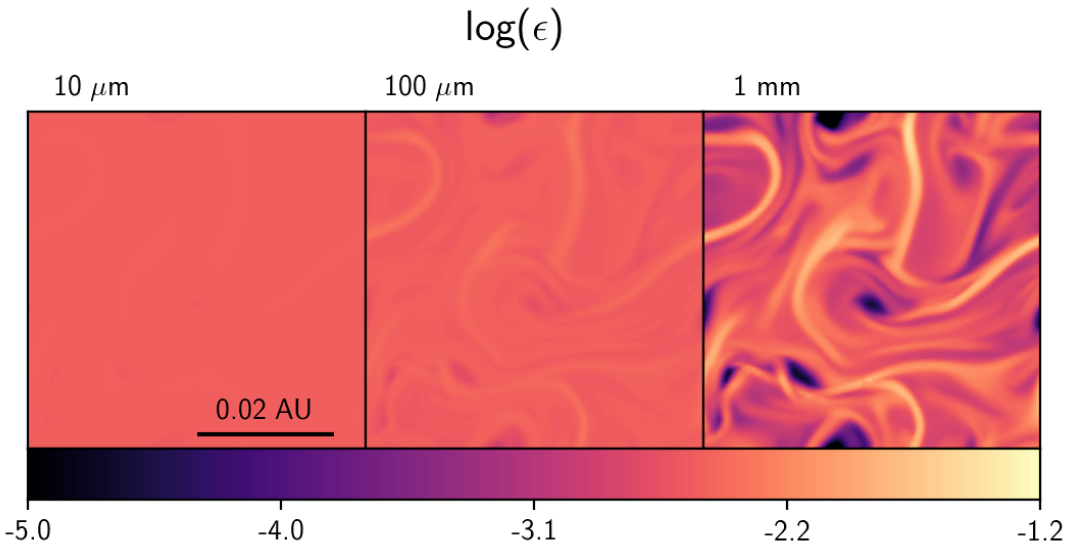

Figure 6.12: Same as figure 6.7 for the UNSTR-O1A1D11R1 model. The colormap is set to match the one in figure 6.7

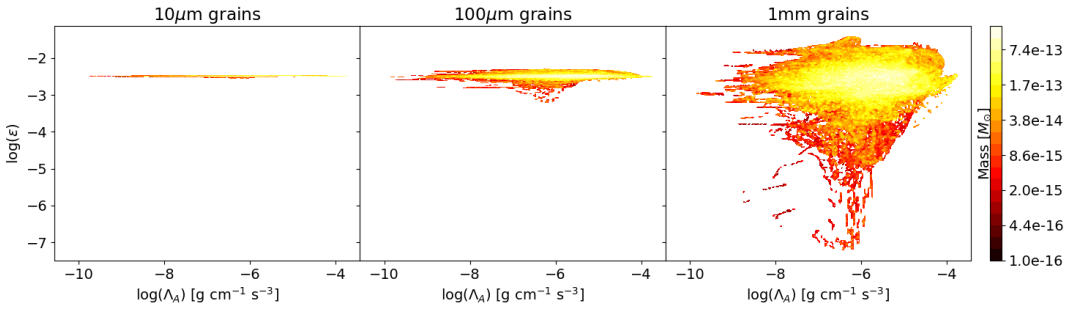

Figure 6.13: Same as figure 6.9 but for the UNSTR-O1A1D11R1 model.

I now explore the impact of resistivity with two additional models, UNSTR-O1A1D11R1 and UNSTR-D11R1. In the first model, the two Elsasser numbers are set to one, and the second model is computed with ideal mhd.

Figure 6.10 and 6.11 show slices of the β index (left) and the current (right) at $t = 5$ years for UNSTR-O1A1D11R1 and UNSTR-D11R1, respectively. As can be seen, in both model similar current sheets structures form as in the fiducial mode. In the case of UNSTR-O1A1D11R1, these sheets are wider than for the fiducial case with a typical size of $\sim 2 \times 10^{-3}$ AU. A widening of the current structures is expecting with an increasing resistivity. As the ambipolar length increases, the magnetic field lines are rearranged over larger scales. In figure 6.11, that shows the ideal case, we observe, on the contrary, a sharpening of the current structure but also an increased number of strong current sheets. We should however keep in mind that, in the ideal case, the current structures are non-dissipative. The magnetic field can however generate high temperatures because the MRI turbulence compresses the gas. However, as stated in McNally et al. (2013), the regions of strong compression might be too short lived to consistently generate enough heat to form chondrules.

Figure 6.12 shows a slice of the dust ratio for the 10 µm (left), 100 µm (middle) and 1 mm grains (right) at $t = 5$ years for the UNSTR-O1A1D1R1 model. We observe local variations of the dust ratio for the 100 µm and 1 mm grains of the same order of magnitude as in UNSTR-O10A10D11R1, however the regions of high dust ratio are wider in this model because the current sheets are also wider. In this model, we see even better that the dust tends to migrate toward regions of small current. However, as explained earlier these regions are not necessarily regions of low dissipation by ambipolar diffusion. As can be seen in figure 6.13, that shows the histograms of the dust ratio for each dust species as a function of Λ_A, a significant fraction of the regions of high ambipolar heating are actually significantly enriched in 1 mm grains. Smaller 10 µm grains are still very coupled everywhere.

6.4.4 Impact of the density

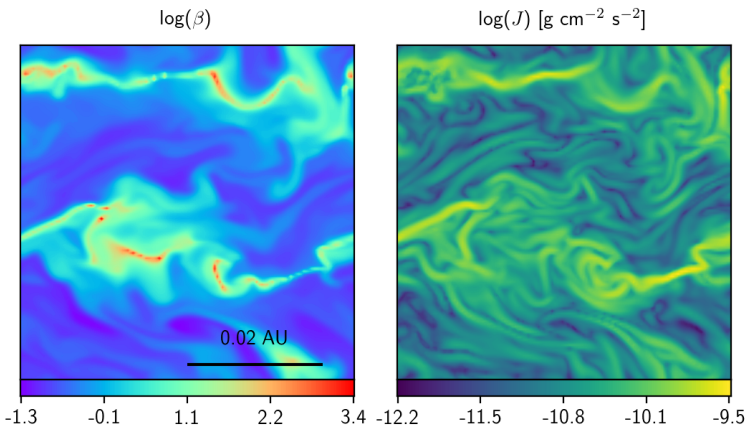

Figure 6.14: Same as figure 6.6 for the UNSTR-O10A10D10R1 model.

As the dust drift velocity scales as $\propto \frac{1}{\rho^2}$, it is essential to study the impact of the initial density on the dust ratio evolution near current sheets. To do this, I have run the UNSTR-O10A10D10R1 model, which is the same model as the fiducial, but with an initial density of 10^{-10}g cm^{-3}.

As can be seen in figure 6.14, that shows again slices of the β index (left) and the current (right) at $t = 5$ years for UNSTR-O10A10D10R1. Sheet-like regions of high current still form at a higher density. In fact, the peak of current measured in this model is actually higher than in the fiducial model. The dust however concentrates less in this model, as was expected. Figure 6.15 shows the slice of the dust ratio for the 10 µm (left), 100 µm (middle) and 1 mm grains (right) at $t = 5$ years for this model. The colormap is still set to match the one from my

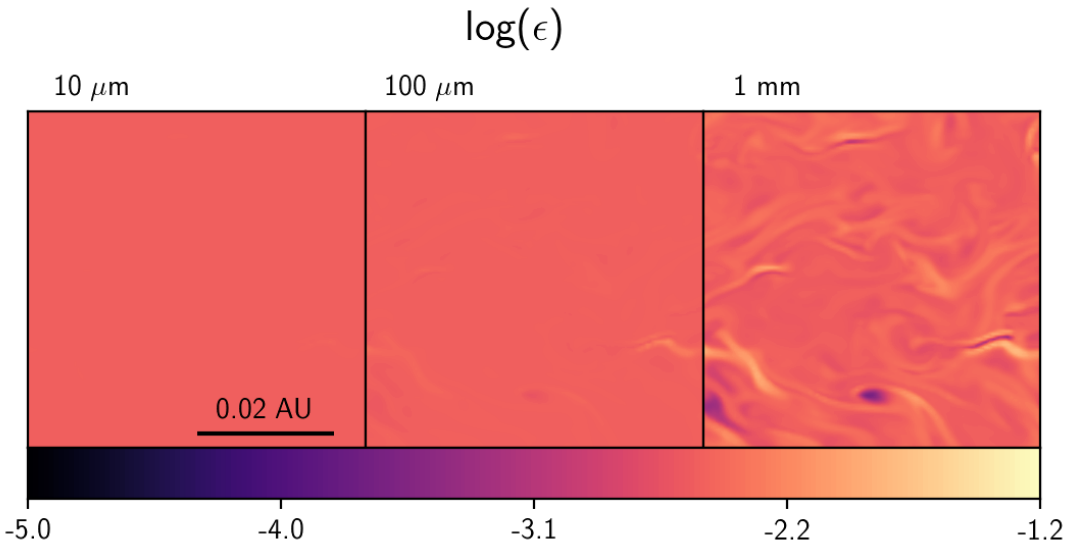

Figure 6.15: Same as figure 6.7 for the UNSTR-O10A10D10R1 model. The colormap is set to match the one in figure 6.7

fiducial model. We do observe less variations of dust ratio in this model than in the fiducial one, however they are still significant. In particular, there are local increases of dust ratio of up to one order of magnitude near current sheets for the millimeter grains. This increase is caused by a strong depletion of grains in the peak of the current sheets. Note that even if the increase of dust ratio for the millimeter grain is one order of magnitude smaller than in my fiducial, the peak millimeter dust densities of the two models are comparable since the initial mixture density of UNSTR-O10A10D10R1 is ten times higher. In summary, the physical conditions in UNSTR-O10A10D10R1 might be as favorable as in UNSTR-O10A10D11R1 to form millimeter size chondrules.

6.5 Future work and conclusion

6.5.1 Heating and cooling

All the models here were computed in the isothermal approximation. My first goal for improvement is to include the resistive heating terms in order to assert that it can generate localized hot spots of temperature $\gtrsim$ 1000 K. I have already run preliminary models with the ambipolar and ohmic heating in the setup and an exponential orbital cooling term to mimic the impact of radiation. This simple prescription for the cooling led to very high temperatures of $\gtrsim$ 5000 K.

In order to accurately describe the thermal evolution, I will first include the thermal conduction flux in the energy equation. This term is already implemented in `RAMSES` and should be relatively straightforward to include. Later, I aim to better estimate the cooling source term in the energy equation by using FUV thermochemical models similarly to Gressel et al. (2020).

6.5.2 Lagrangian dust evolution

It is not straightforward to determine the thermal history of dust grains with an Eulerian dust solver. In order to retrieve it, future models will be computed with Monte-Carlo tracer particles (Cadiou et al., 2019) that I recently coupled with my dust dynamics solver. It will be used to

- follow the temperature of dust grains
- follow their interaction with current sheets
- compute the chondrule mass formation rate.

6.5.3 Stratifed local and global models

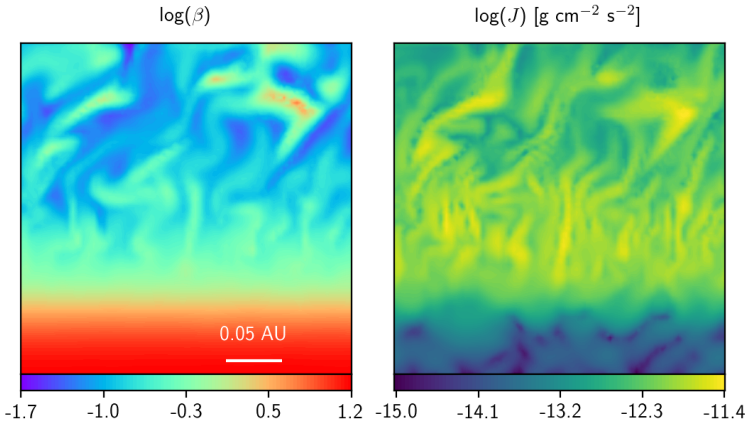

Figure 6.16: Same as figure 6.6 for the STR-OAD1700R1 model at $t = 60$ yr ($\sim 375\Omega^{-1}$). In this case 0.05 AU is also the disk scale height.

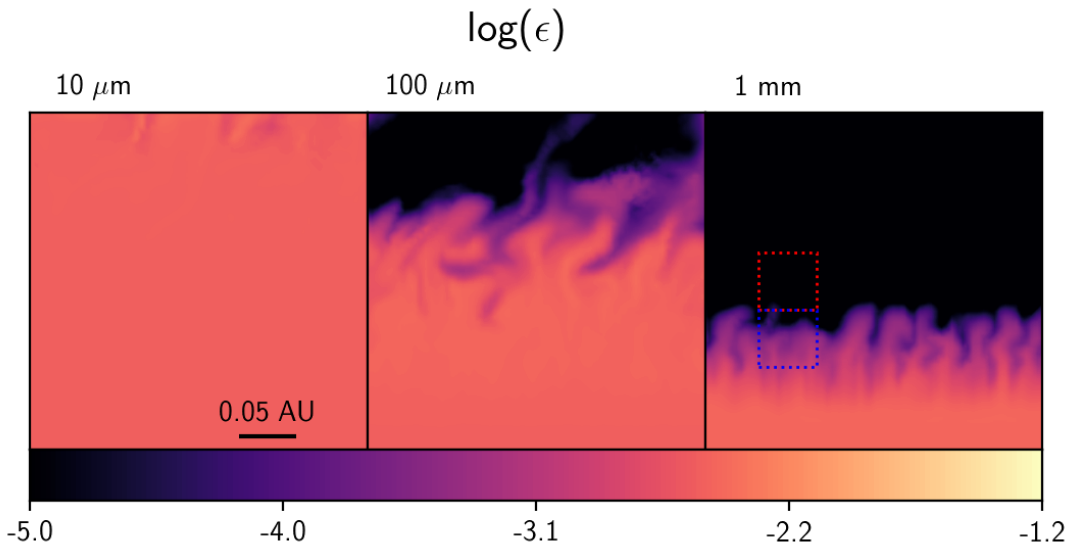

Figure 6.17: Same as figure 6.7 for the STR-OAD1700R1 model at $t = 60$ yr ($\sim 375\Omega^{-1}$). The colormap is set to match the one in figure 6.7. The squares represents the unstratified boxes and are placed in the regions when the physical conditions are roughly similar to UNSTR-O10A10D11R1 and UNSTR-O1A1D11R1 (for the red square) and UNSTR-O10A10D10R1 and UNSTR-O1A1D10R1 (for the blue square).

The long term goal of this study is to investigate chondrule formation in global disk models that include the radial dependency of the disk profile. As a first step, I now consider the vertical stratification. The two main objectives of including stratification are

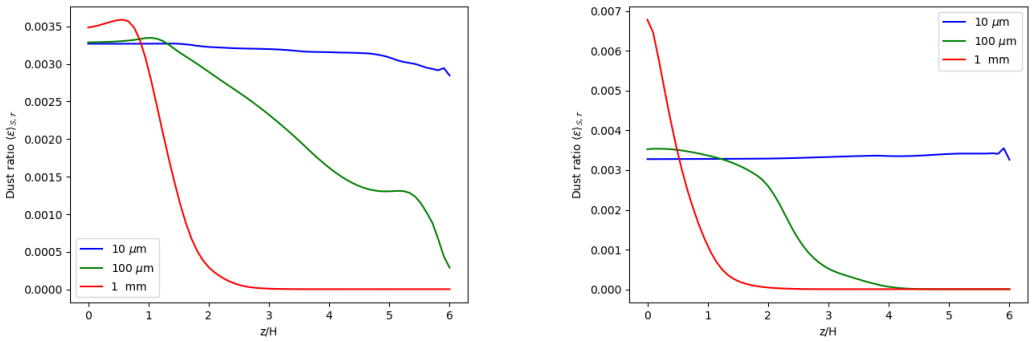

(a) STR-OAD1700R1 model (b) STR-OAD1700R5 model

Figure 6.18: Averaged dust ratio profile for the two stratified runs

- to determine if large dust grains are present far above the mid-plane where the current sheets are believed to form;
- to confirm that current sheets do form even when stratification is included.

My fiducial stratified model is STR-OAD1700R1. The set of parameters used for this model is described in table 6.1. In short, it is a model computed at a radial distance from the star of 1 AU that includes both ambipolar diffusion and Ohmic dissipation. Figure 6.16 show slices of the β plasma (left) and the current (right) at $t = 60$ years for STR-OAD1700R1. We observe a relatively dead zone near the disk mid plane ($z < H$), although the mid-plane β is significantly smaller than expected from this model (that is very similar to 1-OA-5 in Lesur et al., 2014, for example). I also note that the value of α measured in STR-OAD1700R1 is 6.3×10^{-3}, which is higher that what is measured by Lesur et al. (2014) or Bai & Stone (2013) by almost one order of magnitude. In other words, the angular momentum transport is likely to be too efficient and the mid-plane magnetic field is likely to be too strong in my models. This discrepancy with the literature could be due to several reasons, such as an insufficient resolution of the current models (10 points per scale-height while Lesur et al., 2014, have 16 points per scale-height), the fact that I model only the upper half of the disk or that we must use a cubical box with RAMSES. Future models with twice the resolution or that include the two sides of the disk will be dedicated to understand this discrepancy. Until then, the results from the two stratified runs cannot be considered as conclusive.

Above the mid-plane, complex sheet-like current structures can be clearly distinguished. These high-current regions are quite thick compared to those observed in the unstratified runs, but one could expect them to narrow down with an increasing resolution. Figure 6.17 shows a slice of the dust ratio for the 10 μm (left), 100 μm (middle) and 1 mm grains (right) for the fiducial at $t = 60$ yr ($\sim 375\Omega^{-1}$). The squares are placed at the approximate location where the physical conditions in the model are roughly similar to UNSTR-O10A10D11R1 and UNSTR-O1A1D11R1 (red square) and UNSTR-O10A10D10R1 and UNSTR-O1A1D10R1 (blue square). As can be seen, millimeter grains settle efficiently in the inner regions of the mid-plane and the wind, although properly developed, is not sufficiently strong to lift them to regions of density $\sim 10^{-11}$g cm^{-3} (red square), they are however not absent from the regions of density $\sim 10^{-10}$g cm^{-3} (blue square). As explained earlier, the dust sorting near current sheets in these regions is less important for $\rho \sim 10^{-10}$g cm^{-3} than it is for $\rho \sim 10^{-11}$g cm^{-3} but still significant and the initial density of $\rho \sim 10^{-10}$g cm^{-3} compensates for the sorting difference. Figures 6.18a and 6.18b show the average dust ratio profile as a function of height for both stratified

models. As can be seen, the settling is even more efficient in STR-OAD1700R5. Close to the mid-plane, the dust ratio of these grains is almost doubled. As a consequence they are strongly depleted above 1-2 scale heights. Intermediate 100 μm grains are quite present up to 2 scale height in both models and are also depleted above that. As can be seen, the small grains are efficiently redistributed over the entire computational domain by the wind.

6.5.4 Summary

In this chapter, I presented preliminary results of an ongoing study that aims to investigate a model of chondrule formation in current sheets within weakly ionized protoplanetary disks.

After an introduction to the essential theoretical and numerical aspects of protoplanetary disk evolution. I presented two types of models;

- Unstratified models. I have shown that structures similar to current sheets are formed under various initial conditions. I have also shown that the structures in the current can lead to an important sorting for grains of $\gtrsim$ 100 μm. This is particularly interesting in the context of chondrule formation as they are thought to form in regions of high solid concentration (Alexander et al., 2008) and because the typical minimum chondrule size is about $\gtrsim$ 100 μm. It is also worth noting again that, in all the unstratified models, regions of strong ambipolar heating are observed for a wide range of dust ratio for the millimeter grains (and $\gtrsim$ 100 μm in some models).

- Stratified models. I have shown that millimeter grains seem to settle efficiently in the disk mid-plane ($z < 1-2\,H$) and are strongly depleted above $1-2\,H$. In addition, above $1-2\,H$, I observe current structures that are similar to those of unstratified models. It is important to note that, at this stage, the stratified model STR-OAD1700R1 fails to reproduce some aspects of similar models of the literature, e.g. it has a very large α. I am still carefully investigating this puzzling discrepancy. It could be due for example to an insufficient resolution or differences with the literature in the treatment of the mid-plane boundaries.

Chapter 7

Conclusions and perspectives

Jack Sparrow

"No survivors? Then where do the stories come from, I wonder."

- Pirates of the Caribbean

In this PhD thesis, I presented my work dedicated to the study of the early stages of low mass star and planet formation. More particularly, I have put a strong emphasize on dust dynamics and its relation to star formation. This thesis was carried out with the help of both numerical and theoretical tools, I will now present a short summary of its content.

In the chapter 1, I have reviewed some of the essential knowledge of star formation in the theoretical, observational and numerical point of view. I also explained why the dust is an essential component of the star and planet forming interstellar medium. In particular, I have shown that its dynamics, while being largely overlooked, might strongly differ from the gas.

In chapter 2, I presented our current understanding of the dynamics of small neutral grains. After a description of the interaction between a gas and a single dust grain, I presented neutral dust dynamics using a fluid approach. Starting from a multifluid approach for the dynamical equations of gas and dust mixtures, I described how they can be reformulated as a monofluid composed of several phases but with a single advection velocity. Then, I introduced the so-called terminal velocity and diffusion approximations that greatly simplify the monofluid set of equations in the presence of strongly coupled gas and dust mixture. Eventually, I proposed an extension of this formalism to the study of neutral grains in a magnetohydrodynamical context.

In chapter 3, I introduced the main numerical tool used in this thesis, i.e. the `RAMSES` code (Teyssier, 2002). Then, I described the dust dynamics solver that I implemented in the code and that I presented in Lebreuilly et al. (2019). After a description of the principle of my dust dynamics scheme, I benchmarked it against a wide battery of tests all designed to isolated different aspects of the algorithm, i.e. DUSTYADVECT, DUSTYDIFFUSE, DUSTYSHOCK, DUSTYWAVE, a wave propagation test and a SETTLING test. These canonical tests have all been successfully passed by the solver I that implemented which, in addition, proved to be fast and efficient.

In chapter 4, the core of this thesis, I have presented the first 3D protostellar collapse simulations with multiple dust species DUSTYCOLLAPSES. After a description of my methods, I first presented spherical collapse simulations with only one dust species at a time. With these models, I verified that we retrieve the expected free-fall timescale for strongly coupled gas and dust mixtures and also provided a simplified view of DUSTYCOLLAPSES. I then increased the complexity of the DUSTYCOLLAPSES by considering initial solid body rotation, multiple dust species and, in some models, magnetic fields. I have shown that dust grains can decouple significantly from the gas provided that they were large enough (typically $\gtrsim 10 - 100$ µm). However, this

decoupling strongly depends on the initial cloud properties. Conversely, I have also shown that standard MRN dust size distributions, that have a maximum grain size of ~ 0.1 µm, remain very well preserved during the collapse in absence of coagulation/fragmentation of the dust grains. I demonstrated that the cumulative back-reaction of dust grains on the gas is negligible during the collapse for initial dust-to-gas ratio of less than 1%. In addition, I presented a semi-analytical model of dust enrichment. It has shown that during the collapse, the dust-to-gas ratio varies exponentially with the Stokes number, the ratio between the stopping time of the grain and the free-fall timescale of the gas.

In chapter 5, I proposed another extension of the monofluid formalism that is designed to the study of strongly coupled charged dust+ions+electron+neutral mixture. After a description of the derivation of this so-called dustyMHD formalism, I highlighted the main dynamical regimes that it holds. Eventually, I analyzed the critical maximum grain size required for a grain to couple to the magnetic fields in various astrophysical objects such as the protostellar collapse, protoplanetary disks, the cold and warm neutral medium and molecular clouds.

In the chapter 6, I presented the early developments of an ambitious project that aims to study a possible mechanism of chondrule formation in the current sheets of weakly ionized protoplanetary disks. After reviewing the basic theoretical framework necessary to understand protoplanetary disks, I presented unstratified shearing box calculations that simultaneously include three neutral dust species. I have shown that complex sheet-like current structures, similar to current sheets, are formed in the early times of these models and that they strongly affect the dust dynamics for grains of size $\gtrsim 100$ µm. Then, I presented the direct perspectives of this study which are, to introduce the disk heating and cooling, Lagrangian tracer particles for the dust and vertical stratification of the disk.

After this work, many direct prospects could be imagined. In the upcoming years, dusty protostellar collapse calculations will increase in complexity. Among other things I intend to

- evolve them over a long time after the first-core formation using sink particles similarly to Hennebelle et al. (2020).
- self-consistently estimate the resistivities accounting for the dependency on the local dust distribution.
- include a better treatment of the radiation with the use of the flux limited diffusion and a self-consistent estimate of the dust opacity.

These developments should be extremely valuable to constrain dust dynamics during the collapse. In addition, these models will be computed with an accurate treatment of dust growth currently in development at CRAL (Lombart & Laibe, 2019) and that I will soon couple to my `RAMSES` dust module. A direct step, that follows the work I carried out in chapter 5, is to include the dynamics of charged grains in my dust solver and to carry simulations of charged dust dynamics of the protostellar collapse, protoplanetary disks, the cold and warm neutral medium and molecular clouds. A particular attention to the three last objects will be payed since they are the ones where dust grains might be the most coupled to magnetic fields. Naturally, I plan to continue to carry the project to study chondrule formation according to the prospects that I discussed in chapter 6.

List of Figures

List of Tables

Bibliography

Alexander, C. M. O. D., Grossman, J. N., Ebel, D. S., & Ciesla, F. J. 2008, Science, 320, 1617

Alexander, R., Pascucci, I., Andrews, S., Armitage, P., & Cieza, L. 2014, in Protostars and Planets VI, ed. H. Beuther, R. S. Klessen, C. P. Dullemond, & T. Henning, 475

Alfvén, H. 1942, Nature, 150, 405

Allen, A., Li, Z.-Y., & Shu, F. H. 2003a, The Astrophysical Journal, 599, 363

Allen, A., Shu, F. H., & Li, Z.-Y. 2003b, The Astrophysical Journal, 599, 351

André, P. 2002, in EAS Publications Series, Vol. 3, EAS Publications Series, ed. J. Bouvier & J.-P. Zahn, 1–38

Andre, P., Ward-Thompson, D., & Barsony, M. 1993, The Astrophysical Journal, 406, 122

Andre, P., Ward-Thompson, D., & Barsony, M. 2000, Protostars and Planets IV, 59

Andre, P., Ward-Thompson, D., & Motte, F. 1996, Astronomy and Astrophysics, 314, 625

Andrews, S. M. 2020, arXiv e-prints, arXiv:2001.05007

Andrews, S. M., Huang, J., Pérez, L. M., et al. 2018, The Astrophysical Journal Letters, 869, L41

Andrews, S. M., Wilner, D. J., Hughes, A. M., Qi, C., & Dullemond, C. P. 2010, The Astrophysical Journal, 723, 1241

Aresu, G., Kamp, I., Meijerink, R., et al. 2011, Astronomy and Astrophysics, 526, A163

Bachiller, R. 1996, Annual Review of Astronomy and Astrophysics , 34, 111

Bai, X.-N. 2013, The Astrophysical Journal, 772, 96

Bai, X.-N. & Goodman, J. 2009, The Astrophysical Journal, 701, 737

Bai, X.-N. & Stone, J. M. 2013, The Astrophysical Journal, 769, 76

Balbus, S. A. & Hawley, J. F. 1991, The Astrophysical Journal, 376, 214

Balbus, S. A. & Terquem, C. 2001, The Astrophysical Journal, 552, 235

Ballabio, G., Dipierro, G., Veronesi, B., et al. 2018, Monthly Notices of the Royal Astronomical Society, 477, 2766

Barenblatt, G. 1952, Prikladnaya Matematika i Mekhanika, 16, 679

Barnard, E. E. 1907, The Astrophysical Journal, 25, 218

Barnard, E. E. 1910, The Astrophysical Journal, 31, 8

Barosch, J., Ebel, D. S., Hezel, D. C., Alpert, S., & Palme, H. 2020, Earth and Planetary Science Letters, 542, 116286

Barsony, M. 1994, Astronomical Society of the Pacific Conference Series, Vol. 65, Class 0 Protostars, ed. D. P. Clemens & R. Barvainis, 197

Bate, M. R. & Lorén-Aguilar, P. 2017, Monthly Notices of the Royal Astronomical Society, 465, 1089

Belloche, A. 2013, in EAS Publications Series, Vol. 62, EAS Publications Series, ed. P. Hennebelle & C. Charbonnel, 25–66

Berger, M. J. & Oliger, J. 1984, Journal of Computational Physics, 53, 484

Béthune, W., Lesur, G., & Ferreira, J. 2017, Astronomy and Astrophysics, 600, A75

Birnstiel, T., Dullemond, C. P., & Brauer, F. 2009, Astronomy and Astrophysics, 503, L5

Birnstiel, T., Fang, M., & Johansen, A. 2016, Space Science Reviews, 205, 41

Blum, J. & Wurm, G. 2008, Annual Review of Astronomy and Astrophysics , 46, 21

Bodenheimer, P. 1995, Annual Review of Astronomy and Astrophysics , 33, 199

Bodenheimer, P. & Tscharnuter, W. 1979, Astronomy and Astrophysics, 74, 288

Borucki, W. J., Koch, D. G., Basri, G., et al. 2011, The Astrophysical Journal, 736, 19

Boss, A. P. 1980, The Astrophysical Journal, 237, 563

Boss, A. P. 1996, in Chondrules and the Protoplanetary Disk, 257–263

Boss, A. P. & Bodenheimer, P. 1979, The Astrophysical Journal, 234, 289

Brandenburg, A. & Zweibel, E. G. 1994, The Astrophysical Journal Letters, 427, L91

Brauer, F., Dullemond, C. P., & Henning, T. 2008, Astronomy and Astrophysics, 480, 859

Cadiou, C., Dubois, Y., & Pichon, C. 2019, Astronomy and Astrophysics, 621, A96

Charbonneau, D., Berta, Z. K., Irwin, J., et al. 2009, Nature, 462, 891

Chiang, E. 2008, The Astrophysical Journal, 675, 1549

Clausius, R. 1870, The London, Edinburgh, and Dublin Philosophical Magazine and Journal of Science, 40, 122

Colling, C., Hennebelle, P., Geen, S., Iffrig, O., & Bournaud, F. 2018, Astronomy and Astrophysics, 620, A21

Commerçon, B., Debout, V., & Teyssier, R. 2014, Astronomy and Astrophysics, 563, A11

Commerçon, B., Hennebelle, P., Audit, E., Chabrier, G., & Teyssier, R. 2008, Astronomy and Astrophysics, 482, 371

Commerçon, B., Teyssier, R., Audit, E., Hennebelle, P., & Chabrier, G. 2011, Astronomy and Astrophysics, 529, A35

Commerçon, B., Hennebelle, P., Audit, E., Chabrier, G., & Teyssier, R. 2010, Astronomy and Astrophysics, 510, L3

Commerçon, B., Hennebelle, P., & Henning, T. 2011, The Astrophysical Journal Letters, 742, L9

Connolly, H. C., J. & Love, S. G. 1998, Science, 280, 62

Connolly, Harold C., J., Jones, B. D., & Hewins, R. H. 1998, Geochimica et Cosmochimica Acta, 62, 2725

Courant, R., Friedrichs, K., & Lewy, H. 1928, Mathematische Annalen, 100, 32

Courant, R., Isaacson, E., & Rees, M. 1952, Communications on Pure and Applied Mathematics, 5, 243

Desch, S. J. & Connolly, H. C., J. 2002, Meteoritics and Planetary Science, 37, 183

Dipierro, G. & Laibe, G. 2017, Monthly Notices of the Royal Astronomical Society, 469, 1932

Dipierro, G., Laibe, G., Alexander, R., & Hutchison, M. 2018a, Monthly Notices of the Royal Astronomical Society, 479, 4187

Dipierro, G., Laibe, G., Alexander, R., & Hutchison, M. 2018b, Monthly Notices of the Royal Astronomical Society, 479, 4187

Dipierro, G., Price, D., Laibe, G., et al. 2015, Monthly Notices of the Royal Astronomical Society, 453, L73

Draine, B. T. 1985, in Protostars and Planets II, ed. D. C. Black & M. S. Matthews, 621–640

Draine, B. T. 2004, in The Cold Universe, 213

Draine, B. T. 2011, Physics of the Interstellar and Intergalactic Medium

Draine, B. T., Roberge, W. G., & Dalgarno, A. 1983, The Astrophysical Journal, 264, 485

Draine, B. T. & Sutin, B. 1987, The Astrophysical Journal, 320, 803

Drążkowska, J., Alibert, Y., & Moore, B. 2016, Astronomy and Astrophysics, 594, A105

Dubois, Y. & Commerçon, B. 2016, Astronomy and Astrophysics, 585, A138

Duffin, D. F. & Pudritz, R. E. 2008, Monthly Notices of the Royal Astronomical Society, 391, 1659

Elbakyan, V. G., Johansen, A., Lambrechts, M., Akimkin, V., & Vorobyov, E. I. 2020, Astronomy and Astrophysics, 637, A5

Epstein, P. S. 1924, Physical Review, 23, 710

Evans, C. R. & Hawley, J. F. 1988, The Astrophysical Journal, 332, 659

Field, G. B. 1965, The Astrophysical Journal, 142, 531

Fleming, T. P., Stone, J. M., & Hawley, J. F. 2000, The Astrophysical Journal, 530, 464

Foster, P. N. & Chevalier, R. A. 1993, The Astrophysical Journal, 416, 303

Friedrich, J. M., Weisberg, M. K., Ebel, D. S., et al. 2015, Chemie der Erde / Geochemistry, 75, 419

Fromang, S., Hennebelle, P., & Teyssier, R. 2006, Astronomy and Astrophysics, 457, 371

Fromang, S., Latter, H., Lesur, G., & Ogilvie, G. I. 2013, Astronomy and Astrophysics, 552, A71

Fromang, S. & Papaloizou, J. 2006, Astronomy and Astrophysics, 452, 751

Fromang, S., Terquem, C., & Balbus, S. A. 2002, Monthly Notices of the Royal Astronomical Society, 329, 18

Fu, R. R., Weiss, B. P., Lima, E. A., et al. 2014, Science, 346, 1089

Fujii, Y. I., Okuzumi, S., & Inutsuka, S.-i. 2011, The Astrophysical Journal, 743, 53

Galametz, M., Maury, A. J., Valdivia, V., et al. 2019, Astronomy and Astrophysics, 632, A5

Galli, D. & Shu, F. H. 1993, The Astrophysical Journal, 417, 220

Gammie, C. F. 1996, The Astrophysical Journal, 457, 355

Gamow, G. & Hynek, J. A. 1945, The Astrophysical Journal, 101, 249

Godunov, S. K. 1959, Mat. Sb. (N.S.), 47(89), 271

Gonzalez, J.-F., Laibe, G., & Maddison, S. T. 2017, Monthly Notices of the Royal Astronomical Society, 467, 1984

Gonzalez, J. F., Laibe, G., Maddison, S. T., Pinte, C., & Ménard, F. 2015, Monthly Notices of the Royal Astronomical Society, 454, L36

González, M., Vaytet, N., Commerçon, B., & Masson, J. 2015, Astronomy and Astrophysics, 578, A12

Gould, R. J. & Salpeter, E. E. 1963, The Astrophysical Journal, 138, 393

Gressel, O., Ramsey, J. P., Brinch, C., et al. 2020, arXiv e-prints, arXiv:2005.03431

Gressel, O., Turner, N. J., Nelson, R. P., & McNally, C. P. 2015, The Astrophysical Journal, 801, 84

Guillet, T. & Teyssier, R. 2011, Journal of Computational Physics, 230, 4756

Guillet, V., Pineau Des Forêts, G., & Jones, A. P. 2007, Astronomy and Astrophysics, 476, 263

Harten, A. 1983, Journal of Computational Physics, 49, 357

Harten, A., D. Lax, P., & van Leer, B. 1983, 25, 35

Hawley, J. F., Gammie, C. F., & Balbus, S. A. 1995, The Astrophysical Journal, 440, 742

Hayashi, C. 1981, Progress of Theoretical Physics Supplement, 70, 35

Hennebelle, P., Commerçon, B., Chabrier, G., & Marchand, P. 2016, The Astrophysical Journal Letters, 830, L8

Hennebelle, P., Commerçon, B., Lee, Y.-N., & Charnoz, S. 2020, Astronomy and Astrophysics, 635, A67

Hennebelle, P. & Fromang, S. 2008, Astronomy and Astrophysics, 477, 9

Hennebelle, P., Lesur, G., & Fromang, S. 2017, Astronomy and Astrophysics, 599, A86

Hennebelle, P. & Teyssier, R. 2008, Astronomy and Astrophysics, 477, 25

Hewins, R. H. & Connolly, H. C., J. 1996, in Chondrules and the Protoplanetary Disk, 197–204

Hill, G. W. 1878, American Journal of Mathematics, 1, 5

Hincelin, U., Commerçon, B., Wakelam, V., et al. 2016, The Astrophysical Journal, 822, 12

Hopkins, P. F. & Lee, H. 2016, Monthly Notices of the Royal Astronomical Society, 456, 4174

Hopkins, P. F. & Squire, J. 2018, Monthly Notices of the Royal Astronomical Society, 479, 4681

Hopkins, P. F., Squire, J., & Seligman, D. 2020, Monthly Notices of the Royal Astronomical Society

Hoyle, F. 1960, Quarterly Journal of the Royal Astronomical Society, 1, 28

Huang, J., Andrews, S. M., Dullemond, C. P., et al. 2018a, The Astrophysical Journal Letters, 869, L42

Huang, J., Andrews, S. M., Pérez, L. M., et al. 2018b, The Astrophysical Journal Letters, 869, L43

Hubbard, A. & Ebel, D. S. 2015, Icarus, 245, 32

Hubbard, A., McNally, C. P., & Mac Low, M.-M. 2012, The Astrophysical Journal, 761, 58

Huss, G. R., Alexander, C. M. O., Palme, H., Bland , P. A., & Wasson, J. T. 2005, in Astronomical Society of the Pacific Conference Series, Vol. 341, Chondrites and the Protoplanetary Disk, ed. A. N. Krot, E. R. D. Scott, & B. Reipurth, 701

Hutchison, M., Price, D. J., & Laibe, G. 2018, Monthly Notices of the Royal Astronomical Society, 476, 2186

Igea, J. & Glassgold, A. E. 1999, The Astrophysical Journal, 518, 848

Isella, A., Carpenter, J. M., & Sargent, A. I. 2009, The Astrophysical Journal, 701, 260

Jacquet, E. 2014, Icarus, 232, 176

Jacquet, E. & Marrocchi, Y. 2017, Meteoritics and Planetary Science, 52, 2672

Jaupart, E. & Laibe, G. 2020, Monthly Notices of the Royal Astronomical Society, 492, 4591

Jeans, J. H. 1902, Philosophical Transactions of the Royal Society of London Series A, 199, 1

Jessberger, E. K., Stephan, T., Rost, D., et al. 2001, Properties of Interplanetary Dust: Information from Collected Samples, 253

Johansen, A., Oishi, J. S., Mac Low, M.-M., et al. 2007, Nature, 448, 1022

Johansen, A., Youdin, A., & Mac Low, M.-M. 2009, The Astrophysical Journal Letters, 704, L75

Jones, R. H., Grossman, J. N., & Rubin, A. E. 2005, in Astronomical Society of the Pacific Conference Series, Vol. 341, Chondrites and the Protoplanetary Disk, ed. A. N. Krot, E. R. D. Scott, & B. Reipurth, 251

Joos, M., Hennebelle, P., & Ciardi, A. 2012, Astronomy and Astrophysics, 543, A128

Joung, M. K. R., Mac Low, M.-M., & Ebel, D. S. 2004, The Astrophysical Journal, 606, 532

Kanagawa, K. D., Ueda, T., Muto, T., & Okuzumi, S. 2017, The Astrophysical Journal, 844, 142

Kataoka, A., Muto, T., Momose, M., et al. 2015, The Astrophysical Journal, 809, 78

Kataoka, A., Tsukagoshi, T., Momose, M., et al. 2016, The Astrophysical Journal Letters, 831, L12

Keith, S. L. & Wardle, M. 2014, Monthly Notices of the Royal Astronomical Society, 440, 89

Kirchhoff, G. 1859, Wärme. Monatsberichte der Akademie der Wissenschaften zu Berlin, sessions of Dec, 1860, 783

Krapp, L., Benítez-Llambay, P., Gressel, O., & Pessah, M. E. 2019, The Astrophysical Journal Letters, 878, L30

Kunz, M. W. & Mouschovias, T. C. 2009, The Astrophysical Journal, 693, 1895

Kunz, M. W. & Mouschovias, T. C. 2010, Monthly Notices of the Royal Astronomical Society, 408, 322

Kwok, S. 1975, The Astrophysical Journal, 198, 583

Laibe, G. 2014, Monthly Notices of the Royal Astronomical Society, 437, 3037

Laibe, G. & Price, D. J. 2011, Monthly Notices of the Royal Astronomical Society, 418, 1491

Laibe, G. & Price, D. J. 2012a, Monthly Notices of the Royal Astronomical Society, 420, 2345

Laibe, G. & Price, D. J. 2012b, Monthly Notices of the Royal Astronomical Society, 420, 2365

Laibe, G. & Price, D. J. 2014a, Monthly Notices of the Royal Astronomical Society, 440, 2136

Laibe, G. & Price, D. J. 2014b, Monthly Notices of the Royal Astronomical Society, 440, 2147

Laibe, G. & Price, D. J. 2014c, Monthly Notices of the Royal Astronomical Society, 444, 1940

Larson, R. B. 1969, Monthly Notices of the Royal Astronomical Society, 145, 271

Lax, P. & Wendroff, B. 1960, Communications on Pure and Applied Mathematics, 13, 217

Lazarian, A. & Hoang, T. 2007, Monthly Notices of the Royal Astronomical Society, 378, 910

Lebreuilly, U., Commerçon, B., & Laibe, G. 2019, Astronomy and Astrophysics, 626, A96

Lee, H., Hopkins, P. F., & Squire, J. 2017, Monthly Notices of the Royal Astronomical Society, 469, 3532

Lesur, G., Kunz, M. W., & Fromang, S. 2014, Astronomy and Astrophysics, 566, A56

Leu, M. T., Biondi, M. A., & Johnsen, R. 1973, Physical Review A, 7, 292

Li, Z.-Y., Krasnopolsky, R., & Shang, H. 2011, The Astrophysical Journal, 738, 180

Lin, M.-K. 2019, Monthly Notices of the Royal Astronomical Society, 485, 5221

Lofgren, G. & Lanier, A. B. 1990, Geochimica et Cosmochimica Acta, 54, 3537

Lombart, M. & Laibe, G. 2019, in SF2A-2019: Proceedings of the Annual meeting of the French Society of Astronomy and Astrophysics, Di

Lovascio, F. & Paardekooper, S.-J. 2019, Monthly Notices of the Royal Astronomical Society, 488, 5290

Love, S. G., Joswiak, D. J., & Brownlee, D. E. 1994, Icarus, 111, 227

Machida, M. N., Inutsuka, S.-i., & Matsumoto, T. 2014, Monthly Notices of the Royal Astronomical Society, 438, 2278

Marchand, P., Masson, J., Chabrier, G., et al. 2016, Astronomy and Astrophysics, 592, A18

Marchand, P., on, B., & Chabrier, G. 2018, Astronomy and Astrophysics

Marchand, P., Tomida, K., Commerçon, B., & Chabrier, G. 2019, Astronomy and Astrophysics, 631, A66

Masson, J., Chabrier, G., Hennebelle, P., Vaytet, N., & Commerçon, B. 2016, Astronomy and Astrophysics, 587, A32

Masson, J., Teyssier, R., Mulet-Marquis, C., Hennebelle, P., & Chabrier, G. 2012, The Astrophysical Journal Supplement Series, 201, 24

Masunaga, H. & Inutsuka, S.-i. 2000, The Astrophysical Journal, 531, 350

Mathis, J. S., Rumpl, W., & Nordsieck, K. H. 1977, The Astrophysical Journal, 217, 425

Maury, A. J., André, P., Testi, L., et al. 2019, Astronomy and Astrophysics, 621, A76

Maury, A. J., Girart, J. M., Zhang, Q., et al. 2018, Monthly Notices of the Royal Astronomical Society, 477, 2760

Mayor, M. & Queloz, D. 1995, Nature, 378, 355

McKee, C. F. & Ostriker, E. C. 2007, Annual Review of Astronomy and Astrophysics , 45, 565

McNally, C. P., Hubbard, A., Mac Low, M.-M., Ebel, D. S., & D'Alessio, P. 2013, The Astrophysical Journal Letters, 767, L2

McNally, C. P., Hubbard, A., Yang, C.-C., & Mac Low, M.-M. 2014, The Astrophysical Journal, 791, 62

Mellon, R. R. & Li, Z.-Y. 2008, The Astrophysical Journal, 681, 1356

Mellon, R. R. & Li, Z.-Y. 2009, The Astrophysical Journal, 698, 922

Mendoza V., E. E. 1968, The Astrophysical Journal, 151, 977

Miyoshi, T. & Kusano, K. 2005, Journal of Computational Physics, 208, 315

Mouschovias, T. C. & Spitzer, L., J. 1976, The Astrophysical Journal, 210, 326

Ogilvie, G. I. 2012, Monthly Notices of the Royal Astronomical Society, 423, 1318

Ohashi, N., Saigo, K., Aso, Y., et al. 2014, The Astrophysical Journal, 796, 131

Pagani, L., Steinacker, J., Bacmann, A., Stutz, A., & Henning, T. 2010, Science, 329, 1622

Papaloizou, J. & Lin, D. N. C. 1984, The Astrophysical Journal, 285, 818

Parker, E. N. 1966, The Astrophysical Journal, 145, 811

Parker, E. N. 1972, The Astrophysical Journal, 174, 499

Parker, E. N. 1994, Spontaneous current sheets in magnetic fields : with applications to stellar x-rays. International Series in Astronomy and Astrophysics, 1

Pinte, C., van der Plas, G., Ménard, F., et al. 2019, Nature Astronomy, 3, 1109

Pohl, A., Kataoka, A., Pinilla, P., et al. 2016, Astronomy and Astrophysics, 593, A12

Price, D. J. & Bate, M. R. 2007, Astrophysics and Space Science, 311, 75

Price, D. J., Cuello, N., Pinte, C., et al. 2018, Monthly Notices of the Royal Astronomical Society, 477, 1270

Price, D. J. & Laibe, G. 2015, Monthly Notices of the Royal Astronomical Society, 454, 2320

Price, D. J., Wurster, J., Nixon, C., et al. 2017, PHANTOM: Smoothed particle hydrodynamics and magnetohydrodynamics code, Astrophysics Source Code Library

Radomsky, P. M. & Hewins, R. H. 1990, Geochimica et Cosmochimica Acta, 54, 3475

Ragusa, E., Dipierro, G., Lodato, G., Laibe, G., & Price, D. J. 2017, Monthly Notices of the Royal Astronomical Society, 464, 1449

Riols, A. & Lesur, G. 2018, Astronomy and Astrophysics, 617, A117

Riols, A., Lesur, G., & Menard, F. 2020, arXiv e-prints, arXiv:2006.01194

Roe, P. L. 1986, Annual Review of Fluid Mechanics, 18, 337

Rosdahl, J., Blaizot, J., Aubert, D., Stranex, T., & Teyssier, R. 2013, Monthly Notices of the Royal Astronomical Society, 436, 2188

Rosdahl, J. & Teyssier, R. 2015, Monthly Notices of the Royal Astronomical Society, 449, 4380

Ruge, J. P., Flock, M., Wolf, S., et al. 2016, Astronomy and Astrophysics, 590, A17

Sadavoy, S. I., Myers, P. C., Stephens, I. W., et al. 2018a, The Astrophysical Journal, 859, 165

Sadavoy, S. I., Myers, P. C., Stephens, I. W., et al. 2018b, The Astrophysical Journal, 869, 115

Sadavoy, S. I., Stephens, I. W., Myers, P. C., et al. 2019, The Astrophysical Journal Supplement Series, 245, 2

Saffman, P. G. 1962, Journal of Fluid Mechanics, 13, 120

Sano, T., Miyama, S. M., Umebayashi, T., & Nakano, T. 2000, The Astrophysical Journal, 543, 486

Shakura, N. I. & Sunyaev, R. A. 1976, Monthly Notices of the Royal Astronomical Society, 175, 613

Sharma, P., Colella, P., & Martin, D. F. 2009, ArXiv e-prints

Shu, F. H., Adams, F. C., & Lizano, S. 1987, Annual Review of Astronomy and Astrophysics , 25, 23

Simpson, I. C. 1978, Astrophysics and Space Science, 57, 381

Sod, G. A. 1978, Journal of Computational Physics, 27, 1

Spitzer, Lyman, J. 1941, The Astrophysical Journal, 93, 369

Spitzer, L. 1978, Physical processes in the interstellar medium

Squire, J. & Hopkins, P. F. 2018, Monthly Notices of the Royal Astronomical Society, 477, 5011

Stone, J. M., Hawley, J. F., Gammie, C. F., & Balbus, S. A. 1996, The Astrophysical Journal, 463, 656

Suresh, A. 2000, SIAM J. Sci. Comput., 22, 1184–1198

Suzuki, T. K., Ogihara, M., Morbidelli, A. r., Crida, A., & Guillot, T. 2016, Astronomy and Astrophysics, 596, A74

Terebey, S., Shu, F. H., & Cassen, P. 1984, The Astrophysical Journal, 286, 529

Teyssier, R. 2002, Astronomy and Astrophysics, 385, 337

Teyssier, R. & Commerçon, B. 2019, Frontiers in Astronomy and Space Sciences, 6, 51

Teyssier, R., Fromang, S., & Dormy, E. 2006, Journal of Computational Physics, 218, 44

Tobin, J. J., Sheehan, P. D., Megeath, S. T., et al. 2020, The Astrophysical Journal, 890, 130

Tomida, K. 2014, The Astrophysical Journal, 786, 98

Tomida, K., Okuzumi, S., & Machida, M. N. 2015, The Astrophysical Journal, 801, 117

Toro, E. F. 2013, Riemann solvers and numerical methods for fluid dynamics: a practical introduction (Springer Science & Business Media)

Tricco, S. T., Price, J. D., & Laibe, G. 2017, MNRAS

Truelove, J. K., Klein, R. I., McKee, C. F., et al. 1997, The Astrophysical Journal Letters, 489, L179

Trumpler, R. J. 1930, Publications of the Astronomical Society of the Pacific, 42, 267

Tsukamoto, Y., Iwasaki, K., Okuzumi, S., Machida, M. N., & Inutsuka, S. 2015, The Astrophysical Journal Letters, 810, L26

Tychoniec, Ł., Manara, C. F., Rosotti, G. P., et al. 2020, arXiv e-prints, arXiv:2006.02812

Umebayashi, T. & Nakano, T. 1980, Publications of the Astronomical Society of Japan, 32, 405

Umebayashi, T. & Nakano, T. 1981, Publications of the Astronomical Society of Japan, 33, 617

Umebayashi, T. & Nakano, T. 1990, Monthly Notices of the Royal Astronomical Society, 243, 103

Umebayashi, T. & Nakano, T. 2009, The Astrophysical Journal, 690, 69

Valdivia, V., Maury, A., Brauer, R., et al. 2019, Monthly Notices of the Royal Astronomical Society, 488, 4897

van Leer, B. 1974, Journal of Computational Physics, 14, 361

van Leer, B. 1979, Journal of Computational Physics, 32, 101

Vaytet, N., Commerçon, B., Masson, J., González, M., & Chabrier, G. 2018a, ArXiv e-prints

Vaytet, N., Commerçon, B., Masson, J., González, M., & Chabrier, G. 2018b, Astronomy and Astrophysics, 615, A5

Von Weizsäcker, C. F. 1944, Z. Astrophys., 22

Vorobyov, E. I. & Elbakyan, V. G. 2019, Astronomy and Astrophysics, 631, A1

Vorobyov, E. I., Skliarevskii, A. M., Elbakyan, V. G., et al. 2019, Astronomy and Astrophysics, 627, A154

Wardle, M. 1998, Monthly Notices of the Royal Astronomical Society, 298, 507

Wardle, M. & Ng, C. 1999, Monthly Notices of the Royal Astronomical Society, 303, 239

Weingartner, J. C. & Draine, B. T. 2001, The Astrophysical Journal, 548, 296

Whitworth, A. P. & Clarke, C. J. 1997, Monthly Notices of the Royal Astronomical Society, 291, 578

Wurster, J., Bate, M. R., & Price, D. J. 2018, Monthly Notices of the Royal Astronomical Society, 475, 1859

Wurster, J., Bate, M. R., & Price, D. J. 2019, Monthly Notices of the Royal Astronomical Society, 489, 1719

Wurster, J., Price, D. J., & Bate, M. R. 2016, Monthly Notices of the Royal Astronomical Society, 457, 1037

Yamamoto, T., Kadono, T., & Wada, K. 2014, The Astrophysical Journal Letters, 783, L36

Youdin, A. N. & Goodman, J. 2005, The Astrophysical Journal, 620, 459

Zhao, B., Caselli, P., Li, Z.-Y., et al. 2016, Monthly Notices of the Royal Astronomical Society, 460, 2050